Hot Carrier Assisted Plasmonic Photocatalysis

by Ajay Peter Manuel

A thesis submitted in partial fulfillment of the requirements for the degree of
Doctor of Philosophy

in

Microsystems and Nanodevices

Department of Electrical and Computer Engineering
University of Alberta

Abstract

Plasmonic photocatalysis has drawn immense interest due to the innovative possibilities it provides in harnessing photonic energies across the full width of the solar spectrum to drive chemical reactions. Plasmonic noble metal nanoparticles are excellent light absorbers and their ability to focus light into small volumes have led to their use in a variety of applications from bio-molecular sensing, surface catalytic reactions, and as light concentrators for solar energy cells.

These abilities are enabled by the excitation of localized surface plasmon resonances, the coherent oscillations of conduction electrons, within metal nanoparticles. Metals such as gold and silver are particularly popular due to their resonances in the visible region of the electromagnetic spectrum. Utilizing solar energy to drive catalytic chemical reactions is often touted as an environmentally friendly alternative. There has been a tremendous amount of research dedicated to design metal nanostructures, modulate their resonance frequencies, and provide for systems that can enhance electromagnetic fields over the full width of the solar spectrum. The incorporation of metal nanoparticles that can absorb visible light with green semiconductor photocatalysts to form composite plasmonic photocatalytic systems that are far more efficient than their individual counterparts has been a major objective of the field. Nevertheless, there remains much to be learned and understood of the physical processes involving the dynamics of high-energy charge carriers or hot carriers that facilitate the catalytic potential of these unique systems.

This thesis begins by providing a comprehensive overview of the rich history of the field alongside the latest developments and issues for advanced research in hot carrier mediated plasmonic photocatalysis. In-depth discussions on the constituent components of a plasmonic system including the optical properties of noble metal nanoparticles, and the current landscape of noble metal-semiconductor heterojunction photocatalysis are considered. Further insights are provided via electromagnetic finite-difference time-domain simulations that have been extensively performed to guide various experiments and optimize relevant systems. With an incentive toward understanding the deeper fundamental roles of hot carrier phenomena and the relevant charge carrier dynamics in metal nanoparticles to facilitate plasmonic photocatalysis, we begin by examining monometallic silver nanoislands. This is followed by the study of gold nanoislands organized in a bimetallic heterostructure involving a plasmonic gold core and a catalytic platinum shell.

Research into the monometallic and bimetallic nanostructures provides for a comparative study on overcoming the chemical inertness of noble metals by incorporating them alongside another metal that is catalytic in nature. Facile and highly reproducible fabrication techniques involving physical vapor deposition methods are identified and exclusively utilized to build these monometallic and bimetallic nanoisland structures. Primary characterization techniques including ultraviolet-visible spectroscopy, and Raman spectroscopy are utilized to identify the plasmonic potential of these structures. Photocatalytic tests involving surface catalytic reactions with aromatic thiols, surface enhanced Raman spectroscopy, dye degradation, and Raman thermometry provide greater insights into the hot carrier dynamics within these systems. These efforts are extensively supplemented by knowledge from theoretical collaborations in other projects, involving electromagnetic simulations, on the optical characteristics of diverse plasmon-enhanced photocatalytic substrates including nanotubes, nanocubes, nanodimples, nanofractals as well as other exotic nanoparticle morphologies including nanoprisms, nanorods, nanoshells, and trimetallic heterostructures.

We conclude by discussing future directions of research that can be pursued building on what we have learned thus far on physical vapor deposition-based nanostructure fabrication, and plasmonic charge-carrier dynamics in monometallic and bimetallic heterostructures. Critical remarks on the limitations of existing systems and their optimization as potential plasmonic platforms in diverse photocatalytic applications are also provided.

Preface

The work presented in this thesis was completed at the Department of Electrical and Computer Engineering of the University of Alberta. The thesis follows a hybrid format combining elements of a traditional and manuscript-based thesis.

Chapter 1 of this thesis is adapted from material that has been discussed in the candidacy report, the lecture transcripts I developed as a guest lecturer on plasmonics in the ECE 458 – MicroElectroMechanical Systems course supervised by Karthik Shankar, and in a recent review article published and authored by Manuel, Ajay P., Shankar, Karthik, titled, “Hot Electrons in TiO_2 – Noble Metal Nano-Heterojunctions: Fundamental Science and Applications in Photocatalysis” to *Nanomaterials* (2021). I am the primary author and editor of the manuscript. Karthik Shankar was the supervisory author.

Chapter 2 of this thesis is adapted from material that has been discussed in the candidacy report and in a recent review article published and authored by Manuel, Ajay P., Shankar, Karthik, titled, “Hot Electrons in TiO_2 – Noble Metal Nano-Heterojunctions: Fundamental Science and Applications in Photocatalysis” to *Nanomaterials* (2021). I am the primary author and editor of the manuscript. Karthik Shankar was the supervisory author.

Chapter 3 of this thesis is adapted from material that has been discussed in the candidacy report and references collaborative efforts involving theoretical electromagnetic simulations I have provided for various research initiatives and publications in the Shankar group.

Chapter 4 of this thesis has been published as a research article authored by Manuel, Ajay P., Barya, Priyash, Riddell, Saralyn, Zeng, Sheng, Alam, Kazi M., and Shankar, Karthik, titled, “Plasmonic photocatalysis and SERS sensing using ellipsometrically modeled Ag nanoisland substrates,” *Nanotechnology*, Volume 31, Number 36 (19 June 2020). I was responsible for experimental design, data collection, analysis of results, and manuscript completion. Priyash Barya, Saralyn Riddell, Sheng Zeng, and Kazi M. Alam assisted with data collection. Karthik Shankar was the supervisory author.

Chapter 5 of this thesis is adapted from an upcoming and prospective journal submission authored by Manuel, Ajay P., Riddell, Saralyn, Rajashekhar, Harshitha, Vrushabendrakumar, Damini, Alam, Kazi M., Kumar, Pawan, Gusarov, Sergey, Kobryn, Alex, Supur, Mustafa, McCreery, Rick, and Shankar, Karthik, titled, “Bimetallic Au@Pt hemispherical core-shell nanoislands for plasmon-modulated photocatalysis.” I am the primary author of this paper and was responsible for experimental design, data collection, analysis of results, and manuscript completion. Saralyn Riddell, Harshitha Rajashekhar, Damini Vrushabendrakumar, Pawan Kumar, and Mustafa Supur, assisted with data collection. Kazi M. Alam assisted with data collection involving density functional theory studies and x-ray diffraction studies on the substrates with the primary simulation work for density functional theory being facilitated by collaborators Sergey Gusarov and Alex Kobryn at the National Institute for Nanotechnology. Rick McCreery was part of the collaboration and provided access concerning laboratory tests involving Stokes and anti-Stokes Raman thermometry. Karthik Shankar was the supervisory author.

To my loving wife, who has been my pillar of support and motivation,
throughout this adventure.

Acknowledgments

I would like to begin by thanking my supervisor Dr. Karthik Shankar for his outstanding mentorship. My Ph.D. has been a wonderful experience, and I have him to thank for facilitating a welcoming and open research environment that was very productive and enjoyable. I would also like to thank Dr. Shankar for his patience and excellent guidance amidst the long-drawn discussions I troubled him with at his office during the early days of my initiation in his group. Our discussions catalyzed my doctoral research and contributed toward easing my transition into the field of plasmonics, nanoelectronics, and experimental research. I would also like to thank Dr. Al Meldrum and Dr. Bob Fedosejevs for their advice and criticism during my candidacy exam. This was crucial in motivating me to go further in-depth with my research. I would also like to thank Dr. Rick McCreery in being accommodating with lab access and Dr. Mustafa Supur for his patience and assistance with several experiments that were crucial to my research.

Research is a collaborative effort. A large part of my success and the joy I have experienced in my doctoral studies is attributed to my peers and colleagues in the Shankar group. I would like to thank Saralyn Riddell who has been a constant presence of support and enthusiasm during my doctoral research. Saralyn, you have played a major role in all the research projects I have done, and your jovial and positive personality along with your monstrous work ethic has been inspiring and deeply motivating. I would like to thank Aarat Kalra for his intense questioning of my knowledge. The various discussions we have had over the years, despite hailing from different backgrounds, were highly stimulating for my research. My time in the Shankar lab was extremely pleasant and motivating. I have found lifelong friendships among the people I have met during my time in this group. For all the happiness and wonderful memories, my deepest gratitude goes to Ujwal Thakur, Ehsan Vahidzadeh, Sheng Zeng, Najia Mahdi, Ryan Kisslinger, Kazi Alam, Pawan Kumar, Arezoo Hosseini, Harshitha Rajashekhar, Damini Vrushabendrakumar, and Narendra Chaulagain.

I would also like to give a huge shout out to my loving wife Leina who has been an active source of support and encouragement throughout my doctoral studies. Your constant reminders on eating well and taking breaks from work helped my mental and physical health. I look forward to doing the same for you when you begin your doctoral studies down the road.

I would like to conclude by acknowledging the financial support I have received from the University of Alberta, Future Energy Systems, and the Natural Sciences and Engineering Research Council.

Table of Contents

List of Figures

List of Tables

List of Symbols

α	static polarizability
β	full width at half maximum
γ	damping constant/intraband damping frequency
γ_i	surface energy density
δ_i	material component fraction
ϵ	dielectric constant or electric permittivity
ϵ_0	permittivity of free space
ϵ_r	relative dielectric constant
ϵ_m	dielectric constant of medium
θ	x-ray diffraction peak position
κ	extinction coefficient
μ	magnetic permeability
μ_0	permeability of free space
λ	wavelength
ν	frequency
ξ	residual microstrain
ρ	free charge density
σ_i	refractive index of material component
σ_e	effective conductivity
σ_{ext}	extinction cross section
σ_{abs}	absorption cross section
σ_{sca}	scattering cross section
τ	relaxation time
χ	electric susceptibility
ω	angular frequency
ω_0	natural resonant frequency
ω_p	plasma frequency
ω_{LSPR}	localized surface plasmon resonance frequency
Ω	surface

a	radius of nanoparticle
c	speed of light
$\vec{B}$	total magnetic field
$\overrightarrow{B_I}$	incident magnetic field
$\overrightarrow{B_S}$	scattered magnetic field
$\vec{D}$	electric displacement
D	crystallite size
d	interparticle distance
$\vec{E}$	total electric field
$\overrightarrow{E_I}$	incident electric field
$\overrightarrow{E_S}$	scattered electric field
E_S	dewetting force
E_{CB}	conduction band energy
$E_{cut-off}$	cut-off energy
E_{VB}	valence band energy
E_{CB}'	intermediate conduction band energy
E_{VB}'	intermediate valence band energy
E_F	Fermi energy
$E_{reduction}$	reduction energy
$E_{oxidation}$	oxidation energy
E_{redox}	redox potential
e	electron charge
F_A	energy absorbed by nanoparticle
F_S	energy scattered by nanoparticle
F_{ext}	energy lost by nanoparticle
h	Planck's constant
I	light intensity
I_0	initial light intensity
I_S	Stokes intensity
I_{AS}	anti-Stokes intensity

i	imaginary number
$\vec{J}$	free current density
$\vec{k}$	wavevector
k_B	Boltzmann’s constant
k	spring constant
m_e	electron mass
m_0	effective mass of electron
N	number density
$\tilde{n}$	complex refractive index
n	refractive index
$\vec{n}$	surface normal
$\vec{P}$	dielectric polarization
$\vec{p}$	dipole moment
Q	quality factor
$\vec{r}$	position vector
r	distance
R	reflectivity
$\vec{S}$	total energy flux
$\overrightarrow{S_I}$	incident energy flux
$\overrightarrow{S_S}$	scattered energy flux
$\overrightarrow{S_{ext}}$	external energy flux
T	transmittance
V	volume
V_l	laser frequency
V_v	frequency of vibrational mode
W	work function
$\hat{x}$	unit vector in x-direction
x	displacement

List of Abbreviations

4-NBT	4-nitrobenzenethiol
BE	binding energy
CB	conduction band
CCD	charge-coupled device
CID	chemical interface damping
CNPQD	phosphorus doped carbon nitride quantum dots
DFT	density functional theory
DIET	dissociation induced by electronic transitions
DMAB	p,p'-dimercaptoazobenzene
DRS	diffuse reflectance spectroscopy
FDTD	finite-difference time-domain
EBIC	electron beam induced current
EDTA	ethylenediaminetetraacetic acid
EELS	electron energy loss spectroscopy
FANT	high-temperature flame-annealed nanotubes
FESEM	field emission scanning electron microscopy
FWHM	full width at half maximum
GGA	generalized gradient approximation
GUI	graphical user interface
HOMO	highest occupied molecular orbital
IFCT	interfacial charge transfer
IPA	isopropyl alcohol
I-V	current-voltage
LANT	low-temperature annealed nanotubes
LSPR	localized surface plasmon resonance
LUMO	lowest unoccupied molecular orbital
MB	methylene blue
MO	methyl orange
NHE	normal hydrogen electrode

NIH	national institutes of health
NINT	national institute for nanotechnology
NPs	nanoparticles
PATP	para-aminothiophenol
PBE	Perdew-Burke-Ernzerhof
PDOS	projected density of states
PHET	plasmonic hot electron transfer
PICTT	plasmon-induced interfacial charge-transfer transition
PL	photoluminescence
PVD	physical vapor deposition
R6G	rhodamine 6g
rGO	reduced graphene oxide
RTP	rapid thermal processing
SEM	scanning electron microscopy
SERS	surface enhanced Raman scattering
SHG	second harmonic generation
SNOM	single-particle near-field scanning optical microscopy
SPP	surface plasmon polariton
TNTA	titania nanotube arrays
STNTA	square titania nanotube arrays
UV	ultraviolet
UV-VIS	ultraviolet-visible
UV-Vis-NIR	ultraviolet-visible-near infrared
VASE	variable angle spectroscopic ellipsometry
VB	valence band
VMD	visual molecular dynamics
XPS	x-ray photoemission spectroscopy
XRD	x-ray diffraction

Chapter 1
Introduction

1.1 Solar Energy and Photocatalysis

Solar energy is among the cleanest, and most abundant renewable energy sources available to the world. Nature exploits this resource routinely in photosynthesis, a fundamental driving factor in the delicate balance of the global ecosystem. Photosynthesis is the process by which plants, algae, photosynthetic bacteria, and protists derive and capture sunlight along with CO_2 in the atmosphere and water as reactants to promote water-splitting chemistry: the reduction of CO_2 to carbohydrates, and other carbon-rich products as well as the decomposition of water to molecular oxygen which is crucial to the sustainability of the planet's biosphere.[1] The overall chemical reaction in photosynthesis can be described as,

$$6H_2O + 6CO_2 + \text{Sunlight} \rightarrow C_6H_{12}O_6 + 6O_2.$$

Amidst the rapidly rising global energy demand (17.4 Terrawatts (TW) in 2015 and a 2.2% growth averaged in 2017, the fastest since 2013)[2] and environmental crises, the efficient utilization of renewable solar energy in chemical transformations is extremely important for modern industry. For decades, fossil fuels have served as the go-to conventional energy sources to meet global energy demands and for sustainable economic development. 140,000 TWh of energy per year is consumed by mankind, more than 80% of which is accounted by fossil fuels: oil, coal, peat, and natural gas. Our energy consumption is predicted to increase to about twice the current value in 2050.[3,4] The dominance of fossil fuels in the global market infrastructure for energy generation and distribution is largely due to their availability, stability, and high energy density.[5] Over the last century, the proliferation of fossil fuel technology has led to dramatic increases in atmospheric CO_2 levels (up to 100 parts per million by volume),[6] with CO_2 emissions being identified as the major cause of global warming. Beyond the increasing need to mitigate this global crisis, fossil fuels are also a limited energy resource.

To address these issues, considerable effort has been placed on the implementation and development of renewable, environmental-friendly, artificial photocatalytic technologies to sustain modern civilization. The use of said artificial systems is to not only mimic photosynthesis but to improve our knowledge of the process and provide for its selective enhancement via artificial means. **(Figure 1.1)** Solar irradiation on our planet in just one hour equals our annual energy consumption. By tapping into even 0.02% of the incoming solar energy, we could satisfy all our current energy needs.[7,8] Diverse technologies including biological systems (algae), inorganic photocatalysts (transition metal oxides or semiconductors), organic photocatalysts (metal-organic complexes), biomimetic systems (enzyme-activated or dye-sensitized semiconductors), tandem cells, and z-schemes have been developed towards this goal. Among them, semiconductor photocatalysts have set the standard for artificial photocatalytic technology over the recent decade.

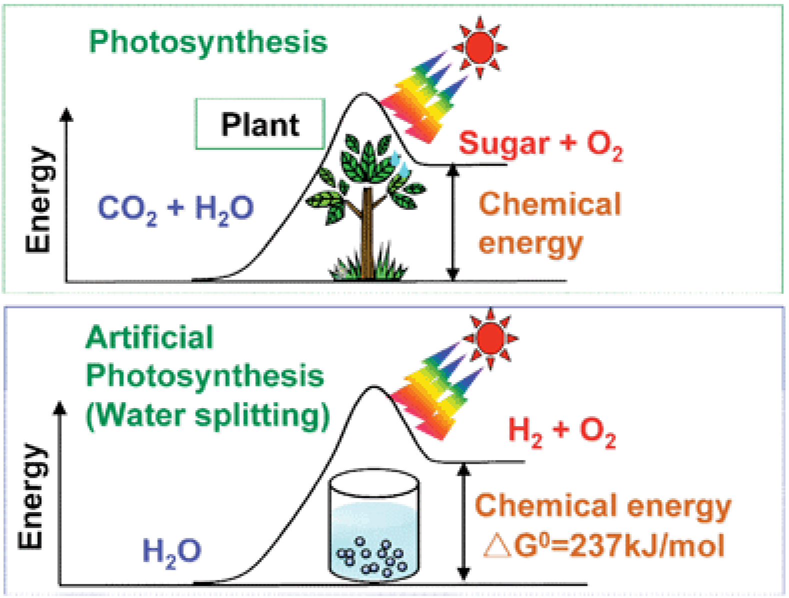

Figure 1.1. Artificial photosynthetic systems based on semiconductors use photocatalysis to provide alternative energetic pathways and selectivity in desirable chemical reactions such as water splitting, CO_2 photoreduction, and the degradation of harmful organic pollutants. Reprinted for academic use from Ref[9]. Copyright Royal Society of Chemistry (2008).

1.2 Semiconductor Photocatalysis

Semiconductor photocatalysts absorb photons to generate active electrons and holes that are then utilized to initiate chemical reduction and oxidation reactions.[10–12] **(Figure 1.2)** A viable semiconductor photocatalyst is distinguished by its abilities for optimal light absorption over a wide range of wavelengths, good band energetics that provide for efficient charge separation, high carrier mobility and long carrier diffusion lengths necessary for charge migration to initiate chemical reactions, as well as strong catalytic activity, stability, and from a commercial viewpoint, high sustainability and low cost. Various semiconductors have been considered as suitable candidates for photocatalysts including metal oxides, metal chalcogenides (group 16 elements including sulfides, selenides, tellurides, and polonides), metal nitrides, carbon nitrides, and III-V compounds.[13] In this front, titanium dioxide (TiO_2) has emerged as the benchmark material when it comes to a semiconductor photocatalyst thanks to its relatively low cost, high availability, low toxicity, stability in both acidic and basic media, and resistance to photocorossion.[14] Altogether, semiconductor photocatalysts have been demonstrated to be useful for a wide range of applications including wastewater treatment, air purification,[11] photoelectrochemical water splitting, carbon dioxide (CO_2) photoreduction and hydrogen (H_2) generation,[15] photocatalytic degradation/aerobic oxidation of organic compounds.[12,16] Yet, large-scale commercialization of semiconductor photocatalytic technology in the environmental and energy industries is still at its advent and remains to be fully exploited.

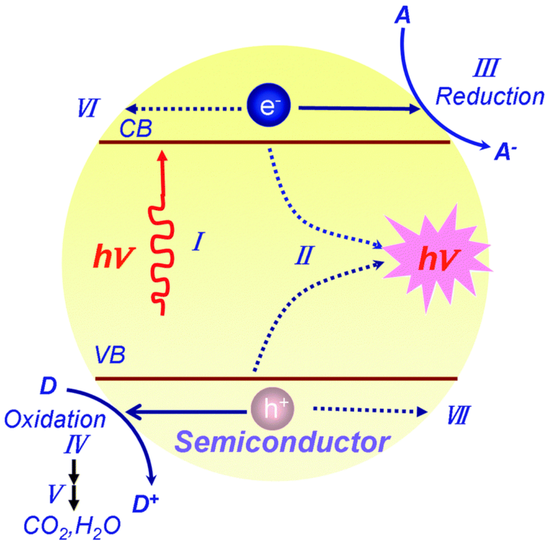

Figure 1.2. Schematic of the working principle and processes involved in semiconductor photocatalysis: (I) electrons and holes are excited via photonic excitation matching the energy bandgap of the semiconductor, (II) charge carrier recombination resulting in release of heat energy, (III) conduction band electrons utilized for reduction reactions, (IV) valence band holes utilized for oxidative reactions, (V) other thermal and photocatalytic reactions are facilitated, such as hydrolysis or reaction with active oxygen species, for mineralization of products, (VI) conduction band electron being trapped in a dangling surficial bond, and (VII) valence band hole trapped at the surface of a semiconductor.[17] Reprinted with permission from Ref[17]. Copyright Royal Society of Chemistry (2014).

This is because, despite their obvious advantages, critical material-related limitations in semiconductor photocatalysts have surfaced. Among many of these limitations, the most debilitating cases involve low photocatalytic efficiencies and a lack of satisfactory photocatalytic materials that are responsive in the visible-light regime.[10,18] The former is attributed to the recombination of excited electrons and holes in the semiconductor before their migration to the surface to initiate redox reactions. In homogeneous semiconductor materials, this migration is largely randomized in nature, resulting in high recombination and low photocatalytic efficiencies. The latter limitation concerns the fact that most commonly used semiconductors have wide band gaps (> 3.1 eV) and only absorb in the ultraviolet (UV) regime ($\lambda < 400$ nm) which consists of 4% of all incoming solar radiation.[13,19,20]

TiO_2, for instance, is a wide bandgap semiconductor (3.2 eV for anatase and 3.0 eV for the rutile phase), with a minority carrier (hole) diffusion length of 70 nm for anatase TiO_2 and 10 nm for rutile TiO_2, and primarily absorbs in the UV-spectrum.[21] Contrastingly, narrow bandgap semiconductors such as silicon (Si), and copper (II) oxide (Cu_2O) lack long-term catalytic efficiency, and photo-corrode easily. Other semiconductors such as iron oxide (Fe_2O_3) are inhibited by extremely low photocatalytic activity.[22] Furthermore, the use of UV light requires artificial light sources, and consequently, consumes electricity, making it less ideal. Although doping can be utilized to extend the light absorption range from the UV to visible wavelengths, the absorption coefficient and photocatalytic activity of the semiconductor typically decreases.[13,14,23,24] Focused efforts in optimizing the optical path length, carrier mobility, charge carrier kinetics, light absorption, and band bending via exotic structural forms such as powders in aqueous solutions, nanoparticles (0D), nanorods (1D), nanosheets and films (2D), integrated 3D nanostructures, and mesoporous supports have all failed to achieve sustained success in extending the photocatalytic activity of semiconductor photocatalysts to visible wavelengths.[13,15,25–29] **(Figure 1.3)**

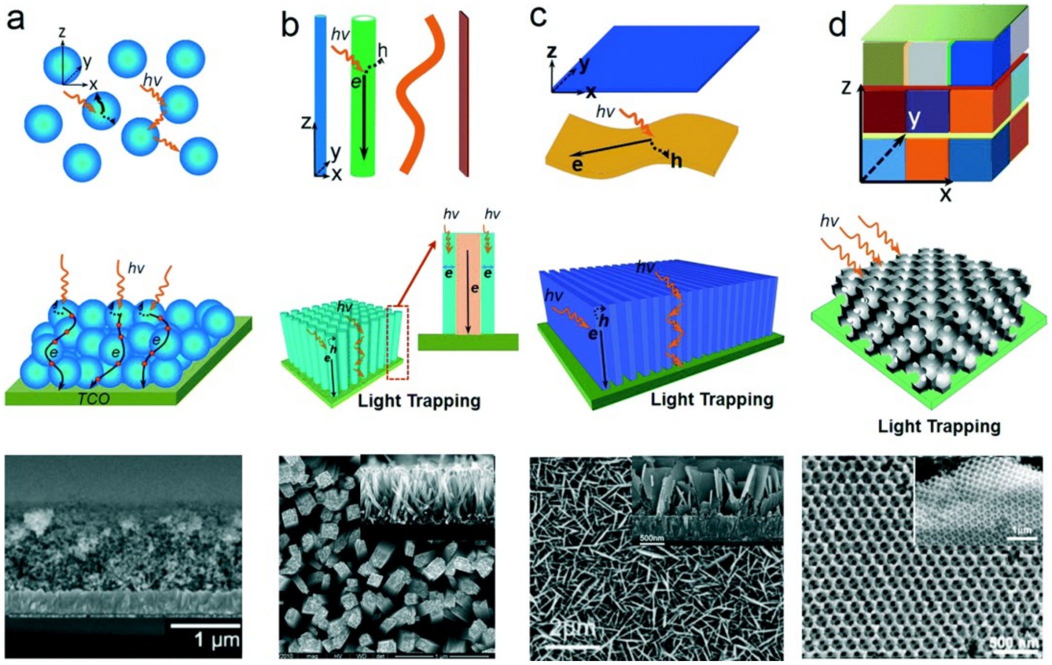

Figure 1.3. Various nanoscale architectures for photocatalytic applications from (a) 0D nanocrystals, (b) 1D nanostructures, (c) 2D nanosheets and films, and (d) 0D-1D-2D integrated 3D nanostructures. (a) Freestanding 0D nanoparticles provide for optimal light scattering and increased effective optical path length. (b) 1D nanomaterials provide a "highway" along one dimension for efficient and enhanced charge transport. By tuning the diameter of the nanowire one can control the light absorption enhancement at a given wavelength. The large surface areas of (c) 2D nanostructures can assist with highly reactive facets for photocatalysis and interfacial charge transfer. Lastly, (d) 3D materials are a composite assembly of 0D, 1D, or 2D nanomaterials and can be characterized by the constituent advantages of all three systems. Reprinted for academic use from Ref[13]. Copyright Royal Society of Chemistry (2015). Figure (2d) originally adapted by Ref[13] from Ref[30]. Copyright John Wiley and Sons (2013).

To forego these limitations, plasmonic photocatalysts have emerged as a promising technology for the harvesting and conversion of solar energy. Plasmon-enhanced photocatalytic systems take advantage of energetic charge carriers or "hot electrons", a consequence of the resonant interaction of light with the collective and coherent motion of electrons in metal nanostructures, to further enhance and support photocatalytic activity. To understand these composite plasmonic nanostructures, we start by considering the synergistic interaction of its individual constituents beginning with metal nanoparticles.

1.3 Light-Matter Interactions

The interaction of light and matter is integral to life on our planet. The existence of the Sun has been crucial to our planet's evolution. Our vision of the world is supported by the interaction of light with our eyes. The lens in our eyes, our vision system, helps refract light to be focused onto the retina allowing us to see the world around us. Various scientific inventions from the Presocratic era to modern day civilization are based on our understanding of light-matter interactions allowing us to scale both the very large (stellar spectra) and very small aspects (light signals in glass fibers) of our universe.

Diffraction places limitations on how we can use light and describes the bending of light or waves around an obstacle. An ideal lens honed and perfected in all aspects will image an object perfectly as a point. However, due to the wave nature of light, diffraction occurs at the limiting edges of the optical system's aperture, or more precisely, when light passes through the corner or opening of a slit that is approximately the size of or smaller than that light's wavelength.[31] This results in an *Airy disk* or a diffraction blur, named in honor of Lord George Biddel Airy (1801-1892), a British mathematician who discovered this phenomenon. Diffraction affects all kinds of propagating waves and has been observed in classical and quantum physics through the Hugyens-Fresnel principle and the Double-Slit experiment, respectively.[32] The latter has demonstrated, via wave-particle duality, that matter or particles just as much as waves, also experience diffraction.

Essentially, diffraction states that all propagating waves cannot be focused to a spot smaller than half their wavelength. For visible light (400 – 700 nm), this means optical systems are limited to a resolution of 200 – 350 nm. This limits the boundaries of minimization for nanotechnology that can be realized through methods such as optical lithography. This would change with the discovery that light can exist not only as free traveling waves, but also as evanescent waves bound to the surfaces of objects.[32] Evanescent waves are such that their intensities decay exponentially with distance from the interface at which they are formed i.e., these near-field waves do not carry their energy or information off into space. Unrestricted by diffraction, evanescent waves can be confined down to nanoscales.[33] Plasmonics involves the use of evanescent waves in noble metal nanoparticles but the journey towards this accomplishment follows a long trail of historical and significant jumps in scientific thought.

1.4 Plasmonics – A Historical Perspective

Plasmonics concerns the study and excitation of *plasmons* in noble metal nanoparticles. *Plasmons*, or plasma waves, are a quantum of plasma oscillation. Plasma is the fourth state of matter and describes a gas composed of charged particles, namely ions and free electrons. A plasma is characterized by its quasi-neutrality, a state of dynamic equilibrium as opposed to static equilibrium, where collective oscillations of the charged particles reinforce quasi-neutrality upon its disturbance.[34] Essentially, areas of excess charge in a plasma are screened by surrounding charges to maintain quasi-neutrality. The Debye length is the physical parameter used to describe this screening mechanism and provides a measure of the distance over which an individual charged particle's electric field can influence other nearby charges in the plasma. In a plasma, the charged particles move in a way such that they shield electric fields within a distance on the order of the Debye length. Analogous to a mass-spring system, the excess charges move from their original position and participate in collective oscillatory motions within the gas until equilibrium has been reached. The natural frequency of oscillation of these collective motions is characterized by the *plasma frequency* (ω_p),[34]

$$\omega_p = \left(\frac{Ne^2}{m_e \epsilon_0}\right)^{\frac{1}{2}} \tag{1.1}$$

where N is the number density of electrons, e is the electron charge, m_e is the mass of the electron, and ϵ_0 is the permittivity of free space. In general, the collective oscillations in a plasma are of high frequency and are attributed to electrons oscillating about positive ionic cores that are unable to follow the motion of the electrons due to their larger mass. These oscillations are stationary, longitudinal, and electrostatic by nature. The collective restoring force between these positive and negative charges is determined by the ion-electron Coulomb attraction. Collisions between electrons and neutral particles are a source of damping and result in the gradual weakening of these collective oscillations and their amplitude. For the case of slight damping, the plasma frequency is greater than the electron-neutral collision frequency as otherwise electrons cannot behave in an independent manner and will be forced by collisions to maintain equilibrium with neutrals, resulting in the medium being treated as a neutral gas.[34]

Metals, in the strictest sense of the word, are not plasmas. However, we will see when one considers the high density of free electrons and the statistical mechanics used to describe the motion of these free charge carriers, a metal can be described equivalently as a gas of free charges or a confined plasma when studying its optical properties. The discovery of metal nanoparticles is not necessarily new as they have been produced for over 1500 years. The Lycurgus cup **(Figure 1.4)**, made in 300 A.D., is a definitive example of the use dilute quantities of gold and silver in a glass solution in the presence of chemical reducing agents.[35] It is unlikely that the makers themselves were aware of the existence of these nanoparticles as the process probably involved accidental on-site contamination.[32,36]

The use of silver (Ag) and gold (Au) nanoparticles continued to persist through history. 16th century alchemists often falsely advertised Ag and Au solutions for medical ailments. Although Ag solutions do have antimicrobial properties, their use as medications were soon prohibited and replaced by safer antibiotics and antiseptics due to adverse side-effects.[32] It wasn't until 1818 that German scientists Johann Kunckel and Jeremias Benjamin Richter proposed that these noble metal solutions were in fact composed of small nanoparticles which were responsible for their representative colors.[37,38] In 1857, Michael Faraday would make the first systematic study of colloidal solutions, and discover that a dilute aqueous solution of $NaAuCl_4$, subject to phosphorus and other reducing agents, could result in the gold being reduced to very small particles that "diffused to produce a beautiful ruby fluid."[39] Faraday's experiment was motivated by his goal to support his wave theory of light. He argued the observed red hue of Au solutions was due to the absorption of light by Au nanoparticles in a demonstration of the interaction of light waves with subwavelength objects.[32,39]

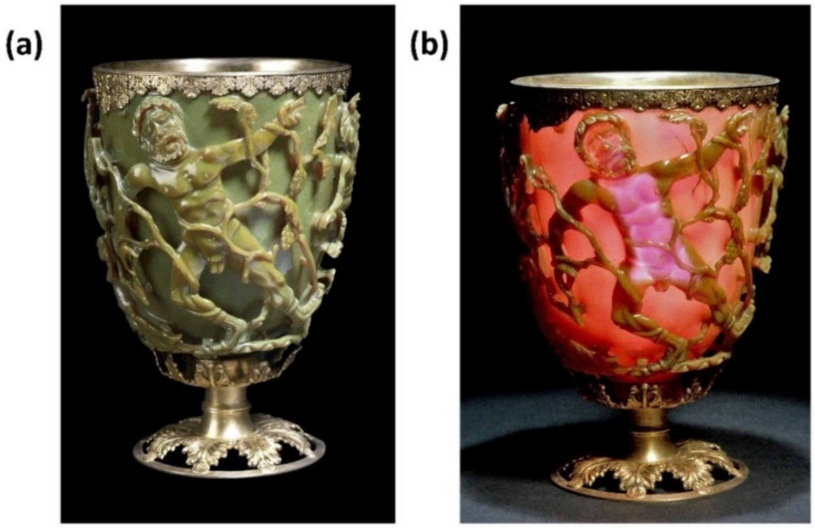

Figure 1.4. The Lycurgus cup has been found to contain small amounts of gold and silver powder embedded in its glass matrix. The existence of this gold-silver alloy results in the cup demonstrating dichroic properties where (a) a green shade is reflected when the cup is lit from the front (attributed to silver), and (b) a red shade is transmitted from the back (attributed to gold).[35] Reprinted with permission from The British Museum with attribution and adherence to Creative Commons Attribution-NonCommercial-ShareAlike 4.0 International (CC BY-NC-SA 4.0) license.

In 1897, forty years following Faraday, Richard Zsigmondy would develop an independent method to make Au nanoparticles, and using an ultra-microscope of his own invention, prove Faraday's hypothesis of the existence of nano- to micro-size particles.[40] It was also around Faraday's time that James Clerk Maxwell developed the electromagnetic wave theory of light. In 1908, a scientist named Gustav Mie would solve Maxwell's equations to theoretically explain the ruby red color of Au solutions and the resonant structures observed in their spectra.[32,41] It wasn't until the 1950s that the term "plasmon" was coined by David Pines to describe high frequency plasma oscillations in metals.[42] These oscillations traveled through the metal much like sound waves, were longitudinal in nature, did not couple with incident light (which is transverse by nature), and were excited by high energy electrons incident on the metal. Pines would identify these plasma oscillations as *bulk (volume) plasmons* to describe the process by which incident electrons lost energy while passing through the metal.[32]

Shortly after Pines, Rufus Ritchie discovered a different type of plasmon, traveling along the surface of the metal as opposed to the bulk, that could strongly interact with electromagnetic fields outside and in the vicinity of the metal surface. Ritchie would subsequently identify this phenomenon as *surface plasmons* that could also be excited by high energy electrons incident on a metal surface.[43] A third and final form of plasma oscillation would be discovered in the 1970s by Martin Fleischmann and Richard van Duyne who observed the enhancement of Raman scattering signals from molecules adsorbed on rough metal surfaces.[44,45] This Surface Enhanced Raman Scattering (SERS) originated from strong, enhanced local electromagnetic fields produced by the excitation of plasmon resonances on the metal surface. Unlike the former cases of "propagating" bulk and surface plasmons, these plasmons were localized and non-propagating in nature, and were aptly named localized surface plasmons or *localized surface plasmon resonance* (LSPR).

Until the late 1990s, the study of plasmons occupied these distinct categories of plasmon phenomena. It wasn't until the advancement of electron microscopy technology and nanofabrication techniques that these independent observations were identified as just different facets of a unified phenomenon in plasmons, provided certain material boundary conditions, that can be encompassed under one branch of study now known as plasmonics.[32]

1.5 The Optics of Metals

In modeling the plasmonics of metallic nanostructures, a classical approach is largely preferred where Maxwell's equations are solved for the relevant system with appropriate boundary conditions to describe the interaction of light and a metal nanostructure:

$$\nabla \cdot \vec{D} = 4\pi\rho, \tag{1.2}$$

$$\nabla \cdot \vec{B} = 0, \tag{1.3}$$

$$\nabla \times \vec{E} = -\frac{1}{c}\frac{\partial \vec{B}}{\partial t}, \tag{1.4}$$

$$\nabla \times \vec{H} = \frac{4\pi}{c}\vec{J} + \frac{1}{c}\frac{\partial \vec{D}}{\partial t}, \tag{1.5}$$

where ρ is the free charge density, $\vec{J}$ is the free current density, c is the speed of light, $\vec{E}$ is the total electric field, and $\vec{B}$ is the total magnetic field. An initial major simplification can be made in that all naturally occurring materials are generally nonmagnetic and as such the magnetic constituents of Maxwell's equations can be ignored. The corresponding constitutive relation, in this case, for a simple homogeneous, isotropic dielectric material is,

$$\vec{D} = \epsilon\vec{E} \tag{1.6}$$

where $\vec{D}$ is the electric displacement and ϵ is the dielectric constant or electric permittivity,

$$\epsilon = \epsilon_0(1+\chi) = \epsilon_0\epsilon_r \tag{1.7}$$

$$\vec{D} = \epsilon_0(1+\chi)\vec{E} = \epsilon_0\vec{E} + \vec{P} \tag{1.8}$$

where χ is the electric susceptibility and is a measure of the electric polarization of the material, ϵ_r is the relative dielectric constant, ϵ_0 is the permittivity of free space, and $\vec{P} = \epsilon_0\chi\vec{E}$ is the dielectric polarization of the material. With these relations in mind and assuming an absence of electric sources, $\nabla \cdot \vec{D} = 0$,[46] we can combine Maxwell's equations to get,

$$\nabla \times \nabla \times \vec{E} = -\mu_0 \frac{\partial^2 \vec{D}}{\partial t^2}. \tag{1.9}$$

Thus, determining the response of an object to an electromagnetic wave is the equivalent of solving the wave equation alongside appropriate constitutive relations and boundary conditions. Generally, the solution to the wave equation can be written as a superposition of monochromatic plane waves of frequency ω and wavevector $\vec{k}$,

$$\vec{E} = Re\left[\vec{E}(\omega)e^{i(\vec{k}\cdot\vec{r}-\omega t)}\right]. \tag{1.10}$$

The corresponding dispersion relation for these plane waves is,

$$\vec{k}^2 = \frac{\epsilon\omega^2}{c^2} \tag{1.11}$$

and determines how these waves behave at interfaces. In general, waves are propagating for $\epsilon > 0$ and are evanescent if $\epsilon < 0$. Therefore, waves are transmitted through a medium if $\epsilon_{med} > 0$ and reflected if $\epsilon_{med} < 0$. By writing the solution to Maxwell's equations as a superposition of monochromatic plane waves, it allows for us to take account of the finite response time of the material to an incident wave. As all real materials have a finite response time, the constitutive relation $\vec{D} = \epsilon\vec{E}$ can be reformulated as,

$$\vec{D}(\omega) = \epsilon(\omega)\vec{E}(\omega). \tag{1.12}$$

As such, the modeling of metallic nanostructures requires the development of a model for the frequency dependent dielectric response function of said metals so that a complete description of their optical response can be formulated.[32]

1.5.1 The Lorentz-Drude Model

The Lorentz-Drude or free-electron model is commonly utilized to capture the dielectric response of a metal. The model, in its original formulation, was developed by Hendrick Antoon Lorentz in 1878 where atoms are considered as oscillating dipoles.[47] In this oscillator model, the electron is assumed to be bound to the nucleus via a spring. The spring represents the restoring force for the electron in the case of small displacements from equilibrium. Like any bound spring, this oscillator system can be characterized by a natural resonant frequency ω_0, which corresponds to the absorption wavelength of the given material.

For frequencies that do not coincide with the resonant frequency, the atom will not absorb, and the medium will be transparent. In such a situation, the incident electric field of the light wave drives non-resonant, lagging oscillations (a feature of forced oscillators as we are not at resonance, resulting in retarded propagation and a reduction of velocity in the medium which is identified by the refractive index), in a repetitive and damping scattering process.[47] Different atoms have different characteristic resonant frequencies corresponding to different spring constants, k. Lorentz used this dipole oscillator model to explain how atoms emit and absorb at discrete frequencies in terms of Maxwell's equations.

Lorentz's model drew the picture of three types of oscillators in any medium. Working inside out from the nucleus of an atom we have *atomic oscillators* or bound electrons held strongly and closest to the nucleus, *vibrational oscillators* (phonons) or mid-valence to valence electrons resonating at lower frequencies in the infrared spectral region, and lastly, *free electron oscillators* or electrons that are not bound to any atoms.[47] These free electron oscillators are the focus of plasmonics, where metals are of primary concern, and correspond to conduction electrons in metals that are free, not bound to any atoms, and consequently do not experience a restoring force (there are no springs); the spring constant and the natural resonant frequency of these oscillators are equal to zero.

The generalized Lorentz oscillator equation of motion describing the interaction between a light wave and an atom with a single resonant frequency ω_0 due to the bound electrons is,[47]

$$m_0 \frac{d^2x}{dt^2} + m_0\gamma \frac{dx}{dt} + m_0\omega_0^2 x = -eE(t). \tag{1.13}$$

where x refers to the displacement of the electrons. The terms on the left-hand side represent the acceleration of electrons (of effective mass m_0), the damping force of the medium modeled as a frictional force proportional to the velocity and impeding motion (γ is the damping rate), and the restoring force. The term on the right-hand side represents the driving force exerted on the system by the total incident electric field of the light wave. This electric field can be considered as a totality acting on the electrons, including internal and external fields generated by the motion of electrons as well. For clarity, arrows indicating vector quantities have been eliminated assuming one works with a set orientation. Note, the subsequent calculation can still be performed in vector form. By applying the condition that the restoring force is zero for free electron oscillators ($\omega_0 = 0$), we arrive at the dipole oscillator model for metals,

$$m_0 \frac{d^2x}{dt^2} + m_0\gamma \frac{dx}{dt} = -eE(t). \tag{1.14}$$

This modification of Lorentz's original equation of motion for free electrons was attributed to physicist Paul Drude, thus resulting in its naming as the Lorentz-Drude model where, for a *bulk* crystal of a metal, its conduction or free electrons can be modeled as a classical gas of free, noninteracting electrons which relaxes through collisions with the lattice or other scatterers in the medium.

The assumption of metals as a gas of noninteracting free electrons in the Lorentz-Drude model may appear questionable but experiments have demonstrated that this model works well for many simple metals particularly at lower frequencies.[32,46] The accuracy of this model can be attributed to the quantum-mechanical nature of electrons in the metal resulting in what is known as a screening effect. The electrons in the metal screen themselves from each other. Electrons not only repel each other due to classical electrostatic repulsion between like charges but electrons with like spins, due to the Pauli exclusion principle, also tend to avoid each other. As no two electrons can be in the same state, electrons with the same spin will have a low probability of being located near each other. In this manner, electrons in materials move somewhat independently of the other electrons.[48]

For solids or crystalline materials, band theory demonstrates that if the lattice is perfectly periodic, electrons can flow freely as waves through the structure at certain energies, whereas waves at other energies do not propagate. The effect of the lattice (amounting to the protons and neutrons that make up the atoms) is accounted for via an effective mass. Similarly, for simple metals, the Schrodinger equation describing electron motion in metals (specifically, the plane-wave envelope function) is nearly identical to that describing free electrons.[32] The resulting envelope wave functions extend through the lattice with the interaction of conduction electrons being described as a mean-field interaction with the average potential of all other conduction electrons in the system. Because of this, each conduction electron can be treated as a noninteracting electron moving in a potential defined by an averaged field. The major difference in this picture is that these quasi-free electrons have an effective mass that is different from the mass of a true free electron. For metals such as gold and silver, the effective electron mass is nearly identical to the bare electron mass. In the case of imperfections in the lattice, wave damping via the scattering of electrons will occur and must be accounted for.[48]

As a result of these deductions, the electron motion in a bulk metal can be simply described using the classical model of a free-electron gas. For an incident oscillatory electric field of an electromagnetic wave of frequency ω, the resultant displacement of electrons within the metal and any induced fields will oscillate at the same frequency ω such that $E(t) = Re\left[E(\omega)e^{-i\omega t}\right]$ and $x(t) = Re\left[x(\omega)e^{-i\omega t}\right]$. Substituting these relations into the equation of motion, we obtain,

$$x(\omega) = \frac{eE(t)}{m_0(\omega^2 + i\gamma\omega)}. \tag{1.15}$$

The corresponding dielectric function can then be written as,

$$D = \epsilon_r\epsilon_0 E = \epsilon_0 E + P = \epsilon_0 E + Np = \epsilon_0 E - Nex \tag{1.16}$$

where the induced polarization is defined as $P = Np = -Nex$ leading to,

$$D(\omega) = \epsilon_0(\omega)E(\omega) - \frac{Ne^2}{m_0}\frac{1}{(\omega^2 + i\gamma\omega)}E(\omega). \tag{1.17}$$

Therefore,

$$\epsilon_r(\omega) = 1 - \frac{Ne^2}{m_0}\frac{1}{(\omega^2 + i\gamma\omega)} = 1 - \frac{\omega_p^2}{\omega^2 + i\gamma\omega}, \tag{1.18}$$

where,

$$\omega_p = \left(\frac{Ne^2}{m_0\epsilon_0}\right)^{\frac{1}{2}}. \tag{1.19}$$

Note, this is the resonant frequency of the free carrier gas (the plasma which we use to represent our bulk metal) not the individual electrons, which is zero as they are free. The total electric field acting on a conduction electron can therefore be defined as,

$$E(t) = E_{ext}(t) + E_{int}(t) = E_{ext}(t) + \frac{Nex}{\chi\epsilon_0}, \tag{1.20}$$

where the induced field within the metal is described via an overall polarization of the material resulting in plasma oscillations. We can therefore rewrite (1.15) as,

$$x(\omega)\left(\omega^2 + i\gamma\omega - \frac{Ne^2x}{\chi\epsilon_0 m_0}\right) = \frac{e}{m_0}E_{ext}(\omega). \tag{1.21}$$

Assuming zero damping, this means that the displacement at the bulk plasmon frequency is finite for a small driving field and corresponds to excitations of the conduction-electron gas.[32] In this scenario, the displacement of the free electrons around the positive atomic cores are longitudinal in nature and akin to sound/pressure waves in the bulk of the metal. The harmonic oscillator approach used by the Lorentz-Drude model to characterize the motion of electrons in metals implies that these oscillations can also be quantized in units of $h\omega_p$. The quasi-particles that correspond to these quantized plasma oscillations are Pines' *bulk (volume) plasmons* whose natural resonant frequency of oscillation (the *bulk (metal) plasmon frequency*) is equivalent to the generalized plasma frequency of the carrier gas in (1.19). Bulk plasmons arise in the limit of long wavelength and are essentially charge-density waves. Due to their longitudinal nature, bulk plasmons do not couple directly to light (which is transverse) and are excited by electron beams.[42]

The Lorentz-Drude model, under the assumption of zero damping, also fundamentally states that the reflectivity of a gas of free electrons is 100% up to the plasma frequency ω_p. With $\gamma = 0$,

$$\epsilon_r(\omega) = 1 - \frac{\omega_p^2}{\omega^2}. \tag{1.22}$$

The complex refractive index $\tilde{n}$ of a medium is related to the dielectric constant by the relation $\tilde{n} = \sqrt{\epsilon_r}$ which implies that $\tilde{n}$ is imaginary for $\omega < \omega_p$, positive for $\omega > \omega_p$, and zero at $\omega = \omega_p$. Reflectivity is defined as,

$$R = \left|\frac{\tilde{n} - 1}{\tilde{n} + 1}\right|^2. \tag{1.23}$$

Considering the frequency dependence of $\tilde{n}$, we see that the reflectivity is 100% for $\omega < \omega_p$, decreases for $\omega > \omega_p$, and approaches zero at $\omega = \infty$. **(Figure 1.5)** The Lorentz-Drude model essentially states that metals tend to be good reflectors at visible and long wavelengths. The reflectivity ceases to be 100% for frequencies above ω_p. For common metals such as aluminum (Al), copper (Cu), silver (Ag), and gold (Au) the corresponding wavelength to their plasma frequencies as calculated by the Lorentz-Drude model are 79 (Al), 115 (Cu), and 138 (for Au and Ag) nm, respectively.[49] Therefore, we expect that all metals will eventually transmit if we go far enough into the UV where $\omega > \omega_p$. This is known as the *ultraviolet transparency of metals*. Reality is a different story.

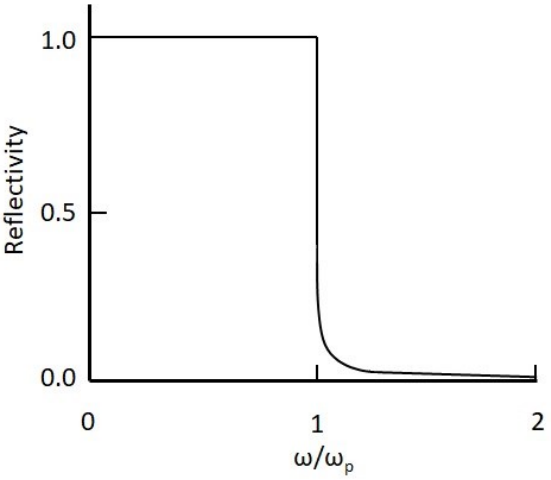

Figure 1.5. Schematic of the reflectivity of an undamped free electron gas as a function of frequency as demonstrated by the Lorentz-Drude model.

Experimental reflectivity studies of Au, Ag, and other noble metals demonstrate that there are discrepancies that the Lorentz-Drude model doesn't account for. **(Figure 1.6)** Although the model accounts for the general shape of the reflectance spectrum for these noble metals, damping associated with electron-electron scattering, electron-phonon scattering, radiative relaxation etc., generally causes the reflectivity to be less than unity for $\omega < \omega_p$. Furthermore, the reflectivity cutoff predicted by the model does not match experiment as for $\omega < \omega_p$ we are also able to observe a substantial drop from 100% reflectivity. These deviations are largely due to interband transitions in metals where an electron is promoted to a higher unoccupied energy level by absorbing an incident photon. In metals such as Au (as well as Cu and Ag), this interband absorption results in a major drop in reflectivity as the electrons from the 3d band with a very high density of states can be easily promoted to the 4s band which is quite broad in energy and has several unoccupied states. The energy differences between the 3d band and the Fermi level (where the lowest energy unoccupied states exist) differs between metals. It is this difference that sets the cutoff energy where the metals are observed to suddenly become less reflective and more absorptive. Copper's reddish color is because the cutoff energy is at 2 eV corresponding to a wavelength of 560 nm. The interband absorption threshold of Au occurs at a slightly higher energy leading to its yellowish color. Silver's interband absorption edge is around 4 eV, near the UV, allowing it to be highly reflective throughout the whole visible spectrum and leading it to have no particular color at all.[46,47]

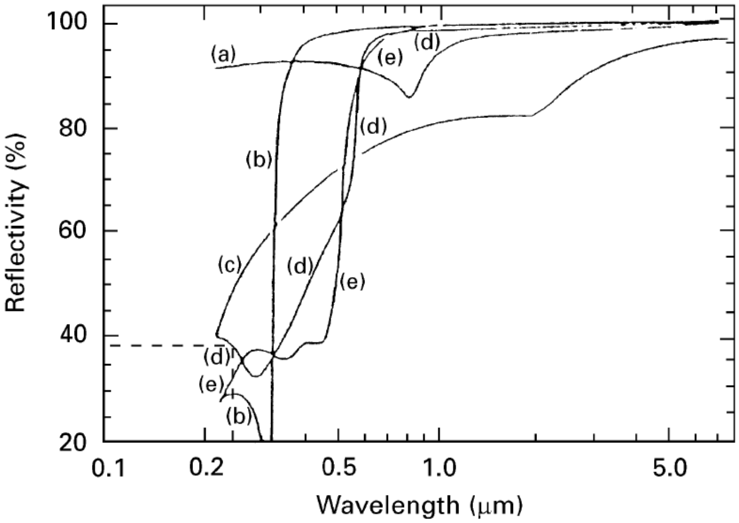

Figure 1.6. Reflectivity of noble metals as a function of wavelength: (a) Al, (b) Ag, (c) Pt, (d) Cu, and (e) Au. Reprinted with permission from Ref[50]. Copyright Springer Link (1997).

Redefining the above discussion in the context of plasmons, with finite damping, bulk plasmons essentially are led to have a finite lifetime. These oscillations can only last for so long. For long wavelengths (low frequencies), the Lorentz-Drude model states that the propagation of electromagnetic waves is forbidden inside the metal plasma. The electrons simply re-emit the light and the metal plasma is largely undisturbed leading to the characteristic reflective properties of metals for $\omega < \omega_p$. At $\omega = \omega_p$, the metal plasma sustains longitudinal oscillations in its bulk or *bulk plasmons*. The Lorentz-Drude model fails to describe the optical response of metals for large frequencies close to $\omega_p$where interband transitions occur. For $\omega > \omega_p$ the metal plasma supports transverse wave propagation, with the metal essentially becoming transparent.[32,46,51] Ultimately, the Lorentz-Drude model's assumption of 100% reflectivity for $\omega < \omega_p$ is only feasible when the metal plasma thickness is much larger than the incident wavelength of light.

Similarly, solving the Lorentz-Drude model for the case where the bulk metal is terminated by a surface, one discovers the existence of longitudinal plasmons that are strongly localized to the surface of the metal, akin to evanescent waves, or *surface plasmons*. Having considered plasmon excitation in bulk metals and metals terminated by a surface, we will now discuss how the Lorentz-Drude model translates to the case of plasmons in metal nanoparticles which are the focus of my thesis.

1.6. The Homogeneous, Isotropic Spherical Nanoparticle

Metal nanoparticles are the equivalent of rolled up surfaces, a 2-D to 3-D transformation. A terminated metal surface leads to the generation of plasmon modes strongly localized to the surface in *surface plasmons*. Therefore, it follows that metal nanoparticles should support discrete plasmon modes in three dimensions, as the charge oscillations and the corresponding electric field distributions are now quantized in three spatial directions.

Understanding the optical response of plasmonic noble metal nanoparticles is integral towards optimizing plasmonic photocatalytic systems. Plasmonic noble metal nanoparticles refer to metal nanoparticles (mostly Au and Ag, in sizes of tens to hundreds of nanometers) of electron densities (Au has electron densities of 10^{28} m^{-3}) that can couple with wavelengths of electromagnetic radiation in the visible spectrum that are far larger than the nanostructure itself. This is due to the dielectric-metal interface between the particles and the surrounding medium.[46] Contrastingly, in pure metals, there is a maximum limit to wavelength magnitudes, defined by the metal's work function, that can effectively couple with the material sizes involved.[52] Diverse shapes of plasmonic noble metal nanoparticles ranging from spheres, prisms, rods, cubes, and shells etc. have been studied in plasmonics. Once again, Maxwell's equations must be solved with the proper boundary conditions to describe the interaction of nanoparticles with incident light. The nanosphere has the simplest geometry and provides analytical solutions in response to an electromagnetic field. The resultant features including dipole behavior, and enhanced local electric fields are retained and can be extended to other nanoparticle morphologies.

A rigorous description of the electrodynamic response of a single spherical particle is provided by Mie theory,[53,54] but for nanoparticles of size $a \ll \lambda$, a simpler analytical description can be utilized. The condition $a \ll \lambda$ stating the particle is much smaller than the wavelength of light in the surrounding medium, invokes what is known as the *quasi-static approximation* i.e., the phase of the electromagnetic wave is constant over the particle volume such that one can calculate the spatial field distribution by assuming the simplified problem of a particle in an electrostatic field. The harmonic time dependence of the oscillating electromagnetic wave can then be added to the solution once the individual field distributions are known. This lower order approximation of the full scattering problem of the individual spherical nanoparticle is only valid up to particle sizes of 100 nm.[46]

As long as the quasi-static approximation remains valid, the following simple physical picture of the polarizability of the spherical nanoparticle can be drawn. **(Figure 1.7)** We begin by considering a homogeneous spherical nanoparticle illuminated by plane-wave electromagnetic radiation. The sphere of radius a is assumed to be in a homogeneous, infinitely large, non-absorbing and non-magnetic environment of dielectric constant ϵ_m. The electric field of the incident light is $\vec{E} = E_0 e^{-\omega t}\hat{x}$, where E_0 is a constant, and $\hat{x}$ is the unit vector of the x-direction. The field lines are parallel to the x-direction at sufficient distance from the sphere. The dielectric response of the sphere is modeled by the dielectric function $\epsilon(\omega)$ which for the moment can be considered as a simple complex number ϵ. In this electrostatic approach, we are generally interested in a solution of the Laplace equation for the potential, $\nabla^2\phi = 0$, from which we will calculate the electric field $\vec{E} = -\nabla\phi$.

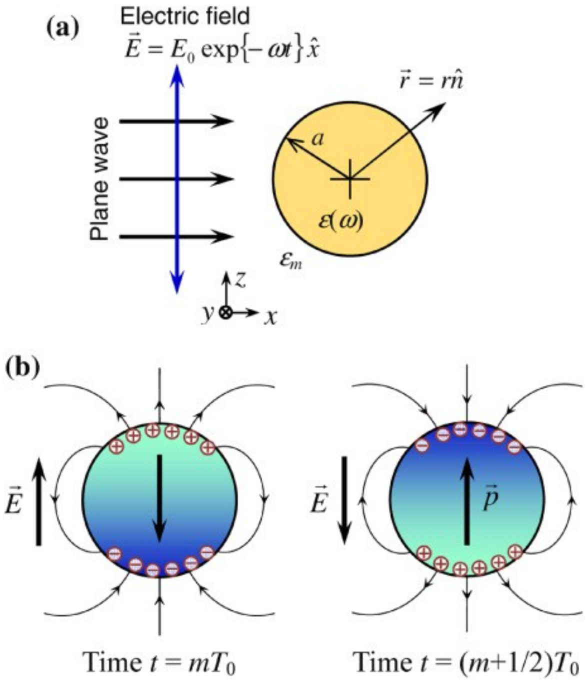

Figure 1.7. Schematic of the optical response of a homogeneous, isotropic spherical nanoparticle. (a) Nanosphere irradiated by an incident plane wave of light. (b) Free electrons in the metal nanoparticle oscillate in phase with the incident electric field resulting in the generation of an oscillating dipole. Reprinted for academic use from Ref[19]. Copyright IOP Science (2013).

Qualitatively, this results in the conduction electrons in the metal nanosphere being displaced by the external electric field and creating separated negative and positive charge centers at either ends of the sphere, thus forming a dipole. **(Figure 1.7b)** As such, the applied field induces a dipole moment $\vec{p}$ inside the sphere of magnitude proportional to $|E_0|$, as given by, $\vec{p} = \epsilon_0 \epsilon_m \alpha \vec{E}$ where α describes the static polarizability of the sphere, ϵ_0 is the vacuum permittivity, and is related to other parameters by,

$$\alpha = 4\pi\epsilon_0 a^3 \frac{\epsilon - \epsilon_m}{\epsilon + 2\epsilon_m}. \qquad (1.24)$$

Under plane-wave illumination where the harmonic time dependence is taken into consideration with $\vec{E}(\vec{r}, t) = E_0 e^{-i\omega t}$, the fields induce an oscillating dipole moment $\vec{p}(t) = \epsilon_0 \epsilon_m \alpha E_0 e^{-i\omega t}$ with α given by the electrostatic result. If ω is not too high, the dipole can oscillate fast enough to follow the phase of $\vec{E}$. The most important and fascinating property of the metal nanoparticle's polarizability lies in the denominator of (1.24). It is apparent from here that the polarizability experiences a resonant enhancement under the condition that $|\epsilon + 2\epsilon_m|$ is a minimum, which under the condition of small or slow-varying $Im[\epsilon]$, is satisfied when,

$$Re[\epsilon(\omega)] = -2\epsilon_m. \tag{1.25}$$

This relationship is called the *Frohlich condition,* and the associated mode of resonance is indeed what is commonly stated as the localized surface plasmon resonance (LSPR) which in the case of the spherical metal nanoparticle takes the form of a dipole surface plasmon mode. The LSPR represents the resonant oscillation of the metal's free electrons with the varying electric field of the incident light[46] and is the origin of the enhancement of the local electric field, absorption, and scattering of the metal nanoparticle. As noted in (1.25), the resonance frequency is strongly dependent on the surrounding environment. Outside the sphere, but in the near-field zone, the electric field is expressed as,[46]

$$\vec{E}_{out} = \vec{E} + \frac{3\vec{n}(\vec{n}\cdot\vec{p}) - \vec{p}}{4\pi\epsilon_0\epsilon_m r^3} \tag{1.26}$$

where the first term represents the incident light and the second represents the point dipole radiation. The $1/r^3$ dependence shows that the dipole contribution decreases quickly as we move away from the sphere and that the enhancement of the electric field is local and limited to the vicinity (usually a few nanometers) of the spherical surface. The accompanying magnetic field present is seen to be much smaller than that of the electric field and vanishes upon the static approximation.[46]

An immediate consequence of the LSPR is that the particle's optical absorption has a maximum at a given frequency otherwise known as the *plasmon resonance frequency*. The plasmon resonance frequency can be derived using the Drude model, where the dielectric function $\epsilon(\omega)$ of metals can be expressed as,[46,47]

$$\epsilon(\omega) = 1 - \frac{\omega_p^2}{\omega_p^2 + i\gamma\omega} = \epsilon_1(\omega) + i\epsilon_2(\omega), \tag{1.27}$$

$$\epsilon_1(\omega) = 1 - \frac{\omega_p^2}{1 + \omega^2\tau^2}, \tag{1.28}$$

$$\epsilon_2(\omega) = \frac{\omega_p^2\tau}{\omega(1 + \omega^2\tau^2)}, \tag{1.29}$$

where ϵ_1 and ϵ_2 are the real and imaginary parts of ϵ, respectively, τ is the relaxation time for the free electron, and $\gamma = 1/\tau$ is the intraband damping frequency. ω_p is the plasma frequency of the bulk metal and is given by (1.19), with N being the electron number density, e the electric charge, and m_0 the effective mass of the electron.[47] Experimentally, the plasma frequency of metals is determined using electron loss spectroscopy where electrons are passed through thin metallic foils. It is seen that ω_p, for most metals, is in the ultraviolet regime, with τ on the order of 100 fs. From the *Frohlich condition*, the localized surface plasmon resonance frequency ω_{LSPR} can be defined as,

$$\omega_{LSPR} = \omega_p \left(\frac{1}{1+2\epsilon_m} - \frac{1}{\omega_p^2 \tau^2} \right)^{\frac{1}{2}} \approx \frac{\omega_p}{\sqrt{1+2\epsilon_m}}. \qquad (1.30)$$

It can be noted that (1.30) describes the resonant frequency to be dependent on the surrounding environment and is redshifted if the surrounding medium has a higher dielectric constant.[55] This is applicable to both Au and Ag particles where the resonant wavelength is observed to shift from ultraviolet to red corresponding to different media from vacuum, water, and TiO_2 respectively.[19] One must remember that the estimations provided by the Drude model adequately describe the optical response of metals only for photon energies below the threshold of transitions between electronic bands. For some noble metals, interband effects initiate around energies in excess of 1 eV, corresponding to a wavelength $\lambda \approx 1\ \mu m$.[46] Furthermore, the Drude model does not account for the size of the nanoparticles. It has been shown, using the more accurate discrete dipole approximation method, that the resonant wavelength is redshifted for increasing nanoparticle sizes. **(Figure 1.8)**

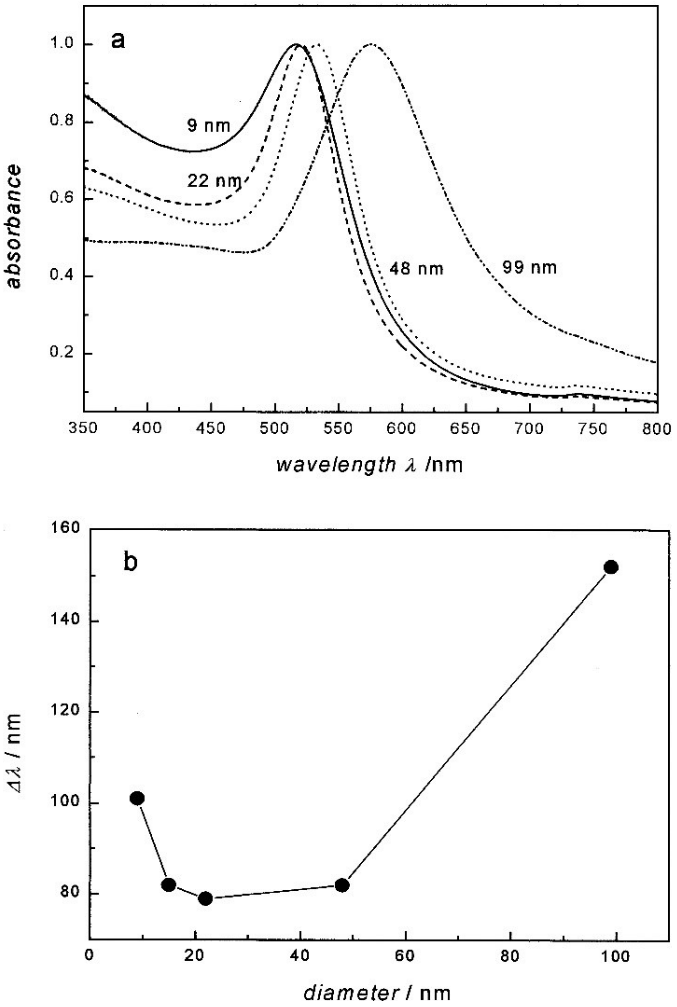

Figure 1.8. (a) Absorption spectra of gold nanoparticles of varying size between 9 – 99 nm demonstrating a redshift in surface plasmon resonance with increasing particle diameter. (b) Plasmon bandwidth $\Delta\lambda$ demonstrating the overall quantitative shifts in resonance as a function of the diameter of the nanoparticle. Reprinted with permission from Ref[56]. Copyright American Chemical Society (1999).

Another consequence of the LSPR is a concomitant enhancement in the light scattering and absorption efficiencies of the metal nanoparticle. The corresponding cross sections for scattering (σ_{sca}) and absorption (σ_{abs}) can be calculated via the Poynting vector.[46,53] The extinction cross section (σ_{ext}) is the sum of the two, and is expressed as,

$$\sigma_{abs} = 4\pi k a^3 Im\left[\frac{\epsilon - \epsilon_m}{\epsilon + 2\epsilon_m}\right], \tag{1.31}$$

$$\sigma_{sca} = \frac{8\pi}{3} k^4 a^6 \left|\frac{\epsilon - \epsilon_m}{\epsilon + 2\epsilon_m}\right|^2, \tag{1.32}$$

$$\sigma_{ext} = \frac{9\omega\epsilon_m^{\frac{3}{2}} V}{c} \frac{\epsilon_2}{(\epsilon_1 + 2\epsilon_m)^2 + \epsilon_2^2}, \tag{1.33}$$

where $k = 2\pi/\lambda$ is the wavenumber, V is the volume of the spherical nanoparticle and c is the speed of light in vacuum. At the resonance frequency, as reported by the *Frohlich condition*, the cross-sections are enhanced. Seeing that σ_{sca} scales with a^6 while σ_{abs} scales with a^3 we can deduce that for nanoparticles with $a \ll \lambda$, σ_{sca} is much smaller than σ_{abs} and is negligible. Contrastingly, for large particles where a is comparable to or larger than λ, the scattering will become significant. Thus, in application to photocatalysis, using small noble metal particles, far-field coupling of nanoparticles can be neglected as the radiation energy of one nanoparticle is not efficiently communicated to other nanoparticles beyond its local region.[57]

1.6.1 The Influence of Nanoparticle Morphology and Size

Relaxing the assumption of a spherical nanoparticle to a more general geometry in ellipsoids (with semi-axes $a_1 \leq a_2 \leq a_3$), two special cases of *spheroidal* geometries can be considered: *prolate*, and *oblate* spheroids. For prolate spheroids, the two minor axes are equal ($a_2 = a_3$), while in oblate spheroids the two major axes are equal ($a_1 = a_3$). Bohren et al.[53] have shown that these spheroidal nanoparticles display two separated plasmon resonances with each peak corresponding to the oscillations of conduction electrons along the major and minor axis upon irradiation. Compared to the plasmon resonance of a spherical nanoparticle, the resonance along the major axis has been observed to show a redshift, yielding the result that the plasmon resonances of metal nanoparticles can be tuned to the near-infrared regime by using nanoparticles with large aspect ratios.

Similar observations have been made for various other nanoparticle geometries including nanorods, nanoshells, and prisms etc. Specific chemical syntheses and fabrication processes are used to tailor the shape and sizes of the nanoparticles for multiple purposes in plasmonic photocatalysis. In general, the dipolar resonance seen in the case of spherical nanoparticles appears in the slightly different form of multiple resonant peaks due to multipolar resonances in different directions in nanoparticles of other shapes. **(Figure 1.9)** These characteristics are observed in the work of Nishijima et al.[58] who demonstrate that a periodically distributed nanopattern of Au rods on TiO_2 single-crystal substrates results in a double-peaked extinction spectra. Rycenga et al.[59] demonstrate the redshift of the resonance wavelength for nanocubes of varying edge lengths of 36, 58, 99, and 172 nm. Similar behavior has also been observed in the work of Mock et al.[60] who demonstrate the shifting of the resonance wavelength from 445 nm to 520 nm to 670 nm for varying shapes of single Ag nanoparticles from spherical to pentagonal to triangular, respectively.[61] Huang et al.[62] and Jain et al.[57] further confirm that Au nanorods of different aspect ratios display two absorption peaks corresponding to separate plasmonic resonances in the transverse (of shorter resonance wavelength) and longitudinal directions.

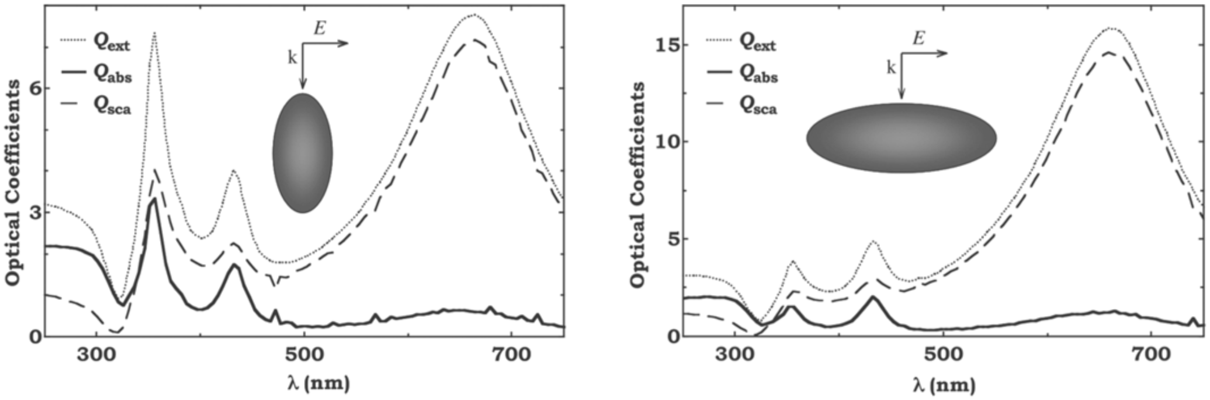

Figure 1.9. Optical coefficients for a silver nanospheroid for an electric field polarization along its minor axis (Left), and along the major axis (Right). Reprinted for academic use from Ref[63]. Copyright American Chemical Society (2003).

As such, plasmonic photocatalysis benefits from the broader spectral range of light source provided by these nanoparticle geometries as opposed to the narrow range and single absorption peak provided by the nanospheres. Furthermore, the influence of nanoparticle geometry on the local electric field enhancement is studied by Kelly et al.[64] who demonstrate that enhancements in the local electric field are generally focused around regions of abrupt shape change or curvature such as the tips of a triangular nanoparticle or along the radius of maximum curvature of an ellipsoidal nanoparticle. These regions experience the greatest enhancement of the local electric field and are identified as "hot spots" of plasmonic resonance.[63]

1.6.2 The Influence of the Local Environment

The LSPR is also influenced by the local environment as presented in the Frohlich condition. In application to plasmonic photocatalysis, noble metal nanoparticles are often exposed to differing levels of contact with the semiconductor photocatalyst in concern. Nanoparticles may decorate the semiconductor photocatalyst surface or may be fully or partially embedded within the photocatalyst. In each case, the nanoparticle is exposed to a different environment, which results in differing resonance behavior. This is observed in the work of Kelly et al.[64] who show that for a 10 nm Ag nanosphere gradually embedded into a 10 nm thick mica shell, the resonance wavelength of the Ag nanosphere experiences a redshift from 350 nm to 430 nm with increasing surface contact area. Seh et al.[65] report that by combining Au with TiO_2 in Janus and core-shell nanoparticle heterojunction nanostructures, a redshift in plasmonic peaks is observed from 543 nm (bare Au), to 555 nm (Janus), and 572 nm (core-shell). **(Figure 1.10c)** This is attributed to the distributive presence of the high refractive index TiO_2 in the differing architectures. These properties are beneficial to applications in plasmonic photocatalysis as has been presented in the work of Farsinezhad et al.[23] who establish that Au nanoparticles embedded in TiO_2 nanostructures provide for greater plasmonic enhancement as opposed to Au nanoparticles decorating TiO_2 nanostructures. Farsinezhad et al.[23] quantify their results via plasmonic enhancement of photoelectrochemical water splitting efficiencies. Altogether, the different levels of embedding of noble metal nanoparticles assists in broadening the absorption spectral range, and results in the utilization of broadband light sources for photocatalysis.

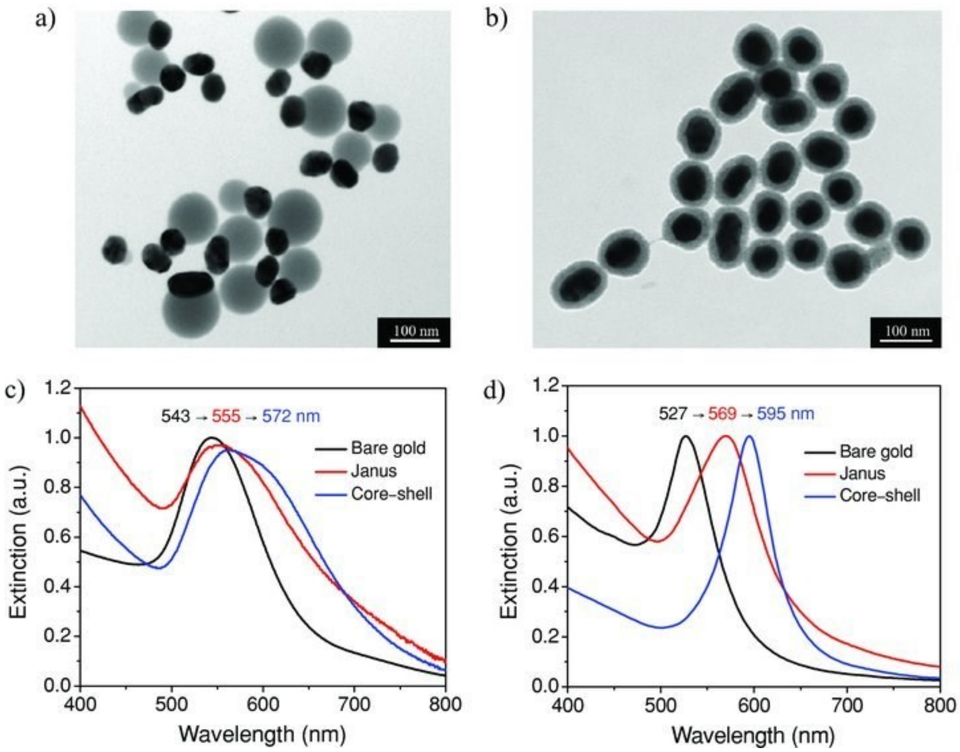

Figure 1.10. TEM images of Janus (a) and core-shell (b) Au-TiO_2 nanostructures. (c) Comparisons of the extinction spectra of nanostructures in isopropyl alcohol, and those from simulations (d) demonstrating the influence of the local environment on the LSPR. Reprinted for academic use from Ref[65]. Copyright Wiley VCH-Verlag (2012).

1.6.3 Nanoparticle Ensembles

As opposed to single and isolated nanoparticles, most plasmon enhanced photocatalytic systems feature ensembles of nanoparticles randomly positioned on the photocatalyst. In such particle ensembles, additional shifts in the resonant wavelength are expected to occur due to the electromagnetic interactions between nearby nanoparticles. For small nanoparticles, these modes are essentially of a dipolar nature, and for particle ensembles, can be treated as an ensemble of interacting dipoles.[46] Much of this depends on the magnitude of interparticle distance d, where two types of plasmonic coupling could be distinguished – near-field dipolar coupling and far-field diffraction coupling.

From (1.26), it can be observed that dipolar coupling scales by a factor of d^{-3} as long as $d \ll \lambda$ and becoming negligible for $d > \lambda$. An intuitive understanding of near-field coupling can be illustrated by considering **(Figure 1.11)**. Assuming a simple approximation of an array of interacting point dipoles, it is easy to observe that the direction of resonance shifts for in-phase illumination is dependent on the Coulombic forces associated with the corresponding polarization of the nanoparticles. An associated transverse mode is excited when the polarization is perpendicular to the array's axis, and an associated longitudinal mode is excited when the polarization is along the array's axis. For the transverse mode, electrons in the nanoparticles oscillate in the same phase, resulting in charge distributions that produce an additive and increasing restoring force that repels the dipole. In contrast, the longitudinal mode experiences a reduction of the restoring force. This leads to a blueshift of the plasmon resonance in transverse modes and redshift of the plasmon resonance in longitudinal modes.

Figure 1.11. Near-field coupling between metallic nanoparticles for two different polarizations. Reprinted with permission for academic use from Ref[66] with attribution and adherence to Creative Commons Attribution 3.0 License.

These resonance shifts are observed as a splitting of absorption peaks in coupled nanoparticles. (1.26) once again shows that the dipolar near-field coupling absorbs energy from the dipole radiation while reducing scattering. This is particularly useful for large nanospheres where scattering is significant and helps to further enhance absorption. Compared to single, isolated nanoparticles, the electric field enhancement in particle ensembles extends beyond the surface region. These features are ultimately beneficial for plasmonic photocatalysis as a larger enhanced region of the local electric field and the higher absorption enhancement factor can be directed toward greater activation of photocatalysts and improved reactivity.[19] The localized hotspots seen in individual nanoparticles can now be identified to exist in between the coupled nanoparticles. Additionally, many of these features of split absorption peaks, enhanced absorption and large electric field regions are not solely limited to long arrays or chains of nanoparticles but are also evidenced in smaller populations of coupled nanoparticles such as dimers and trimers.[67,68] **(Figure 1.12)**

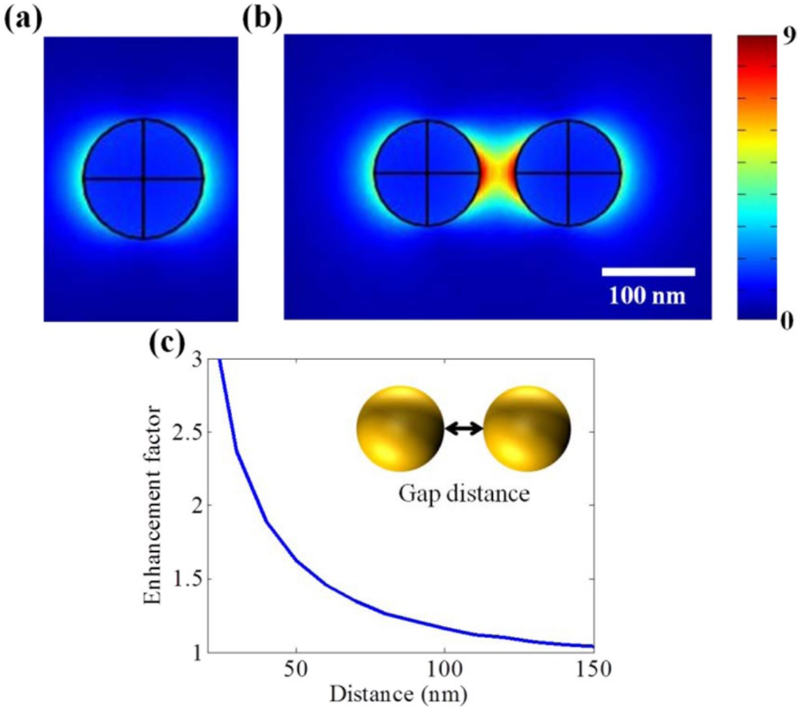

Figure 1.12. Simulated electric field amplitude intensity distributions for (a) single Au nanoparticle and (b) Au dimers at incident light of wavelength 633 nm. The nanoparticles are of diameter 100 nm. (c) The corresponding field enhancement factor relative to gap distance. Reprinted for academic use from Ref[67] with attribution and adherence to Creative Commons Attribution 3.0 License.

For larger particle separations, far-field diffraction coupling dominates where the interactions between particles scale by a factor d^{-1}. This coupling has been observed mainly in 1D and 2D arrays of nanoparticles arranged in a fashion alike to those of gratings[69–71] and can be fabricated using lithographical techniques. Due to their rarity in photocatalytic applications, further discussion of far-field diffraction coupling will not be pursued. Note, the discussion of coupled nanoparticle ensembles, thus far, pertains to ordered arrays. For the sake of simplicity, electromagnetic coupling in disordered arrays and the subsequent localization effects will not be discussed.

1.7 Closing Remarks

It is important to recognize that plasmonics can also be viewed through a quantum mechanical description. Here, plasmons are described as electron-density waves that oscillate against the background of positive charge that is the atomic lattice of the metal. The plasmons are damped by electron-hole pair excitations otherwise known as *Landau damping*.[34,72] The quantum mechanical picture is suitable for bulk systems where translational symmetry can be used to great effect or in the case of small metal clusters with only a few free electrons. Metal nanoparticles are much too large in general to fit this picture and translational symmetry is not possible.[32]

The classical Maxwellian description is the norm in the field where the plasmon response is equivalent to the excitation of a macroscopic polarization of the metal medium by an external electric field. Once the dielectric response of the metal is known, Maxwell's equations can be utilized to determine the plasmon modes and provide an accurate description of the metal's optical response. The classical approach breaks down only when a suitable description of the dielectric response is not possible or if the particle sizes involved are comparable to the Fermi wavelength where quantum effects take over (for plasmonic noble metals, this is ~ 1 nm; quantum dots are one such system).[48]

In the following chapter, we consider how the incorporation of plasmonic noble metal nanoparticles in semiconductor photocatalysts reaps various benefits for photocatalysis.

Chapter 2
Plasmonic Photocatalysis

2.1 Enabling Photocatalysis

Various factors dictate the optimal efficiency of a plasmon-enhanced photocatalytic system. Several said dependencies were identified in the prior chapter, concerning the plasmonic component, including nanoparticle size, morphology, and the surrounding environment. Au and Ag are the two most popular plasmonic metals and support high quality plasmon resonances while experiencing low losses compared to other plasmonic metals. Ag has consistently demonstrated lower losses and stronger plasmon resonances, but Au is more stable (chemically and physically) and is preferred over the former.[32] Other plasmonic noble metals such as Cu also support resonances at optical wavelengths but experience weaker plasmon resonances attributed to high losses via electron-electron scattering and other damping mechanisms. Lastly, Al supports plasmon resonances predominantly in the ultraviolet but also has a high oxidation tendency that critically limits its plasmonic performance.[73,74]

Among the variety of semiconductor photocatalysts, TiO_2 remains the benchmark for the reasons discussed in Chapter 1. The final component in any photocatalytic system involves suitable redox solution groups (Ag/Ag+, O_2/O^-, O_2/OH^-, H_2/H^+ etc.). Ultimately, preceding other miscellaneous variables such as metal loading, pH values, and temperature,[19] the dominant factor in determining the efficacy or suitability of a plasmonic photocatalytic system focuses on the energy band positions of the materials being utilized. It is the energy band positions of the individual components that determine what happens when said materials are brought into direct contact with each other.

2.1.1 How do photocatalytic reactions work?

Electron-hole transfer and generation processes are crucial to initiating redox reactions in photocatalysis. In semiconductor photocatalysts, there is the direct excitation of electron-hole pairs when a photon of energy equal to or greater than the bandgap of the semiconductor excites an electron from the valence band to the conduction band leaving behind a hole in the valence band. The immediate question then concerns the fate of these charge carriers i.e., what happens to the electrons and holes after their generation?

In a typical photocatalytic process, upon generation of an electron-hole pair, the electron and hole have energies E_{CB} and E_{VB}, respectively. The electron and hole can now be considered as active charge carriers that can be utilized for redox reactions and can be transferred to intermediate energy levels E'_{CB} and E'_{VB}. Recombination of the electron and hole can be suppressed provided they are spatially separated. Using appropriate acceptor and donor molecules (from our redox solution groups), the electron can be captured by an acceptor molecule which reduces to an anionic acceptor molecule, and likewise the hole can be captured by a donor molecule which oxidizes resulting in a cationic donor molecule. The defining conditions for charge carrier transfer and redox reaction to occur spontaneously is that the $E_{CB} \geq E'_{CB} \geq E_{reduction}$ for the electron and $E_{VB} \geq E'_{VB} \geq E_{oxidation}$. **(Figure 2.1)**

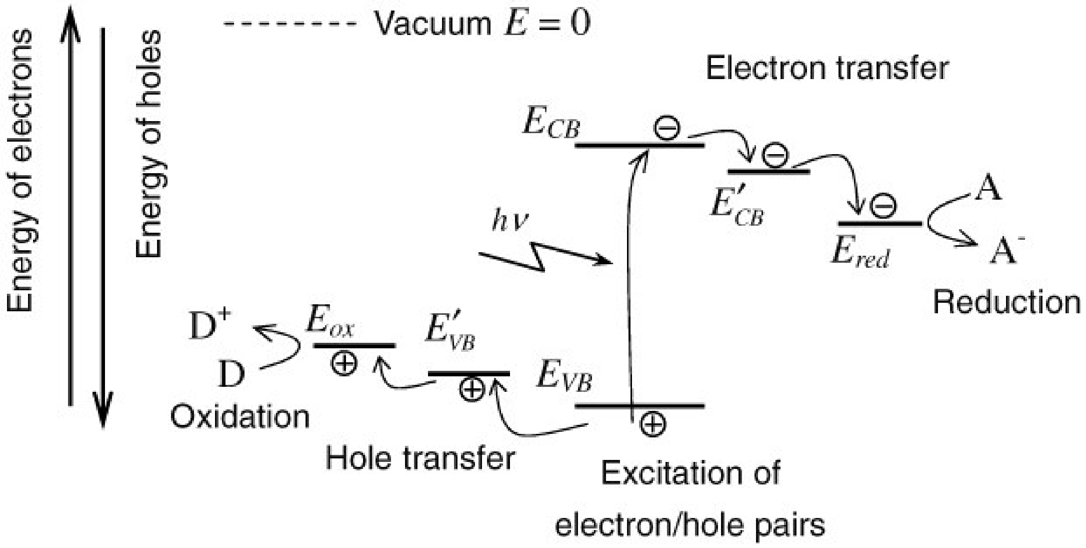

Figure 2.1. Electron-hole pair excitations and charge transfer observed in a typical photocatalytic process to promote redox reactions. Reprinted with permission from Ref[19]. Copyright IOP Science (2013).

2.1.2 Plasmon Resonance and the Schottky Junction

In plasmon-enhanced photocatalytic systems, charge carrier generation is achieved through the synergistic effects of the LSPR feature.[53,54,58,75–78] When placed in intimate contact, the noble metal and the semiconductor form a Schottky junction. Au-(n-type) TiO_2 noble metal nanostructure-semiconductor heterojunctions are particularly ubiquitous and shall be used as our referential system. Noble metals generally have a high work function, and in the case of Au, its Fermi level is located below that of n-type TiO_2. Note, the n-type property of TiO_2 recognizes the existence of an excess population of electrons in the semiconductor.[10] Upon contact, the Fermi levels equilibrate. This causes bending of the conduction band of TiO_2 and the formation of a Schottky barrier, a signature feature of the Schottky junction. Thus, a depletion or space-charge region is formed, where an internal electric field develops inside the photocatalyst but close to the metal/semiconductor interface. This internal electric field is maintained and directed from the semiconductor TiO_2 to the metal Au nanoparticle. This is because upon contact with the Au, the electrons in TiO_2 diffuse from the TiO_2 to the noble metal resulting in a positively charged region in the TiO_2. Upon equilibration, an equal number of electrons are trapped on the Au surface resulting in the internal electric field and space-charge region. If electrons and holes were to be created at the metal/semiconductor interface, the internal electric field would drive the electrons and holes to move to TiO_2 and Au, respectively, thus suppressing and preventing recombination while providing an efficient channel of charge transfer to promote photocatalytic reactions. This, in short, is a plasmonic photocatalytic system.

In the context of photocatalysis, we must also consider the additional component of the redox group in the solution maintaining our referential plasmonic heterojunction. Once again, before contact, the n-type semiconductor is defined by its Fermi energy level E_F located closer to the conduction band versus the valence band, the noble metal by its work function W, and the redox group solution by its redox potential E_{redox}. Each of these parameters may have very different values, but upon contact and the subsequent charge-carrier flow, a new state of equilibrium is established where E_F, W, and E_{redox} equilibrate and line up. **(Figure 2.2)** Just like earlier, a space-charge region builds up in the semiconductor photocatalyst and helps separate the electrons and holes. For the sake of simplicity, we avoid considering the effect where a similar space-charge region could be built given $E_F \neq E_{redox}$ and the semiconductor is in direct contact with the redox solution. This can commonly occur in conventional non-plasmonic photocatalytic systems and can potentially lead to adverse effects on the charge carrier transfer process during photocatalysis.[79]

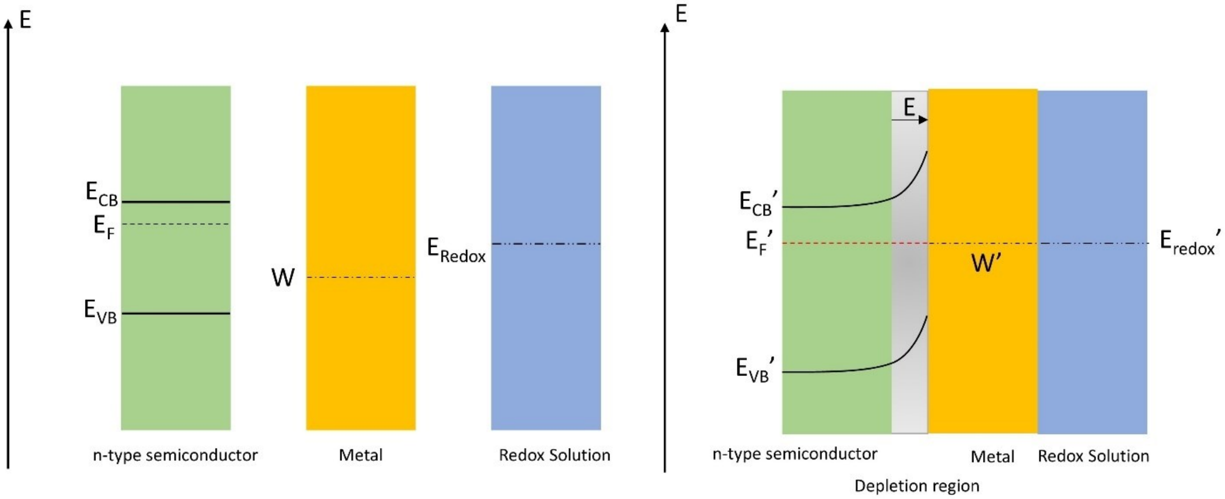

Figure 2.2. Energy diagram schematic of a plasmonic heterojunction before contact (Left) and after contact (Right), demonstrating the equilibration of the Fermi energy level of the semiconductor, work function of the metal, and redox energy level of the redox solution.

It should be noted that due to the fewer available energy states in the semiconductor photocatalyst and the noble metal nanoparticle, because of their relatively small total surface areas as opposed to those in the redox solution, E_{redox} values do not change significantly while E_F and W line up alongside it.[19] It is also important to understand that the band bending observed upon Schottky contact is dependent on the magnitudes of the Fermi energy level of the semiconductor relative to the work function of the noble metal (for metal-semiconductor heterojunctions) and that of the redox potential of the redox group (for semiconductor-redox solution heterojunctions). The Schottky junction plays a crucial role in charge carrier separation and recombination suppression in plasmonic systems but is also presupposed by a variety of factors including the type of semiconductor, the position of the semiconductor's Fermi energy level relative to the metal's work function, the resultant band-bending, and the irradiation state, among many others. The actual effect at the interface on facilitating charge carrier separation and the directionality of charge transfer could vary significantly in these hybrid systems.[19]

In conclusion, band edge positions of the materials utilized in plasmonic photocatalysis play a significant role in promoting photocatalytic reactions; the energy band positions of the photocatalyst define its optimal absorption wavelength, and those of the redox group relative to the photocatalyst determine which specific redox reactions are possible. Band edge positions of common materials utilized in plasmonic photocatalysis are presented in **(Figure 2.3).** The conduction and valence bands must straddle the redox potentials of the photocatalytic reaction in order to facilitate the selective reaction. Now that we have reviewed the major processes in plasmonic photocatalysis, where exactly do hot electrons fit into the picture?

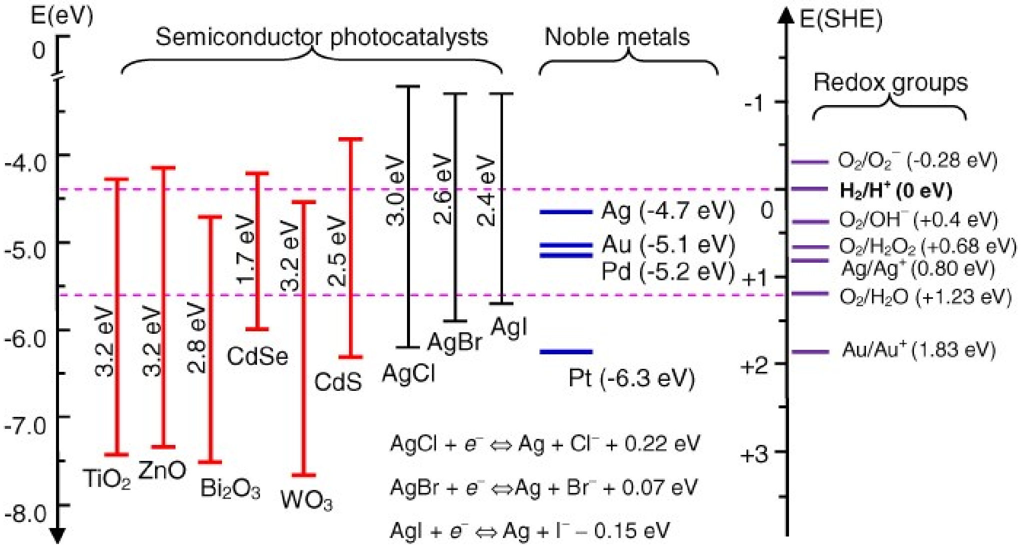

Figure 2.3. Band edge positions of common materials for plasmonic photocatalysis including semiconductor photocatalysts, noble metals, and redox groups. Reprinted for academic use from Ref[19]. Copyright IOP Science (2013).

2.2 Hot Electron Plasmonic Theory

Theoretical work on hot electrons started in the 1930s, when these energetic charge carriers were observed by applying a strong electric field to a conductor. For metals, since high electric fields could result in melting or high joule heating- the process by which the passage of an electric current through a conductor produces heat -most early hot electron work focused on understanding dielectric breakdown in insulators.[80] Hot electrons are electrons that are not in thermal equilibrium with their immediate environment (generally, the atoms that compose a material)[80] and have very high effective temperatures (up to several thousand Kelvin) compared to that of room temperature.

Hot electrons are "hot" due to their high kinetic energies and are considered as the by-product of surface plasmons (or plasmons) – the collective and coherent oscillations of delocalized electrons that are excited by incident photons at a metal-dielectric interface.[81] As we have seen earlier, the collective oscillations of these free electrons are excited by the electric field component of incident light at the metal-dielectric interface. Surface plasmons are categorized into two different modes depending on the morphology of the metallic nanostructure that enables them. One such mode involves Surface Plasmon Polaritons (SPPs) **(Figure 2.4b)** that are excited on continuous metal structures with characteristic dimensions larger than the wavelength of incident light. These are propagating plasmonic oscillations that travel along the metal surface for distances of tens to hundreds of micrometers.[82]

Another mode of surface plasmons is indeed the LSPR **(Figure 2.4a)** that is observed only in metal nanostructures smaller than the electron mean free path within the material as well as the wavelength of incident light.[22] The resonance here refers to the event where the frequency of the electron oscillations (against the restoring force of the nuclei) in the metal nanostructure matches that of the incident light. This is the main factor for the confinement of photonic energy to the surface of the metal nanostructure for a time period that exceeds the time-scales photons would generally spend in the same volume traveling at the speed of light.[83] LSPRs are non-propagating plasmons that are strictly confined to the metal nanostructure, and as discussed earlier, can be excited on metal nanoparticles of various morphologies (spheres, prisms, cubes, shells, etc.) as well as around nanoholes, nanorods, or even nanoscale corrugations in thin metal films.[84]

In general, plasmons (LSPRs or SPPs) can be described as free electron oscillations that are a result of dipole and higher order multipole formation in metal structures due to incident electromagnetic wave excitation.

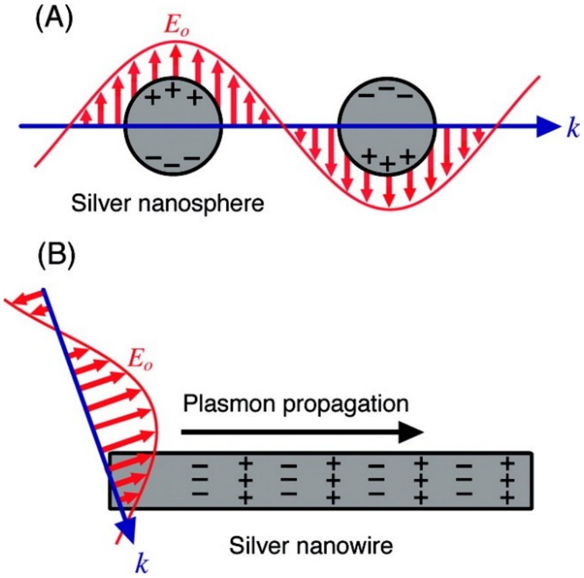

Figure 2.4. Schematic illustrations of (A) Localized Surface Plasmon Resonances and (B) Surface Plasmon Polaritons. Note the differences in morphologies of the structures involved. E_0 refers to the electric field of the incident light with wavevector k. Reprinted for academic use from Ref[59]. Copyright American Chemical Society (2011).

2.2.1 Hot Electrons in Plasmonic Photocatalysis – Why do they matter?

Hot electrons are observed in various critical technologies that take advantage of the LSPR mechanism including cancer tissue targeting,[85,86] lasing,[87] imaging,[88] molecular characterization,[89,90] and photovoltaics[91,92] to name a few. Many of these applications focus on the design of plasmonic systems to optimize the confinement of photonic energy or modify the refractive properties of light and its propagation in certain media while minimizing internal losses[93] or charge carrier formation and transfer processes. Plasmonic photocatalysis falls in the latter category, where the focus is largely on LSPRs in plasmonic nanoparticles rather than SPPs, unless mentioned otherwise. LSPR excitation can be used to drive chemical reactions and transformations directly on the surface of the plasmonic noble metal nanostructure or remotely by transferring the incident photonic energy to nearby metals, semiconductors, or molecular photocatalysts. Taking our reference system of Au-(n-type) TiO_2 heterojunction, let us consider the role hot electrons, via the LSPR, play in plasmonic photocatalysis.

Hot electrons are a transient phenomenon in nature. In general, hot electrons have energy on the order of eV corresponding to the energy of the incident light used to excite them. Hot electrons in bulk gold with energies greater than 1 eV above E_F have a lifetime of less than 50 fs due to extensive relaxation via inelastic electron-electron interactions.[94] This is averted in small Au nanoparticles where hot electron lifetimes range between 100-500 fs, an order of magnitude larger, thanks to confinement effects and reduced electron-electron interactions.[95] In the Au-(n-type) TiO_2 heterojunction, the LSPR of the noble metal nanoparticle, in response to incident light has been observed to play host to a variety of charge generation and transfer processes that help promote photocatalytic reactions.

Essentially, the LSPR results in the generation of more electrons in the semiconductor. These electrons have been observed to have high potential energies and originate from the LSPR excitation of the plasmonic metal. As such, these energetic hot carriers, or hot electrons, have sufficient energy to easily traverse the space-charge region at the metal-semiconductor interface and feed into the semiconductor's conduction band. It is important to note that the term "hot electrons" not only describes the individual electrons themselves, but rather the Fermi-Dirac distribution of electrons in a solid that are at an elevated effective temperature (the effective temperatures when considering the carrier densities in the solid, and not the solid itself) as opposed to thermal equilibrium.[96] The Schottky barrier at the metal/semiconductor interface assists in trapping the now transferred hot electrons in the conduction band of the semiconductor by delaying their travel back to the plasmonic metal.[97] This LSPR mediated hot electron-transfer to the conduction band of the semiconductor effectively prolongs the lifetime of these energetic charge carriers, allowing for their utilization in various photocatalytic reactions.

Why is this of significance? It is well-known that plasmonic metals such as Au and Ag have surface plasmon resonances in the visible spectrum of light. As such, if the Au nanoparticle is able to absorb visible light, independent of the absorption of UV light by TiO_2 itself, the LSPR created in the metal nanoparticle in response to the incident electromagnetic field, will drive a collective oscillation of electrons in the Au nanoparticle, enabling the transfer of electrons to the TiO_2 even in the absence of any light absorption by TiO_2.[11] In such a manner, the LSPR of the Au nanoparticle paves the way for visible light sensitization of the wide bandgap TiO_2 semiconductor.

While it has been assumed that the Au nanoparticle absorbs visible light and the TiO_2 absorbs UV light, this is not a necessity. Various experiments have been run where the Au nanoparticles are tailored to absorb UV light while the TiO_2 is doped with metallic or nonmetallic species, such as N_2-doped TiO_2 to improve its responsivity to visible light.[98,99] Apart from the LSPR's visible light sensitization, the absorption of an incident UV photon by TiO_2 can also create an electron-hole pair near the space-charge region of the metal-semiconductor interface. The internal electric field then forces the electron to move to the TiO_2 region and the hole to the Au nanoparticle. Alongside the hot electrons occupying the semiconductor's conduction band, these photogenerated electrons and holes are driven by the internal electric field and by way of capture by acceptors and donors in the surrounding solution, help initiate further chemical reactions.[22] Apart from noble metal/semiconductor systems, plasmon-generated hot electrons have also been demonstrated to interact directly with molecules adsorbed on the metal nanoparticle's surface.[83,93,100–105] Here, the LSPR excitation of hot electrons assists in polarizing reactant molecules in a surrounding fluid enhancing molecular adsorption to the metal surface. The LSPR has also been demonstrated to heat up the local environment, thus increasing mass transfer of molecules and enhancing reaction rates.[19]

In summary, plasmonic photocatalysis enables the creation of active charge carriers in the semiconductor photocatalyst even in the absence of any or optimal bandgap-energy conforming light absorption by the semiconductor photocatalyst. Compared to the photocatalytic processes found in semiconductor photocatalytic systems (largely governing heterogeneous catalysis) that are so often hindered by high recombination rates, plasmonic noble metal-semiconductor nanostructures, via the LSPR can absorb light separately and contribute to the photocatalytic process in a synergistic manner. The presence of the plasmonic noble metal nanoparticle significantly improves the quantum efficiencies of photocatalytic reactions.[106–108] Despite various demonstrations of the potential of plasmonic photocatalytic systems, there has been very little progress in the commercialization of these systems. This can largely be attributed to the gaps in knowledge and understanding that continue to persist within the scientific community regarding the origin of hot electrons, and the subsequent charge dynamics that play a crucial role in plasmon-enhanced photocatalytic systems to promote photocatalytic activity. Considering the metal/semiconductor heterostructures involved and the influential role the interfacial electronic structure plays on said systems' catalytic activity, precise knowledge of interfacial and hot electron dynamics over time scales that coincide with chemical reactions is fundamental toward understanding related processes and system optimization.

2.2.2 Hot Electrons in Plasmonic Photocatalysis – How do they work?

In describing the charge-transfer dynamics involved in plasmonic heterostructures, the scientific community has for a large part been guided by established knowledge on the physical modeling of extended metal surfaces.

Conventional theory suggests an indirect sequential charge excitation/charge transfer process to describe hot electron charge transfer dynamics when LSPR excitation occurs on a plasmonic metal nanostructure. In this description, an incident photon excites the LSPR of a nanoparticle resulting in the formation of particle plasmons (the collective oscillations of electrons) that dephase nearly instantaneously to yield excited electron-hole pairs within the metal nanostructure. Dephasing here refers to a reduction in the amplitude, a signature of energy loss, of the collective oscillation of free electrons to the excitation of individual electrons and holes in the metal nanostructure. This is also otherwise known as Landau damping.[109] The dephasing of the particle plasmons into electron-hole pairs is a form of non-radiative decay that can involve either intraband or interband transitions.[110] A competing, but typically inefficient, dephasing mechanism is the radiative decay of particle plasmons.[111]

Spectroscopic techniques such as single-particle near-field scanning optical microscopy (SNOM) and second harmonic generation (SHG) have been used to determine that Landau damping occurs on time scales ranging from less than 10 fs to a few tens of fs.[111] For Au and Ag nanoparticles of size ~ 20 nm, formed by electron beam lithography, dephasing times of 4-8 fs and 7-10 fs have been observed, respectively.[109,112] The resultant electron-hole pairs produced in the few femtoseconds following plasmon dephasing are distributed over a range of energies allowing higher energy charge carriers to occupy acceptor states in nearby semiconductors or molecules. What began as an equilibrium thermal distribution of charge carriers in the metal nanostructure has changed to a nonequilibrium athermal hot charge carrier distribution that cannot be described by Fermi-Dirac statistics. The subsequent cooling of this athermal charge carrier distribution to yield a Fermi-Dirac distribution of electrons occurs over tens to hundreds of femtoseconds through contributions from bulk electron-electron scattering, radiative damping, and electron-surface collision damping.[83,93,101,113,114] Further relaxation of the charge carrier distribution occurs via electron-phonon collisions over a few picoseconds while the excited phonons themselves equilibrate over hundreds of picoseconds. **(Figure 2.5a)**

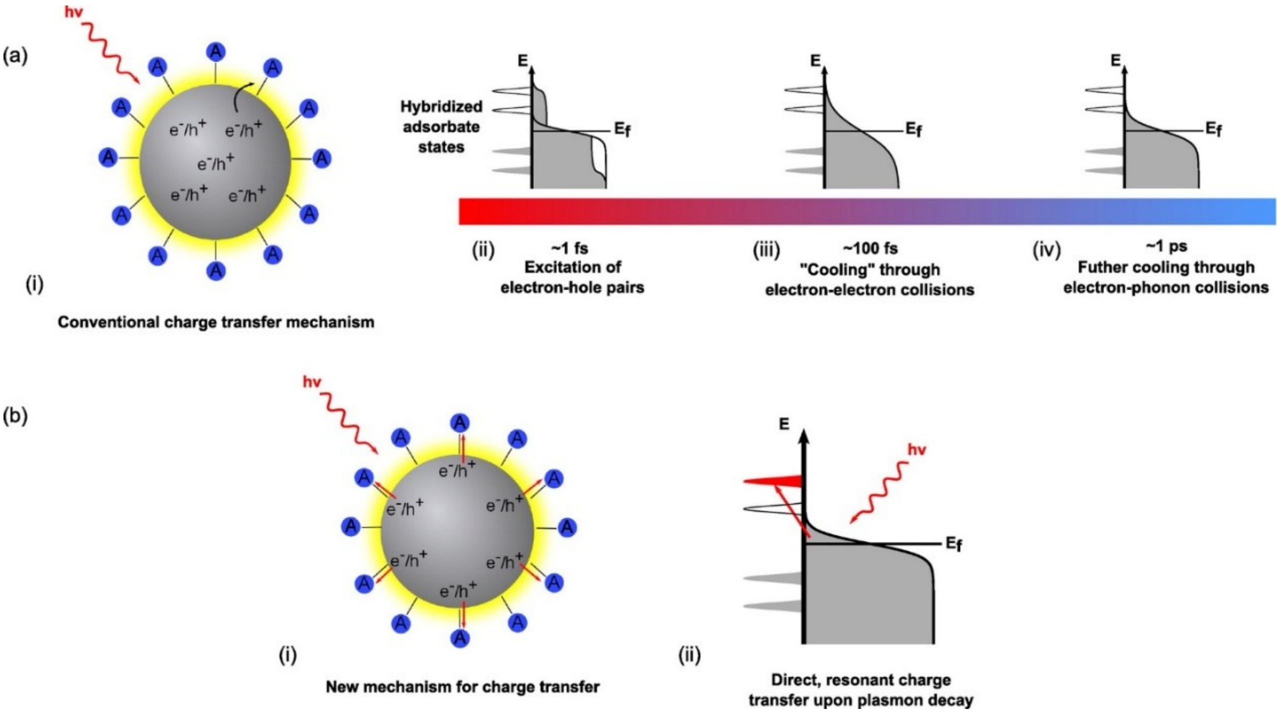

Figure 2.5. (a) The conventional charge transfer mechanism where resonant photon absorption results in the creation of hot electron-hole pairs within the metal nanostructure followed by (i)-(iii) immediate relaxation of the athermal hot carrier distribution via electron-electron and electron-phonon collisions, in what is a momentum relaxation process where the cooling of the distribution is facilitated by d-band holes. (b) DIET mechanism where electrons generated under excitation are directly injected into the conduction band of the semiconductor without and before any interactions with other electrons. Reprinted for academic use from Ref[93]. Copyright American Chemical Society (2016).

Time-resolved studies involving femtosecond pulse experiments have been influential in providing a kinetic representation of these diverse damping processes. From these experiments, a distinction can be made between electrons excited via low-energy and high-energy transitions. As such, a large population of low-excitation energy electrons and a dilute population of high-excitation energy electrons are observed to comprise the total distribution of electrons during the femtosecond pulse. Essentially, conventional theory states that in LSPR excitation of a plasmonic nanoparticle, the final thermal distribution of electrons is comprised of significantly fewer high energy excitation electrons as compared to the initial excited distribution; the rapid cooling of the initial athermal excited distribution of electrons is attributed to rapid relaxation processes with electron-electron scattering occurring at ~ 100 fs followed by electron-phonon collisions at the picosecond timescale.[115,116] These collisions can result in a localized heating effect where an increase in the temperature of the metal nanoparticle may be observed.[19] Phonon-phonon relaxation can also couple the vibrations of the semiconductor lattice to that of the metal nanoparticle, further heating the two materials and the surrounding environment.

In this framework, two types of charge carriers can be distinguished as a result of LSPR excitation: (i) low-excitation energy charge carriers (Drude electrons and holes) found near the Fermi level, and responsible for plasmon oscillations, and (ii) high-excitation energy charge carriers (hot electrons) with energies >> $k_B T$ above the Fermi level, where k_B is Boltzmann's constant and T is the temperature (in units of Kelvin). Ideally, plasmonic photocatalysis would desire the extraction of these hot electrons to promote photocatalytic reactions. But according to the conventional theory, the expected yield of hot electrons is low. This is because most of the charge carrier energy is immediately lost through LSPR dephasing via interactions with other electrons and phonons within the nanoparticle, and thus, a large fraction of the energetic charge carriers that are formed do not have sufficient energy to support photocatalytic activity or energy transfer reactions. Drude carriers do not have the excess thermodynamic energy at room temperature to drive chemical reactions, only hot carriers do. Due to this, conventional theory suggests that the key to facilitate efficient plasmonic photocatalysis would involve the extraction of the hot carriers before they fully equilibrate. However, there have been multiple experimental observations reporting the contrary.

Fundamental deviations from the conventional description of hot carrier charge excitation/transfer have been discovered in systems concerning semiconductor-to-adsorbate charge transfer reactions where extraction processes have involved tunneling or thermionic emission of hot carriers over the Schottky barrier and into the nearby semiconductor.[117] Now, according to the sequential excitation and relaxation picture proposed by conventional theory, if one were to take note of the number of hot carriers with the right energy and momentum to cross the barrier, the nature of the carrier distribution, and the probability that hot carriers will reach the noble metal-semiconductor interface as well as the interface transmission probability, injection efficiencies of ~ 1% are expected.[118] Considering the relaxation timescales involved in the sequential charge transfer framework, ultrafast charge transfer and extraction of hot carriers from the metal to the semiconductor is a strict prerequisite for efficient plasmonic photocatalysis. Surprisingly, this is not the case in reality, as hot electron injection efficiencies of 20-50% for Au nanoparticle - TiO_2 nanoparticle heterojunctions have been observed using femtosecond transient absorption spectroscopy.[97,118] These results are supported by ultrafast charge transfer timescales ranging between 50-240 fs that have been observed in said systems under 550 nm light excitation.[119,120]

These contradictions have called for a completely different mechanistic description for hot electron harvesting involving the direct excitation of interfacial charge transfer (IFCT) states. **(Figure 2.6b)** The IFCT mechanism refers to when an electron in the noble metal is directly excited into the conduction band of the semiconductor. From the perspective of plasmonic systems, the IFCT mechanism refers to plasmon induced metal-to-semiconductor interfacial transitions (PICTT)[121] where it is posited that the plasmon of the noble metal dephases with the direct creation of an electron in the conduction band of the semiconductor and a hole in the metal. **(Figure 2.6c)** This is promoted by strong coupling and mixing of metal and semiconductor energy levels. Plasmon-induced IFCT has been widely demonstrated in Au nanoparticle - CdSe heterojunctions[121] and have also been identified as the major cause of the high visible responses observed in Cu-TiO_2 heterojunction photocatalysts,[23,122–126] but the direct excitation of charge transfer states is most commonly found in experiments where adsorbates are added to the surfaces of plasmonic nanostructures.

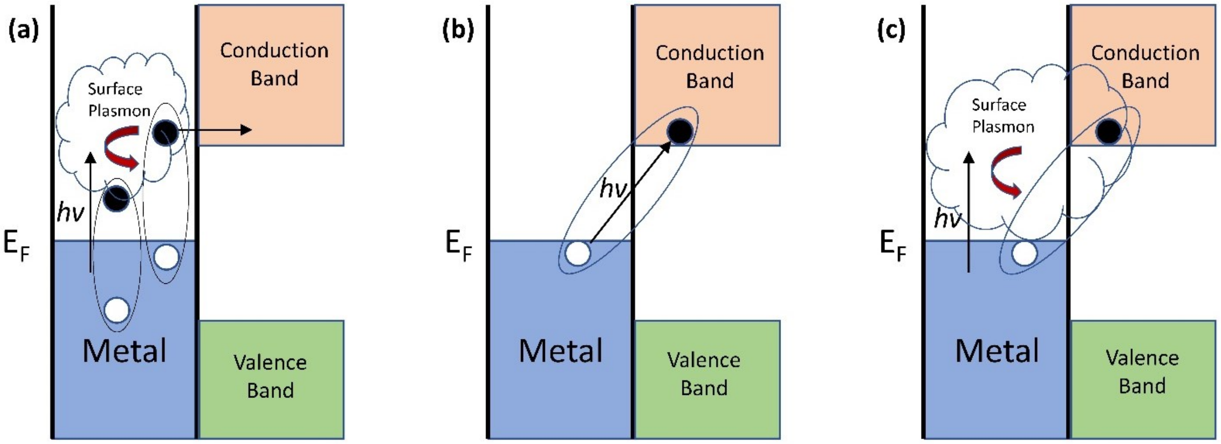

Figure 2.6. The various charge separation pathways in noble metal-semiconductor systems. (a) The conventional plasmonic hot electron transfer (PHET) mechanism where a plasmon (cloud) in the noble metal dephases into a hot electron-hole pair via Landau damping. The electron-hole pairs display a broad distribution of energies and the hot electron is injected into the conduction band of the semiconductor. (b) The IFCT mechanism where an electron in the noble metal is directly excited into the conduction band of the semiconductor. (c) The PICTT mechanism where the plasmon (cloud) dephases with the direct creation of an electron in the conduction band of the semiconductor and a hole in the metal. VB and CB indicate valence and conduction bands, and *hv* is the energy of the incident photon.

In general, molecule-to-semiconductor electron transfer reactions are said to occur at sub-picosecond timescales thanks to the high density of vacant acceptor states in the semiconductor and by invocation of Fermi's golden rule.[127] On the other hand, semiconductor-to-molecule electron transfer reactions are quite slow due to the much lower density of states in the molecule.[128] Given this, conventional theory would draw the conclusion of significant hot electron transfer from the noble metal to vacant molecular states to be highly unlikely, but once again multiple experiments have reported that the very presence of a chemical adsorbate (a molecule for example) on a plasmonic nanoparticle can lead to even faster relaxation of the LSPR over timescales of ~ 5 fs.[83] This chemical adsorbate promoted relaxation of the LSPR is referred to as chemical interface damping (CID). CID suggests the addition of adsorbates, absent in IFCT, to the surface of plasmonic nanostructures induces a direct and additional pathway for plasmon dephasing as well as a broadening of the plasmon band. The mismatch in relaxation timescales here compared to those suggested by the indirect sequential mechanism has led to the development of a contending explanation where molecular adsorbate plasmon-enhanced photocatalysis reactions are involved. Such reactions are said to proceed through a direct excitation mechanism or a "dissociation induced by electronic transitions" (DIET) process where a charge-transfer transition is directly excited while seemingly bypassing other processes including LSPR damping within the noble metal nanoparticle, and the internal relaxation of electrons.[83,93,113] **(Figure 2.5b)**

In this manner, DIET could be identified as a subset of CID (which itself is a subset of IFCT, involving molecular-noble metal heterostructures) describing small molecule-plasmon enhanced interfacial charge transfer processes where the excitation of the charge transfer transition transiently occupies a surface bound anionic state of the adsorbed molecule. Such a state is vibrationally excited according to the conventional theory and will relax rapidly through vibrational cooling followed by the transfer of the electron back into the metal nanoparticle. Dissociation is then activated when the electron excitation rates are greater than electron relaxation rates resulting in reactive species that can initiate photocatalytic reactions.[113] The DIET process has been identified as the primary mechanism behind the high hot electron charge transfer quantum yields evidenced in plasmon-induced oxidation reactions involving resonant photo-electron transfer from Au and Ag nanoparticles to strongly bound molecules or semiconductor dots on the surface of the noble metal nanoparticles.[93,113,129] In fact, DIET is fundamental to systems where an organic molecule is adsorbed to a noble metal-semiconductor heterojunction: the photocatalytic oxidation of CO over Au nanoparticle-TiO_2,[130] the oxidative degradation of organic compounds using TiO_2-Au photocatalysts,[131] vapor phase reduction of CO_2 over TiO_2-Au nanoparticle photocatalysts,[108] and the use of reduced graphene oxide (rGO) bridges to shuttle hot electrons between Ag/Au nanoparticles and TiO_2.[132]

A clear distinction between CID and general electron transfer following plasmon decay remains elusive. There are also doubts if CID and electron-surface scattering are distinct phenomena.[133] A fundamental difference between the direct and indirect charge-transfer mechanisms concerns their description of the exact moment when plasmon dephasing occurs. In the case of the former, it is the charge-transfer reaction itself that leads to plasmon dephasing while in the latter plasmon dephasing is described to occur before charge-transfer reactions. The importance of this distinction between the two processes necessitates further research to be pursued on CID processes that may help shed light on how molecules interact with electrons in metal nanoparticles. This would potentially include studies on the binding modes of reactants on the surface of metal nanoparticles, orbital couplings, and their influence on hot electron generation and transfer.[93,95,129,134] Much of this will be crucial in constructing a full picture of photocatalytic reactions driven by plasmon-induced hot electrons, a prerequisite for modifying relevant nanostructures and achieving full optimization of plasmonic photocatalytic systems by manipulating hot electrons.

For now, in the context of current progress in plasmonic photocatalysis, the indirect sequential mechanism and the IFCT mechanism are both commonly used to describe and postulate the charge transfer processes realized in plasmonic noble metal-semiconductor heterojunctions. Taking our reference system of Au-(n-type) TiO_2 plasmonic noble metal-semiconductor heterojunction, visible light absorption by the Au nanoparticle results in collective oscillations (plasmons) of sp-band electrons along with the creation of hot electrons in the sp-conduction band. The rapid plasmon dephasing results in very poor hot electron injection efficiencies. As such for successful and efficient hot electron injection to occur, a number of conditions must be satisfied: (i) the charges must first be able to reach the surface of the plasmonic nanoparticle, and (ii) from there the charges must have enough energy (above the metal's Fermi level) to overcome the Schottky barrier while (iii) the residual hot holes must be extracted to sustain charge neutrality within the plasmonic noble metal.[135] The hot holes and electrons formed by this charge separation at the metal-semiconductor interface help initiate redox reactions, and promote plasmonic photocatalysis.

2.3 Advantages of Plasmonic Photocatalytic Systems

Photocatalysis can be compressed to four major steps: (i) the absorption of light, (ii) the subsequent generation of a local electric field, (iii) followed by charge carrier generation and separation, and (iv) the facilitation of redox reactions. Plasmonic photocatalysis, by way of the LSPR, promotes all these steps resulting in higher optical absorption and visible light sensitization, optimal light utilization, enhanced local electric fields, enhanced charge carrier generation and separation, as well as enhanced temperature dependence and molecular adsorption. We will briefly consider representative examples of each case in the following sections.

2.3.1 Optical Absorption, Visible Light Sensitization, and Optimal Light Utilization

The LSPR of noble metal nanoparticles as well as their optimized scattering of light facilitates a collective enhancement in optical absorption and visible light sensitization of common semiconductor photocatalysts such as TiO_2 that primarily absorb in the UV-regime.

Linic et al.[92] have demonstrated that the incorporation of large noble metal nanoparticles (> 60 nm) in semiconductor photocatalysts allows for enhanced scattering and increased photon path length in the semiconductor. Additionally, the morphology and loading amount of the noble metal has been proven to play a role in the enhancement of light scattering.[136] It has been observed that large Ag nanocubes of edge length 118 ± 25 nm enhance optical absorption of 400-500 nm wavelength photons by 25% while providing the highest photoreaction rates compared to other morphologies.[137]

Plasmonic photocatalysis also provides for optimal light utilization compared to what is typically observed in semiconductor photocatalysis. In semiconductor photocatalysts, photons only penetrate a few nanometers to a few micrometers into the semiconductor resulting in poor absorption, and usage of light. Furthermore, photons absorbed far below the surface the semiconductor can contribute very little to photoreactions as the subsequently generated electrons and holes would encounter long diffusion lengths and would recombine before reaching the surface.[92] This adversely affects the reaction rates observed in these systems as the electrons easily recombine with the holes in the bulk of the semiconductor before ever reaching the surface where they could be used to promote chemical reactions. This is averted in plasmonic photocatalysis where the space charge layer reduces the chances of electron-hole recombination.[75,92] Furthermore, the charge carriers generated in plasmonic photocatalysis are closer to the surface of the semiconductor and are provided a shorter diffusion path to the surface. Thus, the energy of the incident light is utilized far more effectively in a plasmonic photocatalytic system as compared to a semiconductor photocatalyst alone.

Beyond these improvements, the most inviting aspect of plasmonic photocatalysis is the visible light sensitization of semiconductor photocatalysts. **(Figure 2.7)** Farsinezhad et al.[23] have shown that the incorporation of an Au/TiO_2 composite nanotube structure provides for visible light sensitization of TiO_2 resulting in a larger absorption in the visible range (>400 nm) that can be attributed to the LSPR. Other notable examples include those of Hu et al.[138] who provide a comparative analysis of the absorption spectra of pure TiO_2, Ag/TiO_2 composite, and an Ag/AgBr/TiO_2 composite. Ultraviolet-Visible (UV-Vis) diffuse reflectance spectra show that the Ag/TiO_2 composite has a larger absorption in the visible regime compared to the bare TiO_2 sample. This enhancement is directly attributed to the LSPR. A similar result is also observed with the Ag/AgBr/TiO_2 composite where the indirect bandgap transition of AgBr alongside the LSPR of Ag provides for visible light sensitization of the TiO_2. On a different note, distinct enhancement of light absorption has also been achieved in ZnO nanorods coated with Ag films.[139] An optimal film thickness of less than 30 nm is observed to provide the highest enhancement.

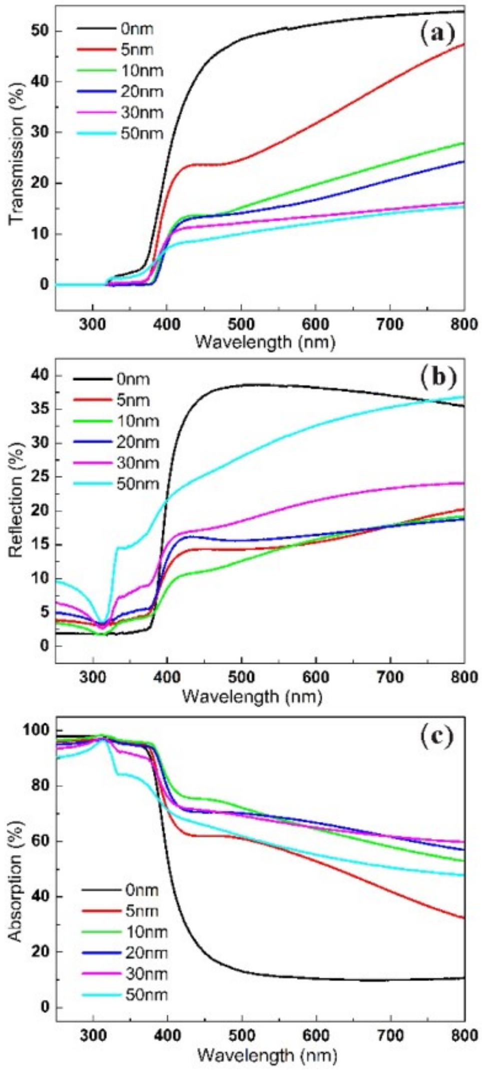

Figure 2.7. UV-Vis spectra for (a) transmission, (b) reflection, and (c) absorption of ZnO nanorods coated with varying thicknesses of Ag films. Within the visible-light range, it is noted that for Ag films of thicknesses less than 30 nm the highest absorption is recorded. This is attributed to LSPR effect induced by interaction between the incident light and the Ag film. For Ag films of thicknesses less than 30 nm, the film is composed of small islands where LSPRs are dominant and dipole-dipole scattering helps enhance visible light absorption. Reprinted for academic use from Ref[139]. Copyright IOP Publishing (2012).

2.3.2 Enhanced Local Electric Field

The LSPR results in an enhancement of the local electric field. Studies of the local enhancement of the electric field proliferate various applications in Raman spectroscopy,[140,141] plasmonic devices and sensors,[142] and metamaterials.[143–148] Finite difference time domain simulations have also confirmed said observations on the enhancement of the local electric field, where the enhancement factor can be tailored by changing the shape and size of the noble metal nanoparticle or via coupling to other nanoparticles.[46,147,149–152] **(Figure 1.9)** The focal region where these enhancements are discovered have been identified as hotspots and are generally located around regions of extreme curvature on the nanostructure that is being observed. Nanocubes are generally shown to have a larger enhancement factor compared to nanospheres and nanowires.[136] These observations are of great importance in plasmonic photocatalytic systems as the enhanced electric field can penetrate the space-charge region of the nearby semiconductor if it has direct contact with the noble metal nanoparticle. We have also seen that in the case of coupled metal nanoparticles the enhanced electric field would extend out of the metal to distances of tens to hundreds of nanometers.[46,143] This behavior in turn helps boost the charge carrier generation rate as in a semiconductor the charge carrier generation rate is directly proportional to the intensity of the local electric field. The enhancement of the local electric field, via the LSPR, would then further facilitate the enhanced generation of electrons and holes.[153,154]

2.3.3 Enhanced Temperature Dependence and Molecular Adsorption

Plasmonic photocatalytic systems also benefit from an enhanced temperature dependence and molecular adsorption. The LSPR of the noble metal nanoparticle converts part of the incident light energy into thermal energy (localized heating effects). While conventional semiconductor photocatalysis observes a reduction in reaction rates due to increased temperatures leading to higher charge recombination,[155] plasmonic photocatalytic systems do not suffer from the same. This has been demonstrated by Nishijima et al.[58] where an array of Au nanorods pattered on a n-type TiO_2 crystal demonstrated a positive dependence of the reaction rate on temperature where an increase in temperature via the LSPR resulted in higher photocurrent.

Enhanced molecular adsorption is another beneficial consequence of the LSPR of the noble metal nanoparticle. The presence of the metal nanoparticle enhances molecular interaction through various means, as if the noble metal were itself a strong catalyst. Pt fits this category and has been used extensively as a catalyst for various catalytic and reduction reactions.[156,157] Surface-enhanced Raman scattering and fluorescence quenching of dyes on metal nanoparticles provides further proof that the LSPR of metal nanoparticles allows for a fast, and efficient pathway of charge transfer.[153,158–160] In their incorporation with a semiconductor, the plasmonic system may result in an accumulation of charges either on the semiconductor or the metal which can assist in the selective attraction and repulsion of charged chemical compounds. The dipolar nature of the LSPR would particularly attract polar molecules such as water, while polarizing non-polar molecules, and ultimately enhance molecular adsorption.

2.3.4 Enhanced Hot Carrier Generation and Separation

The most important facet of plasmonic photocatalytic systems is the generation of hot charge carriers (electrons and holes) via the LSPR of the noble metal nanoparticle that help facilitate photocatalytic reactions. Although the specific mechanism that governs these hot charge carriers is up to contention, their generation and subsequent separation is a fact that has been consistently observed and exploited in multiple experiments.[92,101,136,137,149,153] These experimental efforts largely follow measurements that in and of themselves provide signatures of the enhancements in charge carrier generation and separation whilst also characterizing the potential applications of plasmonic photocatalysis.

2.3.4.1 Photocatalytic Dye Degradation/Aerobic Oxidation of Organic Compounds

Photocatalytic dye degradation involves the de-coloration of dyes. Thin layers of dyes can be deposited onto a plasmonic architecture via spin coating or dip coating.[136,161] The rate of discoloration by oxidation then serves as the signature of hole generation. Plasmonic enhancement of charge carrier generation would then correspond to faster rates of de-coloration as opposed to other photocatalytic systems.

Beyond dye degradation, plasmonic photocatalysis also finds a potential application in efforts for photocatalytic degradation of organic pollutants. These efforts follow the need to eliminate environmental pollution which pose adverse effects to human health and the environment itself. Natural biodegradation is very slow, and while semiconductor photocatalytic degradation of organic pollutants to non-hazardous products has been highly appealing, it is weighed down by the deficiencies that follow semiconductor photocatalysts. Plasmonic hot electron mediated photocatalysis, however, bridges this barrier. The enhanced generation of charge carriers in noble metal nanostructures can be engineered for specific chemical transformations through DIET.

One example involves a plasmonic system of Ag-loaded n-doped TiO_2 photocatalysts reporting the enhancement of visible-light induced photocatalytic degradation efficiency of Ag/n-TiO_2 in the degradation of methyl orange (MO) due to a synergistic effect involving both the incorporation of Ag-loading and n-doping.[162] X-ray Diffraction (XRD), X-ray Photoemission Spectroscopy (XPS), and UV-Vis Diffuse Reflectance Spectroscopy (DRS) techniques are utilized to characterize the Ag/n-TiO_2 which indicates a clear redshift in the optical response of TiO_2 photocatalysts along with higher visible absorbance in n-TiO_2. Comparisons in data between n-TiO_2 and Ag/n-TiO_2 suggest that the silver loading also played a role in promoting visible light sensitization and absorption. Comparative studies of photocatalytic degradation activities of MO dye solutions under visible light irradiation for blank, TiO_2, n-TiO_2, and Ag/n-TiO_2 composites show a dramatic increase from negligible degradation to 8% MO degradation in TiO_2, 37% MO degradation in n-TiO_2, and up to 54% MO degradation in Ag/n-TiO_2. 0.5% wt. Ag content was identified as the optimum loading amount for the highest efficiency of MO photodegradation for the n-TiO_2 photocatalysts.

Similar results have also been observed while comparing various compositions of TiO_2 between amorphous and anatase phases under varying conditions of xenon illumination and thermal annealing, with the conglomerate Ag/AgCl/TiO_2 plasmonic nanostructure expressing the greatest photodegradation activity.[163] Compared to the earlier work with 54% MO degradation in Ag/n-TiO_2 in 120 minutes, an equivalent amount of degradation occurs here within a shorter time period of 60 minutes. **(Figure 2.8)**

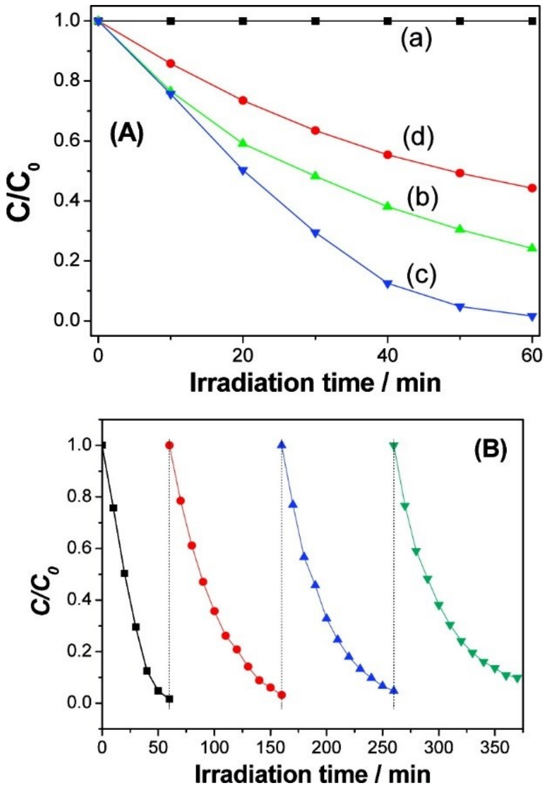

Figure 2.8. (A) Comparisons of photocatalytic decomposition of Methyl orange in water of samples of (a) anatase TiO_2 (b) amorphous Ag/AgCl/TiO_2, (c) anatase Ag/AgCl/TiO2, and (d) anatase $TiO_{2-x}N_x$ demonstrating that the anatase Ag/AgCl/TiO_2 provides for fastest degradation of the Methyl orange in water. (B) Cyclic degradation curve for anatase Ag/AgCl/TiO_2. Reprinted for academic use from Ref[163]. Copyright American Chemical Society (2009).

2.3.4.2 Enhanced Photoluminescence

Relaxation of the excited state of a molecule or a semiconductor is followed by the spontaneous emission of a photon, a process termed photoluminescence.[164]

Photoluminescence (PL) is strongly influenced by surface plasmons when present near the emitter. The presence of an LSPR enhanced local electric field can induce a faster radiative decay of the excited state. At the same time the large free electron density in noble metal nanoparticles can quench the excited state and attenuate photon emission.[158,164] In the end, the occurrence of these phenomena is determined by the quality factor of the LSPR, the distance between the plasmonic nanoparticle and the emitter. If the plasmonic nanoparticle is in contact with the emitter, quenching of the excited state will dominate. Meanwhile, if the plasmon resonance has a high *Q*-factor and the distance between the plasmonic nanoparticle and the emitter is a few nm, an enhancement of the photoluminescence due to the local field enhancement can occur. In the context of photocatalysis, photoluminescence can also happen when there are no redox groups to capture the photogenerated charge carriers. In such a case, the photoluminescence is typically proportional to the amount of generated electron-hole pairs within the semiconductor.

A representative example of photoluminescence as a useful technique and as a resultant signature of plasmonic activity is provided by the work of Paul et al.[165] By comparing the PL spectra of pure TiO_2 with that of the composite Ag-TiO_2 excited using a 355 nm laser, it is observed that the PL intensity is highly reduced in the heterostructure by the introduction of the Ag nanoparticles. **(Figure 2.9)** The PL quantum yield of bulk gold films under UV excitation is 10^{-10}, rising to 10^{-6} in spherical Au nanoparticles, 10^{-4} in Au nanorods, and 4×10^{-2} in Au nanocubes.[166] The higher photoluminescence efficiency in these plasmonic Au nanostructures is attributed to the accelerated radiative decay process thanks to the enhancement of the local electric field via the LSPR. A proportional enhancement of the photoluminescence for increasing Au metal loading in composite Au-TiO_2 systems have been reported by Christopher et al.[136]

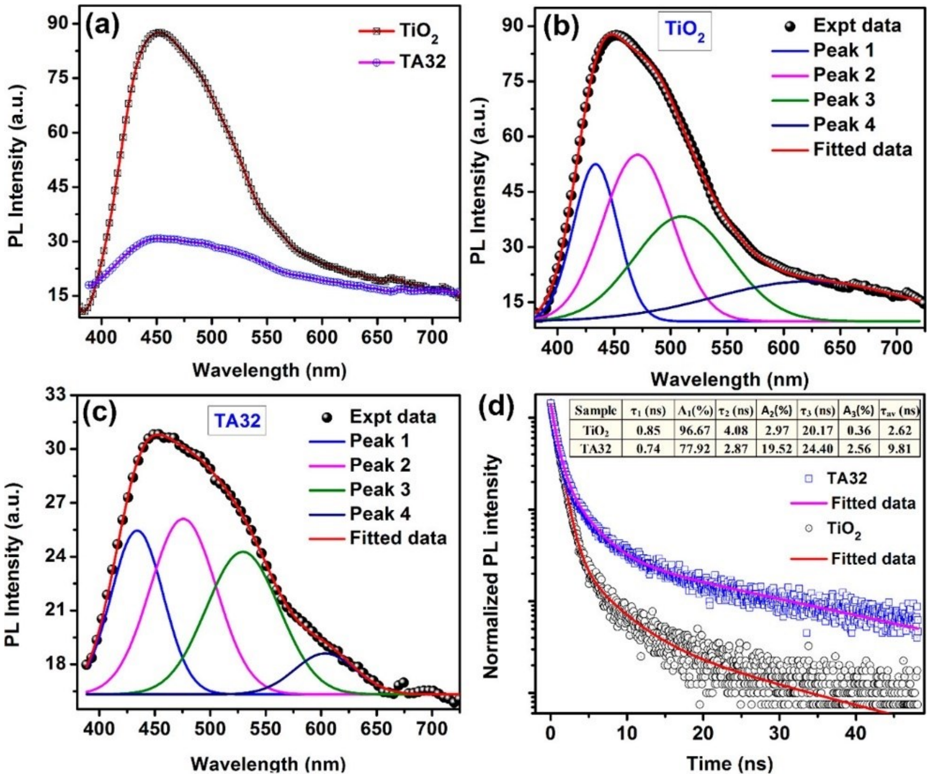

Sample	τ_1 (ns)	A_1(%)	τ_2 (ns)	A_2(%)	τ_3 (ns)	A_3(%)	τ_{av} (ns)
TiO$_2$	0.85	96.67	4.08	2.97	20.17	0.36	2.62
TA32	0.74	77.92	2.87	19.52	24.40	2.56	9.81

Figure 2.9. Photoluminescence can be utilized to probe electronic interactions in plasmonic nanostructures and can elicit the nature of defects, charge recombination kinetics, and the migration of photogenerated charge carriers. Paul et al.[165] demonstrate this in (a) where a PL spectra comparison of pure TiO$_2$ with an Ag-TiO$_2$ composite at 355 nm displays a high reduction in the PL intensity with the introduction of Ag nanoparticles. (b)-(c) present Gaussian fitted PL spectra of TiO$_2$ nanorods and the Ag-TiO$_2$ heterostructure where the PL intensity of TiO$_2$ nanorods is shown to have decreased by a factor of three after decoration by Ag nanoparticles while the spectra relatively remain the same. (d) provides time-resolved PL spectra comparison of the same set of structures (TA32 is Ag-TiO$_2$ with weight ratio 3:2) at 471 nm (emission) with 375 nm excitation. This information can be used to determine the lifetime of charge carriers in the different samples. Reprinted for academic use from Ref[165]. Copyright American Chemical Society (2017).

2.3.4.3 Photoelectrochemical Water Splitting

Measuring the photocurrent is a direct signature of the electron and hole generation rate. This classic method is otherwise known as photoelectrochemical water splitting. Water splitting essentially refers to the decomposition of water to molecular H_2 and O_2,

$$H_2O \rightarrow 2H_2 + O_2 \qquad E = 1.23\text{ V vs. NHE}$$

The process is comprised of two parts: (i) a photo- or electrochemical component that generates the oxidizing or reducing equivalents, and (ii) a suitable redox catalyst that mediates the formation of the molecular gases.[1] With a three-electrode setup involving a working electrode (the plasmonic sample), the counter electrode (Pt plate), and a reference electrode (Ag/AgCl) the photocurrent and the corresponding current-voltage (I-V) curve can be measured between the working electrode and the counter electrode. An enhancement in charge carrier generation would correspond to an enhancement in the photocurrent consisting of the charges being fed through the circuit.[149] Compared to the dye degradation method, water splitting also helps distinguish from localized heating effects as the energy required to split water (1.23 V) is much higher than that generated by the localized plasmonic heating effect.[149]

Ingram et al.[137] utilize water splitting as a means to quantify the photocurrent efficiencies of pure Ag nanocubes, pure n-doped TiO_2 nanoparticles, and Au/Ag@n-doped TiO_2 plasmonic composite systems. Focusing on photocurrents due to broadband visible light (400-900 nm), Ingram et al.[137] observe that pure Ag shows no response, pure n-doped TiO_2 exhibits a low response very similar to that of Au@n-doped TiO_2, and Ag@n-doped TiO_2 producing the highest photocurrent, with an enhancement factor of ~10 compared to the pure n-doped TiO_2 sample. Similar measurements have also been made by Zhu et al.[167] who compared photocurrent measurements made on TiO_2-Pd nanosheet and nanotetrahedron architectures to those of bare of TiO_2 samples. The confirmation of higher photocurrent in TiO_2-Pd nanosheets as opposed to those of bare TiO_2 samples is attributed to plasmonic hot electron injection. The lower performance of TiO_2-Pd nanotetrahedrons is due to poor hot electron injection abilities. **(Figure 2.10)**

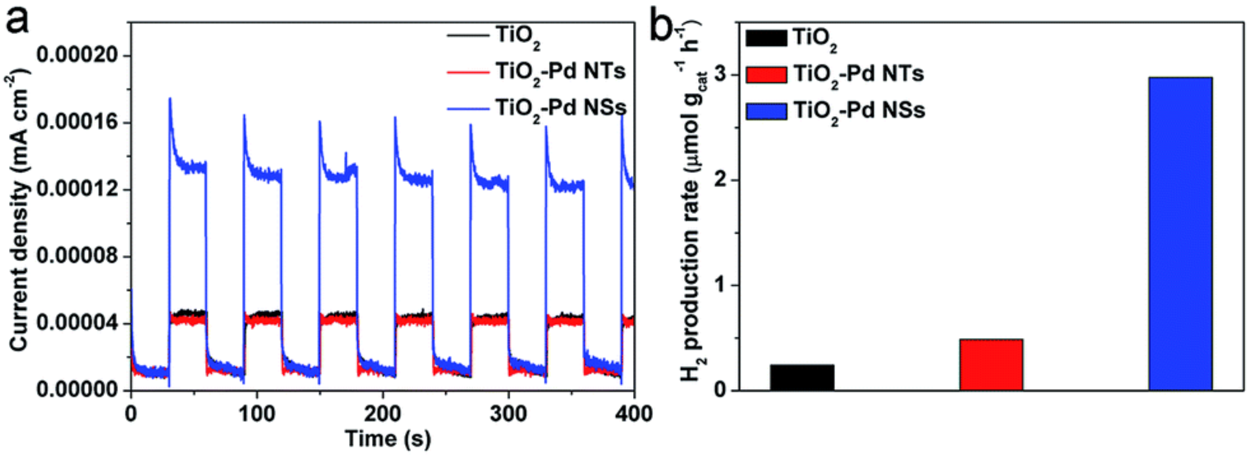

Figure 2.10. (a) Photocurrent measurements on TiO_2-Pd nanosheets and nanotetrahedrons compared to those of TiO_2. The higher photocurrent intensities are proof of plasmonic hot electron injection, while the TiO_2-Pd nanotetrahedrons evidence poor hot electron injection abilities. (b) Hydrogen production rates of the same structures under UV-Vis light. TiO_2-Pd nanosheets exhibit the highest photocatalytic activity among the three samples. Reprinted for academic use from Ref[167]. Copyright Royal Society of Chemistry (2016).

Most interestingly, it has been noted that by tweaking the TiO_2 bandgap to overlap the plasmonic band of Au nanoparticles, one can ensure the plasmonic resonant energy charge transfer processes complement the Schottky junction to produce enhanced photocatalytic water splitting.[168] This has been used to great effect by Zhang et al.[169] who utilize an assembly of plasmonic Au nanocrystals coupled with bottom-up fabricated TiO_2 nanotube photonic crystals onto achieve maximum quantum efficiencies of 8% under visible light irradiation, with photocurrent densities of ~150 µA/cm, the highest values reported in any plasmonic Au/TiO_2 system under visible light illumination.

2.3.4.4 Photocatalytic CO_2 Reduction and H_2 Generation

With motivations similar to what has been considered in organic pollutant degradation, CO_2 photoreduction aims to transform atmospheric CO_2 and CO_2 in exhaust emissions into useful fuels and chemicals.[6] Here again, plasmonic photocatalytic systems have proven effective for the cause as opposed to their semiconducting counterparts.[170–175]

In this context, it is the direct generation of reduced fuels from CO_2 and their corresponding quantities that serves as the signature of enhanced charge generation activity. This has been demonstrated effectively in the work of Hou et al.[108] who presented that Au gold islands formed on TiO_2 films generated 22.4 µmol/m-cat of methane from 51.6 mL of CO_2-saturated water alone at a reaction temperature of 75^0C under 15 hour illumination by the 350 mW output of a 532 nm green laser. This yield was reported to be 24 times higher than that of bare TiO_2 films under identical reaction conditions. Using a different architecture in hexagonal close-packed core-shell Au/TiO_2 nanocrystal arrays Wu et al.[176] reported a dramatic increase in hydrogen production from 20% methanol solution achieved with the plasmonic composite compared to bare TiO_2 thin films and randomly distributed Au/TiO_2 nanocrystals. The significant increase in hydrogen production was correlated to the optimal coupling of the enhanced local electric field from the LSPR of the Au/TiO_2 nanocrystal arrays, with a 16.67% increase in photocatalytic efficiency, which further promoted the generation of hot charge carriers to assist in the photocatalytic reduction process. **(Figure 2.11)**

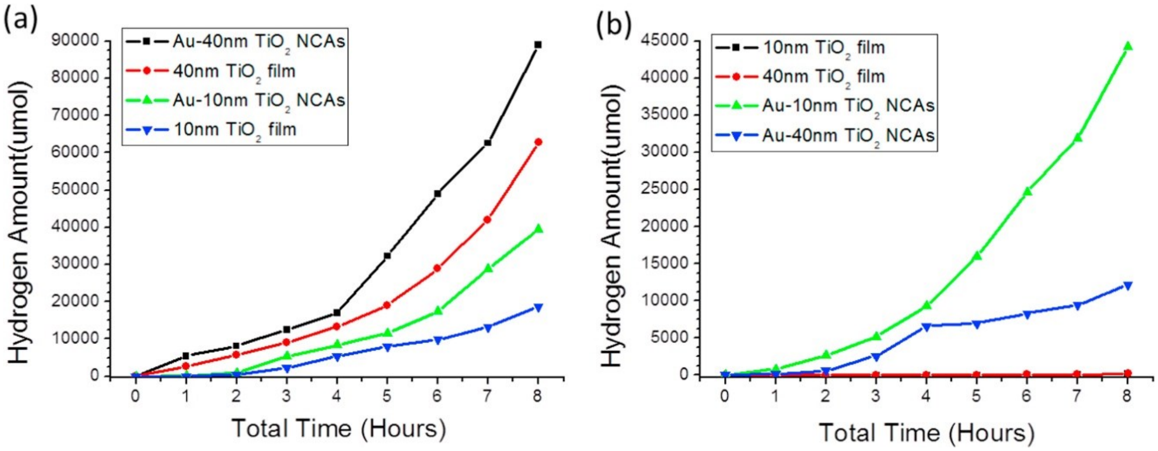

Figure 2.11. Hydrogen generation comparisons for samples of Au/TiO_2 nanocrystal arrays with different coating thicknesses of TiO_2 to that of bare TiO_2 thin films under (a) UV irradiation (Hg lamp), and (b) visible-light irradiation (Xe lamp). A rough approximation by eye shows that under UV-light, 40 nm-Au-TiO_2 nanocrystal arrays generate 90000 µmol of hydrogen while 10 nm-Au-TiO_2 nanocrystal arrays generate 37000 µmol after 8 hours respectively. Under similar conditions it is obvious that the bare TiO_2 counterparts produce generate lower hydrogen amounts. Under visible radiation, the bare TiO_2 generate a very negligible amount of hydrogen while the 40 nm and 10 nm Au-TiO_2 counterparts generate roughly 12000 µmol and 45000 µmol of hydrogen after 8 hours. In other words, the plasmonic heterostructure presents higher photoreduction activity. Reprinted for academic use from Ref[176]. Copyright Elsevier (2016).

2.4. Closing Remarks

Having discussed the fundamental principles of plasmonic photocatalysis, we will now shift our focus toward modeling plasmonic nanostructures. In particular, the following chapter will consider various unique architectures for plasmonic noble metal-semiconductor heterojunction platforms I have had the opportunity to investigate using electromagnetic simulations through collaborative experiments with my peers at the Shankar group. These efforts have laid the foundation for my own doctoral research focusing more on fundamental insights into the hot carrier dynamics of plasmonic systems.

Chapter 3
Modeling Plasmonic Nanostructures

3.1 Introduction

Studies on the optical properties of nanoparticles have been a subject of considerable interest since Mie's original work in 1908 explaining the red color of gold nanospheres.[177] For particles in the quasistatic limit, the optical responses for geometries including planar interfaces, cylinders, spheres, and spheroids can be found by solving Maxwell's equations with the proper boundary conditions.[46] The simplest case involving spherical nanoparticles was provided previously in Chapter 1.

Beyond the quasistatic approximation, the optical response of nanoparticles becomes much more complicated, resulting in multipolar resonances and higher order modes. Mie theory provides the full solution for the local and far fields scattered by a spherical metal particle under these conditions.[41] The relevant equations, in terms of spherical Bessel and Hankel functions, are only straightforward in special limits where they reduce to simpler forms. Otherwise, Mie scattering is generally a numerical exercise. Analytical solutions can also be found for diverse geometries including cubes, edges, and hemispheres.[178–180] These solutions are dependent on simple models for the dielectric response such as the Drude model. Here too, quantitative results based on empirical dielectric functions generally require the use of the numerical approach. Moreover, the numerical approach becomes a necessity for understanding the optical response of more complicated structures.

Several numerical methods have been developed to model the near, and far-field optical responses of nanoparticles with each having its fair share of advantages and disadvantages. Mie theory,[41] near-field efficiencies,[181] T-Matrix,[182] and time-dependent local-density approximations are system and geometry dependent methods.[183] These methods are constrained by symmetry limitations resulting in excessively complex solutions for arbitrary nanostructures.[184–187] Other methods including the discrete dipole approximation,[64] coupled-dipole approximation,[188] and the multiple multipole method[189] are deficient in that they are not fully retarded. Contrastingly, fully retarded methods such as the boundary charge method,[190] boundary element method,[191] and finite element method[191] are prone to large computational loads.[177] With these factors in mind, my research will focus on the use of the finite-difference time-domain (FDTD) method to model the optical responses of bimetallic nanostructures.

3.2 The FDTD method

The FDTD method is an intuitive approach where Maxwell's equations are solved directly. The corresponding electric and magnetic fields are discretized in both time and space on a spatial grid that encompasses the nanostructure to be analyzed, and the surrounding regions where the fields are to be determined. Such an approach allows for the study of the near and far-field electromagnetic responses for heterogeneous nanomaterials of arbitrary geometry.[32,177] In fact, FDTD has often been used to model the nanostructure geometries mentioned earlier as well as others including photonic crystals,[192] NSOM tips,[193] and pyramidal recording probes.[194]

We begin by solving Maxwell's curl equations in non-magnetic media:

$$\nabla \times \vec{E} = -\frac{1}{c}\frac{\partial \vec{B}}{\partial t} \tag{3.1}$$

$$\vec{D}(\omega) = \epsilon(\omega)\vec{E}(\omega) \tag{3.2}$$

$$\nabla \times \vec{B} = \frac{1}{c}\frac{\partial \vec{E}}{\partial t} \tag{3.3}$$

This is achieved by replacing all time derivatives with central differences. For example, we can rewrite (3.3) as,

$$\vec{B}(\vec{x}, t + \delta t) = \vec{B}(\vec{x}, t - \delta t) - 2(\delta t)c \times \vec{E}(\vec{x}, t). \tag{3.4}$$

$\vec{B}$ at time $(t + \delta t)$ can be found in this manner if $\vec{B}$ at time $(t - \delta t)$ and $\vec{E}$ at time t are known. In other words, the fields are found by propagating the discretized Maxwell's equations forward in time. A similar analysis can be applied to the second Maxwell curl equation where $\vec{E}$ can be propagated forward in time. Alternatively, the curl operator could also be expanded in sums of central differences with $\vec{E}$ and $\vec{B}$ now being propagated forward in space. Knowledge of field values at an initial time makes it straightforward to implement the forward propagation in both schemes.

Grid discretization must be carefully monitored. With regards to spatial discretization (Δx), the grid must be fine enough to resolve the smallest spatial features of the nanostructure as well as support the relevant wavelengths utilized. Generally, 10-20 grid points is found to be adequate to satisfy these conditions.[177] Similarly, the conditions for time discretization (Δt) must not violate causality, as with every time-step, information is to travel from one grid cell to the next. The time-step must be small enough such that the information does not travel faster than the speed of the light in the given medium. Together, these restrictions define what is considered as the *Courant condition*,[195]

$$\Delta t = S_C \frac{\Delta x}{c_0 \sqrt{d}} \tag{3.5}$$

where d is the dimensionality, S_C is the Courant number and lies between 0 and 1. The Courant condition is far more significant as opposed to deciding the appropriate mesh size. This is because errors in mesh size translate to a simulation error, but errors in the time step can result in an exponential error growth leading to unstable and diverging simulations.

In simulating our nanostructures, it is also important to take into consideration the material properties of the nanostructure as well as its environment. Many said properties can be characterized, in this case, under one absolute parameter: the dielectric function, ϵ. A value for ϵ must be specified at every grid point in our simulation. Multi-coefficient models are often used to automatically generate a material model based on tabulated refractive index and extinction coefficient (n, κ) data as a function of wavelength (often via ellipsometric studies). Other specific models do exist in characterizing material properties including the Drude, Debye, and Lorentz models. For example, the material properties of gold and silver nanoparticles are often simulated using the Drude dielectric function,

$$\epsilon(\omega) = \epsilon_\infty - \frac{\omega_p^2}{\omega^2 + i\gamma\omega} \tag{3.6}$$

where ϵ_∞ is the high frequency limit of $\epsilon(\omega)$ and is equivalent to $(1 + \chi)$. Bulk dielectric data for metals and other materials for select frequency ranges can be found in well-known material databases.

With this, we can now move on to the problem of determining the local fields within and around our metal nanoparticle. The initial fields utilized depend on the properties that are of concern. A plane wave is commonly used for illumination, in which case, the initial fields correspond to a plane-wave pulse originating far away from the nanoparticle. The simulation time is set in mind with the knowledge that the field is propagated over a duration of time that is much longer than the time necessary for the plane-wave pulse to pass through the nanoparticle to the boundary of the simulation region. Absorbing boundary conditions are necessary to ensure that outward propagating fields are not reflected back into the simulation region. Frequency dependent properties of our nanostructure can be extracted by repetitive calculations for a series of monochromatic incident fields at different frequencies. Alternatively, a broadband pulse could be utilized while performing Fourier analysis of the simulation results to extract the frequency dependent properties. In this manner, one can obtain the near-field distributions around the metal nanoparticle. Far-field distributions including scattering and absorption cross-sections can then be calculated from these near-field approximations via appropriate surface integrals over the fields.[32]

As described by Pelton et al.[32], this helps us describe the total electric field around the metal nanoparticle as the sum of the incident plane wave field and the scattered field $\left(\vec{E} = \overrightarrow{E_I} + \overrightarrow{E_S}\right)$. Consequently, the total Poynting vector is $\vec{S} = \overrightarrow{S_I} + \overrightarrow{S_S} + \overrightarrow{S_{ext}}$ where $\overrightarrow{S_I}$ is the incident field energy flux, $\overrightarrow{S_S}$ is the scattered field energy, and $\overrightarrow{S_{ext}}$ is the remaining energy flux originating from interference terms $\left(\overrightarrow{E_I} \times \overrightarrow{B_S} + \overrightarrow{E_S} \times \overrightarrow{B_I}\right)$. The Poynting vector helps us determine the energy flux through any surface Ω that encompasses the nanoparticle. Assuming the nanoparticle is in a non-absorbing medium, the energy absorbed by the nanoparticle is,

$$F_A = -\int_{\Omega} \vec{S} \cdot \vec{n} d\Omega \tag{3.7}$$

where $\vec{n}$ is the outward surface normal. The energy scattered outward through Ω is,

$$F_S = -\int_{\Omega} \overrightarrow{S_s} \cdot \vec{n} d\Omega \tag{3.8}$$

and the inward energy flow from the interference terms is,

$$F_{ext} = -\int_{\Omega} \overrightarrow{S_{ext}} \cdot \vec{n}\, d\Omega. \tag{3.9}$$

It follows from energy conservation that $F_{ext} = F_A + F_S$ where F_{ext}, or *extinction*, describes the energy lost from the incident plane wave via *absorption* by the nanoparticle and *scattering* out of the incident plane wave. By normalizing the individual energy flow components from extinction, scattering, and absorption with respect to the incident intensity of the plane wave one can obtain the cross sections for extinction (σ_{ext}), absorption (σ_{abs}), and scattering (σ_{sca}). σ_{abs} can be determined by calculating the total Poynting vector including the incident field. For σ_{sca} only the scattered field is required and thus the incident field is excluded.

3.3 Lumerical FDTD Solutions

Lumerical FDTD Solutions was utilized for FDTD modeling of the plasmonic nanostructures. Lumerical provides for 2-D and 3-D FDTD modeling of optoelectronic and photonic devices. 2-D, and 3-D Maxwell solvers based on the FDTD method for complex geometries are provided in an easy-to-use GUI for the determination of a full range of useful optical quantities such as the complex Poynting vector, scattering and absorption cross sections, as well as the transmittance and reflectance of light.

Much of what has been discussed in the prior section on the FDTD method carries through into Lumerical. The FDTD method solves equations (3.1) - (3.3) on a discrete spatial and temporal grid. Each field component $\left(E_x, E_y, E_z, B_x, B_y, B_z\right)$ is solved at a slightly different location within the grid cell. The data collected by the FDTD solver is interpolated to the origin of each grid point, making analysis far easier. In discretizing the grid, Lumerical uses a rectangular, Cartesian style mesh with the fundamental simulation quantities such as the material properties, geometrical information, electric and magnetic fields being calculated at each mesh point. A smaller mesh generally accounts for a more accurate representation of the nanostructure but comes at the cost of longer simulation times and larger memory requirements. Lumerical, by default, allows for the simulation mesh to be generated automatically. The solver provides various meshing algorithms that allow one to obtain accurate results even if the mesh used is relatively coarse. The meshing algorithm generally suggested is a conformal mesh **(Figure 3.1)** that uses an integral solution of Maxwell's equations near interfaces.[195,196]

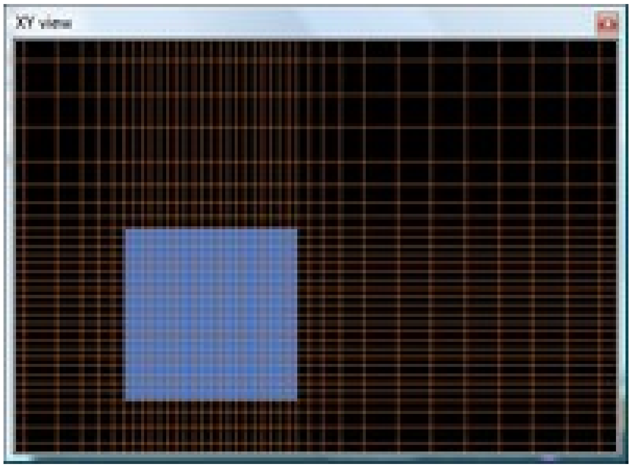

Figure 3.1. Lumerical's conformal meshing algorithm.

Therefore, a smaller mesh is created in high index and highly absorbing materials. This helps maintain a constant number of mesh points per wavelength in the case of the former and assists in resolving penetration depths in the case of the latter. Additional meshing constraints can be added manually i.e., forcing the mesh to be smaller near the edges of complex nanostructures where we expect the fields to be changing very rapidly or in areas of hotspots.

Lumerical supports a range of material models. One may import material data from known material databases, also referred to as sampled 3-D data. Otherwise, an assortment of models is provided including the dielectric (create a material with a constant real index), (n, κ) material (create a material with a specific n and κ value at a single frequency), conductive 3-D, Drude, Debye, Lorentz, Sellmeier, and the Perfect Electrical Conductor (PEC) model. An analytic material model also allows the user to enter an equation for the real and imaginary part of the dielectric function. Generally, we import sampled 3D data from recognized material databases to model the material properties of the metal nanoparticles that are simulated in our work. Lumerical also provides an in-built library for various such common metals and materials. The Material Explorer interface can then be used to assess the material fits for relevant wavelength ranges in the simulation.

In our studies, the most relevant field calculations involve determination of the absorption and scattering cross-sections, reflectance and transmittance, and electric-field profile distributions around the metal nanoparticle. This is achieved using Lumerical's analysis objects that allow us to group monitors and analyze the monitor data. A set of monitors can be grouped together to form a closed box. Two such boxes, one encompassing the source and the nanostructure, and the other encompassing the nanostructure alone can be grouped and analyzed to calculate absorption and scattering cross-sections. **(Figure 3.2)** Similarly, monitors can be placed above (and behind the illumination source), and below the nanostructure (beyond the initial location of the illumination source) to calculate reflectance and transmittance. Near-field profile, and far-field projection monitors can be utilized to capture Poynting vector, and electric-field distributions around the metal nanoparticle. Lumerical's in-built scripting interface further allows us to manually code and program the necessary mathematics to calculate the relevant physical parameters.

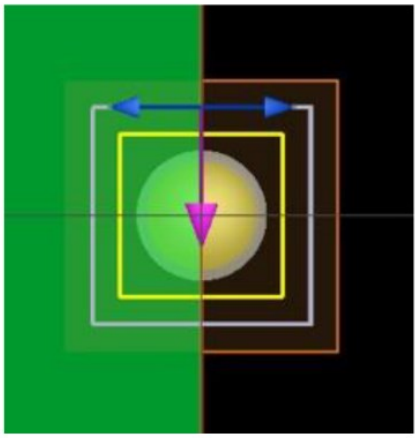

Figure 3.2. A spherical bimetallic nanostructure simulated in Lumerical FDTD Solutions. The polarization of the incident electric field is illustrated by the blue arrow. The pink arrow is the propagation vector of our TFSF source. An absorption cross-section monitor (yellow) encompasses the nanoparticle, with a conformal mesh (orange) focused around the vicinity of the nanostructure.

Lastly, Lumerical provides a diverse range of sources that can be used to illuminate the nanostructure including dipoles, Gaussian and Cauchy/Lorentzian beams, plane-waves, total-field scattered-field (separates computation region into two distinct regions – the total field and the scattered field), mode sources (inject guided modes), and imported sources (allow the user to specify a custom field profile for the source). The use of differing incident fields helps us investigate different aspects of metal nanoparticle plasmonics. A dipole radiation source makes it possible to determine how radiation from a localized emitter is modified by the presence of a metal nanoparticle (leading into the study of plexcitonics). The total-field scattered-field source is particularly useful to study the scattering behavior of individual, standalone objects as the scattered field can be isolated from the incident field. Plane-wave sources, on the other hand, serve the same purposes for periodic structures.

3.4 Advantages and Limitations of the FDTD method

The FDTD method has its fair share of strengths and weaknesses. The greatest strength of the FDTD method is its intuitive approach which makes it easy to understand and know what to expect from a given model. Being a time-domain technique, FDTD enables us to describe the response of a given system over a wide range of frequencies, given a broadband pulse is used as the source. This is particularly useful in plasmonic simulations where resonant frequencies must be characterized over large wavelength ranges. FDTD also allows the user to specify material properties at all points within the given computational domain. This allows for a wide variety of linear and nonlinear dielectric and magnetic materials to be easily modeled. In particular, the ability to obtain detailed profile distributions of electric and magnetic fields at crucial interfaces, and around the nanostructure of interest is extremely useful in characterizing light-matter interactions at the nanoscale.[177,195,197]

However, since the FDTD method is inherently a volumetric method, it suffers from the necessity that for larger system simulations the corresponding computational resources increase rapidly. This is especially true in Lumerical where far-field properties of nanostructures are required. Likewise, systems of multiple length scales are equally difficult to study with the uniform grids that are typically used, along with the fact that treating media of high dielectric contrast and damping is often complicated. In Lumerical, conformal meshing technology and other algorithms help alleviate these difficulties to a certain extent, although results often require extensive convergence analysis. Despite these limitations, the immediate availability of many commercial packages, and the possibility for high-efficiency, parallel computation makes FDTD the most widely used and successful numerical approach in providing an explicit means toward understanding the interaction of light and matter at the nanoscale.[32]

Using Lumerical FDTD simulations, I have been able to contribute to various pathways of research in the fabrication and optimization of plasmonic noble metal-semiconductor heterojunction platforms. The following sections explores these representative works. The immediate focus of these simulations is the optical properties of the relevant structures including absorption and scattering cross sections, reflectance and transmittance spectra, and electric field intensity profiles. The conclusive goal of these simulations is to test these platforms for incorporation with plasmonic nanomaterials, and the subsequent matching of simulated data with experimental results.

3.5 Representative Works

3.5.1 Plasmonic Nanodimples

Electrochemical anodization has been a proven method to produce ordered nanostructured surfaces. Kisslinger et al.[198] demonstrated the same in the formation of Ta_2O_5 nanodimple arrays on non-native substrates through a combination of anodization and thermal annealing processes. Gold nanoparticles were incorporated on Ta_2O_5 arrays by annealing sputtered Au thin films in a procedure similar to the fabrication of my work on monometallic nanoislands to be discussed in the following chapter. Three different sets of simulations were performed exploring the effect of the high-index, dimpled Ta_2O_5 substrate on gold nanoparticles.

The combination of simulations tested the effect that the dielectric medium had on the LSPR of the gold nanoparticle by considering Au nanoparticles partially embedded in a planar film of Ta_2O_5, Au nanoparticles partially embedded in a nanodimple of Ta_2O_5, and an array of Au nanoparticles partially embedded in an array of Ta_2O_5 nanodimples. **(Figure 3.3)** The simulations matched and confirmed the partial embedding of Au nanoparticles within the Ta_2O_5 matrix to explain the relevant redshifts observed of the localized surface plasmon resonances. The resulting composite plasmonic system was also demonstrated to exhibit a significantly higher ensemble-averaged local field enhancement compared to the monometallic constituents on quartz substrates. These results also served to support the efficiency of the composite Au-Ta_2O_5 system for higher catalytic activity for plasmon-driven photo-oxidation of PATP to DMAB.

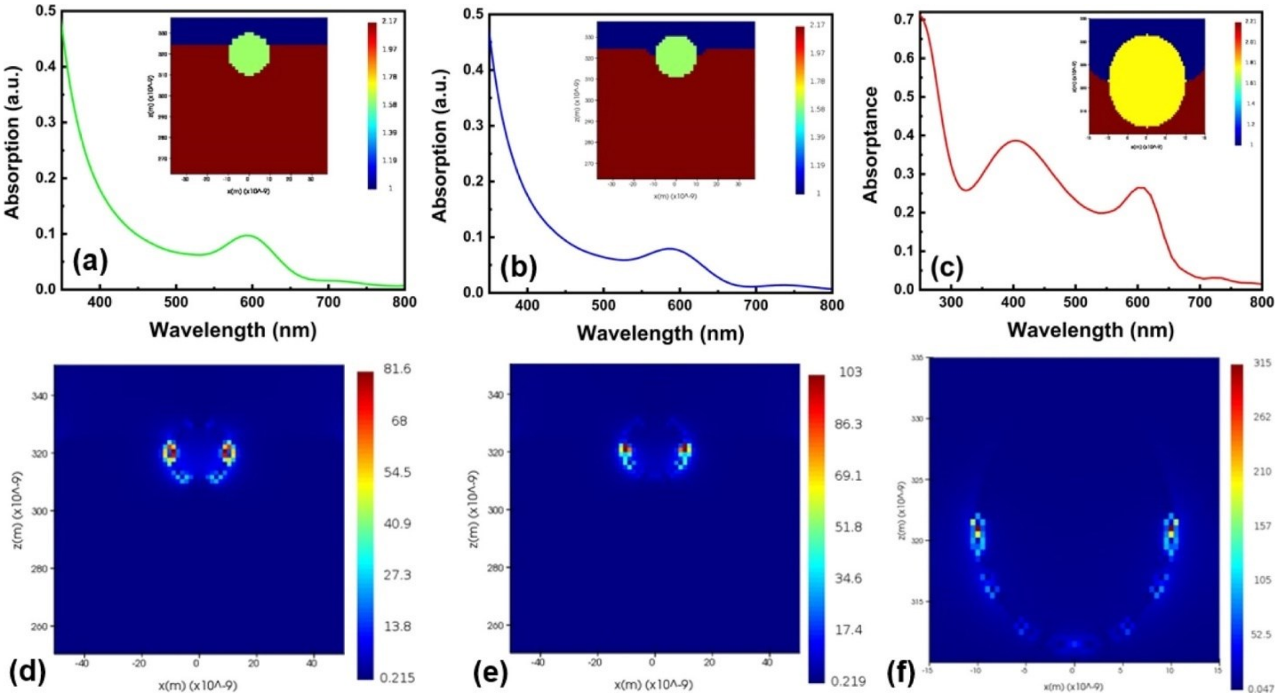

Figure 3.3. (a) – (c) Simulated absorption cross- sections of Au nanoparticle/Ta_2O_5 nanodimple configurations. Inset displays the corresponding refractive index profiles of the structures captured using an index monitor and demonstrating the embedding of the Au nanoparticles in Ta_2O_5 nanodimples. (d) – (f) Corresponding electric field intensity profiles calculated along the xy-plane. Incident light source was set normal to the xy-plane. Simulated absorption cross-sections of the Au nanoshell structure for varying inner core and outer shell radii (Core radius-Shell radius) combinations of (2 nm – 3 nm), (2 nm – 7 nm), (4 nm – 5 nm), (6 nm – 7 nm), (7 nm – 12 nm), (8 nm – 10 nm), (9 nm – 10 nm), and (10 nm – 12 nm). High quality factor plasmonic resonances are observed in the far visible regime for select core-shell radii combinations. Reprinted with permission from Ref[198]. Copyright American Chemical Society (2021).

3.5.2 TiO_2 Nanotubes

TiO_2 remains the popular standard for a semiconductor photocatalyst. To compensate for its shortcomings, various morphologies of the photocatalyst have been explored. Kar et al.[199] explored the use of flame annealing to fabricate a nanotubular morphology of TiO_2 but with square-shaped cross sections to improve the visible light response of the photocatalyst. Through their efforts, Kar et al.[199] would demonstrate an enhanced CH_4 yield via the photoreduction of CO_2, a challenging reaction in its own right, using these flame annealed TiO_2 nanotubes. The improved performance of these substrates was due to their sensitization, via their unique square morphology, to visible light photons as well as their rutile crystalline phase with photoreduction activities peaking at 450 nm and extending to a wavelength of 620 nm.

Lumerical simulations were used for comparative analyses of nanotubular structures that were fabricated at low (450^0C) and high (750^0C) temperatures resulting in circular and square cross sections. Material specific optical properties of the relevant structures were simulated using the appropriate refractive index data as obtained via ellipsometry. Effective-medium approximation for mixed-phase materials was determined via Bruggeman's model,

$$\sum_i \delta_i \frac{\sigma_i - \sigma_e}{\sigma_i + (n-1)\sigma_e} = 0 \tag{7.2}$$

where δ_i and σ_i are the fraction and refractive index of each component, respectively, and σ_e is the effective conductivity of the medium. The resultant simulations were used to demonstrate the importance of morphology and phase content to their performance abilities by considering the propagation of light and the corresponding spatial distribution of the electric field intensity profiles of these substrates.

Subsequently, it was observed that light propagation in low-temperature annealed nanotubes (LANT) and high-temperature flame annealed nanotubes (FANT) differed extensively. As displayed in **(Figure 3.4)** Poynting vector plots of LANT and FANT substrates were examined at the peak LSPR wavelength of 450 nm. Hot spots, being particularly beneficial for photocatalysis, were observed exclusively on the outer surfaces of LANT substrates **(Figure 3.4a)** while they were found in both the inner and outer surfaces of FANT substrates. **(Figure 3.4b)** Investigating the same behavior from the plane orthogonal to the substrate and the incident polarization, this time at the band edge wavelength of 400 nm, the simulations confirmed that FANT substrates **(Figure 3.4d)** absorb band-edge photons more effectively compared to LANT substrates. **(Figure 3.4c)** This is a significant observation as the utilization of photons at the semiconductor band-edge is a loss mechanism in most solar energy harvesting devices.[199] Supplementary analyses of the simulated absorption and scattering cross sections for the two substrates support experimental observations of the FANT type nanotubes and their broad, multi-peaked scattering features in the visible light spectral range.[199]

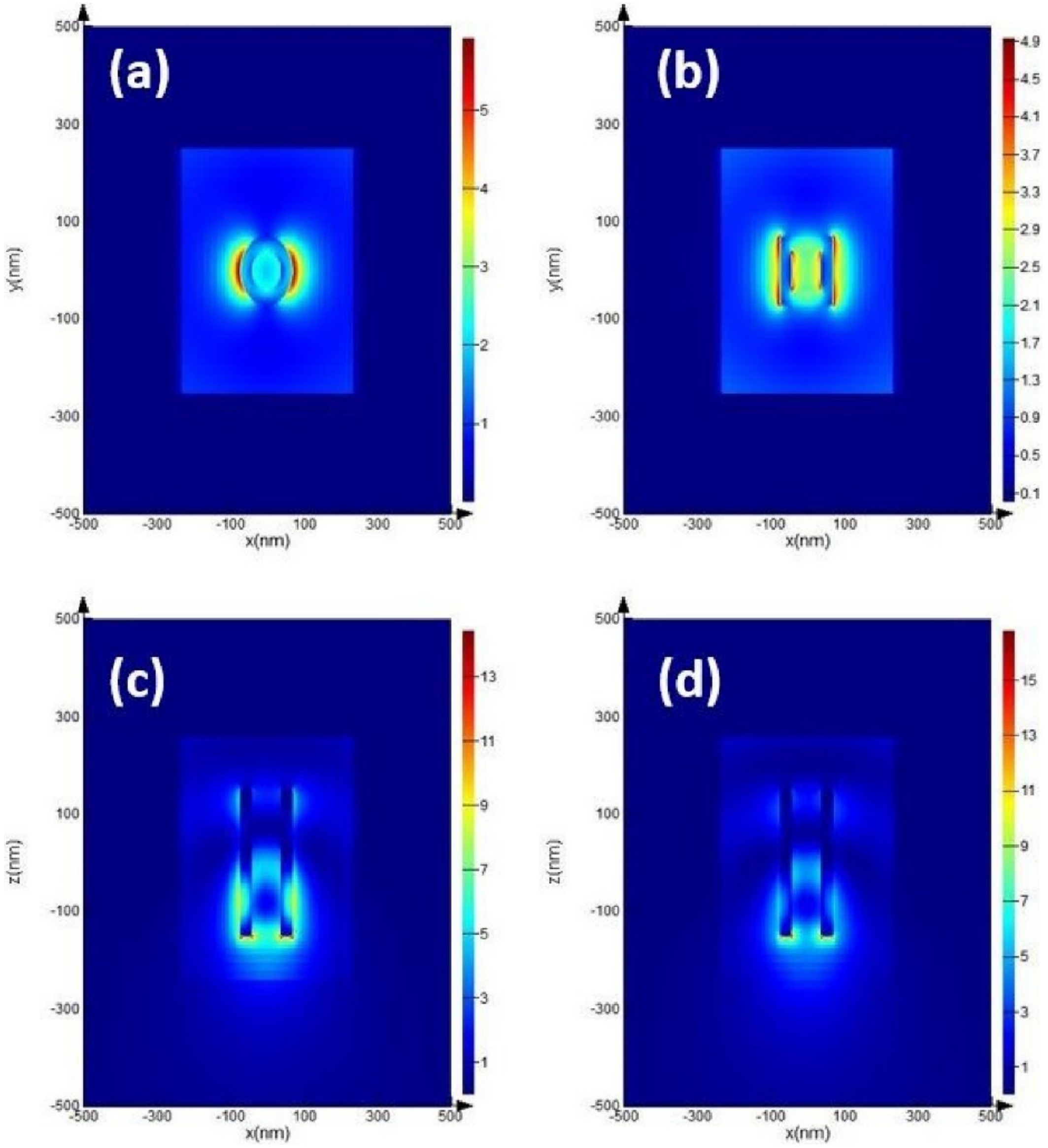

Figure 3.4. Electric field intensity profiles of LANT and FANT nanotubes for (a) – (b) incident light of 450 nm and (c) – (d) 400 nm, respectively. Reprinted with permission from Ref.[199] Copyright Elsevier (2018).

Similar studies of TiO_2 nanotube arrays for CO_2 photoreduction were utilized in the work of Vahidzadeh et al.[200] Here, the combined use of Ag and Cu nanoparticle decorated TiO_2 nanotube arrays (TNTAs) resulted in the formation of ethane from gas-phase photoreduction of CO_2 without the need for sacrificial agents or hole scavengers. Ethane is a far more significant by-product of CO_2 photoreduction compared to methane as it is more energetically dense and of greater economic value.[200] Consequently, it was found that the bimetallic composite of AgCu-TNTA substrates demonstrated the highest ethane selectivity of 60.7% while the monometallic counterparts of Ag-TNTA and Cu-TNTA demonstrated selectivities of 15.9% and 10%, respectively.

FDTD simulations were used to study the interaction of light with TiO_2 nanotubes decorated by a single layer of the bimetallic nanoparticles and to confirm the morphological characteristics of the composite system. To begin, Ag@Cu nanoparticle homodimers were simulated upon the pore openings of the nanotubes where the Ag core was kept at a constant diameter of 100 nm while the thickness of the Cu shell was varied from 5 to 20 nm. The simulated absorption spectra were found to be at a lower amplitude compared to experimental DRS spectra, and for the most part, did not fully capture relevant LSPR characteristics found in the experimental spectra.[200] The corresponding electric field intensity profiles demonstrated that the Ag@Cu decorated TNTAs provide for enhanced visible light absorption with the highest electric field intensity profiles found at the Ag-TiO_2 and Ag-air interfaces as opposed to in between the two particles due to the strong damping of the plasmon resonance by the Cu shell. Altogether, neither of the simulations of TNTAs decorated with Ag@Cu homodimers or their monometallic constituents involving small, separated Ag and Cu nanoparticles could fully explain the huge differences in performance for CO_2 photoreduction selectivity.

Further insights to match the experimental and simulated optical characteristics of the system were gleaned by considering a complementary structure involving AgCu heterodimer decorated TNTAs. **(Figure 3.5)** This setup was utilized by considering the possibility of Ag nanoparticles deeper in the pores of the nanotubes being the dominant species for light-matter interactions. In which case, the corresponding electromagnetic characteristics of Ag-TNTA samples and AgCu-TNTA samples would be similar. This was supported by the fact that the overall amount of Cu deposited on the substrates were quite small.[200] The corresponding simulations involving close-lying Ag-Cu heterodimers on TNTAs were found to more closely match the experimental behavior of the substrates. The corresponding simulated electric field intensity profiles supported the formation of asymmetric charge distributions in adjacent adsorption sites of the photocatalyst due to broad quadrupolar and multipolar resonances of the Ag-Cu heterodimers. These asymmetric charge distributions were found to be crucial in decreasing adsorbate-adsorbate repulsion and facilitating for the C_2 coupling of reaction intermediates which is integral to the formation of ethane.

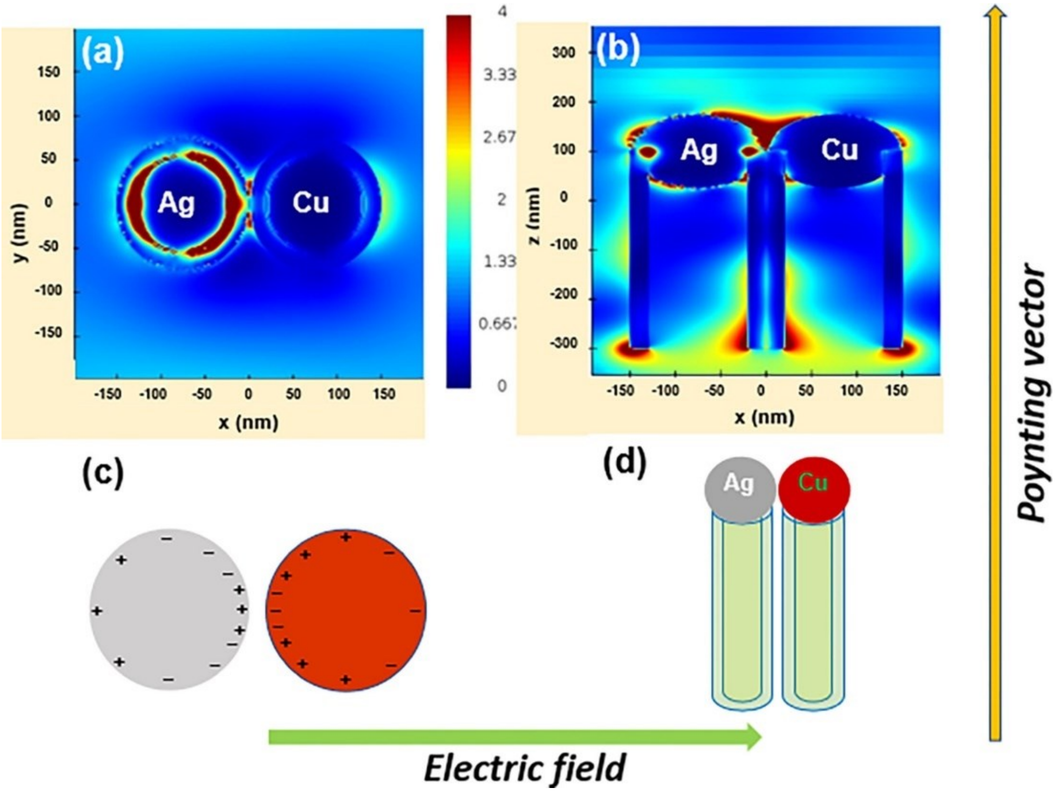

Figure 3.5. (a, c) Electric field profile along the xy-plane for Ag-Cu heterodimers decorating the pore openings of TiO_2 nanotubes and the corresponding surface charge distribution. (b, d) Electric field profile along the xz-plane of the same structure and the corresponding schematic of the composite system. The incident light source is a plane wave polarized along the x-axis and propagates along the z-direction. Reprinted with permission from Ref.[200] Copyright American Chemical Society (2021).

3.5.3 Plexcitonic photocatalysts

Plexcitonic photocatalysts consider the combination of plasmonic and excitonic materials. Plexcitons are hybrid quasiparticles that are the result of coupling between plasmons and excitons.[201] Plexcitonic enhancement of photocatalytic reactions have been evidenced most commonly in hybrid systems of 2D semiconductors where strongly bound excitons couple to the nearby surface plasmon resonances of noble metal nanoparticles. Plexcitonics requires that plasmonic and excitonic components are close to one another to facilitate coupling. While plexcitonic systems generally observe the excitonic material directly upon the surface of the plasmonic noble metal nanostructure, spacer layers have also been utilized to avoid extensive quenching of the organic excitons by single-particle excitations in the metal at close contact.[202] Zhou et al.[203] use one such spacer layer of 80 nm thickness in their modeling of a plasmonic metal-spacer-organic exciton system using topological band theory. In modeling plexcitonic systems, insights into the nature of the coupling can be drawn by studying the near-field behavior of these structures. This can be facilitated using Lumerical's electric field and profile monitor as well as the option to use polarization dependent measurements. Such techniques have been utilized in the work of Schlather et al.[204], who examine near-field strong coupling in metallic dimers, and Karademir et al.[205], who analyze direction-dependent plexcitonic coupling in plexcitonic crystals.

Plexcitonics has opened the door to the investigation of heterojunctions involving plasmonic noble metals and excitonic nanostructures. Graphenic semiconductors are popular 2D materials known for their remarkable thermal and photochemical stability, efficient charge transport, as well as tunable band edges and band gaps.[206] Alam et al.[207] have shown large area CVD grown nitrogen doped graphene (NGr) decorated by rounded Ag nanocubes to form NGr/Ag plexcitonic hybrids are excellent visible-light driven photocatalysts for surface catalytic reactions such as the chemical transformation of 4-NBT to DMAB. The coupled plexcitonic system showed superior photocatalytic performance compared to the bare plasmonic Ag catalyst. FDTD simulations involving Ag nanocubes with and without the presence of the NGr were conducted. In both cases, electric field amplification between the Ag nanocubes as well as between NGr and Ag nanocubes was observed. This local field enhancement was crucial in amplifying electron concentration in NGr primarily through classical Landau damping and hot electron injection from the Ag nanocubes to the NGr. FDTD simulations were shown to provide a direct signature of this mechanism of plasmon induced energy transfer by the reduction of electric field intensities in the regions where Ag nanocubes were set in direct contact with NGr. **(Figure 3.6d)**

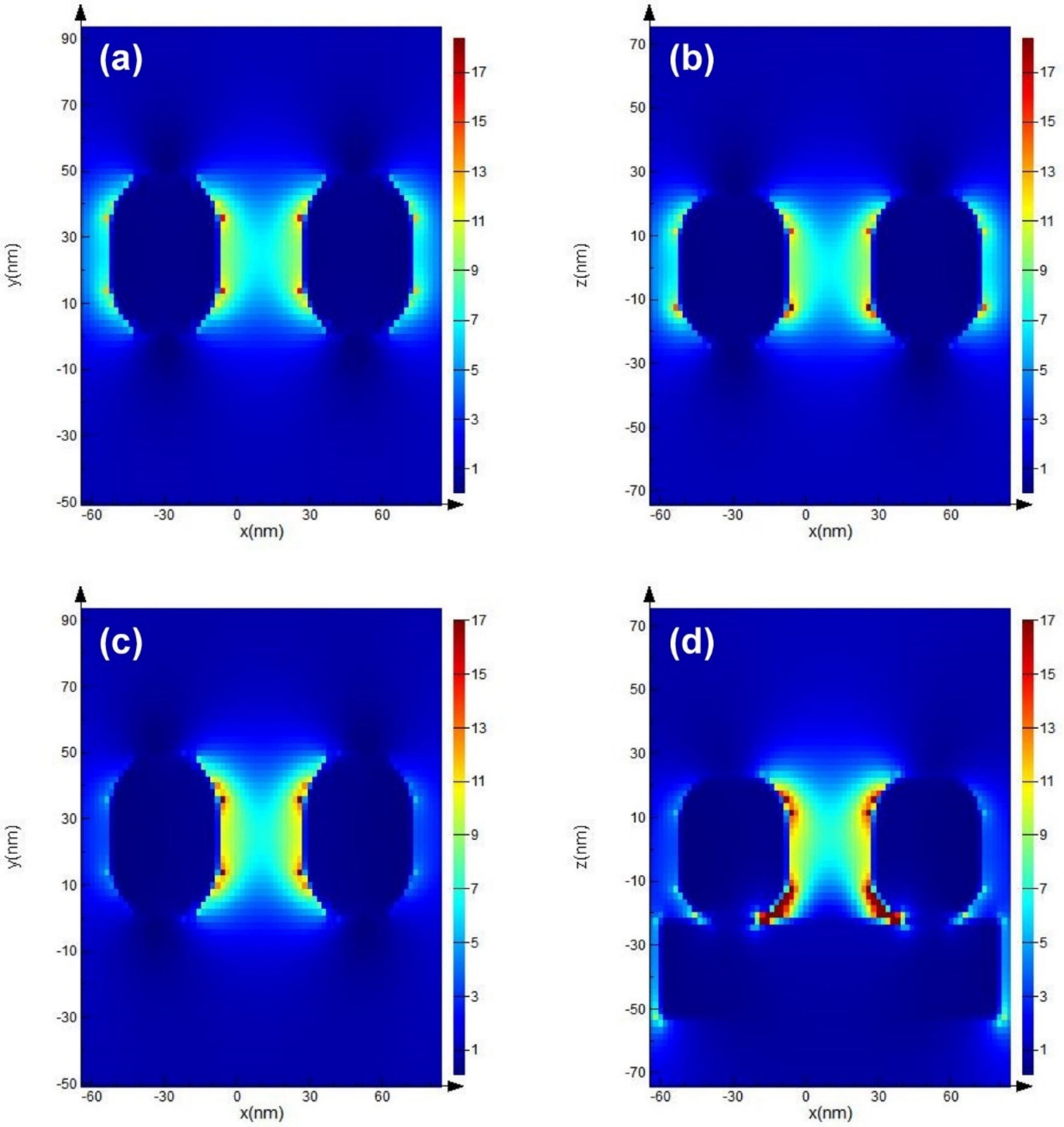

Figure 3.6. Electric field intensity profiles of Ag nanocube dimers with rounded corners at an incident light source of wavelength 532 nm, (a,b) xy-plane and xz-plane views, respectively, without substrate and (c,d) xy-plane and xz-plane views, respectively, with NGr substrate. Reprinted with permission from Ref.[207] Copyright IOP Publishing (2019).

Supplementary studies on the absorption and scattering spectra of the composite systems demonstrated a larger absorption cross section compared to scattering for the plexcitonic system and being indicative of a faster plasmon dephasing mechanism similar to Landau-damping based hot electron injection as opposed to PIRET or DIET.[207] **(Figure 3.7)** As such, it was shown that Landau-damping based hot electron injection is a significant process in narrow bandgap semiconductors as opposed to being generally termed exclusive to wide bandgap semiconductors alone.

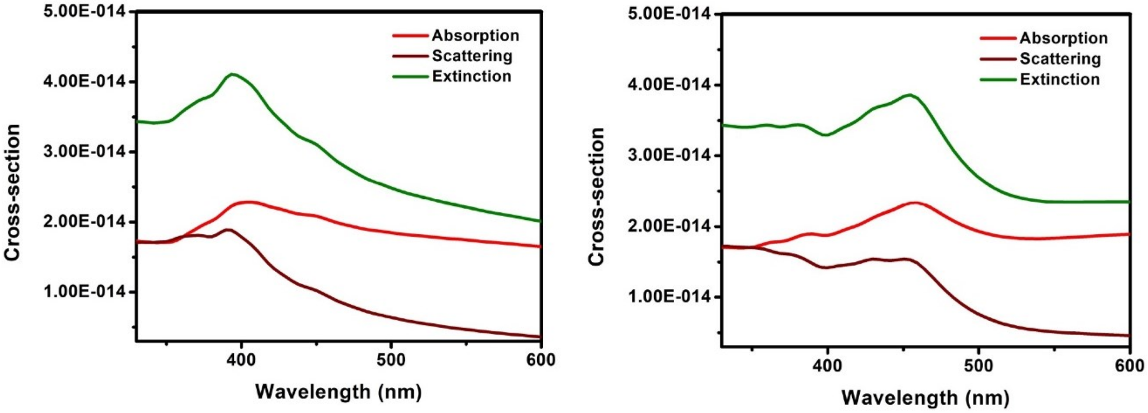

Figure 3.7. Simulated absorption and scattering profiles for (Left) Ag nanocube dimer separated by a 34 nm gap on NGr substrate, and (Right) Ag nanocube dimer with zero gap separation on NGr substrate. Reprinted and modified with permission from Ref.[207] Copyright IOP Publishing (2019).

Lastly, in a complementary study to those of FANTs, Kumar et al.[206] combined the use of bulk graphitic carbon nitride on anatase-phase and rutile-phase TNTA scaffolds for plexcitonic visible-light driven water-splitting and transformation of 4-NBT to DMAB. FDTD simulations were used to analyze cylindrical and square-cross section titania nanotubes and their behavior as symmetric hollow core waveguides for incident light due to the large contrast in refractive index between the TiO_2 annulus and the surrounding air.[206,208] Comparative studies of the electric field intensity profiles between bare cylindrical and square titania nanotubes, and those decorated with p-doped carbon nitride (C_3N_5) quantum dots (CNPQD) were made. **(Figure 3.8)** In **(Figure 3.8a),** the electric field intensity at 500 nm for bare cylindrical anatase-phase TNTAs does not decrease exponentially in the air cladding but rather spreads into the surrounding medium. For the same system illuminated with 350 nm photons, the waveguiding effect is much stronger as evidenced by a strong electric field distribution confined within the hollow area of the nanotube. **(Figure 3.8b)** The same observations when applied to rutile-phase STNTAs show that at 500 nm the resultant electric field is strongly confined within the hollow core of the nanotube while at 350 nm the incident light is attenuated due to absorption by TiO_2 resulting in a small evanescent field surrounding the outer wall of the nanotubes. Upon decoration of the STNTAs with CNPQDs, the electric field intensity is a lot weaker and confined to a much smaller volume within the nanotube core due to absorption by the CNPQDs. **(Figure 3.8c)** Contrastingly, the same cannot be said for TNTAs where an appreciable electric field intensity is still observed. **(Figure 3.8d)**

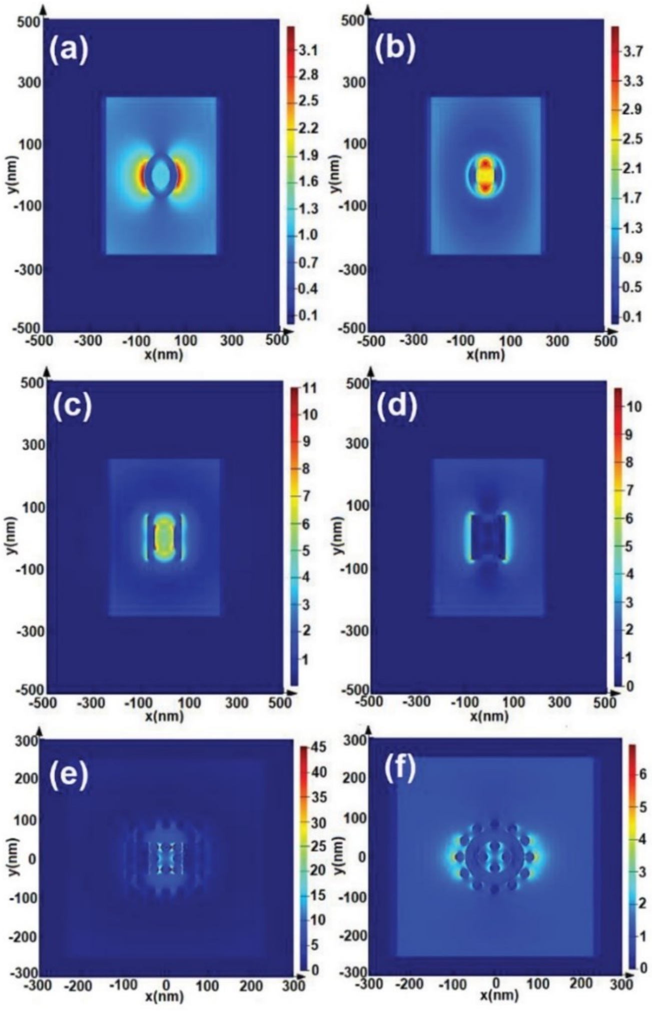

Figure 3.8. Simulated electric field intensity profiles for (a) TNTAs at 500 nm, (b) TNTAs at 350 nm, (c) STNTAs at 500 nm, (d) STNTAs at 350 nm, (e) CNPQD-STNTAs at 500 nm, and (f) CNPQD-TNTAs at 500 nm. Reprinted with permission from Ref.[206]. Copyright Wiley-VCH (2019).

These results indicate the CNPQD-STNTAs to be excellent absorbers of visible light compared to their circular counterparts. Supplementary analyses of the absorption and scattering spectra were shown to match very well with experimental results and correlated appropriately to the greater absorption efficiency of CNPQD-STNTAs over CNPQD-TNTAs in the 350 – 550 nm spectral ranges for surface catalytic reactions. In conclusion, Kumar et al.[206] demonstrated that the incorporation of graphenic materials in TiO_2 heterojunctions as a promising platform for plexcitonic photocatalysts that are photochemically and thermally stable, nontoxic, and efficient.

3.6 Closing Remarks

Several of the representative works discussed in this chapter involved experiments and simulations that were performed concurrently with my own doctoral research. By working on these projects, I was not only able to contribute my knowledge of plasmonics, alongside fabrication techniques utilized in my own doctoral research, to my colleagues but also gained valuable information on the working advantages of plasmonic noble metal-semiconductor heterojunction system and their weaknesses.

Lumerical FDTD simulations provided theoretical insights into understanding the optical and electromagnetic behavior of these diverse nanomaterials while helping optimize said systems for plasmonic and plexcitonic photocatalysis. These FDTD simulations can capture an impressive number of features that can be utilized to guide our experiments as well as improve our understanding of the inherent physical processes and dynamics involved in plasmonic photocatalytic systems.

While the inherent potential of plasmonic photocatalytic systems, including the representative examples seen in this chapter, is apparent, fundamental understanding pertaining to the behavior of the individual constituents of these systems and their characterization as stand-alone plasmonic substrates is essential for their optimization. The focal theme of my doctoral research involves addressing this very objective by exploring the hot carrier processes and interactions of the standalone plasmonic constituents that are at the crux of the photocatalytic phenomena facilitated by these systems.

Chapter 4

Monometallic Plasmonic Photocatalysis

4.1 Introduction

Noble metal nanoparticles (NPs) have emerged as key components for a wide range of applications in sensing, optical data storage, photovoltaics, photocatalysis, and plasmonics.[32,33,201,209] The localized surface plasmon resonances (LSPR) of Ag and Au NPs provide for the strong enhancement and confinement of electric fields near the metal surface. LSPR is a nano-optical phenomenon resulting from the collective oscillations of conduction electrons at the metal/dielectric interface upon excitation by incident light.[46,210] The LSPR can be affected by various properties including nanoparticle morphology and size, surface coverage, and the dielectric properties of the local environment.[19,46,211] Silver has the lowest losses and the strongest plasmon resonances of all known materials in the visible and near-infrared region making it a suitable candidate for various plasmonic applications.[210,212] Ag NPs on thin films of graphene, carbon nitride, MoS_2, and other 2D materials have shown excellent promise in plasmon-exciton co-driven catalysis.[207,213,214]

Both top-down and bottom-up fabrication techniques have been utilized for the synthesis and fabrication of metal nanoparticles.[215–217] The polyol synthesis of shaped silver nanoparticles remains popular among various other colloidal techniques where silver nitrate is reduced at high temperature by ethylene glycol which serves as the solvent. Polyvinylpyrrolidone (PVP) is utilized as a capping agent, enabling the synthesis of highly non-spherical silver nanoparticles. Greater control and modulation of nanoparticle morphology is obtained by separating the nucleation and growth processes involving different initial seed particles.[59] Despite their obvious advantages, difficulties in reproducibility alongside high-sensitivity and extended growth procedures hinder colloidal synthesis techniques.

Alternatively, the combination of physical vapor deposition (PVD) techniques such as sputtering and thermal dewetting provide a facile means to fabricate metallic nanoparticles.[91,209]

The subsequent formation of NPs has been attributed to solid state dewetting during annealing performed at high temperatures approaching the melting point of the metal involved. Ultimately, this is not ideal as high-temperature processes are often expensive, time-consuming, and can result in device deterioration.[218] The present report focuses on the fabrication of plasmonic Ag NPs on glass substrates using a facile, and highly-reproducible technique comprising of *low-temperature* thermal annealing (150°C – 400°C) of magnetron sputtered Ag thin films (5 nm–20 nm). The metallic film deposited using sputtering is metastable in nature. By annealing such a film, the atoms at the surface migrate to become individual islands that form metallic nanoparticles in a process governed by the minimization of the surface energy of the deposited metal film.[219–221]

The combination of magnetron sputtering, and thermal annealing thus provides for the formation of hemispherical nanoisland structures with highly consistent optical properties that can be modulated by simply modifying the corresponding temperatures and durations used for thermal annealing. This provides for a facile process in fabricating plasmonic nanoisland structures that can also be transposed to gold films while being less time-consuming compared to wet-chemical methods or colloidal synthetic techniques that frequently suffer from poor consistency. Plasmonic Ag NP substrates that experienced annealing at 150°C consisted of polydisperse, irregularly shaped islands that exhibited pronounced optical resonances at ~ 475 nm and ~ 360 nm. The quality factor (Q) of the optical response (given by $\omega_{peak}/FWHM$) is a key metric to evaluate plasmonic substrates since the LSPR-mediated local electromagnetic field enhancement and plasmon dephasing time are directly dependent on Q.[222] The Q values extracted from UV–Vis spectra provide information about the ensembled averaged enhancement factors.[23] The 475 nm extinction peak which had a quality factor (Q) of 2.9, corresponded to a dipolar resonance of the Ag nanoislands while the 360 nm peak was associated with a hybrid quadrupolar resonance[223] and exhibited a relatively high Q of 11.7. Plasmonic Ag NP substrates that were formed by thermal dewetting at 400°C consisted of hemispherical islands 60–100 nm in diameter and a redshifted dipolar resonance ($\lambda_{max} = 570$ nm) with a Q value of 4.8.

Finite-difference time-domain (FDTD) simulations and novel ellipsometric modeling provided greater insight into the electromagnetic response characteristics, and the subsequent optimization of the plasmonic substrates. Spectroscopic ellipsometry has been used to generate refractive index and complex permittivity data in a novel study to draw physical insights on the LSPR behavior of the Ag nanoisland substrates from their dielectric properties. This is highly significant as the main principles of LSPR sensing and LSPR stimulated photochemical transformations lie in the dependence of the LSPR on the refractive index of the surrounding medium. In the case of a luminophore set within the proximity of these plasmonic substrates, fundamental understanding of the luminophore's density of states and its interaction with the plasmonic nanoparticle requires knowledge of the complex permittivity of the plasmonic substrate. Although Mie theory can be utilized to model dilute solutions of colloidal nanoparticles, the same cannot be easily translated to metal films on a substrate. This situation is further complicated in prominent photocatalytic applications such as water splitting and CO_2 photoreduction often utilize metal films as photoanodes. Thus, the extraction of dielectric properties of Ag nanoislands using spectroscopic ellipsometry is of great significance in this work.

The Ag nanoislands themselves are found to be good SERS substrates for detection of R6G and excellent plasmonic photocatalysts for the photochemical transformation of 4-NBT and PATP into DMAB. Although SERS of nanomolar and higher concentrations of R6G has been previously reported for various Ag substrates, the novelty of the nanoisland substrates is directly related to the facile means utilized to fabricate the nanostructures and their high consistency performance in SERS for detection of R6G molecules at picomolar (down to 100 pM) concentrations. The corresponding LSPR spectra of the Ag nanoislands confirm their consistent plasmonic behavior and their subsequent generation of hot carriers for not only reduction of 4-NBT but also oxidation of PATP into DMAB is a further demonstration of their versatility as plasmonic substrates.

4.2 Materials and Methods

4.2.1 PVD Sputtering

PVD techniques constitute a versatile coating technology that can be used to deposit a variety of metals, alloys, ceramics, inorganic compounds, and polymers.[224] The two most important PVD techniques are evaporation and sputtering. Thin films in integrated circuits and other micro- and nanosystems are deposited using either evaporation or sputtering. Raw source materials for PVD reactors can be in solid, liquid, or vapor forms. Suitable substrates generally include glass, plastics, metals, and semiconductors. Our discussion will focus specifically on sputtering as it has been our technique of choice in depositing noble metal thin films for monometallic and bimetallic nanostructures.

The basic working principle of most PVD processes involves three elementary steps: (1) the synthesis of the coating vapor from the raw source material, (2) the transport of the coating vapor onto the substrate, and (3) the condensation of the vapor onto the surface of the substrate.[224] The whole process is carried out in a vacuum chamber with the chamber being evacuated prior to deposition in a "pump-down" procedure that gets the system to the required pressures necessary for deposition. Due to the generally low pressures encountered in PVD reactors, the coating vapor experiences few intermolecular collisions in its journey to the substrate which is generally held upside down to prevent particulate contamination.

Sputtering is a physical phenomenon where ions are accelerated through a potential gradient and bombard a "target" or cathode. Simply put, we are kicking atoms off the surface of the target using energetic ions (~500 eV, in most cases). The ions in consideration must be nonreactive with Argon gas being a common candidate in most sputtering systems as it is cheap, inert, and moderately heavy. After the chamber has been evacuated to $\approx 10^{-6}$-10^{-7} Torr, Argon gas is introduced into the chamber at a few mTorr of pressure. A plasma discharge of the inert gas is then ignited with Ar+ ions being created by electron impact ionizations. A large negative potential is utilized to accelerate the ions into the target (cathode) and assists in powering the discharge; the applied power can be of either a radio frequency or direct current source. The energetic ions of this plasma discharge bombard the surface of the target. Here, the physical aspect of sputtering relates to the transfer of momentum from the bombarding ions to the atoms from the surface of the target, resulting in them becoming volatile, escaping the surface, and being transported as vapor to the substrate where they are deposited and form a thin film. These steps generally dictate what is observed in the case of diode sputtering systems where the cathode is covered with the raw source material (the "target").

However, diode sputtering suffers from two major deficiencies: slow rates of deposition, and an extensive electron bombardment of the substrate which can result in overheating and structural damage.[224] Alternatively, magnetron sputtering systems **(Figure 4.1)** resolve these issues simultaneously. In magnetron sputtering, magnets behind the cathode are used to trap free electrons in a magnetic field that extends directly above the target surface. By confining the electrons near the target, not only is the deposition process efficiency greatly improved but the trapping of the electrons also lends to enhanced probability of ionizing a neutral gas molecule. These factors directly result in a larger population of ions and increasing the rate at which target material is sputtered and deposited onto the substrate. Furthermore, discharge plasmas in magnetron sputtering systems can be generated at lower pressures reducing both the background gas' incorporation in film growth and the loss of energy of the sputtered atoms via gas collisions. The Nanofab at the University of Alberta hosts several such systems with gun/substrate configurations designed for both co-sputtering and sequential sputtering.[225]

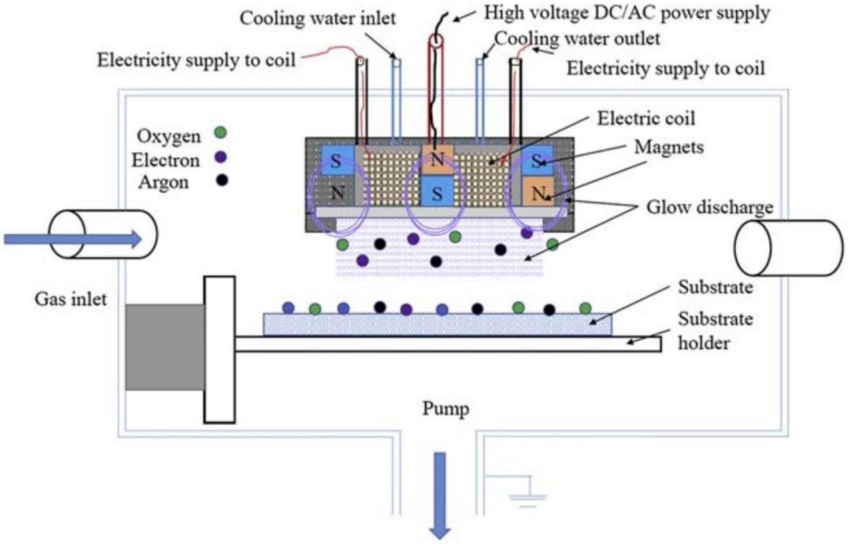

Figure 4.1. Schematic rendering of a magnetron sputtering system. Reprinted for academic use from Ref[226]. Copyright Elsevier (2018).

Sputtering is now considered to be the dominant PVD method due to its provisions for better coverage, films of higher density and larger grains, facile deposition of alloys and compound films, and very good repeatability and control. Dielectric materials can be sputtered using RF plasmas with capacitive coupling, while metals can be DC or RF sputtered.[224] Alloy targets are quite easy to sputter as one does not have to worry about the widely different vapor pressures. Compound films can be formed using reactive sputtering where a reactive gas is introduced during the deposition phase. The highly energetic sputtered particles and the plasma activation of the gases assist for reactions to occur upon the substrate. The low vacuum, plasma path in sputtering provides for less line-of-sight deposition. Nevertheless, sputtered films have better uniformity than those of evaporation. The high energy plasmas in sputtering also help overcome the temperature limitations of evaporation.

Despite its myriad positive aspects, deposition results from sputtering are highly sensitive to initial conditions. The use of magnets in magnetron sputtering can result in nonuniform target usage. Sustaining the plasma discharge is highly important in sputtering. This requires pressures of 1-20 mTorr (magnetron) or 40-100 mTorr (diode). As a result, gas contamination levels in sputtered films are generally higher than for evaporation. The mean free path at 5 mTorr is ~ 1 cm, which means the depositing flux experiences several collisions with gas particles en route to substrate deposition. Every collision substantially reduces the particle's energy, and so sputtered films and their qualities are highly sensitive to the initial vacuum and pressure conditions in the chamber. Still, as with other plasma processes, sputtering generally takes account of these vulnerabilities and is among the most efficient and popular of PVD techniques available today. This is largely thanks to the high level of tailoring one can achieve in sputtering film deposition by easily monitoring and moderating properties such as the substrate bias, target voltage, pressure, flow rates etc.[224,225,227]

4.2.2 Thermal Annealing

Hot-plating and thermal annealing treatments are essential to the growth of colloidal nanoparticles and sputtered films. Thermal treatments are necessary to break sputtered films in what is otherwise known as thermal dewetting.

Thermal dewetting is generally used to convert a deposited metallic thin film on a substrate into metallic nanoparticles. The metastable nature of the sputtered film, and the reception of a thermal energy stimulus results in the atoms at the surface to migrate to form individual islands which ultimately result in metallic nanoparticles. The entire process is driven by the requirement of minimizing the surface energy of the deposited metal film, the substrate, and the metal-substrate interface.[228] The driving force for dewetting increases with decreasing film thickness. This is because the thinner the metal film the higher its surface-to-volume and its surface energy, and the lower the activation energy for metal atom surface mobility. This is one of the primary reasons as to why dewetting can occur at temperatures well below the melting point of a metal film while allowing it to dewet in the solid state.[219,228]

Key factors to initiate dewetting in films on a given surface are defects including holes, edges, impurities, and grain boundaries.[228] The use of pre-patterned substrates can enable dewetting driven by substrate surface topography but that is not the focus of this work. For the case of a thin film, dewetting begins with the formation of a hole that can reach the substrate and influence subsequent recession of the film. Metal films can either be of crystalline or amorphous nature, and in general, dewetting initiation sites for film rupture are observed as a result of impurities, thickness variations, and grain boundaries, particularly in polycrystalline metal films.[229,230] Upon film rupture, the driving force for dewetting is driven by a minimization of the total free energy or a reduction of the interfacial area between the film and its substrate, leading to agglomeration into three-dimensional islands. This driving force can be defined by the Young-Dupré principle[219] for dewetting as

$$E_S = \gamma_A + \gamma_{AB} - \gamma_B, \tag{4.1}$$

where γ_i is the surface energy density of the material (with $i = A$ (film), B (substrate)) and γ_{AB} the interfacial energy density. Dewetting of a film occurs when $\gamma_A + \gamma_{AB} > \gamma_B$ for a positive E_S.

While it may be experimentally difficult to distinguish the primary parameters responsible for the final state of the thermally dewetted metal film and its kinetics, certain key parameters have been identified including initial film thickness, capillary energies and film surface curvature, annealing temperatures, the thermodynamic driving force E_S, stress and strain effects, defects, crystallographic orientations, and triple line pinning related to adsorption or defects between the outer edge and interface of the film and its substrate.[228]

4.2.3 Fabricating Monometallic Ag Nanoislands

The growth of plasmonic Ag NPs was achieved using direct current magnetron sputtering of 99.9% pure Ag on glass substrates followed by thermal annealing in a furnace. Prior to deposition, the glass substrates were cleaned via ultrasonication in methanol for 20 min. The vacuum chamber was evacuated to a base pressure of 10^{-6} Torr, and then filled with argon gas flowing to maintain a constant pressure of 7×10^{-3} Torr during sputtering. 5–20 nm thick, thin films of Ag were deposited at room temperature for 10 s at a rate of 300 W, and subsequently subjected to thermal annealing at 150°C and 400°C. A two-hour ramping procedure and a 15-minute dwell cycle was used in the former, while a one-hour ramping procedure and a 15-minute dwell cycle was used in the latter. Annealing was performed in open-air conditions, and post-annealing, the samples were left to cool to room temperature. Ag films annealed at 150°C experienced a distinct change in color from silver blue to pale brown, while those annealed at 400°C exhibited a pale yellow-green hue.

4.2.4 Characterization

Transmission spectra of annealed (150°C and 400°C) and non-annealed Ag films alike were measured using a Perkin Elmer Lambda 1050 UV–Vis-Nir Spectrophotometer. The dielectric properties of the Ag thin films were investigated using a variable-angle spectroscopic ellipsometer (VASE) M-2000V (J.A. Woollam & Co) in a novel effort to generate physical insights on the substrates. The surface morphology of the annealed films was studied using a Hitachi S-4800 field emission scanning electron microscope (FE-SEM), and an Asylum MFP-3D/Dimension atomic force microscope (AFM). Elemental analyses were performed via EDX analysis using a Zeiss Sigma FE-SEM. ImageJ software from the National Institutes of Health (NIH) was utilized to obtain size distributions of the nanoislands. Corresponding histogram plots were fit to Gaussian distributions to determine the average size of nanoislands, their standard deviation, and polydispersity (the percent ratio of standard deviation to average size).

4.2.5 SERS sensing and photocatalytic studies

Raman spectroscopy is a technique used to measure rotational, vibrational, and low-frequency modes in a system. Raman spectroscopy focuses on the inelastic scattering of monochromatic light incident on a sample, resulting in molecular vibrations, phonons, and other forms of excitation.[231]

When it comes to plasmonics and hot electrons, Surface Enhanced Raman Spectroscopy (SERS) is a widely used technique. The SERS effect is fundamentally equivalent to the Raman effect except that it refers to the amplification of Raman signals from molecules adsorbed on metallic (typically noble metal) surfaces. The amplification of the signals in SERS is attributed to the electromagnetic interaction of light with noble metals resulting in amplification of the laser field through plasmon resonance excitations. With SERS, the technique involves measuring the Raman signals of the adsorbed molecules which serve as the probes, offering insight into the molecules' electronic and vibrational structures[83] as well as help understand the interfacial nature of transitions occurring at the adsorbate-metal surface which is essential in the context of plasmonic photocatalysis and interfacial hot electron transfer processes.[232]

A typical Raman system is composed of four major parts: (1) excitation source (laser), (2) sample illumination system and light collection optics, (3) wavelength selector (filter or spectrophotometer), and a (4) detector (photodiode array, CCD, or PMT).[47,233] The sample is usually illuminated with a laser beam in the UV-Vis-NIR range. Light that is scattered from the sample is collected with a lens and is passed through the interference filter or spectrophotometer to obtain the sample's Raman spectrum. The main complication in Raman spectroscopy concerns the intensity of stray light from Rayleigh scattering which may exceed the Raman signal intensity near the laser wavelength. The sample can be oriented appropriately such that reflected laser light can miss the light collection optics. Still, this does not prevent a large population of elastically scattered laser photons entering the spectrometer and causing detector saturation.[47]

To alleviate this problem, a high-resolution spectrometer with efficient stray light rejection characteristics is required. Commercially available interference filters are often used for this specific purpose. Holographic gratings are also preferable as they produce stray light of intensities lesser by about an order of magnitude as opposed to ruled gratings. Multiple dispersion stages also serve as an alternative means to reduce stray light reduction. Modern Raman systems generally consist of multi-channel detectors like Photodiode arrays or CCDs to detect the Raman scattered light. These detectors provide for greater sensitivity, faster performance, and finer refinement of the Raman signal.[231,234]

NINT hosts a Nicolet Omega XR Raman Microscope which can be used for sample characterization and analysis. Multiple laser options are available and are user exchangeable. All lasers are depolarized and minimize orientation dependence in measurements. A laser power regulator allows for the power at the sample to be controlled. The range of laser powers differs for different laser wavelengths with the 532 nm laser providing a maximum power of 10 mW, the 633 nm laser providing a maximum power of 8 mW, and the 780 nm providing a maximum power of 24 mW. Full-range (2 cm^{-1} per CCD pixel element) and high-resolution (1 cm^{-1} per CCD pixel element) gratings are available and can be interchanged for each standard excitation wavelength. The system's Rayleigh filters account mainly for Stokes bands observations. Lastly, the spectrograph has a spectral range between 400-1050 nm and comes with four software-selectable apertures (25 and 50 µm pinhole confocal; 25 and 50 µm slit) that can be utilized accordingly.

In testing the Ag nanoisland substrates for SERS, Methanolic R6G solutions of varying molar concentration (10^{-2} M – 10^{-10} M) were drop-coated onto the annealed plasmonic Ag film substrates and reference samples using standardized solution volumes to form thin coatings. Raman spectra were collected shortly thereafter using the Nicolet Omega XR Raman Microscope under a laser illumination power of 2 mW at wavelengths of 532 nm and 633 nm. For photocatalytic studies, solutions of 4-nitrobenezenethiol (4-NBT) and para-aminothiophenol (PATP) were drop-coated onto the annealed plasmonic Ag film substrates and reference samples to form thin coatings. Raman spectra were once again collected using a Nicolet Omega XR Raman Microscope under laser illumination at wavelengths of 532 nm, and 633 nm. The light-induced transformation of the thiols (4-NBT and PATP) into their DMAB products were monitored by gradually increasing laser power from 0.1 mW to 8 mW and observing the evolution of the corresponding Raman spectral peaks of the reactant and product. Other experimentally relevant parameters included the use of an aperture size of 50 µm pinhole, 2 µm spot size, a 10 x objective, and for DMAB analyses, exposure times of 20 s in air at room temperature at relevant laser power values.

4.2.6 Lumerical FDTD Simulations

Lumerical was used to model and simulate the optical and near-field electromagnetic response properties of annealed Ag film nanostructures. The relevant results were compared with experimental data obtained through characterization and morphological studies to provide further insight into the electromagnetic field responses and optimization of these plasmonic substrates. Optical and near-field electromagnetic response properties of annealed Ag films were investigated using Lumerical Nanophotonic FDTD simulation software. The simulations were performed for various combinations of hemispherical nanoisland structures in vacuum including individual and arrayed nanoislands (at separation distances of 100 nm) on a glass substrate. Absorption cross sections, reflection and transmission spectra, and electric field intensity profiles were captured using near, and far-field profile and frequency monitors. Material data for the nanoislands are provided in Lumerical FDTD simulations and are sourced from Palik et al.[235] A light source of bandwidth range 300 – 800 nm was set incident upon the nanoislands at a normal angle from above.

Lumerical's in-built refractive index monitor was utilized to confirm the nanoislands were appropriately configured and modeled throughout the course of the simulations. PML absorbing boundary conditions were utilized for the simulation, allowing for the absorption of light waves (propagating and evanescent) in the simulation region with minimal reflections. Periodic boundary conditions were utilized for simulations involving nanoisland arrays to capitalize on the symmetrical nature of the system, and further shorten simulation time.

4.3 Results and discussions

4.3.1 Morphology and composition of Ag nanoislands

(Figure 4.2a) and **(Figure 4.2b)** present secondary electron FESEM images of Ag films for annealing treatments at 150°C and 400°C, respectively. In both cases, thermal treatment of the samples induces thermal dewetting of the films allowing atoms at the surface to migrate and form individual nanoislands. Ag films annealed at 150°C consistently exhibited the development of an irregular island-like nanoparticle morphology with a polydisperse size distribution and indistinct interparticle distance. These observations are further supported by the topographical AFM image **(Figure S1b)** of Ag film samples annealed at 150°C. **(Figure 4.2b)**, in contrast, indicates that Ag films annealed at 400 °C exhibit an almost monodisperse spherical morphology while maintaining a non-uniform size distribution. After thermal treatment at 400 °C, the vacuum deposited Ag film is broken into randomly distributed nanoparticles of a largely hemispherical morphology. Some deviations are observed where some particles are elongated rather than being spherical. For Ag films annealed at 150^0C, average nanoisland size with error was determined to be ~ 50 ± 25 nm and a polydispersity of ~ 50%. **(Figure S2a)** Similarly, for Ag films annealed at 400^0C, average nanoisland size with error was determined to be ~ 117 ± 33 nm and a polydispersity of ~ 30%. **(Figure S2b)** It is noted that for Ag films annealed at 150^0C we obtain a bimodal size distribution **(Figure S2a)** compared to Ag films annealed at 400^0C where we obtain a monomodal size distribution. **(Figure S2b)** This can be attributed to the temperatures used for annealing the films. The temperatures used to treat these films affect the kinetics of the system. It is well-known that the adatom mobility increases exponentially with increasing temperatures.[228] When heated to temperatures that provide for high surface mobility of adatoms metastable films experience dewetting to form metal islands. In fact, a characteristic temperature for the dewetting of thin films can be identified to be between 0.3 (the H*ü*ttig temperature at which atoms at defects become mobile) and 0.5 (the Tammann temperature at which atoms in the bulk metal start to diffuse) of the melting point of the metal.[236] Ag films annealed at 400^0C satisfy this condition for dewetting as the melting point of Ag is approximately 961.8^0C. Ag films annealed at 150^0C do not satisfy this criteria and this correlates to the greater polydispersity observed in the morphology of the nanoislands. Quan et al.[237] demonstrate a similar dependence with Ag films annealed at temperatures above a critical temperature of 300^0C where dewetting results in a monodisperse distribution of hemispherical islands of similar size and shape, and consequently supporting a monomodal size distribution. The glass substrate itself is not damaged during thermal annealing, and only the deposited film is affected by the dewetting process which is largely governed by the minimization of the surface energy of the deposited metal film. These observations demonstrate the dependence of the morphology and uniformity of nanoparticle size distributions of sputtered continuous Ag film layers on the annealing temperatures, and treatment durations. It can be inferred that by increasing the duration of annealing at both temperatures further coalescence among the particles can occur due to increased surface diffusion resulting in larger particle sizes and more spherical shapes. The morphological changes of Ag films due to thermal annealing treatment at different temperatures for various time durations can be explained by considering the reverse configuration of thin film growth which involves several processes such as adsorption, cluster formation, surface diffusion, desorption, nucleation, island growth, and agglomeration, all of which can be observed in the end product of our sputtered and annealed Ag films.[238] Barman et al.[212] provide an extensive discussion of the same on the systematic formation of Ag nanoparticles from sputtered Ag films using rapid thermal processing (RTP).

Elemental and chemical characterization of Ag films annealed at 400 °C via energy dispersive x-ray spectra collected during scanning electron microscopy is presented in (**Figure S1a)**. The corresponding atomic percentages and peaks of Ag in **(Figure S1c)** provide a preliminary confirmation of the formation of Ag nanoislands. Crystallographic analysis of Ag films annealed at 150°C and 400°C were investigated via x-ray powder diffraction presented in **(Figure S3)**. The lack of peaks corresponding to Ag_2O formation is readily observable in **(Figure S3)**. Furthermore, it is well-known that for Ag_2O films, the Ag_2O phase completely transforms into Ag for temperatures round 400°C and beyond via thermal decomposition during vacuum thermal annealing.[239] As the samples fabricated in this work involve very thin films of thicknesses ranging between 5–20 nm, the growth of a consistent Ag_2O layer is limited. Also, as Ag_2O requires strong oxidizing conditions, facilitated only under pure oxygen flow at high temperatures, it is AgO that typically forms. AgO itself is unstable at room temperature, and alongside Ag_2O, decomposes under visible light irradiation to regenerate Ag.[240] The lack of evidence in damping of the plasmonic resonances, and the consistent high intensity absorption profiles **(Figures 4.2c – 4.2d)** support this.

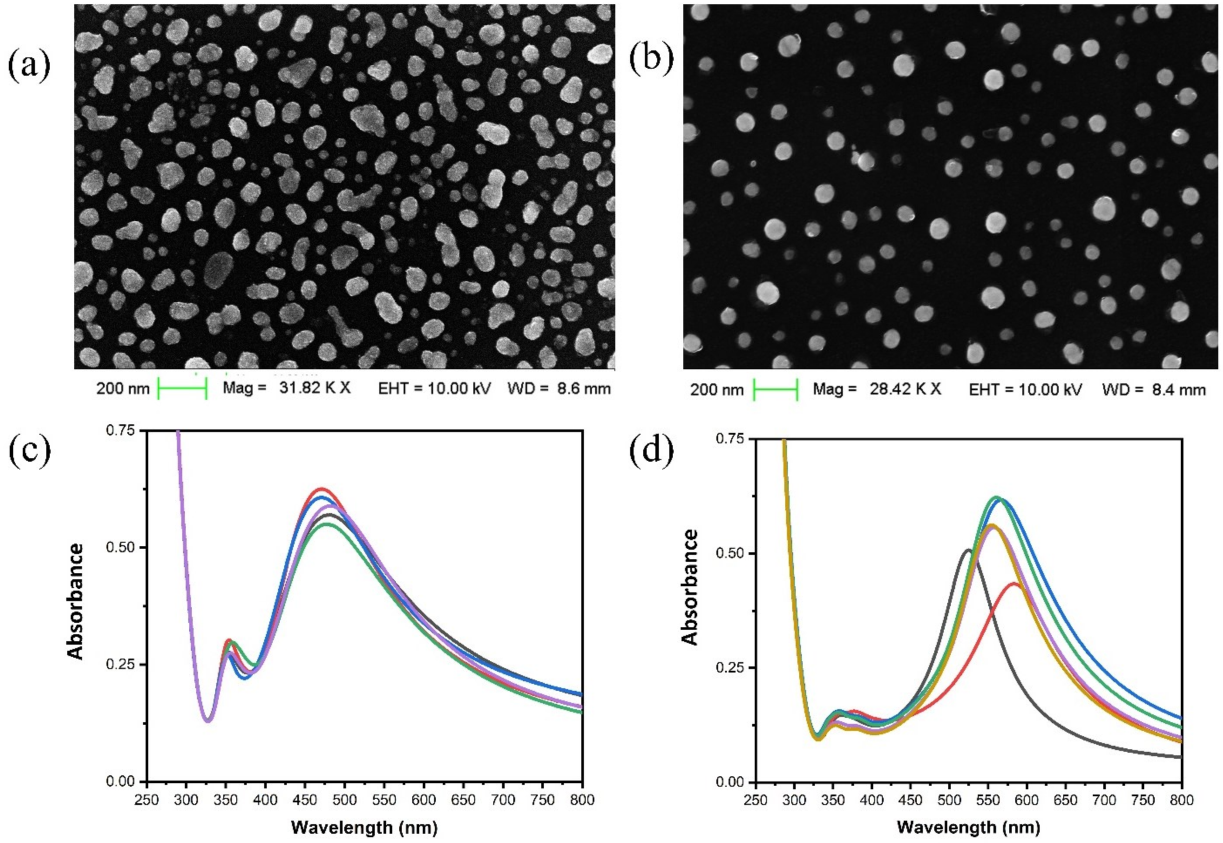

Figure 4.2. (a) Secondary electron FESEM image of Ag film annealed at 150 °C; (b) FESEM image of Ag film annealed at 400 °C; the scalebars in both FESEM images correspond to lengths of 200 nm; (c) UV–Vis absorbance of Ag films annealed at 150° C; (d) UV–Vis absorbance of Ag films annealed at 400 °C. The color-coded spectra help distinguish the spectra of individual films while helping identify the similar characteristics in their absorbance spectra under the corresponding conditions. It can be noted that for films annealed at 400 °C the secondary resonances at shorter visible wavelengths are broadened while the primary resonances are redshifted to longer wavelengths.

4.3.2 LSPR phenomena in Ag nanoislands

(Figure 4.2c) and **(Figure 4.2d)** present the UV–Vis-Nir spectra of Ag films annealed at 150 °C and 400 °C. The effects of thermal annealing on the optical properties of the Ag nanoisland substrates can be understood by considering Mie scattering theory.[19,46] The absorption spectra of Ag films on glass substrates experience redshift and a clear broadening of the primary resonance peak with increasing annealing temperatures.[210] This can be understood by the corresponding increase in the average particle size due to the coalescence of individual smaller particles via surface diffusion. The quadrupole resonance is responsible for the secondary absorption peak observed at the lower wavelength regions and is not observable for as-sputtered Ag films. Similarly, the secondary peak also experiences broadening with increasing annealing temperatures and originates from the electronic coupling of conduction electrons of the agglomerated Ag NPs that are larger in size.[241]

In Ag films annealed at 150°C, the primary absorption maximum is due to a broad dipolar LSPR resonance and is observed at wavelengths between 470–485 nm. The linewidth for the dipolar resonance consists of contributions from both homogeneous and inhomogeneous broadening as shown in (**Figure S4)**, and the *Q*-factor is ~ 2.9. In water ($\epsilon = 1.33$), citrate-capped colloidal Ag nanospheres with a diameter of 80 nm are known to exhibit a LSPR peak at 458 nm.[242] The redshift of the LSPR peak of Ag nanoislands to ~ 500 nm **(Figure 4.2c)** is a consequence of both the hemispherical shape and the high index glass substrate ($\epsilon = 1.5$). The hemispherical shape is due to the wetting configuration of silver nuclei on the surface dictated by the Young-Dupré equation wherein faceting is only significant for particle sizes > 100 nm.[243] The close match of the results of FDTD electromagnetic simulations of isolated Ag hemispheres on a glass substrate **(Figure 4.3d)** with the experimentally observed optical spectra **(Figure 4.2c)** provides further validation.

Following a dip in the wavelength range 374–387 nm, a secondary peak is observed at the UV spectra region corresponding to wavelengths between 352–358 nm. This secondary peak corresponds to a hybrid quadrupolar resonance which is due to the size of the Ag nanoislands, the bulk (volume) plasmon resonance at ~350 nm, and also involves longer range interparticle interactions through the higher permittivity glass substrate.[223] Isolated solid Ag nanospheres with diameters smaller than 60 nm exhibit merely a dipole resonance (the quadrupole resonance is absent) since the driving electric field incident on the nanoparticle can be assumed to be uniform in intensity over the entire nanoparticle.[244] This assumption is untenable for larger nanoparticles and gives rise to higher order plasmon resonances. Isolated colloidal Ag nanospheres with diameters of 60–100 nm exhibit weak, indistinct quadrupole resonances which occur purely due to a weakening of the quasi-static approximation for larger spheres. It is noteworthy that a quadrupole resonance in the short wavelength spectral region is not observed either for gold nanoislands or for colloidal gold nanospheres.[223,245] The hybrid quadrupolar resonance seen in **(Figure 4.2c)** in the short wavelength region has a high Q-factor of 11.7 **(Figure S5)** and is not related to the agglomeration of Ag nanoparticles which typically results in broadened and redshifted resonances.[54,241,246] An asymmetric quadrupole resonance is more prominent for plasmonic nanoparticles with a lower dissipation (e.g. Ag) and a smaller size parameter $(2\pi a/\lambda)$ where a is the particle radius.[247]

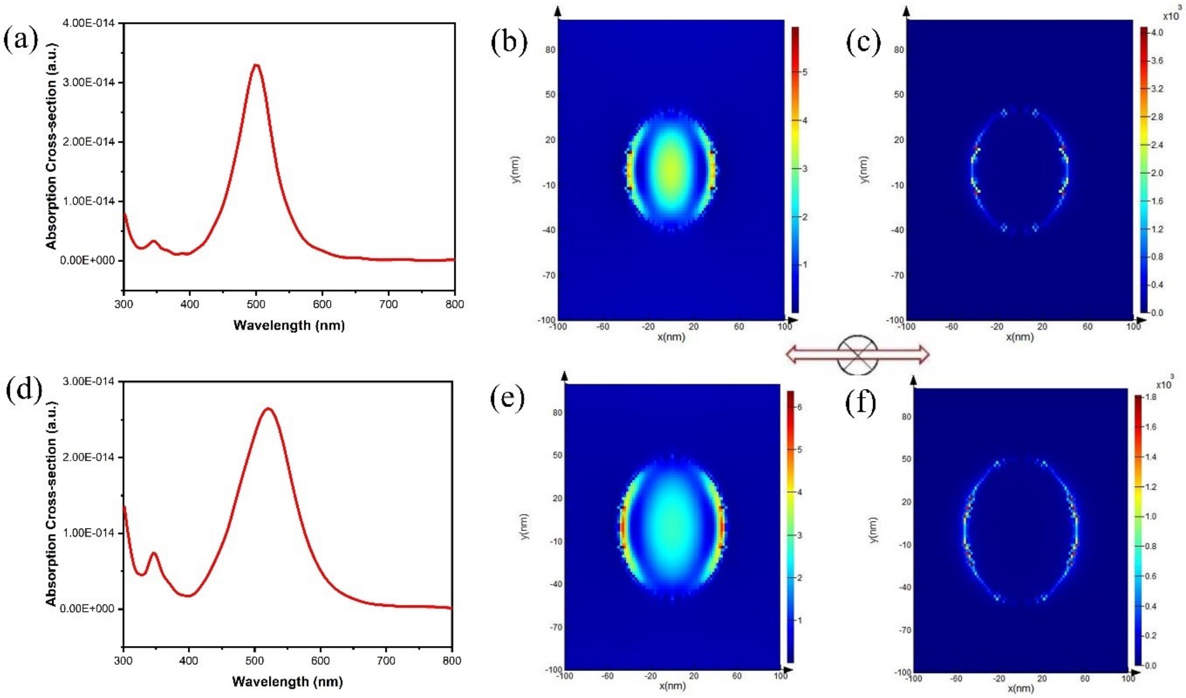

Figure 4.3. (a) Simulated absorption cross-section for an individual hemispherical nanoisland of radius 40 nm, and (b)–(c) its corresponding electric field intensity profiles along the xy-plane at resonant wavelengths of 345.852 nm and 498.113 nm, respectively. (d) Simulated absorption cross-section for an individual hemispherical nanoisland of radius 50 nm, and (e)–(f) its corresponding electric field intensity profiles along the xy-plane at resonant wavelengths of 345.852 nm and 519.912 nm, respectively. The polarization of the incident electric field (parallel to the *x*-axis) and its direction of propagation (into the page) have been indicated correspondingly.

For Ag films annealed at 400 °C, the dipole resonances are more redshifted and occur at 525 – 583 nm **(Figure 4.2d).** The dipole resonance of the 400°C annealed Ag films exhibits a nearly perfect Lorentzian profile as seen in **(Figure S6)** with almost no contribution from inhomogeneous Gaussian broadening. In the short wavelength region, two resonances are seen with the higher energy peak occurring at 352 – 360 nm, and the lower energy peak at 378 – 381 nm and are attributed to overlapping size-related quadrupolar resonance and the characteristic minor dipole resonances of hemispherical particles illuminated with the electric-field polarization along the long axis of the hemispheres. Even though these overlapping resonances in **(Figure 4.2d)** appear less prominent to the untrained eye, they were each found to have similar or higher Q-factors compared to the quadrupolar resonance of the Ag films annealed at 150°C following baseline subtraction and peak deconvolution. The redshifting of the dipole resonance for Ag films annealed at 400°C can be attributed to the growth dynamics of the Ag film at higher temperatures resulting in the coalescing of individual particles via increased mass transfer and higher surface diffusion from smaller nanoparticles to nearby larger particles. The redshift, thus observed, corresponds to an increase in average particle sizes to ~ 100 nm. The measured optical extinction spectra of the Ag films annealed at 400°C **(Figure 4.2d)** closely resembles the FDTD simulation results for an array of hemispherical nanoislands with a center-to-center spacing of 100 nm **(Figure 4.4a)** which indicates the negligible role of Coulombic interactions from neighboring particles (which are too weak for interparticle spacings of 100 nm).

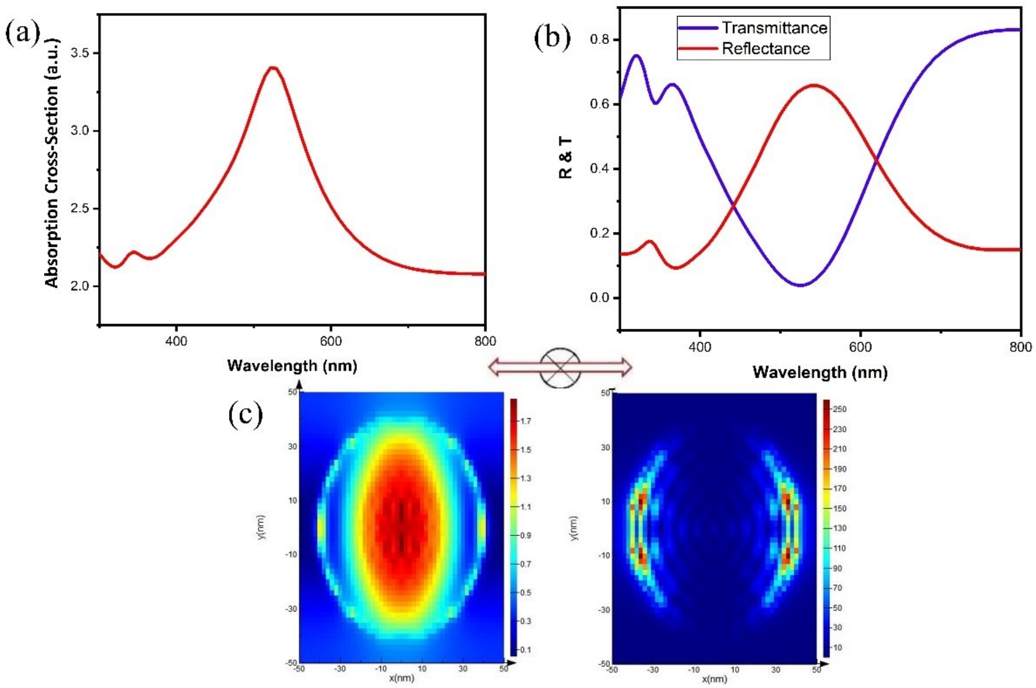

Figure 4.4. (a) Simulated absorption cross-section for an array of hemispherical nanoislands of radii 40 nm, and (b) its corresponding transmittance and reflectance spectra. (c) Electric field intensity profiles along the xy-plane at resonant wavelengths of 346.154 nm (left) and 521.739 nm (right), respectively. The polarization of the incident electric field (parallel to the x-axis) and its direction of propagation (into the page) have been indicated correspondingly.

Among the various FDTD simulations that were performed, results involving individual 40 nm and 50 nm radii nanoislands, and their array counterparts demonstrated agreement with experimental observations. **(Figures 4.3a – 4.3c)** present the absorption cross-section along with the electric field intensity profile for an individual 40 nm radius Ag nanoisland on glass. The electric field intensities were measured (along the xy-plane) at the corresponding resonant wavelengths observed in the absorption spectra at 345.852 nm **(Figure 4.3b)** and 498.113 nm **(Figure 4.3c). (Figures 4.3d – 4.3f)** present the same for an individual 50 nm radius Ag nanoisland on glass with resonances at 345.852 nm **(Figure 4.3e)** and 519.912 nm **(Figure 4.3f).** Both results share similarities with the UV–Vis spectra obtained for Ag films annealed at 150 °C and 400 °C with dipolar and quadrupolar resonances observed. The spectrum of the 50 nm radius nanoisland provides a better match and demonstrates the relevant redshift of the primary resonance as would be expected from theory. The electric field intensity profiles also demonstrate concentrated hotspots of greater intensity (by three orders of magnitude) at the quadrupole resonance as opposed to the diluted hotspots observed at the dipole resonance. In the case of the former, the hotspots are concentrated around the bounding edge of the nanoisland with the greatest intensities observed at locations of maximum curvature. These observations agree with our theoretical understanding of the LSPR and its behavioral dependencies on the morphology and size of the nanostructure. A separate set of simulations involving the nanoisland arrays were also run. The arrays were composed of hemispherical nanoislands of either radii 40 nm or 50 nm. Interestingly, the best agreement was found for the array consisting of nanoislands of radii 40 nm as presented in **(Figure 4.4)**. The absorption cross-section in **(Figure 4.4a)** is similar to those of the UV–Vis spectra with a secondary resonance at 346.154 nm, and a primary resonance at 521.739 nm. Furthermore, the corresponding transmittance spectra in **(Figure 4.4b)** matches the transmittance spectrum as modeled via VASE. **(Figure 4.4c)** is another demonstration of the electric field intensity profiles at the secondary and primary resonance. Much of the presented observations on the experimental and simulated absorption profiles and resonance shift behavior of the Ag nanoislands agree with the existing literature.[210,248,249]

4.3.3 Variable angle spectroscopic ellipsometry (VASE) of Ag nanoislands

Ellipsometry is a sensitive, non-destructive, and indirect characterization technique where changes in the polarization state of the incident polarized light upon the sample can be used to glean information into the sample's optical constants, composition, morphology, and thickness.[250] VASE was performed on Ag film samples annealed at 150°C at angles 55°, 65°, and 75° in the wavelength range of 330 nm – 1500 nm. Transmission intensity scans were also performed to obtain a unique solution to the thickness and optical constants of the annealed and non-annealed Ag films.[250] The obtained ψ, Δ (related to the ratio of Fresnel reflection coefficients for p- and s-polarized light) and transmission data were modeled using the VASE32 software. The as deposited Ag films not subject to thermal annealing were modeled using Palik's optical constants[235] and the obtained thickness was 13.48 nm with a mean squared error (MSE) of 18.29. By varying the optical constants, the MSE was further reduced to 2.94.

The annealed Ag films, or silver nanoislands, were modeled using various oscillators on a glass substrate. Initially, a point-to-point analysis was performed by providing appropriate initial conditions and were fit for ψ, Δ and transmission data to obtain a unique solution to thickness and optical constants. This was later used as reference to fit the real (ϵ') and imaginary parts (ϵ'') of the sample's permittivity using three general oscillators obeying Kramers-Kronig's consistency relations. Two Gaussians (corresponding to the LSPR and bulk plasmon resonances) and one Tanguy oscillator (to account for the 4d → 5s interband transition at ~ 3.8 eV) were used to perform the fit.[251] This model was utilized to calculate the predicted response from Fresnel's equations which can help describe the thickness and optical constants of the material. When these values are not known, an estimate is usually given for the preliminary calculation. The calculated values are compared to experimental data with the lowest MSE being used as a metric for the best answer. The obtained effective thickness of the layer was 33.19 nm with an MSE of 14.28. The fits and effective optical constants of the nanoisland layer are presented in **(Figure 4.5).** Film thickness is defined by the interference between light reflecting from the surface and light traveling through the film. This interference may be constructive or destructive depending on how the light rejoins with the surface reflection and the light's relative phase. It can be observed that the effective thickness is lower than the nanoparticle sizes obtained in AFM. This is because the effective layer is equivalent to a uniform material approximating the optical properties of discontinuous islands, rather than describing the physical average height of the nanoparticles.[252–254]

The significance of these results pertains to the fact that prior works have not generated complex permittivity data to derive physical insights on plasmonic nanostructures. This would be highly essential in the macroscopic modeling of said nanostructures, for example, if we wish to learn how a luminophore would interact with a nearby nanoparticle. Mie theory, which is generally suitable to model situations where dilute solutions of colloidal nanoparticles are utilized, does not carry over well when it comes to modeling metallic films. VASE modeling of the Ag substrates helps us understand the surface roughness and the discontinuous nature of the substrate as well as provide a means to directly model these substrates using the obtained complex permittivity data. While it is generally ideal to make ellipsometric measurements on a Si wafer, due to its overall bulk flatness and better local surface roughness accompanied by the homogeneity of refractive index and absence of secondary back reflection, the presented results were made on glass substrate where tape was utilized to avoid excess back reflection.

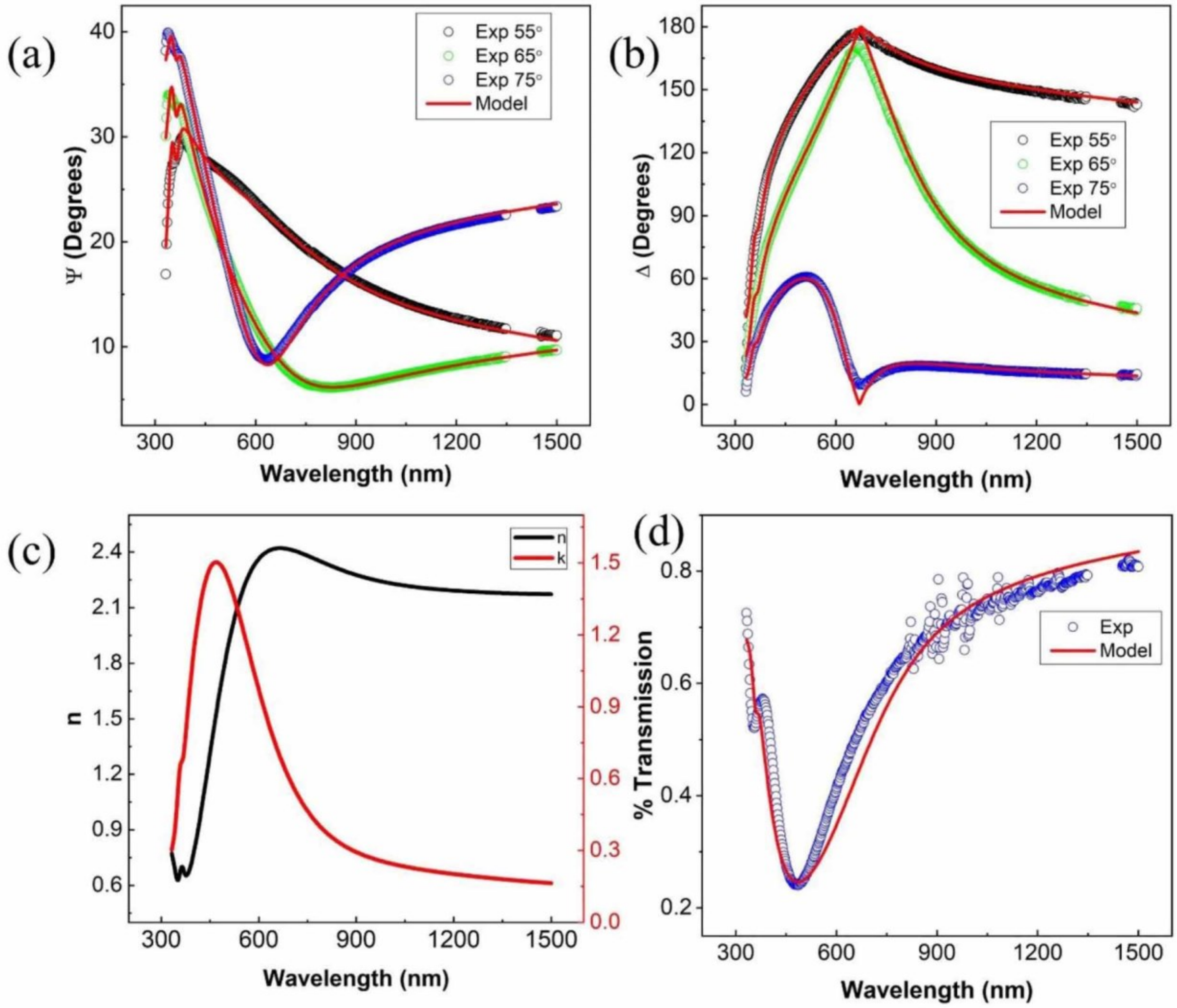

Figure 4.5. (a)–(b) ψ, Δ data values for Ag films annealed at 150°C. (c)–(d) Corresponding optical constants (n, κ) and the predicted transmission spectra for Ag films annealed at 150°C.

4.3.4 Plasmon-enhanced SERS of R6G

Plasmonic substrates can provide for strong ensemble-averaged electric field enhancements that are highly beneficial for applications in molecular sensing involving the detection of specific peaks in the Raman spectra of target analytes. The potential of our plasmonic Ag nanoisland substrates was tested by considering SERS of R6G molecules drop-coated onto the annealed plasmonic substrates.

R6G has often been used extensively to probe SERS effects. It is a highly recalcitrant textile dye, often used for coloring cotton, wool, silk, and paper. R6G is unfortunately associated with toxicity, carcinogenicity, mutagenicity, and teratogenicity in cells, tissues, and organisms.[255] Further studies have also demonstrated that water holding R6G dyes can cause allergic dermatitis, and irritation of the eyes, skin, and respiratory system while dealing severe damage to retinal cells.[256] Thus, finding an appropriate means to detect R6G for varying concentrations is of great importance. It is particularly ideal in testing the as-fabricated Ag films as it is an extremely strong fluorophore upon excitation by visible light making it ideal as a probe for our Ag films that exhibit primary and secondary plasmon resonances within the visible light regime. In general, for single molecule detection the Raman signal of R6G is not observed except with near-infrared radiation, but in the case of SERS the strong adsorption of R6G to the plasmonic noble metal surface results in strong quenching of this fluorescence and a strong, and enhanced Raman signal.[257,258]

Varying molar concentrations between 10^{-2} M–10^{-10} M of R6G were utilized. For reference, Raman spectra of bare R6G thin coatings on glass were also collected providing a comparative study of Raman signal amplification due to plasmonic enhancement of the local electric fields of the Ag nanoislands. The corresponding wavenumbers for R6G Raman peaks are 609 cm^{-1}, 785 cm^{-1}, 934 cm^{-1}, 1137 cm^{-1}, 1204 cm^{-1}, 1303 cm^{-1}, 1357 cm^{-1}, 1433 cm^{-1}, 1508 cm^{-1}, 1572 cm^{-1}, and 1647 cm^{-1}.[258]

R6G exhibits an excitonic absorption peak at ~530 nm, with a sharp drop-off in absorption at ~ 555 nm. Therefore, 532 nm excitation fulfills the resonance Raman condition. Comparative Raman spectra of the bare R6G samples and R6G coated Ag nanoisland samples (formed by annealing at 150°C and 400°C) were obtained for excitation wavelengths of 532 nm and 633 nm, to consider the response of the plasmonic substrates under resonant and off-resonance excitations. For the sake of brevity, we will mainly consider SERS results involving R6G concentrations between 10^{-6}–10^{-10} M. **(Figure 4.6)** presents the corresponding Raman spectra for R6G coated Ag films annealed at 150°C at excitation wavelengths of 532 nm and 633 nm, and **(Figure 4.7)** presents the same for R6G coated Ag films annealed at 400°C.

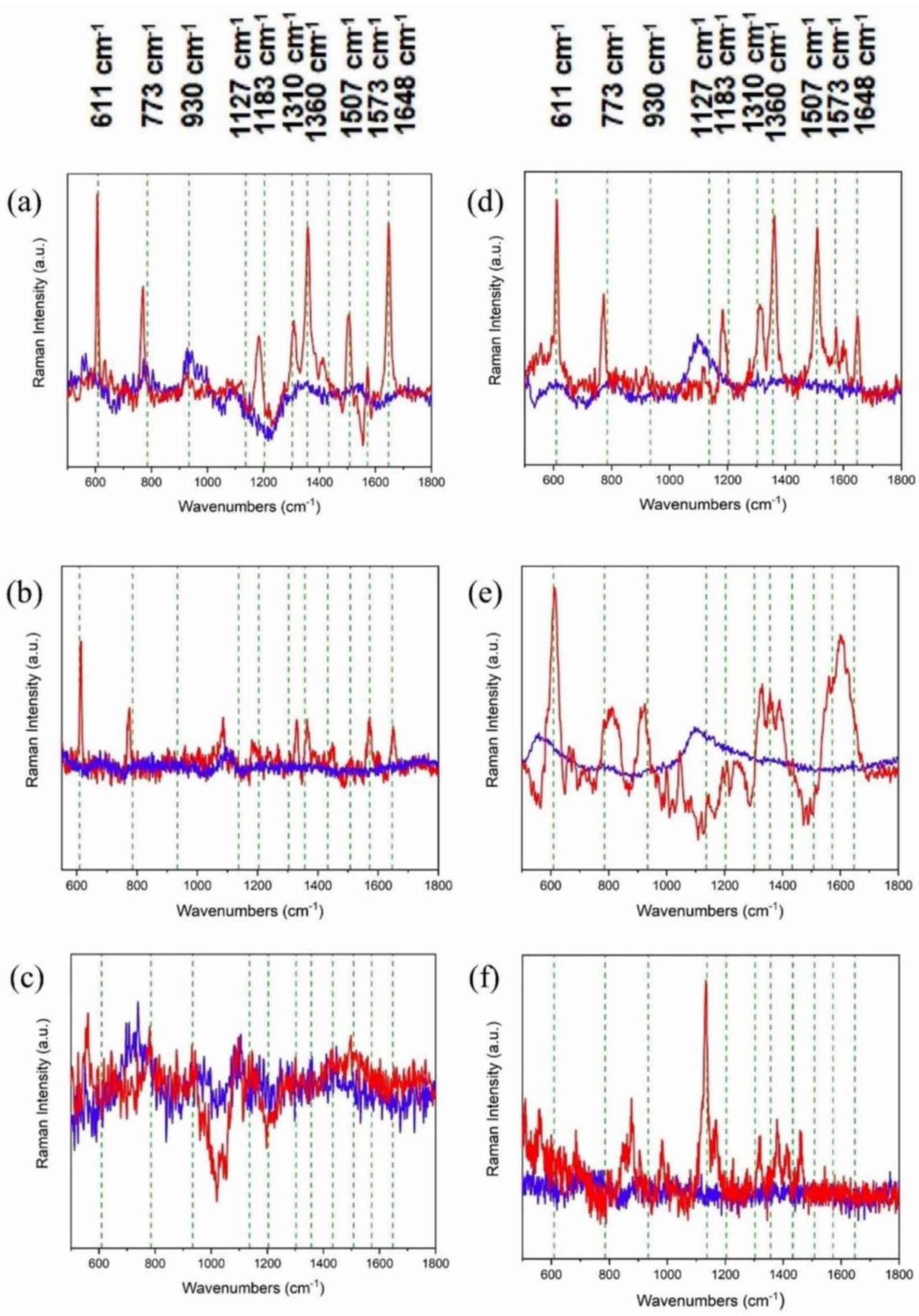

Figure 4.6. (a)–(c) Raman spectra for Ag films annealed at 150°C and drop-coated with R6G molecules of concentration (a) 10^{-6} M, (b) 10^{-9} M, and (c) 10^{-10} M. The samples were excited with laser wavelength of 532 nm. (d)–(f) Raman spectra for the same films under excitation with laser wavelength of 633 nm. The red curves correspond to those of Ag@R6G samples while the blue curves correspond to bare R6G samples of the same concentration. Corresponding wavenumbers for R6G Raman peaks are highlighted by vertical, green transition lines.

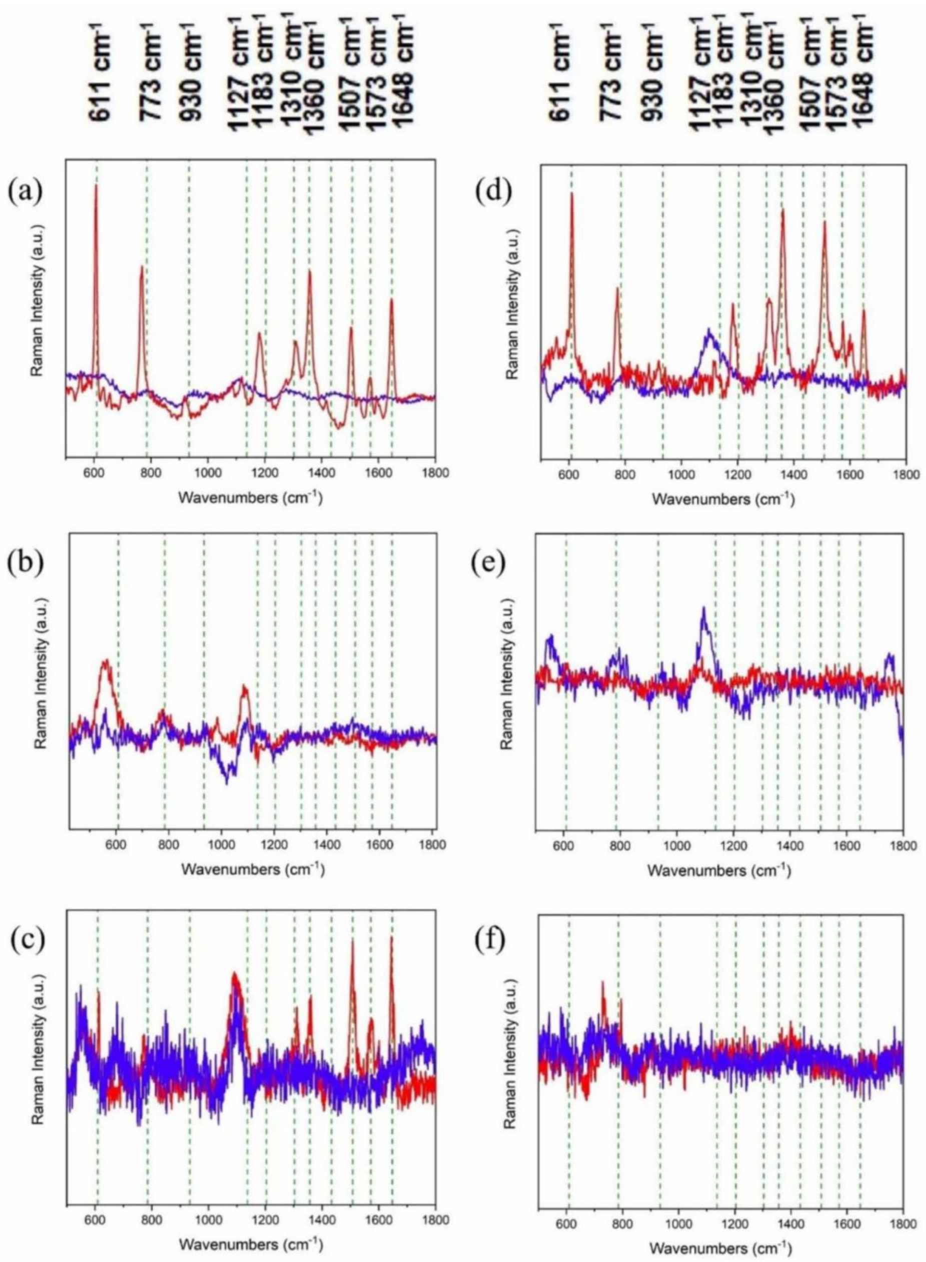

Figure 4.7. (a)–(c) Raman spectra for Ag films annealed at 400°C and drop-coated with R6G molecules of concentration (a) 10^{-6} M, (b) 10^{-9} M, and (c) 10^{-10} M. The samples were excited with laser wavelength of 532 nm. (d)–(f) Raman spectra for the same films under excitation with laser wavelength of 633 nm. The red curves correspond to those of R6G samples on Ag nanoisland while the blue curves correspond to bare R6G samples of the same concentration on glass substrates. Corresponding wavenumbers for R6G Raman peaks are highlighted by vertical, green transition lines.

It is seen in **(Figure 4.6f)** that for the 150°C annealed Ag nanoisland samples stimulated by the 633 nm laser, the 1127 cm^{-1} Raman mode is clearly visible and has significant intensity versus the background signal event at R6G concentration of 0.1 nM. It is well-established that only 0.1%–1% of Ag NPs in an ensemble are optically hot, and only 0.01% of the surface sites on an optically hot NP exhibit significant electromagnetic field enhancement.[259] Therefore, the identification of Raman signal amplification at R6G molar concentrations of 0.1 nM for Ag nanoisland ensembles formed through 150 °C thermal treatment without recourse to lithography or templating is of particular significance. It is understood that the Raman spectrum under SERS conditions is affected by the localized surface plasmon resonance of the Ag nanoislands which are typically wavelength dependent.[260,261] Consequently, different parts of the Raman spectrum experience different amplification intensities in an effect that can be considered dependent on the dispersion of the underlying resonance that is producing the electromagnetic enhancement. This can also be explained by referring to the chemical structure of R6G. Different peaks of R6G are most prominent at different concentrations and dilutions. This has to do with orientation. For a concentrated film of R6G, the benzene rings stack vertically. For dilute solutions, there is more room for the rings to lie horizontally on the substrates. The coupling of R6G to Ag (the phonon coupling) is stronger (a ring-phonon mode) when it is lying flat on the Ag substrate as opposed to vertically standing. There are also intermediate cases where it is either of both. R6G aggregation is also dependent on concentrations to a certain degree with single monomers interacting with an Ag surface at dilute solutions, and dimers at higher concentrations. It has also been noted that the vibronic coupling of higher frequency modes of R6G to the 0–1 transition results in higher frequency modes demonstrating more intense Raman signals under visible light radiation around 514.5 nm compared to that of low-frequency modes.[258] In general, it has also been observed that off resonant excitation (633 nm) results in Raman enhancements lower in intensity in all bands, thus requiring the employment of higher laser intensities in compensation.[81] Altogether, these results demonstrate the synergistic effects of Ag induced plasmonic enhancement, and the potential of these Ag nanoislands as efficient SERS sensing substrates. The higher efficacy in generating adequate Raman signal enhancement during off resonance 633 nm excitation in comparison to 532 nm resonant excitation of the Ag nanoisland-R6G system is in line with reports of Au nanorods showing maximum Raman enhancement for a plasmon resonance blue-shifted from the laser excitation wavelength.[262]

Although plasmon-enhanced SERS of R6G has been reported for diverse plasmonic nanostructures including stars,[263] pyramids,[264] and cubes,[265] the novelty of these nanoisland substrates is directly related to the facile means utilized to fabricate the nanostructures as well as their consistency in high quality optical properties and high-performance SERS results. In particular, the plasmon resonances of these Ag nanoisland substrates provide a mix of both high-quality factors and suitable wavelengths of absorption. This contrasts with other plasmonic nanostructures such as cubes, dendrites, and stars where there are two extremes of resonances: broad or narrow. The resultant electromagnetic field enhancements in plasmonic nanostructures are greatly influenced by the geometry of the nanostructure being utilized.[19,46] Nanoislands, thanks to their hemispherical structure and elongated curvature, provide for a uniform electromagnetic enhancement reflected by their wide absorption profiles making them suitable for SERS testing of various dyes. In contrast, the aforementioned nanostructures and others such as bipyramidals,[266] and shurikens[267] where the electromagnetic enhancements are restricted to the sharp tips of the nanostructure result in narrow absorption profiles that limit the applicability of said plasmonic nanostructures for SERS studies of specific dyes where the absorption profiles match the absorption wavelength of the relevant dye. The wet-chemical methods used to synthesize said nanostructures also make it more difficult to provide for consistent results in fabrication, and device testing. This reinforces the potential applicability of the nanoislands fabricated in this work as efficient plasmonic substrates for plasmon-enhanced photocatalysis.

4.3.5 Plasmon-enhanced photocatalytic transformation of aromatic thiols

Surface catalytic reactions of 4-nitrobenzenethiol (4-NBT) and p-aminothiophenol (PATP) to p,p'-dimercaptoazobenzene (DMAB) by surface-enhanced Raman spectroscopy have been demonstrated by Sun et al.[268] and You et al.[269], respectively. In this current work, these thiols are used as candidates to demonstrate the potential of plasmonic substrates consisting of Ag nanoislands for plasmon-enhanced thiol photoreduction. Much like R6G, 4-NBT and PATP are both azo dyes/compounds commonly used in the chemical/textile industries and have detrimental effects on the environment. Thus, means toward degradation of these compounds is an essential environmental initiative. The fabricated Ag nanoislands samples were drop-coated with the respective 4-NBT and PATP thiol solutions. The SERS spectra of 4-NBT and PATP are well documented, with the signature Raman peak of 4-NBT at 1330 cm^{-1} and the signature Raman peaks of PATP at 1080 cm^{-1}, 1144 cm^{-1}, and 1190 cm^{-1}. The Raman spectra of the product (DMAB) are characterized by two modes at 1390 cm^{-1} and 1430 cm^{-1}.

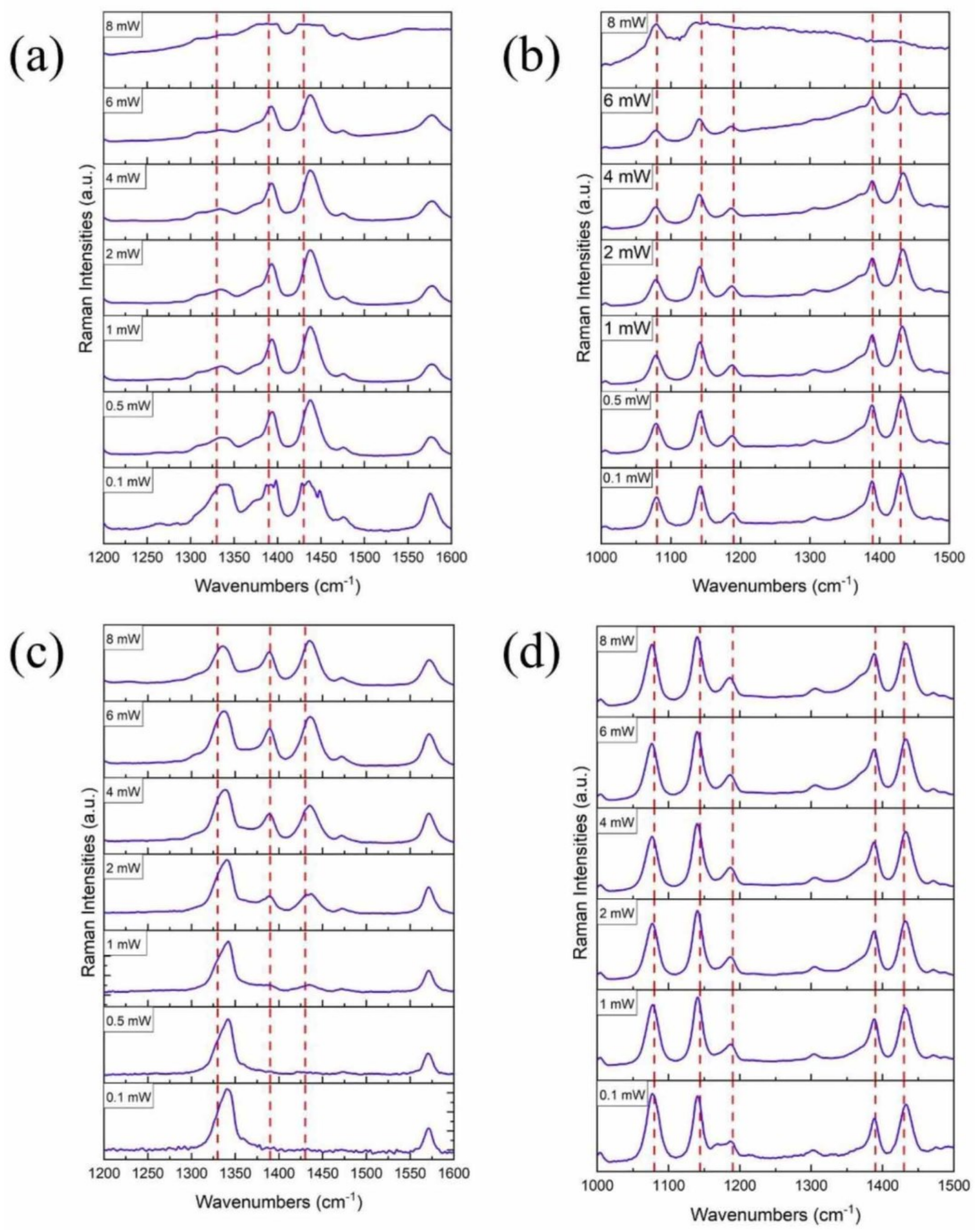

Figure 4.8. Raman spectra on thiol photoreduction results for Ag films annealed at 150°C for increasing laser power from 0.1 mW to 8 mW. The corresponding Raman peaks of 4-NBT, PATP, and DMAB are identified via red, vertical transition lines. (a)–(b) For laser excitation wavelength of 532 nm, Raman spectra of Ag@4-NBT and Ag@PATP, respectively. (c)–(d) For laser excitation wavelength of 633 nm, Raman spectra of Ag@4-NBT and Ag@PATP, respectively.

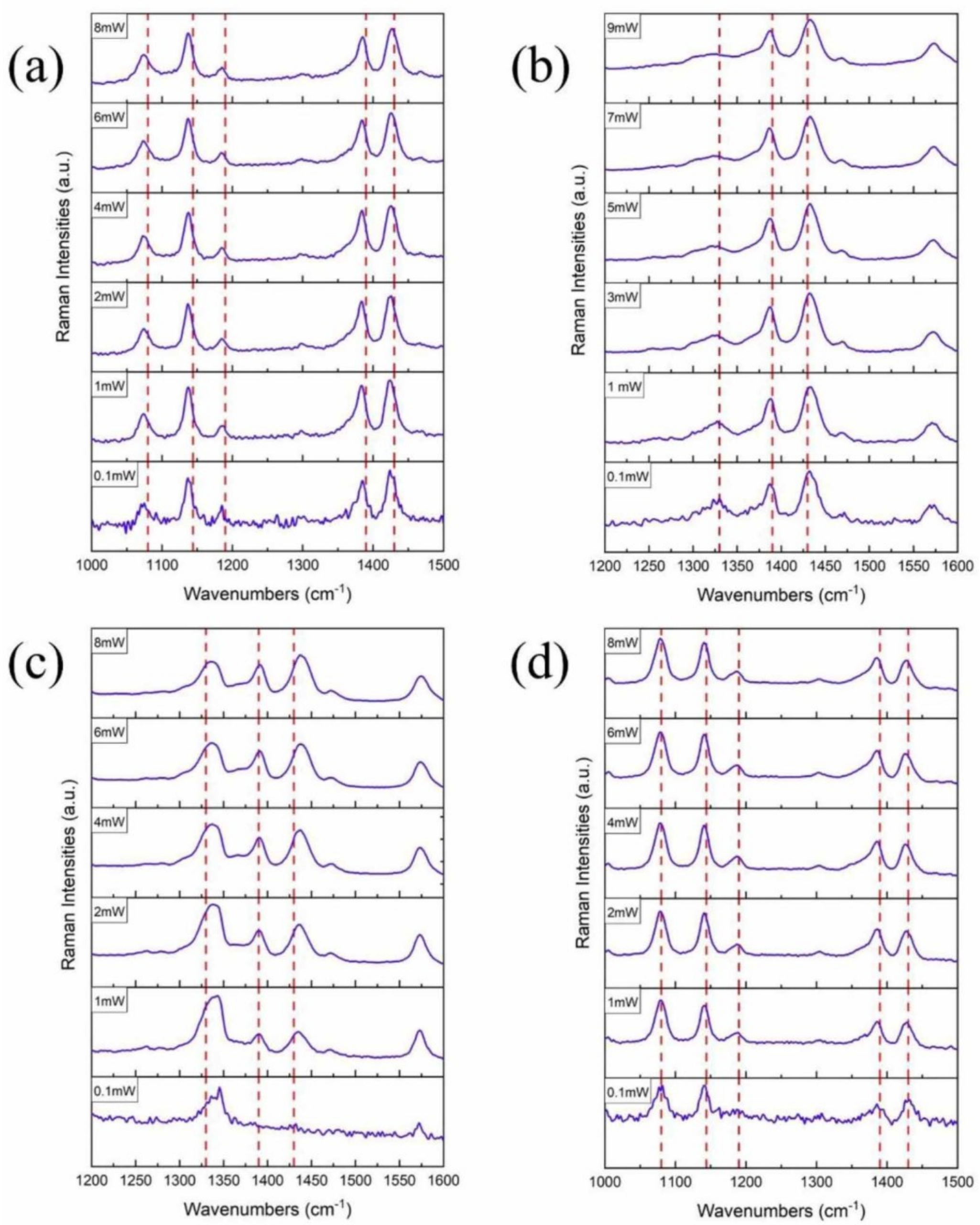

Figure 4.9. Raman spectra on thiol photoreduction results for Ag films annealed at 400°C for increasing laser power from 0.1 mW to 8 mW. The corresponding Raman peaks of 4-NBT, PATP, and DMAB are identified via red, vertical transition lines. (a)–(b) For laser excitation wavelength of 532 nm, Raman spectra of Ag@4-NBT and Ag@PATP, respectively. (c)–(d) For laser excitation wavelength of 633 nm, Raman spectra of Ag@4-NBT and Ag@PATP, respectively.

By varying laser power between 0.1 mW to 8 mW for laser excitation wavelengths of 532 nm and 633 nm, the evolution of the Raman peaks for 4-NBT, PATP, and their product DMAB can be monitored through a decrease in Raman intensities of the reactants and a concomitant increase in the Raman intensities of the product DMAB in our plasmonic substrates as presented in **(Figure 4.8)** and **(Figure 4.9)**. Ag nanoislands formed by the thermal annealing of Ag thin films at both 150°C and 400°C demonstrate effective photoreduction of 4NBT and PATP to the product DMAB.

SERS synthesis of DMAB from 4NBT and PATP is achieved via catalytic coupling of the Ag nanoislands. Prior research has proven that the six strongly generated vibrational modes of the two molecules are enhanced by the plasmons from the noble metal nanoparticles.[268,270] The catalytic mechanisms behind the photoreduction and photooxidation of 4NBT and PATP respectively to DMAB have been explored in various works.[271,272] In both cases, plasmonic hot carriers provide the relevant kinetic energy to overcome the reaction barrier for dissociation, and electrons for photodissociation. Apart from the generation of hot electrons, enhanced dissipation of thermal energy (via hot spots), and increased scattering also serve to enhance the above reactions. Considering the monometallic system of Ag nanoislands, it can be surmised that the conversion of 4NBT and DMAB (requiring four electrons) is accomplished through hot electrons (generated via plasmon decay) with high enough kinetic energy to drive the reaction.[273]

Similar mechanistic insights have been demonstrated by Zhang et al.[274] for the conversion of PATP to DMAB confirming that the plasmonic excitation of the Ag nanoislands results in the generation of hot electrons that transiently occupy empty states above the Fermi level while leaving hot holes below the Fermi level of Ag (−4.3 eV vs. vacuum). These hot electrons are of insufficient energy to be injected to the lowest unoccupied orbital of PATP but can be transferred to the $2\pi^*$ orbitals of $^3O_2$ adsorbate to form $^2O_2^-$. The short lived $^2O_2^-$ species can then react with the chemisorbed PATP initiating the coupling reaction. The leftover electron rapidly recombines with the hole in the plasmonically excited Ag nanoisland, preventing Ag oxidization. The photocatalytic coupling of PATP is altogether quite complex but two major rate-determining steps have been identified: (1) The photoactivation of interfacial oxygen through the injection of plasmonic hot electrons from Ag to surface-adsorbed O_2, and (2) The rate-limiting step of the photoactivated oxygen reaction with the surface-adsorbed PATP to initiate oxidative dehydrogenation and azo-coupling reactions to form DMAB.[274]

Ag nanoislands constitute the source and sink for the generated hot electrons and holes via the excitation of the plasmonic resonance using laser light at 532 nm (on resonance), and 633 nm (off resonance). In both cases, it is notable that conversion of the thiol compounds to their DMAB products have been observed. The plasmon generated hot electrons provide electrons for the reactions but also convert the resultant kinetic energy into thermal energy for the molecules to overcome the reaction barrier. By increasing the laser power intensities, the probability of the plasmon driven catalytic reactions is further enhanced, as indicated by the corresponding reduction in reactant peaks.[156,275] The study of these DMAB reactions and their evolution is a continuing study with various mechanisms proposed for the appropriate plasmonic systems.[268,272,276]

In comparing the two samples, a basic calculation of peak-to-peak conversion ratios for the relevant products and reactants shows that Ag films annealed at 400°C provide for better and greater conversion efficiencies in comparison to the Ag films annealed at 150°C for both laser excitation wavelengths (532 nm and 633 nm). A representative calculation of the peak to peak conversation ratios for Ag@4-NBT at 532 nm wavelength excitation shows that for Ag films annealed at 400°C **(Figure 4.9a)** we have a conversion efficiency of almost 99% (for 4-NBT:DMAB peaks at 1330 cm^{-1}:1390 cm^{-1}) and almost 99% (for 4NBT:DMAB peaks at 1330 cm^{-1}:1430 cm^{-1}). Meanwhile the same peak conversion ratios for Ag films annealed at 150°C **(Figure 4.8a)** results in a conversion efficiency of 70% (for the 4-NBT:DMAB peaks at 1330 cm^{-1}:1430 cm^{-1}). Similar trends are observed for the cases of excitation under 633 nm wavelength, and for the photooxidation of PATP to DMAB. For the laser intensities considered, it has been observed that the morphology of the Ag nanoislands experience no change. This has also been reported by Zhang et al.[274] Extinction spectra of the samples before and after Raman illumination have been presented in **(Figure S7).** Additionally, bare samples of 4NBT and PATP under the highest intensity of laser-light illumination (10 mW) demonstrate no evidence of the production of DMAB providing further proof of the plasmon-enhanced photocatalytic transformation of these aromatic thiols using Ag nanoislands. **(Figure S8)**

Time-resolved Raman spectroscopy would best assist in obtaining detailed information on the timescales of the hot charge carrier dynamics that facilitate these thiol-photoreduction reactions. In what is essentially a pump-probe spectroscopy approach, a pump could be utilized to conduct the relevant thiol reaction while a probe is utilized to analyze the product DMAB absorption. With various delays between the pump and probe, one can observe when the probe beam is strongly absorbed, following which the appearance and evolution of the DMAB peak can provide a timestamp of the reaction's dynamics. With consideration of the conventional timescales observed of hot carrier dynamics, one would expect absorption to be facilitated in 100 fs with the product DMAB peaks being evident in the picosecond timescale. Other time-resolved spectroscopic methods such as two-photon photoelectron spectroscopy could also provide greater insights into the time-dependent behavior of plasmon-enhanced thiol photoreduction reactions.

4.4 Closing Remarks

Using a combination of magnetron sputtering followed by thermal annealing, at two different temperatures of 150°C and 400°C, Ag nanoisland plasmonic substrates were fabricated. The 150°C annealed samples showed a strong dipole resonance at 2.61 eV and a sharp peak at 3.51 eV. The dipole resonance was fit to a typical Voigt profile with clear contributions from both homogeneous and inhomogeneous broadening. The slightly asymmetric resonance at 3.51 eV was explained to be a hybrid quadrupole resonance consisting of contributions due to a breakdown of the quasistatic approximation (owing to larger particle sizes of 50 – 200 nm), island shape and high index substrate (breaking symmetry), interparticle interactions and the close-lying bulk (volume) plasmon resonance. The 400°C annealed samples showed a clear quasi-spherical morphology with a strongly redshifted strong dipole resonance at ~ 2.25 eV, and a twin-peaked feature at shorter wavelengths. Somewhat unusually, the dipolar plasmon resonance exhibited nearly perfect Lorentzian line shape indicating a minor contribution from inhomogeneous broadening. Our interpretations of the optical spectra were validated by FDTD simulations of isolated and arrayed hemispherical islands, which closely resembled the experimentally measured spectra. Ellipsometric analysis was used to determine the thickness and optical constants of the composite Ag nanoisland-air films. Extraction of the wavelength dependent n and k values of the Ag nanoisland films enables facile description, prediction, and exploitation of the macroscopic optical properties of Ag nanoisland ensembles in photovoltaic devices, photocatalysts, and sensors.

Device testing of these Ag nanoisland plasmonic substrates involved studies of SERS of R6G drop casted onto the plasmonic substrates for diverse concentrations from $10^{-2} - 10^{-10}$ M where samples annealed at 150°C showed a detection of the vibrational modes of 0.1 nM R6G for 633 nm excitation. The potential of Ag nanoisland films in plasmonic catalysis was demonstrated through the photocatalytic transformation of aromatic thiols, namely 4-NBT and PATP into DMAB at on- and off-resonance conditions.

Chapter 5
Bimetallic Plasmonic Photocatalysis

5.1 Introduction

Over the recent decade, plasmonic photocatalysis has emerged as a promising pathway for promoting chemical reactions through the excitation of collective charge density oscillations in metal nanoparticles (NPs).[277] Plasmonic noble metal NPs such as gold (Au) and silver (Ag) interact strongly with incident electromagnetic radiation due to the localized surface plasmon resonance (LSPR) phenomena resulting in enhanced absorption and the ability to harvest light in nanoscale volumes.[39,54,278–280] The LSPR excitation, as observed in Chapter 4, can dephase radiatively through the emission of a photon or non-radiatively by the generation of a transient population of non-equilibrium excited charge carriers or hot electrons. These photoexcited electrons can be transferred directly to adsorbed reactant molecules or elevate the temperature of the nanoparticle by releasing their energy in the form of heat.[281–283] Enhanced photothermal effects increase the overall kinetics of chemical reactions. Increased photonic radiation helps enhance local chemical reactions such as photodegradation, photoisomerization, and light collection.[100,281] Hot electrons promote metal-adsorbate systems to an excited state effectively allowing for lowered activation energy barriers.[282,284] Thus, plasmonic noble metal NP photocatalysts can be utilized to exploit and increase the reaction rates and product selectivity of numerous industrial and environmentally relevant reactions under relatively mild conditions.[95,281,293,285–292]

Traditional plasmonic noble metals such as Au, Ag, Cu, etc. are highly attractive as their LSPRs can be tuned along the visible to near-infrared spectrum where solar irradiation is strongest. Further tuning of the LSPR can be facilitated by modifying the morphology, size, and dielectric environment of the nanoparticles.[64,277,294] A central limitation in the wider application of plasmonic photocatalysis is its restriction for facilitating chemical transformations on the surfaces of inert plasmonic noble metals. A simple solution to this is facilitated by the integration of a plasmonic metal with another metal that has high catalytic activity for the desired chemical reaction.[134,295,296] The inclusion of the second metal has been demonstrated to create new active sites for chemical reactions as well as provide additional pathways to assist in charge separation and improved photocatalytic activity.[20] Composition and morphology, to a large part, dictate the properties of plasmonic nanomaterials.[297–299] The synthesis of bimetallic heterostructures inherently involves the modification of these two fundamental properties to develop nanomaterials that provide enhanced catalytic activity and selectivity,[300,301] fine tuning of optical properties (absorption, scattering etc.),[302] and other applications in various fields spanning electronics and medicine.[303–305] Recent studies have adopted the development of plasmonic bimetallic heterostructures to facilitate for enhanced charge heterogeneity, and separation of plasmon-generated hot electrons and holes with improved photocatalytic activity compared to their monometallic plasmonic counterparts.[18,61,288]

The synthesis of plasmonic bimetallic heterostructures of diverse morphologies has been achieved through various means including wet chemical synthesis, sono-chemical synthesis, photochemical synthesis, microwave synthesis, sputter deposition, electroless plating, and electrochemical synthesis.[299] Three bimetallic heterostructures commonly recognized in the field include: core-shell, random, or separated structures. **(Figure 5.1)** Depending on the synthesis technique utilized, the distribution and organization of each metal can be varied to develop these three bimetallic heterostructures.[306] These inherent structural differences significantly alter the plasmonic properties of the bimetallic complex.

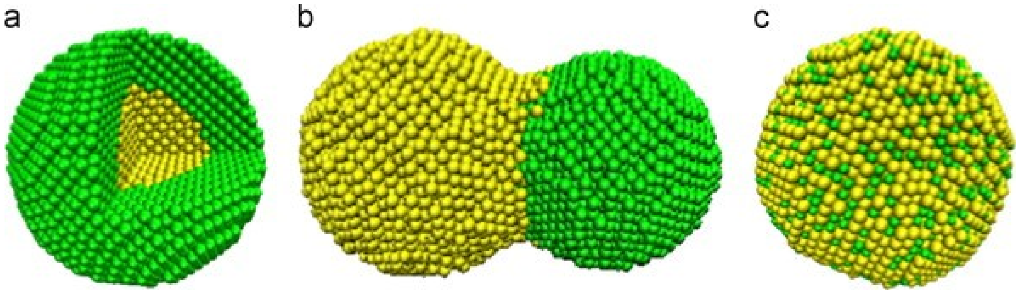

Figure 5.1. Bimetallic heterostructures: (a) Core-Shell, (b) Separated, and (c) Random. Reprinted for academic use from Ref.[307] Copyright Elsevier (2013).

In the case of bimetallic core-shell structures, Mie theory demonstrates that the plasmon resonance can be tuned between the UV and mid-IR region by varying the ratio of shell thickness to the overall size of the bimetallic nanoparticle.[54] The solutions to Maxwell's equations can be translated to a bimetallic system where it has been shown that an interfacial plasmon mode can exist at the boundary between two metals.[308] In a bimetallic system involving two different metals, we are looking at two samples of different electron densities and thus different plasma frequencies. Stern et al.[308] have shown that the plasma resonance frequency at the bimetallic interface is given by,

$$\omega = \left(0.5\left(\omega_p^2 + \omega_p'^2\right)^{1/2}\right) \tag{5.1}$$

where ω_p retains the classical plasma frequency while ω_p' represents the plasma frequency based off the dielectric constant calculated at the interface of the two metals.[309] For bimetallic structures, the dielectric function utilized is a weighted linear combination of the dielectric constants of the constituent metals. This is to account for the fact that noble metals such as Au and Ag are not purely free electron materials and that interband contributions must be considered at certain wavelengths.[310] The most interesting property of bimetallic nanoparticles that arises from this theory is their ability to tune their plasmon resonances across a wide range of the electromagnetic spectrum. Theoretical simulations by Zhang et al.[311] have shown that the surface plasmon resonance in bimetallic core-shell nanoparticles involving Au@Pt and Au@Pd nanoparticles can occur in the visible regime with high tunability by changing the core to shell size ratios. Experimental confirmations of the same have been made by Gao et al.[312] who have demonstrated tunable plasmon resonances of Ag-Pt bimetallic nanoparticles where the amount of precursor H_2PtCl_6 used in the fabrication of the particles redshifts the LSPR peaks of the bimetallic structure. Many other groups have demonstrated similar shifts with bimetallic nanoparticles with functional dependencies on morphology and composition.[61,157,313]

Bimetallic nanoparticles offer a solution to this problem whereby the combination of plasmonic noble metals with catalytic transition metals such as Pt, Pd, Rh, Ru, etc. an ideal photocatalyst with optical properties of the plasmonic metal and the reactive properties of the catalytic metal can be realized. These bimetallic nanostructures are largely fabricated in the form of antenna-reactor,[314,315] core-shell,[277] or alloy structures,[20,316,317] and compared to their monometallic counterparts have demonstrated greater optical sensitivity,[286,288] product selectivity,[295,314] and increased reaction rates[157,318–320] for diverse chemical reactions compared to their monometallic counterparts.[281]

Here, we investigate the properties of Au@Pt core-shell nanoislands as promising candidates for plasmonic photocatalysis. Catalytic metals such as Pt, have a weak optical response in the visible, and strongly absorb in the UV regime. The addition of an Au core, as a plasmonic antenna, and thin shells of Pt, as catalytic layers, help develop a bimetallic photocatalyst retaining the optical behavior of the plasmonic metal and reactive behavior of the catalytic metal for catalytic applications beyond the boundaries of its constituents.[277,284,321] Building on the methods utilized in constructing our monometallic Ag nanoislands, a combination of magnetron sputtering and thermal annealing is once again used to form hemispherical Au@Pt core-shell nanoislands on glass substrates in a facile process that is less time-consuming while providing greater consistency compared to wet-chemical or colloidal synthetic techniques.[322] The choice of an Au core was to take advantage of an even more suitable plasmon resonance in the visible regime (compared to Ag) as well as to offset for the lack of stability of Ag as a generally oxidative metal. The bimetallic architecture of an Au core and a Pt shell was also decided as major experiments involving R6G sensing or CO_2 photoreduction with Au nanoislands do not demonstrate the same level of efficacy as Ag nanoislands due to their limited adsorption of these molecules.[323,324] The addition of Pt thin shells for varying durations of deposition provides insights in modulating the plasmonic behavior of the core-shell composite and is observed to directly influence the use of these plasmonic substrates for efficient dye degradation of methylene blue (MB). Raman thermometry studies of the Stokes and anti-Stokes surface-enhanced Raman scattering (SERS) intensities of the bimetallic-adsorbate system clarify the microscopic mechanism of the excitation and the flow of energetic charge carriers in a Dissociated Induced Electron Transfer (DIET) process between the plasmonic and adsorbate systems.[93,121] This analysis provides us a direction of control of the charge excitation and transfer process that may be explored using interfacial and local electric field engineering strategies.

Preliminary knowledge on the plasmonic substrates is obtained via FDTD simulations on the electromagnetic response characteristics and the influence of morphology on the overall behavior of the macroscale structure. Density functional theory simulations have also been utilized, with the assistance of collaborators Sergey Gusarov and Alex Kobryn at NINT, to explore the influence of chemical and interfacial characteristics of the Au@Pt core-shell substrates.

Although it is favorable to provide for semiconducting scaffolds in conjunction with plasmonic substrates, these studies, overall, demonstrate the versatility of the method utilized to synthesize these bimetallic structures, their standalone potential as promising nanostructures for plasmon-driven catalytic reactions and chemical conversion, all the while permitting for facile incorporation in semiconductor scaffolds.[93,322,325]

5.2 Materials and Methods

5.2.1 Fabricating Bimetallic Au@Pt Nanoislands

The growth of bimetallic core-shell Au@Pt nanoparticles was achieved using direct current magnetron sputtering of 99.9% pure Au on glass substrates. The Au films were thermally annealed in a furnace to form hemispherical nanoislands upon which 99.9% pure Pt films were subsequently sputter deposited to complete the core-shell structure. Prior to deposition, the glass substrates were cleaned via ultrasonication in methanol for 20 min. For direct current magnetron sputtering of Au and Pt, the vacuum chamber was evacuated to a base pressure of 10^{-6} Torr, and then filled with argon gas to maintain a constant pressure of 7×10^{-3} Torr during sputtering. Thin films of Au were deposited at room temperature for 40 s at a rate of 75 W, and subsequently subjected to thermal annealing at 400^{0}C. A one-hour ramping procedure and a 15-minute dwell cycle was used. Annealing was performed in open-air conditions, and post-annealing, the samples were left to cool at room temperature. The as-formed Au hemispherical nanoislands were then sputtered with thin films of Pt deposited at room temperature for varying durations from 10-30 s at a rate of 75 W. The bimetallic samples exhibited a pale pink-grey hue.

5.2.2 Characterization

Transmission spectra of the bimetallic Au@Pt films were measured using a Perkin Elmer Lambda 1050 UV-Vis-NIR Spectrophotometer. Surface morphology of the films was studied using a Hitachi S-4800 field emission scanning electron microscope (FE-SEM). ImageJ software from the National Institutes of Health (NIH) was utilized to obtain size distributions of the bimetallic nanoislands. Corresponding histogram plots were fit to Gaussian distributions to determine the average size of nanoislands, their standard deviation, and polydispersity (the percent ratio of standard deviation to average size). Chemical composition and binding energy studies of Au and

Pt in pristine and core-shell morphologies were determined using X-ray photoelectron spectroscopy (XPS) on an Axis-Ultra, Kratos Analytical XPS equipped with a monochromatic Al-Kα source (15 kV, 50 W) and photon energy of 1486.7 eV operating under ultrahigh vacuum of ~ 10^{-8} Torr. Binding energies of all constituent elements were referenced using the binding energy of C-1s ≈ 284.8 eV as a standard. Acquired raw data files were deconvoluted into various peak components using CasaXPS software and were subsequently plotted. Ultraviolet photoemission spectroscopy (UPS) was performed using the same tool to determine the work functions of pristine Au, Pt, and Au@Pt systems where a He lamp of 21.21 eV was used as an excitation source. Glancing angle X-ray powder diffraction (XRD) spectra of pristine Au, Pt, and Au@Pt systems were collected on a Bruker D8 advance diffractometer with a radiation source of Cu X-ray tube (Cu-Kα, $I_{\mu}S_{\mu}$, $\lambda = 0.15418$ nm) operating at 50W. This tool is equipped with a 2D detector (VANTEC-500). The average crystallite sizes of the pristine Au, Pt, and Au@Pt substrates are derived using the Debye-Scherer formula,[326,327]

$$D = \frac{k\lambda}{\beta cos\theta}, \tag{5.2}$$

where $k = 0.9$ and is the Scherrer constant, λ corresponds to the wavelength of the X-ray source, β is the FWHM (radians), and θ is the peak position (radians). The residual microstrains ξ of pristine Au, Pt, and Au@Pt substrates are calculated using a single line approximation method leading to the following relation,[328]

$$\xi = \frac{\beta}{4tan\theta}. \tag{5.3}$$

5.2.3 Lumerical FDTD Simulations

Lumerical Nanophotonic FDTD solutions was used to model and simulate the optical and near-field electromagnetic response properties of core-shell Au@Pt nanostructures. The simulations were performed for various arrayed bimetallic Au@Pt nanostructures on a glass substrate. 2-D and 3-D Maxwell solvers and monitors based on the FDTD method for complex geometries were used to determine optical quantities such as absorption spectra as well as near and far-field electric field profiles. Material data for Au and Pt was provided in Lumerical FDTD simulations and are sourced from Palik et al.[235] A light source of bandwidth range 300 - 800 nm was incident upon the bimetallic nanostructures at a normal angle from above. Lumerical's in-built refractive index monitor was utilized to confirm the bimetallic nanostructures were appropriately configured and modeled throughout the course of the simulations. Symmetric and anti-symmetric boundary conditions were utilized for both sets of simulations involving arrayed nanostructures to capitalize on the symmetrical nature of the system, and further shorten simulation time. The relevant results were compared with experimental data obtained through characterization and morphological studies to provide further insights into the electromagnetic field responses and optimization of the plasmonic substrates. The simulations also provided a preliminary confirmation of the core-shell structures of the plasmonic substrates via the matching of plasmonic modulation behavior observed for varying Pt shell thicknesses.

5.2.4 Density Functional Theory (DFT) Studies

Density functional theory (DFT) studies were performed on the bimetallic substrates for greater insights into interfacial intermetallic effects, and plasmonic coupling. The bimetallic structure building prior to density functional theory-based quantum chemical calculations was done following XRD data analysis. As displayed in **(Figure S9)**, the sputtered bare Au and Pt films showed crystal planes of typical fcc phase.[329] In the bimetallic Au@Pt system, only Au planes are visible, indicating possible lattice matching during sputter-deposition of the Pt shell atop the Au substrate. For the bare Pt, it is observed that all corresponding fcc planes have slightly lower d-spacings compared to fcc planes of bare Au. Another possible reason for non-visibility of Pt planes arises from the fact that the sputtered Pt films are quite thin in nature ranging between 1-3 nm in thickness. Thus, a lattice-matched dominant plane (111) for the hybrid system was constructed using *Materials Studio* software in both far and close configurations. DFT calculations were performed using *OpenMx 3.9.2* (Open source package for Material eXplorer) package,[330] where norm-conserving pseudopotentials[331] and pseudo atomic localized basis functions[330] were used. Generalized gradient approximation (GGA)[332] with Perdew–Burke–Ernzerhof (PBE) exchange-correlation functional was employed in all the computations with consideration of periodic boundary conditions and spin polarization. The threshold for convergence criterion and energy cut-off value for self-consistent loop was set to be as low as 10^{-5} and 220 eV respectively. Highest occupied molecular orbital (HOMO) and lowest unoccupied molecular orbital (LUMO) were generated using VMD (visual molecular dynamics) visualization software. Projected density of states (PDOS) plots were obtained using Gaussian broadening method, where the broadening parameter was 0.08 eV.

5.2.5 Methylene Blue dye degradation and photocatalytic studies

Photocatalytic potential of the bimetallic Au@Pt core-shell nanoislands was probed through degradation of 5 ppm concentrations of aqueous MB blue dye solutions under AM 1.5G one sun solar illumination. A Xenon (Xe) lamp was the primary light source. Substrates of varying Au@Pt ratios corresponding to varying deposition times of Pt (10 s, 20 s, and 30 s) were immersed in the dye solution in a beaker 5 cm from the source. The tests were run in ambient conditions under dark for 60 minutes and the samples were recovered every 20 minutes. The solutions were exposed to solar illumination and the samples recovered after a 20-minute interval. 3 mL of the reaction solution, in each case, was used to obtain the absorbance spectrum to evaluate the dye degradation rate at the dye's primary peak at 664 nm, corresponding to the relevant samples, using a Perkin Elmer Lambda 1050 UV-Vis-NIR Spectrophotometer. Photolysis tests of MB were also carried out with bare Au nanoislands and Pt films on glass as a standard to validate plasmon-enhanced degradation of the MB dye. Further confirmation of the same was achieved by performing the dye degradation tests under a UV filter, and in the presence of electron and hole scavengers including ammonium dichromate, ethylenediaminetetraacetic acid (EDTA), isopropyl alcohol (IPA), and p-benzoquinone. 5 mL of 10 mM solutions of electron and hole scavengers were used in 50 mL of dye solution to test the photocatalytic performance of the bimetallic substrates. Reproducibility of the measurements was ensured by double testing of selected samples. Quantitative understanding of dye degradation results was achieved by examining the change in MB concentration (C) after photodegradation relative to the initial concentration (C_0)
of the MB dye. The photocatalytic activity of the bimetallic photocatalysts was described using a pseudo-first-order kinetics model,

$$-ln(C/C_0) = kt, \tag{5.4}$$

where k is the kinetic rate constant of the degradation process.

5.2.6 Stokes and anti-Stokes Raman Thermometry

As a technique, Raman spectroscopy has been ubiquitous in many different fields of scientific inquiry. The molecular vibrations and systematic excitations because of Raman scattering can cause the energy of incident photons on the sample to be shifted up or down. These shifting modes of energy provide the relevant information regarding the electronic and vibrational structure of the system, and are categorized into three bands: Rayleigh, Stokes, and anti-Stokes. The Rayleigh band signifies scattering without loss of energy of energy, while the Stokes and anti-Stokes bands relate scattering where a vibration is excited with a down-shift in photon energy and scattering where a vibrational excited mode is de-excited with an up-shift in photon energy, respectively. The measurement of the Stokes and anti-Stokes scattering signals arising from the Raman effect encompasses the technique that is Raman spectroscopy.[333]

Advanced characterization involving Stokes and anti-Stokes Raman spectroscopy provides great insights toward plasmon carrier dynamics. An example of the significance of such analyses comes from the work published by the Linic group.[129,334] Linic et al.[100,129,334] were able to obtain unique insights by analyzing anti-Stokes intensities for a case study on MB molecules adsorbed on Ag nanocubes. Using laser sources with photon wavelengths of 532 and 785 nm, Linic et al.[100,129,334] observed the anti-Stokes and Stokes SERS signals to simultaneously measure the vibrational temperature of the plasmonic nanoparticle and the attached adsorbate. This allowed them to track the flow of excited charge carriers in the system as the charge flow is directly related to the temperatures of the probe molecule and the plasmonic nanoparticles. Surprisingly, their experiments showed that charge transfer between the nanoparticle and the adsorbate took place under excitation by 785 nm photons as opposed to 532 nm photons, followed by selective heating of the molecule.

This is a relevant result when one considers that the lowest energy of photons absorbed by free MB molecules is ~ 665 nm, providing proof that the charge transfer is interfacial in nature (metal to molecule) as opposed to intraband transfers within the MB molecule. Using these results, Linic et al.[100,129,334] were able to demonstrate the discrepancies in conventional plasmonic charge transfer theories which would suggest higher rate of charge transfer for the 532 nm laser due to the higher energy photons involved as well as the higher extinction coefficient for the Ag SERS substrate at 532 nm compared to 785 nm. These results supplement other observations that have confirmed discrepancies in the application of the conventional theory of metallic surfaces applied to studies of LSPR phenomena. This unique approach using the anti-Stokes intensities to gauge the nature of hot electron charge transfer is unprecedented and proves the efficacy of SERS as a great technique that can be used to examine LSPR and hot electron dynamics.

Stokes and anti-Stokes Raman spectra on the MB adsorbate-Au@Pt bimetallic core-shell nanoisland sample surfaces were obtained using a custom-built *f*/2 Raman spectrometer with an Andor Newton 940, back-thinned charge-coupled device (CCD) detector, cooled to –80 °C.[335] 100 µL of aqueous MB dye (5 ppm) was drop-casted onto the bimetallic substrates. The substrates were gently heated on a hot plate at less than 60^0C prior to and during drop-casting to ensure optimal chemisorption of the dye onto the nanoislands. Raman spectra were generated using an Innovative Photonic Solutions 532 nm spectrum stabilized laser module. Laser output was directed to the sample through a 105 mm single mode fiber patch cable and collimated by a Thorlabs collimation package. Semrock 532 nm MaxLine laser-line filter and StopLine single-notch filter were used to collect Stokes and anti-Stokes Raman signals. To minimize radiation damage, the laser power was adjusted to less than 10 mW on a 50 µm diameter point focus. The Raman shift axis was calibrated with anhydrous benzonitrile. The determination of the Raman temperature was achieved by measuring the signal strengths of the Raman bands of the MB dye at the Stokes and anti-Stokes positions. The temperature is subsequently calculated based on a Boltzmann distribution of the ground and first excited state populations. The corresponding expression utilized to describe this relationship is,[336]

$$\frac{I_{AS}}{I_S} = \frac{(V_l + V_v)^3}{(V_l - V_v)^3} exp\left(\frac{-hV_V}{k_B T}\right) \tag{5.5}$$

where T is the temperature, k is Boltzmann's constant, h is Planck's constant, V_l is the frequency of the laser, V_v is the frequency of the vibrational mode (Raman band position), and the Stokes (I_S) and anti-Stokes (I_{AS}) Raman scattering strengths are defined by energy detection of the signals. The spectra reported in this work were acquired on a photon counting basis.

5.3 Results and Discussion

5.3.1 Morphological and compositional studies of Au@Pt nanoislands

Annealing of the Au films induces thermal dewetting allowing Au atoms at the surface to migrate and form individual nanoislands. **(Figure 5.2a)** indicates that Au films annealed at 400^0C generally exhibit a hemispherical morphology while maintaining a non-uniform size distribution. These observations are similar to monometallic Ag nanoislands fabricated with the same procedure.[322] Deviations are observed where particles are elongated and oblate in shape as opposed to spherical. Average nanoisland size with error was determined to be ~ 80 ± 25 nm and a polydispersity of ~ 30%. **(Figure S10)** The size distribution is monomodal in nature, a behavior that can be attributed to the temperature at which the bimetallic substrates are treated (similar to what was observed of monometallic Ag nanoislands) and which satisfies the condition of dewetting as required by the Hüttig and Tammann limits for Au (whose melting point is 1064^0C).[228,236] This dependence of dewetting behavior with annealing temperature is also observed in the work of Kracker et al.[337] who recognize that for higher temperatures Au particles become extremely rounded and similar leading to a monomodal size distribution. This is also supported by the work of Müller et al.[338] where only dewetted Au layers with a thickness of more than 10 nm showed bimodal size distributions. This works in our favor as Nanofab's magnetron sputtering system registers an average deposition rate of 7.6 nm/min for Au. 40 s of deposition of Au films would then correspond to a 5 nm thick film. The glass substrate is not damaged during thermal treatment and the dewetting process is largely governed by the minimization of the surface energy of the deposited metal film.[322] The morphological changes observed of the Au films are similar to the general conditions of thin film growth which involves adsorption, cluster formation, surface diffusion, desorption, nucleation, island growth, and agglomeration, all of which is observed in our sputtered and annealed Au films.[238] By changing the duration of annealing at a given temperature, the extent of particle agglomeration can be monitored.[322] Following the annealing of the Au films, Pt thin films are sputtered for varying durations between 10 s – 30 s to form conformal shells coating the Au nanoislands. Due to the thin nature of the films, the presence of Pt is difficult to discern via FESEM. The morphology of the Au@Pt composite, and the presence of the shell layer is confirmed via XPS studies.

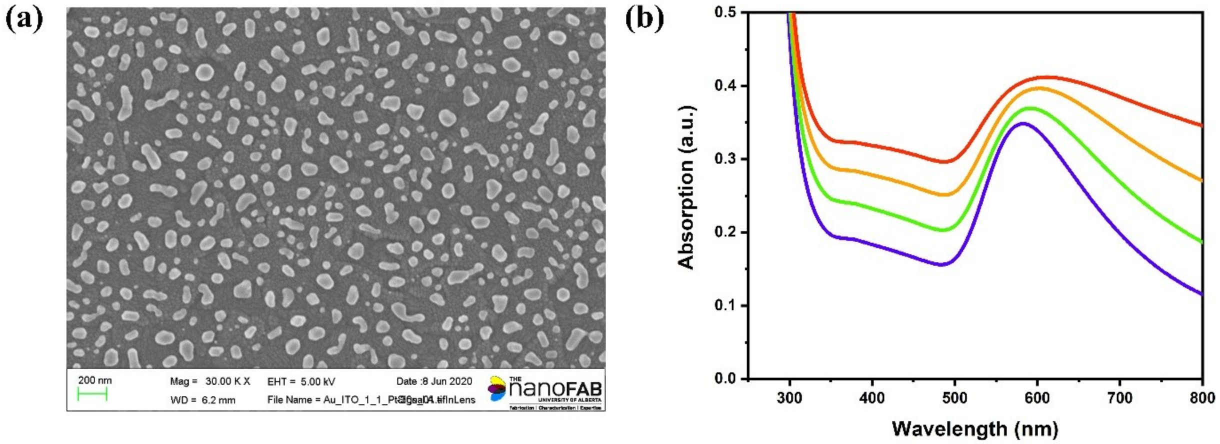

Figure 5.2. (a) Secondary electron FESEM image of Au@Pt hemispherical core-shell nanoislands. (b) UV-Vis absorbance spectra of monometallic Au film on glass annealed at 400^{0}C (violet), and post Pt depositions of 10 s (green), 20 s (orange), and 30 s (red).

The surface and sub-surface (up to ~10 nm) chemical composition of samples was determined by measuring the binding energies using XPS. (**Figure 5.3a, Figures 5.3c-5.3d**) Survey scan XPS spectra of monometallic Au and Pt samples as well as bimetallic Au@Pt samples displayed all the core level (Au-4f, Pt-4f) and sub-core-level peaks (Au-3d, Au-3p, Pt-3d and Pt-3p) confirming the presence of the constituent elements. **(Figure 5.3b)** Deconvoluted high-resolution XPS spectra of Au in Au-4f region show two well-resolved peaks at binding energies (BE) 83.6 and 87.3 eV assigned to Au-4$f_{7/2}$ and Au-4$f_{5/2}$ peak components of metallic Au in zero oxidation state. The absence of any additional peak or shoulder peak excludes the possibility of oxidation during sputtering.

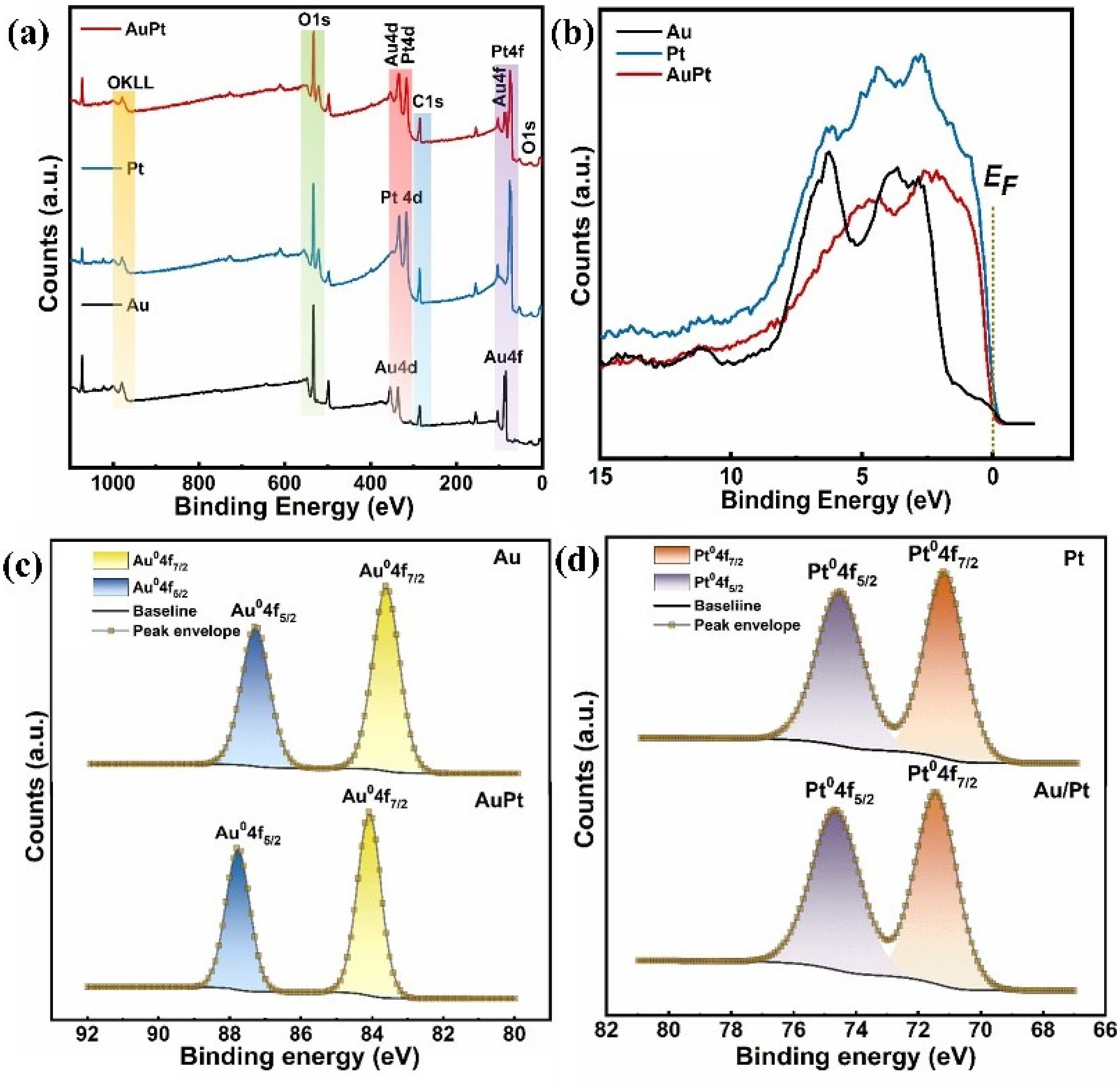

Figure 5.3. (a)-(b) Survey scan XPS spectra of monometallic Au and Pt as well as bimetallic Au@Pt samples that confirm the presence of the constituent elements. (c)-(d) Binding energies of the Au and Pt constituents in the monometallic and bimetallic counterparts.

Following the formation of Au@Pt core-shell structures, the BE of Au was slightly shifted toward higher energies and new peaks were observed at 84.1 and 87.8 eV. The positive shift in the binding energy value of Au in core-shell bimetallic suggests transfer of electrons from Au core to the Pt shell. As the Fermi level of Pt is lower than Au, the electrons in an Au@Pt bimetallic system will flow from Au to Pt due to the built-in electric field until Fermi level equilibration. This electron transfer leads to decreased electron density (increased positive charge) on Au resulting in a positive shift in BE. Furthermore, increased BE also exclude the possibility of Au@Pt alloy formation, as in alloys the higher electronegativity of Au (2.54) than Pt (2.2) and perturbed electronic interaction between Pt and Au atomic orbitals would lead to charges being transferred from Pt to Au while the opposite has been observed here.[317] The appearance of two well resolved peak components at 71.2 and 74.5 eV in Pt4f XPS of Pt metal, assigned to $Pt4f_{7/2}$ and $Pt4f_{5/2}$ orbital splitting, validates the presence of Pt in its metallic state. Contrary to prediction, no negative peak shift in the BE value of Pt was observed in the Au@Pt core-shell structure. This could be due to the accumulation of electrons at the Au@Pt interface or deactivation of surface electron via O_2 which works as an electron scavenger. XPS valence band spectra of Au show a characteristic doublet of 5d band with a d band edge at ~2 eV below the Fermi level while the 6s band edge as free electrons were observed at zero binding energy. For Pt, the 5d band was observed at the Fermi level.[324,339]

These observations match multiple studies of Au@Pt systems where the core-shell structure is often characterized by a positive shift in BE for Au and a mostly unchanged Pt BE in the XPS spectra. Tan et al.[340] utilize the corresponding shifts in binding energies of the Au 4f and Pt 4f orbitals to confirm charge transfer phenomenon in their Au@Pt bimetallic substrate. Wang et al.[341] demonstrate large numbers of Au bimetallic systems where electropositive hosts, such as Pt, may often result in a positive BE shift in the Au 4f levels, which is also observed in our work. Bond et al.[342] further argue that the Au-Pt phase diagram exhibits a considerable miscibility gap meaning the solubility of each metal in the other is strictly limited. Atomistic calculations and thermodynamic studies of nanoalloys as demonstrated by Wang et al.[343] suggest the possibility of a core-shell structure as opposed to an Au-Pt alloy considering the low temperatures and low Pt amounts involved. **(Figure 5.4)**

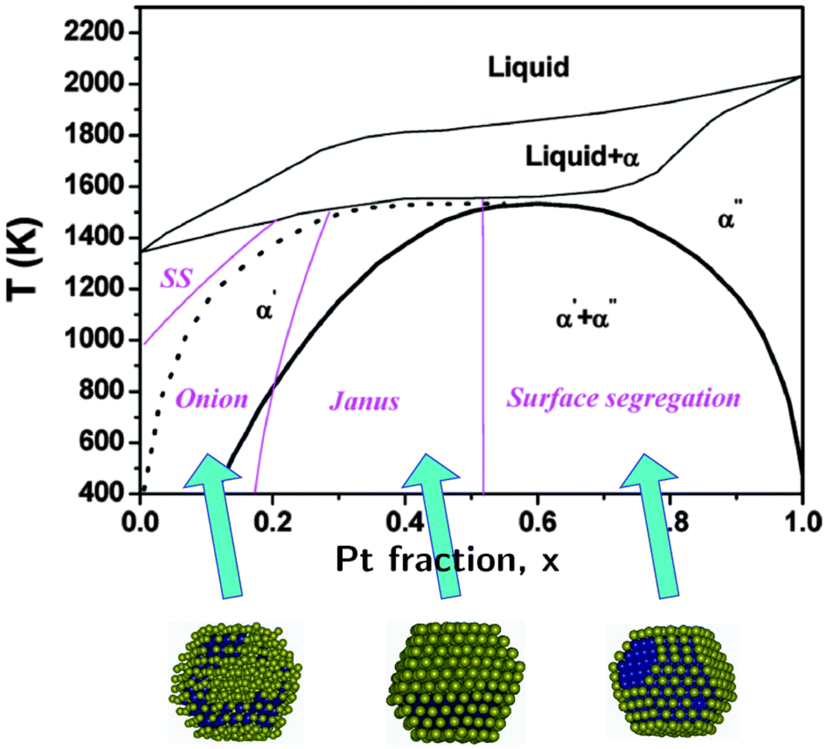

Figure 5.4. Simulated phase diagram of Au-Pt nanoalloys as demonstrated in the work of Wang et al.[343] using an analytical potential and an off-lattice description. For the low Pt fractions and the corresponding temperatures utilized in the fabrication of our bimetallic substrates the results predict a structure closer to onion or Janus/core-shell. Reprinted with permission from Ref.[344] Copyright Royal Society of Chemistry (2015).

Ultraviolet photoelectron spectroscopy (UPS) was used to determine the work function for Au, Pt, and Au@Pt core-shell nanoisland substrates. **(Figures S11 - S13)** To calculate the work function, the formula $W(\phi) = 21.21 - E_{cut-off}$ was utilized, where 21.21 eV refers to the energy of the incident He I line of the He discharge lamp, and $E_{cut-off}$ is the cut-off energy of secondary electrons. The point of intersection of the leading edge of the graph provides the value for $E_{cut-off}$ and is determined via extrapolation. The value of $E_{cut-off}$ for Au, Pt, and Au@Pt samples were found to be 16.5 eV, 16.7 eV, and 16.07 eV, respectively, resulting in corresponding work function values of 4.71 eV, 4.51 eV, and 5.14 eV, respectively. **(Figures S11 – S13)** The true Fermi level for Au, Pt, and Au@Pt samples are observed at -0.2 eV instead of 0 eV. This can be attributed to charging or insufficient grounding due to the glass nature of the substrate. The secondary electron cut-off for Au@Pt is noticeably shifted toward lower energies compared to its monometallic components. The work function of Au is observed to be well-within the range of values commonly reported for gold while the low work function of Pt could be attributed to the incomplete development of metallicity due to the low thicknesses of the deposited film.

As mentioned earlier, XRD studies **(Figure S9)** demonstrate that the sputtered bare Au and Pt films display crystal planes of typical fcc phase. **(Table 1)** lists the crystallite sizes and microstrains of pristine Au, Pt, and Au@Pt substrates.

	Average crystallite size (nm)				**Microstrain (10^{-3})**			
	hkl (111)	*hkl* (200)	*hkl* (220)	*hkl* (311)	*hkl* (111)	*hkl* (200)	*hkl* (220)	*hkl* (311)
Au	5.54	5.06	5.37	6.53	19.1	18.2	11.8	8.5
Au@Pt	5.40	5.31	5.31	6.57	19.6	17.3	11.9	8.4
Pt	4.7	5.96	5.63		21.7	14.9	11.1	

Table 1. Average crystallite size and microstrain values for pristine Au, Pt, and Au@Pt substrates extracted from XRD peak widths in **(Figure S9).**

The incorporation of Pt upon Au nanoislands does not result in a significant change in crystal size. In fact, it can be observed that the average crystallite size is largely consistent among the monometallic constituents and the bimetallic composites for the various crystal planes. While 5 nm is a small value for the average crystallite size metallicity is generally expected to manifest around this landmark. Vacuum deposition usually results in polycrystalline films unlike colloidal methods where one obtains monocrystalline films. As demonstrated by Goubet et al.[345] and Staechelin et al.[346] for the similar crystallite sizes calculated, the broadening of the peaks observed in the LSPR spectra (an increase in linewidth) can be attributed to faster electron-phonon coupling, which reduces the thermal equilibration time of hot carriers, and surface scattering of electrons on defects and grain boundaries. Strain in Au films is generally expected as thermal dewetting implies inefficient lattice matching due to Au's poor adsorption onto a glass substrate. Strain magnitudes for the Pt films are generally around the same magnitude except for the (111) direction where there is a near 10% increase. Between the two metal constituents, Au is known to have a larger lattice constant than Pt. Thus, the latter is subject mainly to tensile strain while Au would be under compressive strain.[347] It is observed that there is a lattice strain accumulation largely at (111) planes followed by a lattice relaxation effect acting upon the remaining crystal planes in (200), (220), and (311). This leads us to conclude that any expected tensile strain in the bimetallic substrates is released through the formation of lattice defects in the form of distortions or dislocations on (111) planes.[347]

5.3.2 LSPR modulation in Au@Pt nanoislands

(Figure 5.2b) presents the UV-Vis-NIR spectra of monometallic Au nanoislands (violet) and bimetallic Au@Pt core-shell nanoislands (green, orange, red). The bimetallic nanoislands are fabricated with varying thicknesses of Pt shells evidenced via differing magnetron sputtering deposition times between 10 – 30 s. In Au films annealed at 400^0c, the primary dipolar plasmon resonance of the nanoislands is observed at a wavelength of 582 nm. This can be because the incident electric field of light is uniform over the entire volume of the Au nanoparticle.[244] The hemispherical shape and the high index glass substrate ($\epsilon = 1.5$) are responsible for the redshifted plasmon resonance of the Au nanoislands. The redshifted values of the plasmon resonance and the clear broadening of the primary resonance peak are a consequence of the high annealing temperature utilized, are indicative of the average particle size due to thermal dewetting of the gold nuclei, and subsequent coalescence of individual smaller particles to nearby larger particles via surface diffusion and mass transfer. The resultant morphology of the Au nanoislands thus match what is expected by the Young-Dupré equation for particle sizes > 100 nm.[243] The absence of quadrupole resonances in the short wavelength spectral region for these Au nanoislands agrees with what has been observed in literature.[223,245]

Adding catalytic shells of Pt onto the Au nanoislands results in the damping of the plasmon resonance that is directly observable from the absorption spectra. (**Figure 5.2b**) For increasing sputtering deposition times of 10 s (green; LSPR peak at 592 nm), 20s (orange; LSPR peak at 603 nm), and 30 s (red; LSPR peak at 614nm) the plasmon resonance of Au@Pt core-shell nanoislands experience a damping of the plasmon resonance observed as a collective broadening of the LSPR resonance peak, and further redshifting of the peak. The increase in absorption magnitude follows the rising trend of greater thicknesses of Pt shells being deposited atop the Au nanoisland. The evolution of the quality factor (*Q*) of the plasmon resonances (given by ωpeak/FWHM) also demonstrates the progression of damping with ~ 4.64, 3.50, 2.54, and 2.49 from the bare Au sample and to those post-deposition with Pt for 10 s, 20 s, and 30 s, respectively. The quality factor can also be used as a key metric to evaluate plasmonic substrates as the resultant local electromagnetic field enhancement and plasmon dephasing times due to the LSPR are directly proportional to Q.[222] The Q values calculated from the UV-Vis spectra also provide information about the ensembled averaged enhancement factors.[23]

This overall behavior is unique as compared to what has been generally observed in bimetallic substrates involving Au and Pt where the damping of the plasmonic response is usually observed with the LSPR blue shifting in energy and losing intensity.[281,311,348] The broadening of the resonance in spectral shape does concur with the consensus that intermetallic effects between the plasmonic noble metal and catalytic transition metal can lead to optical and catalytic behavior distinct from the sum of their parts.[277,281,284,348] As the plasmon resonance itself is highly dependent on the morphology of the nanoparticle, these observations may differ between core-shell nanostructures of varying morphology.

The origin of this behavior can also be traced to the electronic band structures of plasmonic and catalytic metals. It is well-known that the d-band for plasmonic metals are far from the Fermi level. This allows for high quality, intraband plasmons (s to s) at optical frequencies until the onset of interband transitions (d to s). In contrast, catalytic metals have d-band centers close to the Fermi level resulting in their optical responses to be dominated by interband transitions. Thus, there is an increased probability of interband transitions that dampens the LSPR at all frequencies resulting in a broadening of the resonance peak.[281,311,339]

For Au@Pt bimetallic substrates, the constituent LSPRs of Au and Pt are highly nondegenerate due to differences in free carrier density and the effective masses of the two materials. Thus, the Au electrons do not oscillate in resonance with Pt electrons, and therefore, both components contribute very little to the other's LSPR.[277,349,350] It has been experimentally demonstrated that a single monolayer of Pt on an Au core leads to a dramatic drop of ~ 90% in absorption intensity.[350] This has also been recognized in studies of other bimetallic systems.[277,311,351–354]

The facile means of fabrication and the subsequent modulation of the plasmon resonance by varying the thickness of the catalytic metal shell provides an important design parameter for optimizing the performance of bimetallic core-shell photocatalysts. FDTD electromagnetic simulations provide additional insights into this behavior as well as help demonstrate the mechanisms of plasmon modulation due to the addition of a catalytic shell and the corresponding local electric field enhancement behavior.

5.3.3 FDTD studies of LSPR modulation in Au@Pt nanoisland

Using Mie theory, Zhang et al.[311] found that spherical core-shell structures support two types of plasmon resonances: ordinary and extraordinary modes. The energy of the ordinary mode is concentrated at the outer surface of the shell while the energy of the extraordinary mode is concentrated at the interface between the core and the shell. This is similar to bonding and antibonding modes in plasmon hybridization though this is not evident in all systems in the visible range.[183,355] The LSPR peak of bimetallic systems thus will be redshifted or blue-shifted depending on the type of mode or the effective permittivity of the shell.

Various FDTD simulations on glass substrates were performed with results involving Au nanoislands of radii 30 nm matching best with a dipole resonance peak value at 584 nm. It was observed that for an array of Au nanoislands conformally coated with Pt shells of varying thicknesses ranging from 1 nm – 3 nm the general trend in bimetallic spectra was observed. **(Figure 5.5b)** As shown in Zhang et al.[311], the plasmon resonance is an ordinary LSPR mode that experiences a loss in intensity, broadens in spectral shape, and blue-shifts as the thickness of the catalytic Pt shell increases. The local electric fields are concentrated at the air/Pt interface which is induced by the metallic features of Pt at visible wavelengths. **(Figures 5.5c-5.5d)** By modulation of the thickness of the Pt shell, it is observed that the local electric field gets weaker for thicker Pt shells as observed in **(Figures 5.5c-5.5d)** where Pt shell thickness increase from 1 nm to 3 nm. The amplification of the local field for thinner shells is beneficial for photocatalysis and is in accord with the results presented by the work of Engelbrekt et al.[277] These observations also agree with other existent literature.[281,284,311,348]

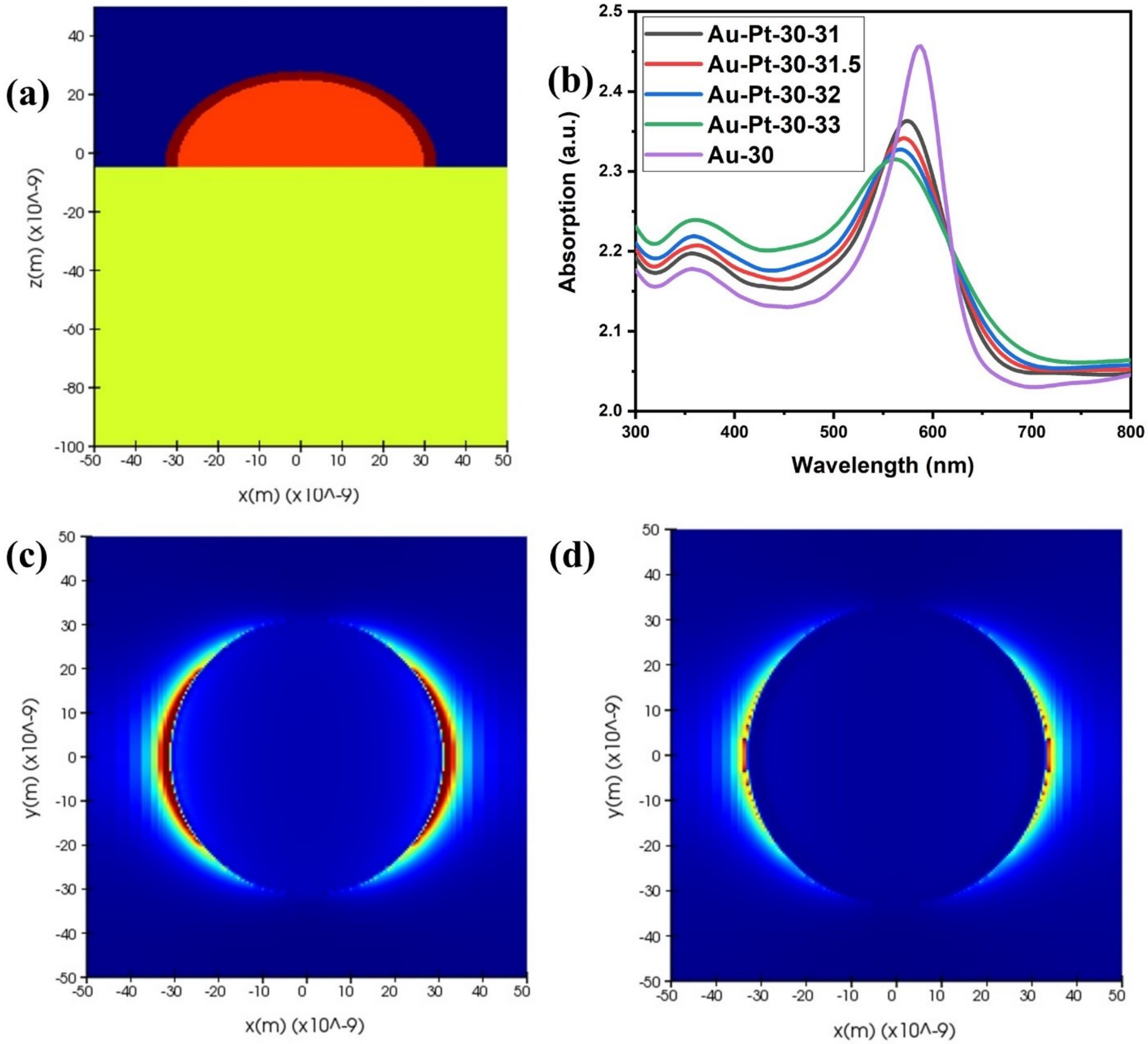

Figure 5.5. (a) Index monitor profile of the Au@Pt bimetallic hemispherical nanoisland core-shell structure depicting the Au core (light red), Pt shell (dark red), and glass substrate (green). (b) Absorption spectra of Au@Pt bimetallic core-shell structure with an Au core radius of 30 nm and Pt shell thicknesses from 1 – 3 nm. The characteristics ratios of these radii are presented in the legend as 30 nm – 31 nm, 30 nm – 31.5 nm, etc. (c) Electric field profile intensity graph of Au@Pt core-shell structure with a core radius of 30 nm and a shell thickness of 1 nm. (d) Electric field profile intensity graph of Au@Pt core-shell structure (along the xy-plane) with a core radius of 30 nm and a shell thickness of 3 nm.

(Figure 5.2) confirms there is a marked difference in morphology that provides for the unique resonances observed in our Au@Pt substrates compared to these general trends. Following thermal treatment of Au films, Pt films are deposited along the entire surface of the glass substrate. Thus, unlike earlier simulations of individual hemispherical core-shell nanoislands, FDTD simulations of Au nanoislands with Pt shells that conformally coated both the plasmonic core as well as the glass substrate were investigated. The corresponding results (**Figures 5.6a-5.6d)** match experimental observations and confirm the morphology of our Au@Pt substrates. Upon addition of Pt shells, the corresponding broadening and redshift of the primary plasmon resonance of Au is observed. The subsequent redshift can be attributed to the morphological and structural characteristics of the Au@Pt substrates. Unlike isolated bimetallic Au@Pt nanoparticles, the nanostructured films consist of hemispherical Au nanoislands separated from each other by inter-island channels. The width of these inter-island channels can be modulated by changing the duration and temperature of the annealing process with narrower channels generally being observed for lower temperatures and shorter durations.[210,238,322] The shifts in resonance observed can also arise due to charge transfer and may vary for asymmetric particles.[311]

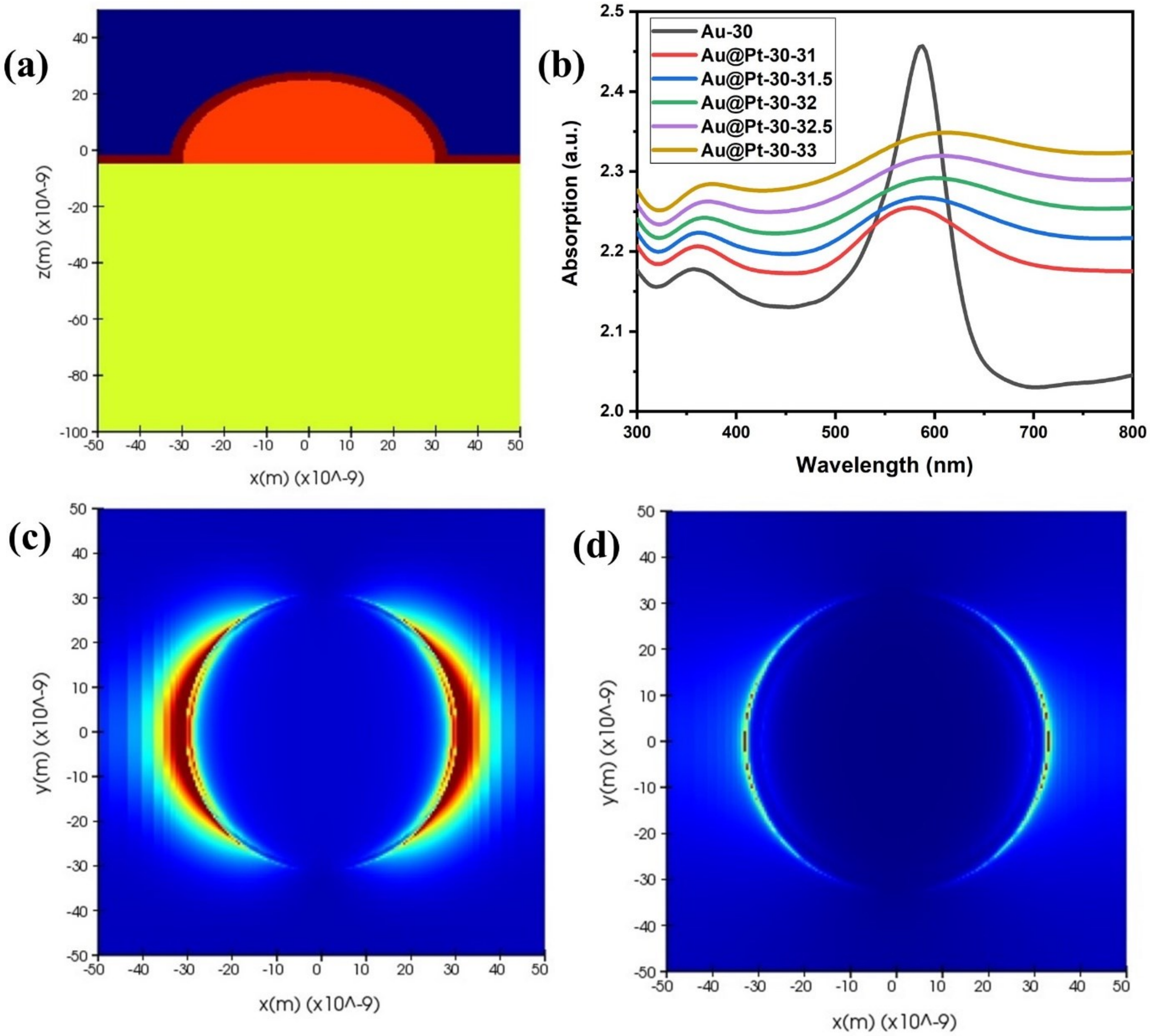

Figure 5.6. (a) Index monitor profile of the Au@Pt bimetallic hemispherical nanoisland core (light red)-shell structure with a thin film of Pt (dark red) on the glass substrate (green) as well. (b) Absorption spectra of Au@Pt bimetallic core-shell structure with an Au core radius of 30 nm and Pt shell thicknesses from 1 – 3 nm. The characteristics ratios of these radii are presented in the legend as 30 nm – 31 nm, 30 nm – 31.5 nm, etc. (c) Electric field profile intensity graph of Au@Pt core-shell structure with a core radius of 30 nm and a shell thickness of 1 nm. (d) Electric field profile intensity graph of Au@Pt core-shell structure (along the xy-plane) with a core radius of 30 nm and a shell thickness of 3 nm.

As before, the electric field density profiles follow the trend where for increasing Pt shell thickness the plasmon resonance is damped. But unlike earlier, the presence of a thin Pt layer surrounding the bimetallic nanoisland results in the generation of a more intense local electric field around the vicinity of the nanostructure. The generation of a stronger local electric field correlates to a stronger plasmon resonance while the Pt film serves as an offsite catalytic surface and as a protective insulating layer for the plasmonic noble metal Au core. As demonstrated by Huang et al.[286] the presence of Pt as a conformal shell on the Au nanoisland and surrounding its vicinity helps increase the ratio of light absorption to scattering due to Pt's large imaginary dielectric permittivity at visible and near-infrared frequencies. This is attributed to Pt's high density of d-states at the Fermi level and strong sp ← d interband transitions.[286] Together, the combination of a large imaginary dielectric permittivity and high plasmonic field intensity result in strong light absorption in the shell, and helping transfer light energy from the core to the surface. This is beneficial for plasmonic enhancement of molecular adsorption and chemical reactivity.

Also, as observed in Agarwal et al.[325], the existence of inter-island channels between Au nanoislands provide additional amplification of the localized electromagnetic field, with the highest enhancements occurring at the channel-shaped gaps between adjacent islands. These intense local electric fields generated by these structures can be used to trigger chemical reactions[356] and also work as in situ probes of reaction mechanism via surface enhanced Raman spectroscopy (SERS).[129,357] The deposition of Pt in these areas provides for an effective composite bimetallic photocatalyst. The facile means of fabrication of these bimetallic substrates and the modulation of their plasmon resonance characteristics for broad optical absorption makes them viable for visible light photocatalytic and plasmon-driven chemical reactions.

The preliminary UV-Vis-NIR spectra now supplemented by electromagnetic FDTD analyses demonstrate the potential of Au@Pt core-shell nanoislands as standalone substrates for plasmon-enhanced photocatalysis. The resultant LSPR peaks observed in the simulations and experiments are beneficial for photocatalytic applications where one tries to match the broad solar spectrum. All the simulations discussed above involved arrays of hemispherical bimetallic nanoislands structured with a center-to-center spacing of 100 nm indicating that there is negligible role of Coulombic interactions from neighboring particles.[322]

5.3.4 DFT studies

FDTD simulations are limited in their ability to fully capture the behavior of plasmonic-adsorbate systems. Taking the case of the Ag-R6G systems discussed in Chapter 4, FDTD simulations would be unable to capture the electron-phonon coupling interaction that is crucial to said systems. This is because FDTD is a classical theory and cannot model what is a quantum mechanical phenomenon. While FDTD may provide information on the macroscopic characteristics of said systems, such as field intensity and enhancement, a quantum mechanical approach would be necessary to capture the intermetallic effects, plasmonic coupling, and electronic-chemical behavior of said systems. Similar observations can be made for the Au@Pt bimetallic system where the use of thin shells necessitate the importance of capturing plasmon coupling effects between the core and shell components when their separations decrease to 15 nm, and for below 1 nm, where the near- and far-field properties require the inclusion of quantum mechanical effects.[358] It is important to note that the simulations in prior sections provide a macroscopic understanding of the plasmon resonance modulation behavior expected of core-shell structures using the FDTD method where the relevant absorption and field enhancement behavior have been modeled using Mie theory with results being complementary to those presented by Zhang et al.[311] Similar studies have also been made of other core-shell structures using an FDTD approach.[359] To supplement the knowledge we have obtained via the compositional and morphological characterization of the Au@Pt systems as core-shell structures, and to fine-tune our deductions from FDTD simulations, DFT is used to investigate the electronic, and interfacial properties of the Au@Pt system.

The intermetallic effects of bimetallic core-shell nanostructures are heavily influenced by the geometry of the bimetallic structure and can potentially provide for optical coupling via plasmon hybridization, electronic coupling via charge transfer, and possibly even atomic coupling via the formation of a new electronic structure.[281] DFT based quantum chemical calculations were pursued in order to garner valuable insights into the electronic structure of the bimetallic system. **(Figure 5.7)** shows the first, second and third highest occupied molecular orbital (HOMO) and lowest unoccupied molecular orbital (LUMO) when Au (111) and Pt (111) are far away from each other and when Au (111) and Pt (111) are in close configuration. The highest occupied and lowest unoccupied molecular orbitals are positioned predominantly on Au and Pt clusters respectively in close configuration. Such molecular orbital locations suggest possible charge transfer phenomenon from gold to platinum under illumination. **(Figures 5.8a-5.8b)** show the average projected density of states (PDOS) of Pt and Au systems for Au (111) and Pt (111) hybrid system in far and close configurations, respectively. Density of states refers to the number of different states at a particular energy level that electrons can occupy. The PDOS is the relative contribution an atom or orbital makes to the total density of states. It is analogous to the Aufbau principle but generalized to larger molecular systems. The PDOS plots show discrete energy levels or narrow bands akin to molecules as opposed to the broad bands expected in real metals. The average PDOS was obtained by averaging over all the DOS projected on individual atomic sites. (**Figures 5.8c-5.8d)** show the orbital-resolved PDOS of selected Pt and Au atoms at the interfacial region in the far configuration, which show the relative contribution of different orbitals to the occupied and unoccupied regions of the metallic systems under study.[360,361] Note that these plots are generated for Au and Pt clusters containing only a few hundred atoms (similar to molecules). This is the best DFT can currently do using available high-performance computing (Dorval Cluster) resources. Real plasmonic particles contain tens of thousands of atoms. For Au, one requires at least a thousand atoms for metallicity to manifest. As such, the PDOS plots for Au and Pt are rough approximations of the band-structure of Au and Pt nanoparticles. From **(Figures 5.8a-5.8b)**, a sharp decrease of available states in the unoccupied region close to the Fermi level (FL) for Au atoms can be observed in close geometry compared to the far configuration. This reduction of states indicates a reduced probability of electronic transition within Au. On the other hand, the almost unchanged spectrum for Pt indicates the unaltered transition probability within Pt. However, in the close geometry, the relatively less-affected occupied states for Au and unoccupied states in Pt in the immediate vicinity of FL, clearly shows the likelihood of a high transition rate from Au d to Pt d states. Hence, molecular orbital and projected density of states analysis strongly corroborate to the feasibility of electron transfer from gold to platinum.

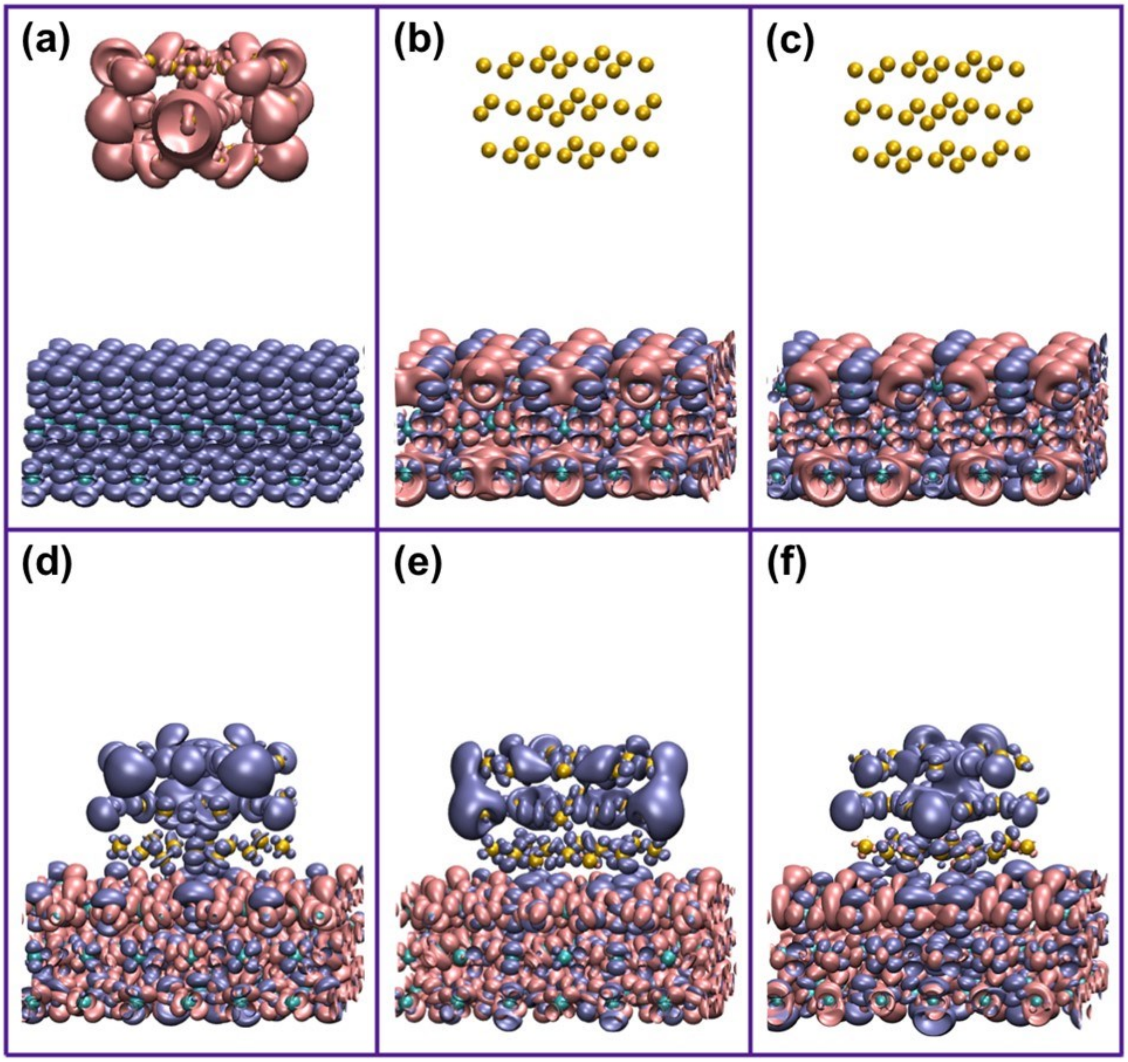

Figure 5.7. DFT calculated HOMO and LUMO of Au@Pt heterosystem are represented by blue and pink colors respectively. (a), (b) and (c) show first, second and third HOMO/LUMO locations respectively, when Au (111) and Pt (111) are far away from each other. (d), (e) and (f) show first, second and third HOMO/LUMO locations respectively, when Au (111) and Pt (111) are in close configuration. Orange and cyan colours are for Au and Pt atoms respectively.

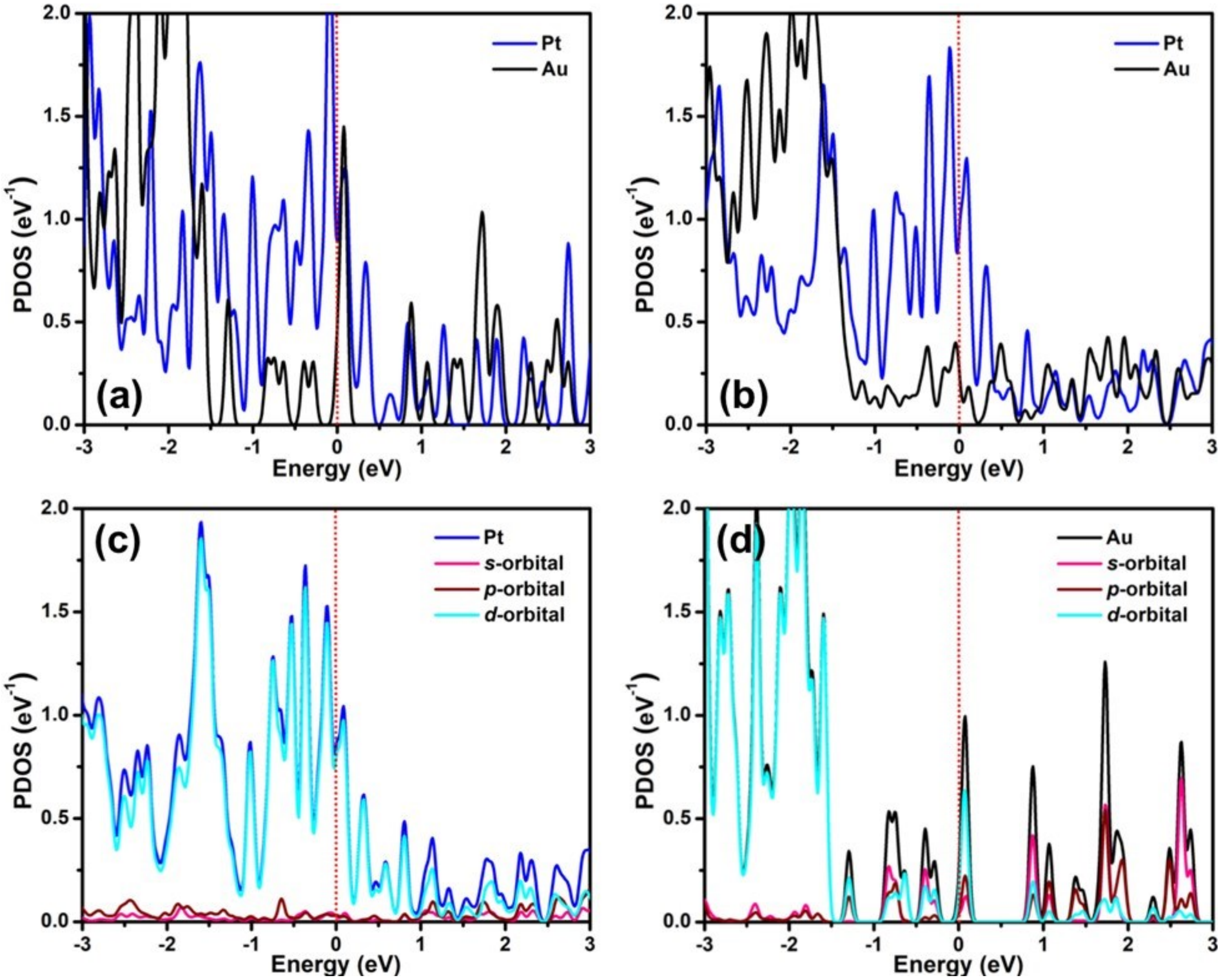

Figure 5.8. Average projected density of states (PDOS) of Pt and Au systems when (a) Au (111) and Pt (111) are far away from each other and (b) when Au (111) and Pt (111) are in close configuration. Orbital-resolved PDOS of selected (c) Pt and (d) Au atoms at the interfacial region in the far configuration.

5.3.5 Plasmon modulated Methylene Blue dye degradation

Photocatalytic potential of the Au@Pt core-shell nanoislands were investigated by considering the degradation of MB dye. MB is utilized as a dye for paper and office supplies as well as to tone up silk colors. It is also commonly used in human and veterinary medicine for therapeutic and diagnostic procedures. Much like its counterpart in R6G, MB cannot be degraded through conventional water treatment processes due to its complex aromatic structure, hydrophilic nature, and high stability against light, temperature, water, and chemicals, etc., resulting in its cause for extensive environmental pollution.[362] The degradation of MB dyes is therefore an important initiative in photocatalysis. The characteristic absorption peak of MB at 664 nm was used for monitoring the catalytic degradation process. Absorption spectra of aqueous solutions of MB were tested at different time intervals, following illumination under AM 1.5G light using a Xenon arc lamp solar simulator, and in the presence of the Au@Pt core-shell substrates. At AM 1.5G condition, 1 sun is defined as equal to 100 mW/cm^2 of irradiance with the standard spectra defined accordingly by the American Society for Testing and Materials. The plasmonic substrates were immersed within the dye solutions. As seen in **(Figure 5.9a)**, the main absorption peak of MB demonstrated a gradual decrease with the extension of exposure time (from 60 minutes in dark to 120 minutes under AM1.5G), indicating the photocatalytic degradation of the dye. In the absence of the nano-catalyst or in dark conditions, the reaction did not have any progress.

For a quantitative understanding of the degradation process, the change in MB concentration (C) after photodegradation relative to the initial concentration (C_0) of the MB dye was examined. The C/C_0 ratios were measured with reference to a calibrated absorbance curve corresponding to MB dye samples under AM 1.5 G illumination, and their concentrations at similar time intervals as observed in this experiment. Among the varying ratios of Pt deposition cycles used to fabricate the Au@Pt core-shell nanoislands, samples of Au@Pt with a 40 s to 10 s/20 s deposition ratio of Au and Pt demonstrated the greatest degradation efficiencies in correspondence with maximum decrease in intensity in the dye's absorption peak. **(Figure 5.9b)** These results align with the points that have been made in the prior section on thinner catalytic shells providing for better catalytic performance of the bimetallic substrate. These samples performed consistently under AM1.5 G solar illumination as well as illumination under a UV filter with decolorization efficiencies of 24% and 11% (for 40 s – 10 s Au@Pt ratio) and 31% and 17% (for 40 s – 20 s Au@Pt ratio), respectively. Despite these efficiencies being on the lower end, it is important to note that these numbers are dictated for bare bimetallic substrates without the support of a semiconducting scaffold and perform equally if not better than similar substrates fabricated via colloidal techniques. For reference, the bare counterparts involving Au (40 s) and Pt (20 s) demonstrated decolorization efficiencies of 21% and 19%, respectively, under AM 1.5 G solar illumination and efficiencies of 14% and 13%, respectively, under UV filter. The bimetallic counterparts, generally, outperformed the monometallic systems. The facile means of fabrication involved for these bimetallic hemispherical nanoislands and the modulation of their plasmon resonances provides an open potential for their ease of incorporation with a semiconductor scaffold for greater performance.

The photocatalytic activity of the bimetallic substrates is as follows: Au@Pt (40 s – 20 s ratio) > Au@Pt (40 s – 10 s) > Au@Pt (40s – 30 s ratio). The photocatalytic activity of the bimetallic substrates can also be described using a pseudo-first-order kinetics model, $-\ln(C/C_0) = kt$, where k is the kinetic rate constant of the degradation process. **(Figure 5.9c)** depicts the kinetics of the MB decomposition for the bimetallic photocatalysts of varying Au and Pt ratios. The measured values of k are 0.00299 (Au@Pt, 40 s – 10 s), 0.00296 (Au@Pt, 40 s – 20 s), and 0.00148 min^{-1} (Au@Pt, 40 s – 30 s). The greatest degradation rate constants are contested between samples where 10 s to 20 s of Pt were deposited. Investigations on the contribution of primary active species during the photocatalytic degradation process were performed to gain a detailed understanding of the photocatalytic reaction mechanism. $^{\cdot}O_2$- and $^{\cdot}OH$ radicals are fundamental to photocatalytic degradation and are activating agents for the oxidation of organic pollutants. Radical trapping experiments of the Au@Pt substrates were performed in the presence of hole and hydroxyl radical scavengers including ethylenediaminetetraacetic acid (EDTA) and isopropyl alcohol (IPA), electron scavenger in ammonium dichromate, and a superoxide radical scavenger in p-benzoquinone, respectively. 5 mL of 10 mM solutions of these scavengers were used in 50 mL of dye solution to test the photocatalytic performance of the bimetallic substrates. In all four cases, the Au@Pt substrates demonstrated consistently strong dye degradation of the MB dye.[363]

(Figure 5.9d) illustrates the effects of the various scavengers in the degradation of MB by the Au@Pt (40 s- 20 s ratio) bimetallic nanoisland photocatalyst. The photodegradation efficiency of MB is significantly lower following the addition of IPA. In comparing the various scavengers, Ammonium Dichromate provides for the greatest degradation followed by EDTA, p-benzoquinone, and finally, IPA. This suggests that the $^{\cdot}OH$ is the major and $^{\cdot}O_2$- is the minor radical species in the photocatalytic decomposition of MB over Au@Pt bimetallic nanoisland substrates under solar illumination. The elevated degradation rates in the presence of ammonium dichromate also demonstrates that the plasmonic degradation process is strongly driven by the generation of hot holes. All organic dyes have one or more conjugated rings (5 or 6 membered rings usually constitute an aromatic system). This aromacity allows for their strong interaction with light. Quantum mechanically, this leads to a higher oscillation strength. The larger the rings, the greater the number of electrons, and the stronger the interactions with light. MB is composed of three fused aromatic rings. Degradation of dyes can proceed through two paths: by attacking the core (aromatic ring) or the periphery (alkyl groups). An attack from the periphery usually involves the process of de-alkylation. An attack on the core is considered chromophore cleavage or ring destruction. MB is generally resilient to the latter, and in our case, we likely observe degradation of MB through demethylation via the generation of $^{\cdot}OH$ radical species promoted by hot holes. A plausible combination of reaction steps to facilitate this degradation mechanism is listed as follows:

$$(1)\ Au + h\nu \rightarrow Au\ (e^{-} + h^{+})$$

$$(2)\ Pt\ (e^{-}) + O_2 \rightarrow Pt + {}^{\cdot}O_2^{-}$$

(Pt is a good electron acceptor)

$$(3)\ {}^{\cdot}O_2^{-} + H_2O \rightarrow {}^{\cdot}OH + {}^{\cdot}HO_2$$

$$(4)\ Au\ (h^{+}) + H_2O \rightarrow {}^{\cdot}OH + H^{+}$$

$$(5)\ {}^{\cdot}O_2^{-} + H^{+} \rightarrow {}^{\cdot}HO_2$$

$$(6)\ 2({}^{\cdot}HO_2) \rightarrow H_2O_2 + O_2$$

$$(7)\ H_2O_2 + {}^{\cdot}O_2^{-} \rightarrow {}^{\cdot}OH + OH^{-} + O_2$$

$$(8)\ Au\ (h^{+}) + OH^{-} \rightarrow Au + {}^{\cdot}OH$$

$$(9)\ {}^{\cdot}OH + MB \rightarrow \text{degradation}$$

Through the effective degradation of methylene blue, we are able to demonstrate the potential for these bimetallic substrates to degrade a larger family of aromatic compounds with similar chemical structures that are responsible for environmental contamination.

Our results correlate effectively with observations that thinner shells of Pt provide for better plasmonic performance. The thinner Pt shells help maximize the core plasmon field strength, plasmon-adsorbate coupling, and hot carrier density at the catalytic metal surface. Post 30 s of Pt deposition, the extensive broadening and damping of the plasmon resonance begins to work against the photocatalytic effectiveness of the substrate. The thicker shells increase the distance and reduce the coupling between the plasmonic core and the catalytic surface resulting in damped plasmon resonances, and as observed in FDTD simulations, dimmer electric field profiles. These results also correlate with what was observed in the UPS spectra. The utilization of thinner Pt shells around Au nanoislands prove to be beneficial as larger shell thicknesses of Pt cause excessive damping leading hot carriers to relax to thermal equilibrium too soon. As the Fermi level of Au@Pt is deeper and more distant from the vacuum level compared to Au, hot holes on the surface of Au@Pt nanoislands will be more strongly oxidizing than hot holes on the surface of bare Au nanoislands. It is well-known that the hot carriers generated in the plasmonic core from the dephasing of the Au LSPR as well as electron intra/interband excitations are generally produced within a fraction of the electron mean free path from the catalytic surface. For Au at 298 K, this equates to a characteristic length of ~ 40 nm.[364] Thus, for thinner Pt shells, one can facilitate the efficient transfer of hot carriers to the adsorbed molecules. Due to this, bimetallic substrates with lower Pt deposition rates provide for efficient photo-absorption and charge/energy delivery to catalytic sites on the surface.[20,113,286,365,366]

It is also important to note that the average electric field enhancement on the surface of an isolated Au nanoparticle is larger for smaller sizes.[367] These intense local fields can effectively help trigger chemical reactions on the surface of the substrate. For thicker shells, effective charge-energy transfer will be weakened due to weaker plasmon-surface coupling as the hot carriers will consistently lose energy as they move from the core to shell surface. It is observed that ~ 20-30% of hot carriers scatter and lose their excess energy transiting a 2 nm thick Pt shell.[368–371] Post 30 s of Pt deposition, the existence of a thicker shell maximizes these losses. These losses could be attributed to faster carrier cooling in Pt due to stronger e-p coupling or alternatively rapid e-e transfer from the Au core to the Pt shell at a < 1 ps timescale.[277,372] For thicker Pt shells, these effects collectively manifest in the form of the strong interfacial damping and broadening of the Au LSPR further debilitating visible-light photocatalytic processes.

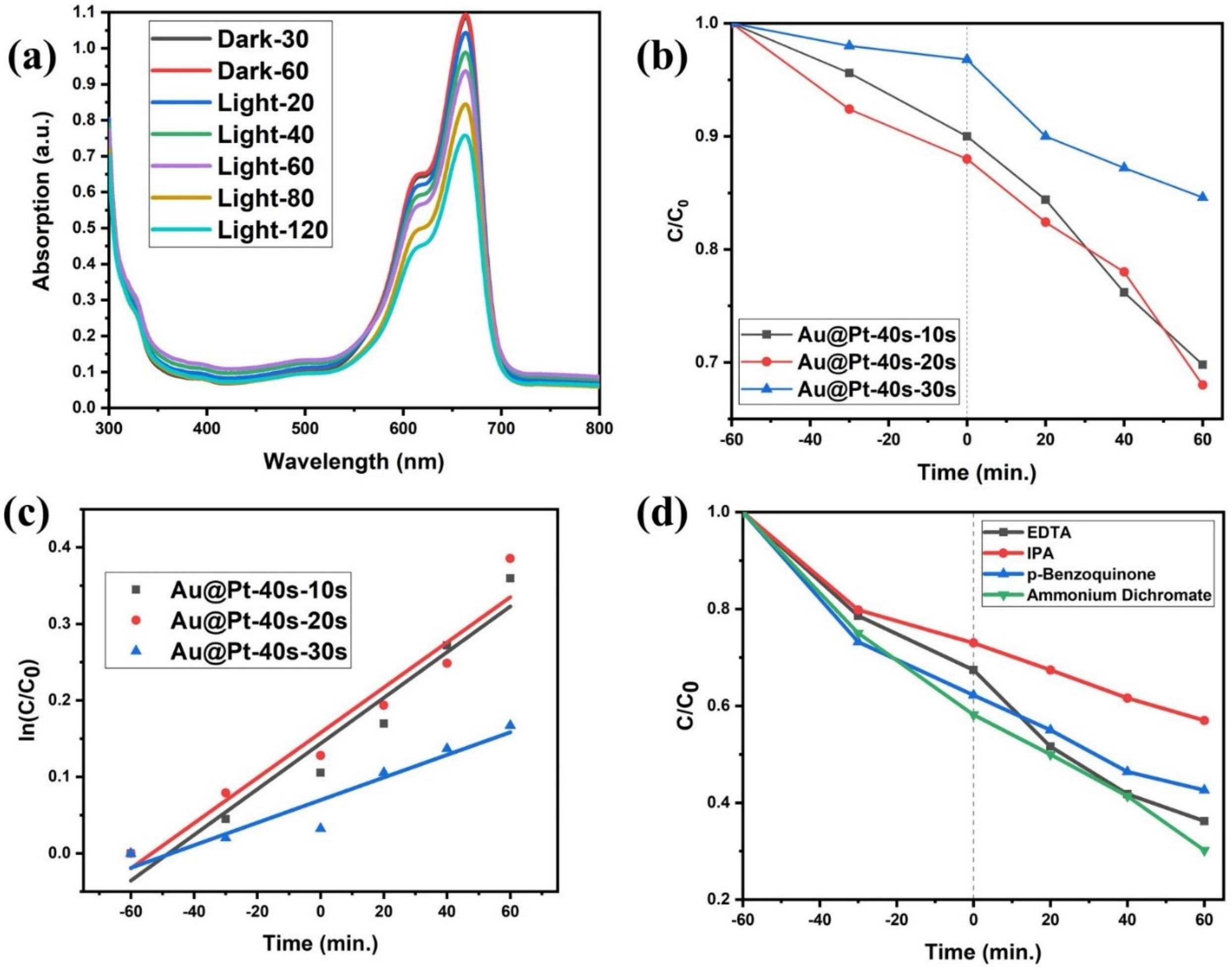

Figure 5.9. (a) Photodegradation of MB under solar light illumination in the presence Au@Pt core-shell hemispherical nanoisland photocatalyst. (b) Photodegradation of MB for Au@Pt core-shell photocatalyst for varying Pt deposition durations. (c) Kinetic rates study of MB degradation for Au@Pt samples with varying Pt deposition durations. (d) Photodegradation of MB degradation for Au@Pt samples in the presence of electron and hole scavengers.

The strong damping of the Au LSPR and the red shifting of its resonance wavelength offer the contrary possibility that Pt electrons also participate in the collective charge density oscillations. Essentially, the Au core acts as a plasmonic antenna for light harvesting. The resultant energy and generation of hot carriers of the LSPR is delivered to the catalytic Pt shell. By engineering the catalytic shell one can modulate the flow of electromagnetic energy from the plasmonic core to the catalytic surface though it is far from clear how this happens. Raman thermometric studies of the MB adsorbate – bimetallic substrate system may offer some basic insights to the process.

5.3.6 Raman Thermometry studies

Raman thermometry studies provide a basic tool in studying the dynamics of plasmonic charge transfer of hot carriers on bimetallic substrates and has been investigated by Boerigter et al.[93] Wavelength-dependent Stokes and anti-Stokes surface-enhanced Raman spectroscopy (SERS) of MB molecules chemisorbed on Au@Pt core-shell nanoisland substrates structures has been used to probe plasmon induced direct charge transfer. The Stokes Raman signal is indicative of the rate of transition of a molecule excited from its ground state to its first vibration state. The reverse-transition is indicated anti-Stokes Raman signal.[373] As such, by monitoring the vibrational temperature of the plasmonic substrate and the attached adsorbate simultaneously upon resonant illumination, one can discern the flow of charge carriers from the metal nanoparticle to the adsorbed molecules via plasmon induced hot carrier injection.[129]

Stokes and anti-Stokes scattering signals were measured for the most consistent of our bimetallic Au@Pt core-shell nanoisland substrates. These substrates involved a 40 s Au to 20 s Pt deposition ratio. Lattice temperatures were calculated and the corresponding Stokes and anti-Stokes Raman spectrum of the bimetallic composite upon illumination by a 532 nm laser is shown in **(Figure 5.10).** We note that under 532 nm illumination, due to weak anti-Stokes signals, we were only able to confidently measure the temperatures of the 328 cm^{-1}, 442 cm^{-1} and 491 cm^{-1} modes. **(Table 2)**

Raman Mode (cm^{-1})	Temperature (K)
328	397.81
442	332.38
491	397.05

Table 2. Raman Temperatures for corresponding Raman modes.

The rise in temperature though seemingly small is comparable to those generated involving bimetallic substrates with a MB adsorbate under 532 nm illumination.[93,129] The low temperatures can also be attributed to the strong damping, as observed from the broadened linewidths of the LSPR spectra in **(Figure 5.2),** in the Au@Pt bimetallic system when compared to monometallic Au nanoislands. As seen in the work of Boerigter et al.[93], illumination closer to the redshifted resonance value of the Au@Pt bimetallic substrate may provide greater anti-Stokes signal intensities. The rise in temperature is still indicative of an elevated vibrational population in the adsorbate-plasmon system and is a signature of plasmon generated hot carrier injection from the bimetallic substrate to the surface. This is also particularly impressive considering that Au in general does not provide temperature enhancement for MB adsorbates while its counterpart in Ag does a much better job, furthering the potential of Au@Pt as a standalone plasmonic substrate.

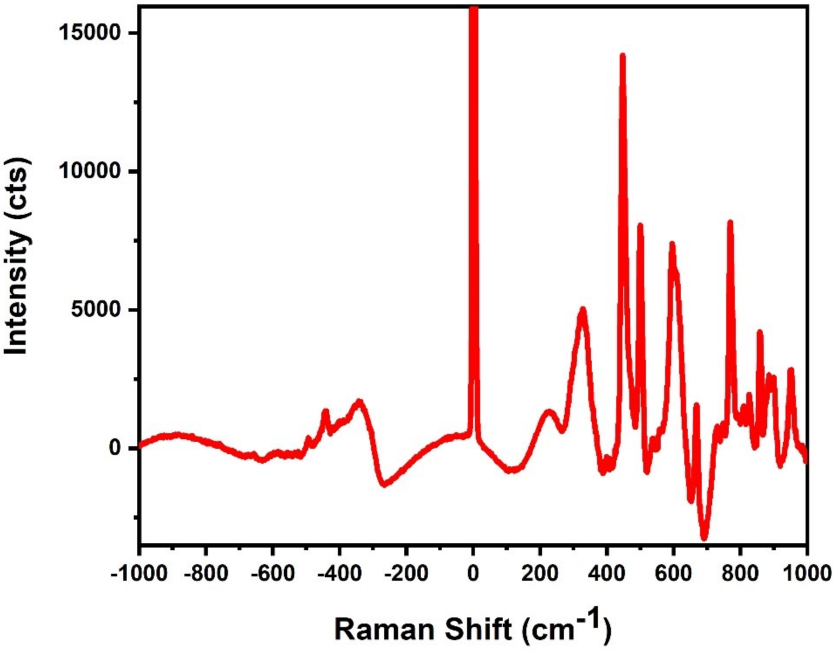

Figure 5.10. Raman thermometry Stokes and anti-Stokes spectra of MB on Au@Pt substrate. The corresponding temperatures of the measured Raman modes are presented in Table 2.

5.4 Conclusion

Au@Pt core-shell nanoislands on glass were fabricated using a combination of magnetron sputtering and thermal annealing in a process that provides greater consistency compared to wet-chemical or colloidal synthetic techniques. The addition of Pt shells of varying thicknesses provided for the modulation of the plasmonic response of the bimetallic composite while offering insights on the photocatalytic potential of the bimetallic substrates in the absence of a semiconductor support via methylene blue dye degradation. The corresponding results suggested the necessity and importance of shell engineering to provide for efficient plasmon-mediated chemical conversion with thinner Pt shells providing greater scope for dye degradation as opposed to thicker shells. FDTD simulations provided fundamental insights into the crucial influence of morphology and the advantage of inter-island channels and gaps to amplify the plasmonic activity of the bimetallic substrates. The addition of the Pt film provides for a general increase in absorption intensity as well as a catalytic surface for adsorption and surface insulation allowing for sample stability. Pt loading of the Au nanoislands progressively broadens the Au LSPR and is proof of strong electronic coupling between the Au LSPR and the catalytic metal at the substrate surface. The resulting resonance is ever so slightly redshifted but indicates that the LSPR effect is largely delegated by the plasmonic Au core. The integration of both metals does offer for broadband excitation which is a prerequisite for many applications in photocatalysis. Altogether, our study demonstrates a facile means to fabricate Au@Pt bimetallic substrates that are effective as standalone plasmonic materials, and whose potential can be improved upon via shell engineering of the Pt surface. Raman thermometric studies confirm the existence of plasmon generated hot carrier injection that facilitates dye degradation where the LSPR of the Au core dephases via the generation of hot carriers expelled into the Pt shell. With a preference towards thinner catalytic shells to provide for chemical reactivity while not compensating on sample stability, and the damping of resonant coupling our study establishes that these Au@Pt substrates meet the standards of an efficient core-shell bimetallic plasmonic catalyst by demonstrating plasmon-adsorbate coupling, effective plasmonic field strengths, and hot carrier densities.

Chapter 6
Future Directions

6.1 A Retrospective

Plasmonic photocatalysis is driven by the presence of noble metal nanoparticles that can perform photochemical reactions when illuminated with relatively low-intensity light.[83,95,102,134] The LSPR of plasmonic noble metals results in high extinction of light and the generation of large localized electric fields on the surfaces of said materials. Together, this paves the way for high generation rates of energetic charge carriers that assist in catalyzing chemical transformations.[100,103,360,374–376]

The incorporation of plasmonic noble metal nanoparticles for photocatalysis is a promising endeavor, but as a field, plasmonic photocatalysis lacks an established theoretical framework supported by experiments that can comprehensively describe the hot carrier dynamics crucial to the functionality of plasmonic noble metal nanoparticles. My doctoral research was largely motivated by these challenges to explore the individual constituents of plasmonic photocatalysis in a bottom-up approach building from monometallic to bimetallic systems. My thesis focused on understanding the nanoscopic plasmon mechanisms of these nanostructures alongside their evaluation as potential photocatalytic platforms. Beginning with monometallic constituents, I constructed Ag nanoislands that demonstrated great potential for surface catalytic reactions involving aromatic thiols and surface enhanced Raman spectroscopy of Rhodamine 6G molecules. Silver's chemical stability notwithstanding, I gradually switched to utilizing Au nanoislands as a better platform for plasmonic photocatalysis. With a similar fabrication procedure to that used to fabricate Ag nanoislands, I developed a set protocol for high quality Au nanoisland samples with great consistency and high quality plasmon responses.

As individual components, Au and Ag nanoislands are limited in their use for photocatalytic applications. This led me to consider bimetallic nanostructures beginning with Au@Pt core-shell nanoislands. The significance of my work revolving around the fabrication of these monometallic and bimetallic substrates is highlighted by the consistency, and reproducibility of the methods utilized to fabricate these nanostructures. The same method can be applied to construct nanoislands of other representative plasmonic metals and core-shell structures as well. The added benefit of PVD methods as opposed to wet-chemical synthesis methods to fabricate plasmonic nanostructures is the easy modulation and production of strong plasmon resonance behavior that is crucial to their functionality. The high-quality resonances observed of monometallic nanoislands, and the plasmon resonance modulation of bimetallic nanostructures demonstrated a facile approach toward the construction of these nano-architectures. This is in sharp contrast with wet-synthesis techniques where consistency is hard to come by. My experimental efforts were supplemented by theoretical studies of my nanostructures using Lumerical FDTD simulations.

These efforts have set the stage for various future directions of research to further develop and optimize these systems in higher level architectures for plasmonic photocatalysis.

6.2 Exotic Bimetal Nanostructures

Extending the established fabrication and simulation protocols to include exotic bimetal nanostructures to diversify plasmon modulation using various materials would be crucial. On this objective, by collaborating with my colleagues in various projects (as outlined in Section 3.5) and my own doctoral research I have been able to identify unique architectures for plasmonic bimetal platforms.

6.2.1 Other Bimetallic Combinations

Homodimer and heterodimer arrangements of Ag-Cu nanoparticles (Section 3.5.2) have focused on taking advantage of the asymmetric charge distributions of the LSPR for photocatalysis.[200] Bimetallic Au@Pt core-shell nanoislands have demonstrated great potential in their facile means of fabrication and use for dye degradation. It is imperative that we extend the fabrication techniques utilized to create nanoislands toward more exotic bimetallic combinations such as Au-Pd, Ag-Au, Au-Ru, Ag-Ir, Co-Au, Mn-Au, Zn-Pd etc.

To begin with, Lumerical FDTD simulations have been utilized to model a few of these combinations. These simulations constituted the early foundations of my work involving plasmonic bimetallic photocatalytic architectures and have been continually improved. The simplest and most analytically feasible geometries of spherical (not hemispherical) nanostructures was analyzed. With reference to the work of Zhang et al.[311] Mie theory was used to investigate the LSPR properties of pristine bimetallic core-shell nanoparticles consisting of metals including Au, Ag, Pt, Cu, Ni, Cr, and Pd. The simulations were utilized to discern the ordinary and extraordinary LSPR modes that together determine the line shape of the extinction spectrum and the shifts of the LSPR peaks for diverse parametric constraints such as varying core to shell radii ratios, varying environments, diverse morphologies (nanocubes, etched bimetallics, spherical shells), etc.

While the current standard of bimetallic core-shell structures involves a plasmonic core and a catalytic shell (like Au@Pt), diverse morphologies involving a catalytic core and a plasmonic shell (Pt@Au), an evacuated core (Air@Au), and etched-shell architectures were considered, accounting for some unique results. Practical noble metal architectures involving the standard configurations have demonstrated a high tunability of the LSPR in the visible spectral regime. Similar results were observed for bimetallic core-shell nanocubes. Reverse core-shell nanosphere configurations of the same metals also produced LSPR shifts towards the visible regime with particularly high-quality factor LSPR peaks in the far visible spectral range that have not been observed in prior theoretical studies. **(Figure 6.1)** Unlike before, similar such behavior was not evident in the case of reverse core-shell nanocubes that rather demonstrated a broadened plasmon resonance over the visible spectral range. While the observation of LSPRs in the visible and far-visible spectral range is of paramount importance in photocatalysis the direct application of reverse bimetallic core-shell configuration is by theory less ideal. This is because the catalytic metal is now embedded within another and does not have direct contact with the environment.

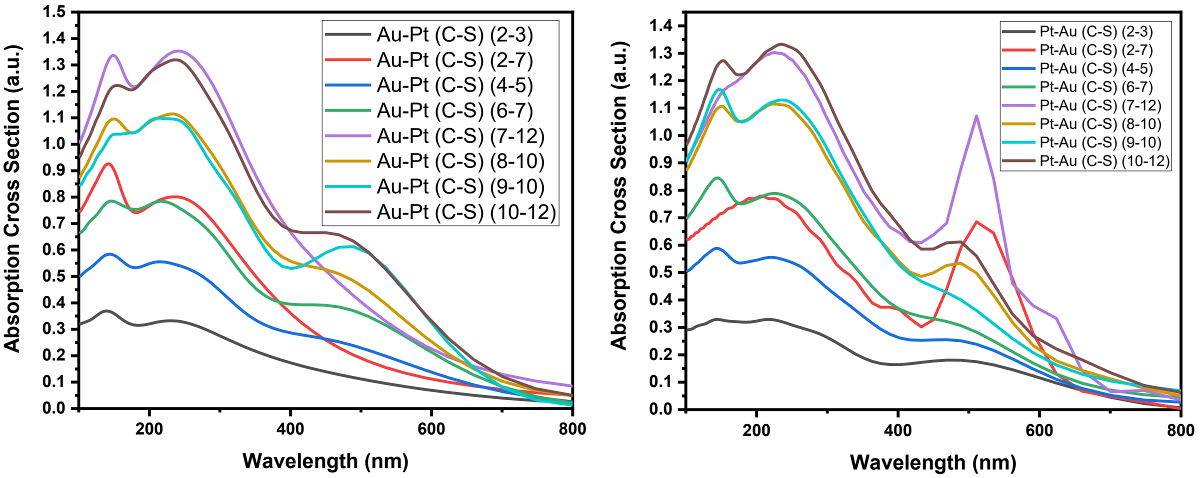

Figure 6.1. Simulated absorption cross-sections of bimetallic Au@Pt and Pt@Au core-shell (C-S) structures for varying inner core and outer shell radii (Core radius-Shell radius) combinations of (2 nm – 3 nm), (2 nm – 7 nm), (4 nm – 5 nm), (6 nm – 7 nm), (7 nm – 12 nm), (8 nm – 10 nm), (9 nm – 10 nm), and (10 nm – 12 nm). Multiple resonance peaks, of ordinary and extraordinary modes, are observable with high absorption peaks in the visible regime for the reverse core-shell (Pd-Au) configurations. The variation in core-shell radii also exhibits an influence in the redshifting of the resonance peaks.

6.2.2 Etched Core-Shell Nanostructures

A noble metal nanoparticle can produce a photocatalytic effect as its LSPR can provide for localized heating effects and energetic electrons that would help jumpstart thermally assisted reactions and photoreductions. This has been observed for pure Au and Ag nanoparticles.[102,377] Pt is also a noble metal but catalytically more active than Au and Ag. Pt has been particularly effective for hydrogen dissociation and H_2 reactions as the Pt surface can adsorb high concentrations of hydroxyl groups that can scavenge photogenerated valence band holes.[378,379] Pt also has a lower Fermi level (i.e. a higher work function) of -6.3 eV compared to -4.7 eV and -5.1 eV for Ag and Au. Because of this, Pt functions as an efficient trap center for electrons, and can assist in increasing the lifetime of electron-hole pairs leading to its prevalence in bimetallic applications where it most often serves as the catalytic shell. To provide for exposure of the catalytic core in the reverse bimetallic configuration, etched bimetallic structures were simulated where the shell is selectively etched to provide for the environment's contact with the core. Compared to earlier results, the LSPR of the bimetallic complex demonstrated high tunability of the LSPR in the visible spectral range with a broad LSPR plasmon band. This included high quality factor LSPR peaks in the far visible spectral range of even greater quality compared to the earlier reverse bimetallic configurations. **(Figure 6.2)**

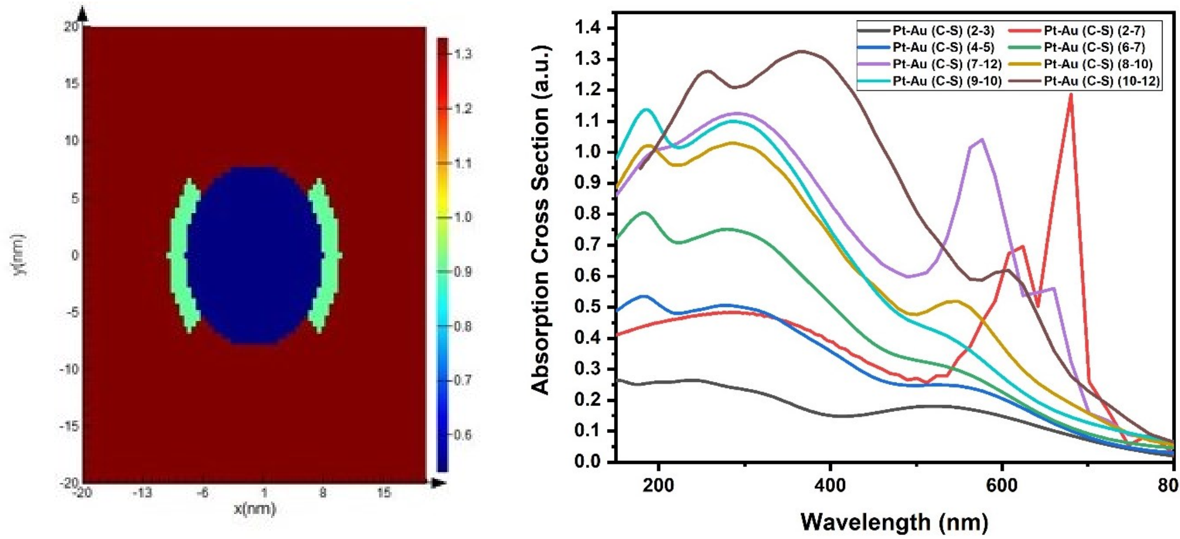

Figure 6.2. (Left) Simulated refractive index monitor of a bimetallic structure where the outer Au shell is etched to provide access to the catalytic Pt core. Simulated absorption cross-sections of the etched Pt-Au core-shell (C-S) structure for varying inner core and outer shell radii (Core radius-Shell radius) combinations of (2 nm – 3 nm), (2 nm – 7 nm), (4 nm – 5 nm), (6 nm – 7 nm), (7 nm – 12 nm), (8 nm – 10 nm), (9 nm – 10 nm), and (10 nm – 12 nm). Multiple broadened resonance peaks are observable with particularly high-quality factor resonance peaks in the far visible regime for the combination of (2 nm – 7 nm) core-shell radii.

6.2.3 Void Plasmons

Another exotic configuration considered involved metallic nanoshells or nanovoids. The simplest nanovoid can be described as a spherical inclusion of dielectric material in a homogeneous metallic body where an electromagnetic dipole resonance can be sustained in a manner akin to a metallic nanoparticle. Maier et al.[46] present that the polarizability of such a nanovoid is,

$$\alpha = 4\pi\alpha^3 \frac{\epsilon_m - \epsilon}{\epsilon_m + 2\epsilon} \tag{6.1}$$

where we have basically substituted ϵ_m for $\epsilon(\omega)$ and vice versa in (1.24). The induced dipole in the nanovoid is antiparallel to the applied electric field on the outside. The Frohlich condition then takes the form $Re[\epsilon(\omega)] = -\frac{1}{2}\epsilon_m$. A 3-D void resonance would consist of a core/shell particle with a dielectric core and a thin metallic shell. Here too, we are able to excite dipolar resonances in the nanoshells that can be attributed to the bonding and anti-bonding combinations of the fundamental sphere and void modes.[46,183] Control of the plasmon dipole resonance via the nanoshell geometry enables shifts in the resonance frequencies in the near-IR spectral region and reduced plasmon linewidths.[46,183,380] **(Figure 6.3)**

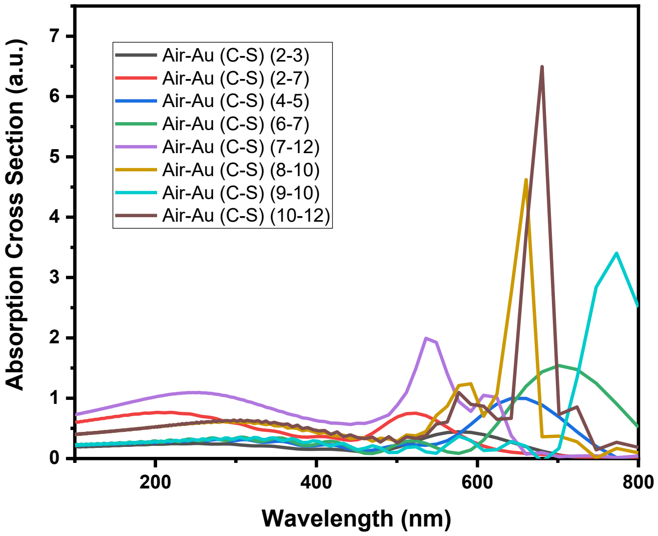

Figure 6.3. Simulated absorption cross-sections of the Au nanoshell structure for varying inner core and outer shell radii (Core radius-Shell radius) combinations of (2 nm – 3 nm), (2 nm – 7 nm), (4 nm – 5 nm), (6 nm – 7 nm), (7 nm – 12 nm), (8 nm – 10 nm), (9 nm – 10 nm), and (10 nm – 12 nm). High quality factor plasmonic resonances are observed in the far visible regime for select core-shell radii combinations.

6.2.4 Closing Remarks

By adapting Mie theory, I have calculated and analyzed the extinction spectra and modal profiles for a series of bimetallic spherical core-shell nanoparticles involving various combinations and composition ratios of noble metals described by the ideal Drude model. Two resonance peaks are observed to exist in the extinction spectrum and can be attributed to two different LSPR models in the bimetallic nanoparticle: extraordinary, and ordinary.[311] The extraordinary mode occurs at short wavelengths and is a signature of the interfacial electric field energy between the core and shell metals. The ordinary mode occurs at long wavelengths and describes the electric field energy concentrated at the outer surface of the bimetallic nanoparticle. The localization of the fields in these two modes also exhibit opposite shifts in peak position, being either redshifted or blue-shifted, depending on variations in the core to shell ratio (i.e. the metal thicknesses), and the locations of the constituent metals.

The incorporation of two metals and their different optical response characteristics leads to LSPR response over a broad spectrum with intricate electromagnetic interactions occurring at the interface and at the surface of the bimetallic nanoparticle. The high tunability of the LSPR in bimetallic nanoparticles is highly attractive for creating unique optical properties and features that cannot be facilitated by single component nanostructures. Furthermore, the double LSPR modes and the associated enhancements in the local electric field can be employed for light-matter interaction processes that capitalize on two or more enhancement modes for maximum efficiency, such as molecular fluorescence. Many of these properties are fundamental to the improvement of photocatalytic functionality, and the development of versatile plasmonic systems.

In conclusion, these simulations set the foundation for the construction of these bimetallic systems. The independent optical, physical, and chemical properties including couplings, interactions, and synergistic effects of the constituent metals can be used for enhanced and multi-functional photocatalytic systems. In the context of plasmonics, bimetallic nanoparticles are proof that we can combine the LSPR resonance of a noble metal nanoparticle such as Au and Ag at the visible regime with that of non-resonant material such as Pt and Pd in a single system that is effective for various devices in optics, biology, photocatalysis, and photovoltaics.

6.3 Bimetallic Alloys

The various characterization tests performed in exploring Au@Pt nanoisland structures such as XPS, XRD, and DFT studies have demonstrated how the mixing of metals, electronic structure, and crystallinity can influence the plasmonic behavior of the bimetallic composite. In extending the fabrication protocols utilized in the construction of monometallic and bimetallic nanoislands, the fabrication of bimetallic alloys may prove fruitful to explore this avenue of research. I have fabricated various bimetallic alloys involving Au-Ag, Au-Pt, Ag-Pt, Ag-Cu, and Au-Cu combinations. These alloys have been made using similar PVD techniques to those I have discussed in the fabrication of core-shell nanostructures and involve the deposition of thin films and collective annealing of the samples. The fabrication of these alloys has also led me to consider the use of trimetallic core-shell substrates where I have been able to demonstrate consistent plasmon modulation involving combinations such as AuAg@Pt. It will be important to consider improving the bimetallic library of nanoparticles to include other catalytic metals such as Cu, Pd, and Co, etc. for selective applications in plasmonic photocatalysis. In lieu of the insights I gained from FDTD simulations it would be integral to test different ratios of these bimetallic alloys and understand their plasmon damping behavior to exercise their full potential for photocatalytic applications.

6.4 Exploring Diverse Semiconductor Scaffolds

Having collaborated with my colleagues and peers in various projects where I have provided FDTD simulations modeling noble metal-semiconductor heterojunctions, I have learned that there is great potential to the incorporation of plasmonic monometal and bimetal nanostructures in semiconductor scaffolds. The PVD methods utilized to fabricate bimetallic and monometallic nanostructures are easily transferable and provide for the conformal coating of the semiconductor scaffold. Combined with separate or collective thermal annealing, we can develop systems where the plasmonic metals can either decorate or be embedded within the semiconductor lattice providing for greater plasmonic performances, a strategy that has been utilized by Farsinezhad et al.[23]

A vast library of literature exists in the use of noble metal-TiO_2 semiconductor heterojunction photocatalysts in various architectures. To a certain degree, the popularity of TiO_2 has led to the field being saturated with research focusing exclusively on this material. Moving forward, it would be beneficial to consider the use of other equally unique and promising semiconductor photocatalytic platforms of note including Fe_2O_3, MoO_3, WO_3, and Cu_2S. In the case of the latter, I have grown Cu_2S in the form of fractal dendrites on three different substrates including glass, FTO, and Cu-foil. The growth of Cu_2S is achieved through electrochemical anodization and is easily reproducible. Preliminary results on the optical characteristics of the fractal dendrite samples have demonstrated broad resonances in the visible as well as high quality resonances in the far-IR regions of the electromagnetic spectrum. Current efforts are being made to optimize the growth of these samples in terms of large-scale uniformity followed by the incorporation of monometallic colloidal Au/Ag nanoparticles or bimetallic Au@Pt core-shell nanoparticles. Concerning Fe_2O_3 and MoO_3, electrochemical anodization techniques to create Fe_2O_3 and MoO_3 nanotubes in a manner reminiscent to TiO_2 nanotubes are available and can be readily replicated. Preliminary experiments involving the use of MoO_3 films in conjunction with monometallic nanoislands have been achieved demonstrating broad plasmon resonances in the visible spectral range for a potential z-scheme system. The use of p-type semiconductors such as WO_3 would motivate harnessing the energy of hot holes as opposed to hot electrons for photocatalysis in applications such as CO_2 photoreduction.

6.5 Engineering the Schottky Barrier

The functionality of noble metal-semiconductor heterojunction systems involving plasmonic nanodimples, TiO_2 nanotubes, and others explored in Chapter 3 depend on the injection of hot charge carriers over or through the established Schottky barriers. The use of PVD protocols to fabricate plasmonic nanostructures in this thesis can also be readily applied toward addressing the idea of engineering the Schottky barrier that is formed in noble-metal nanoparticle-semiconductor systems so that low-energy Drude electrons can be harvested alongside hot electrons themselves. Drude electrons, due to their low energy, are closer to equilibrium and normally would not be worth harnessing. Rather than lowering the Schottky barrier, a thinner barrier would allow for these carriers to be transferred via tunneling. By embedding semiconductor nanoparticles in thin, transparent or translucent films of plasmonic noble metals such as gold or silver, one can form nanocomposites that exploit this idea. The smaller size of semiconductor nanoparticles would mean that they are too small to sustain a wide depletion region. The hypothetical anomalous high concentration of injected charge carriers in the semiconductor nanoparticle can be demonstrated via UV-Vis-NIR spectroscopy, hole scavenger reactions, and by measuring the electrical conductivity of the composite before, during, and after visible light illumination.

6.6 Plexcitonics and Colloidal Nanostructures

The incorporation of 2D and excitonic materials with plasmonic platforms has been promising.[207] Hybrid architectures involving graphenic supports can help expand on the suite of systems that can be utilized for plexcitonic photocatalysis. These systems can be constructed similarly to what has been discussed in Section 6.4. Apart from plasmonic nanoislands and colloidal nanoparticles, I have also successfully synthesized stable citrate-capped silver nanoprisms and nanorods that demonstrate high quality dipolar and quadrupolar resonances between 350 – 700 nm. The use of these nanostructures in semiconductor scaffolds and as individual systems alike would be highly promising. Nanoprisms and nanorods allow for modulation of the plasmon resonance via their unique morphologies. The tips of nanoprisms provide for greater hotspots and concentrated local field enhancements compared to rounded nanostructures while nanorods provide for resonances along selective axes of illumination. These characteristics lean toward diverse uses of these nanostructures for plasmon-enhanced photocatalysis.

6.7 Studying Plasmonic Damping

In plasmonics, there are four major damping mechanisms: Landau damping, Radiative damping, CID, and surface scattering. Landau damping is an intrinsic feature of wave-like oscillations and follow the motion of particles that either tend to accelerate along the wave or move in phase with the wave. This very phenomenon has been identified to result in the dephasing of the LSPR. Radiative damping follows relaxation of the LSPR via the re-emission of photons. CID has been observed in plasmonic noble metal-molecular adsorbate systems and proceeds through the direct relaxation of the LSPR through DIET. Surface scattering is governed by relaxation through electron-electron collisions at the surface of the plasmonic noble metal as well as through surface reflection. CID and surface scattering largely occur in smaller nanoparticles around sizes of 5 nm and mostly vanish for particles of size larger than 20 nm where Landau damping and radiative relaxation dominate.

In my thesis the latter two are more influential, but it is difficult to distinguish between these mechanisms when it comes to bimetallic systems. This is where electron energy loss spectroscopy (EELS) can be very helpful. Using EELS to identify and characterize the bulk plasmon modes of the individual metal components in bimetallic substrates can help us understand the damping mechanisms at play in the composite system. Shifts in the bulk resonances due to changes in the carrier density or effective mass via alloying or mixing of metals would be signatures to consider. FDTD simulations have come to play a significant role in optimizing the experimental efforts involved by simulating the EELS setup within Lumerical.

6.8 Tailored Nanoislands

The modulation of the LSPR of Au@Pt nanoislands was facilitated by varying deposition times and the development of inter-island channels providing active catalytic sites for adsorption as well as near-field enhancements of the plasmon resonance. Similar observations were made for monometallic Ag nanoislands. Thus, the optimization of fabrication methods focused on the development of these modified surface nanostructures would be essential to future experiments involving plasmonic nanoisland systems devised using PVD methods.

By varying not only the annealing temperature but also the duration of annealing, one can modulate the extent of dewetting as defined by the Young-Dupré principle, thus resulting in variations of nanoisland structures, that demonstrate a clear influence on LSPR wavelengths and their quality.[381] Oblique angle deposition methods, or glancing angle deposition, would provide for the direct formation of metal nanoislands on a variety of substrates without the need for heating providing further control of the growth process by moderating the quantity of evaporated metals, and the tilt angle between the substrate and the metal source.

Pre-textured or templated surfaces can extend the size of the nanoislands alongside improved uniformity, and the formation of three-dimensional nanoisland structures. Repeated solid-state dewetting can also assist in precise modulation of nanoisland gaps for optimal field enhancement and overcome the limitations of single solid-state dewetting for small gap spacings, as average nanoisland size and gap space increase with film thickness. Kang et al.[382] have demonstrated the repeated dewetting scheme can overcome this deficiency where nanoislands formed in the first dewetting run accelerate the coalescence of nanoislands as opposed to nucleation in the second dewetting run. The second dewetting run then increases the nanoisland size but reduces the gap spacing between islands. These methods can be applied in a relatively straightforward manner for the fabrication of core-shell nanoisland structures as well as alloyed films, and other nanoisland based plasmonic substrates.

6.9 Conclusion

To conclude, we must also address the weaknesses of the methods utilized in this thesis. Although magnetron sputtering is a facile means to fabricating these plasmonic nanostructures, sputtering and the subsequent process of annealing does not offer effective control on the monodispersity and uniformity of samples. Colloidal nanoparticles are well-known for their monodisperse properties and are highly effective in that aspect to creating uniform coatings of plasmonic nanoparticles. Thermal annealing in open air conditions can lead to oxidation of samples and contamination. This can be overcome via annealing in an inert gas environment such as Argon. The formation of nanoislands is quite dependent on the substrates utilized with spherical and monodisperse nanoislands most evident in glass substrates as opposed to other conductive substrates such as fluorine-doped tin oxide glass substrates. This makes it difficult for these samples to be utilized for applications that may require conductive substrates such as photoelectrochemical water splitting. This could be offset by fabricating nanoislands on fluorine-doped tin oxide glass substrates instead, with the caveat of greater non-uniformity and varying plasmon behavior. Tailored nanoisland substrates have been suggested to rectify said issues. Further efforts can also be made to explore other aspects of Lumerical FDTD solutions including diverse simulation suites such as MODE, HEAT, etc. for greater insights into plasmon device behavior. Most importantly, more extensive Raman thermometric studies of bimetallic systems in diverse architectures and involving different molecular adsorbates would be useful to gain further understanding of hot carrier mechanisms crucial to these systems. These ideas constitute the myriad and diverse avenues of research that remain to be explored of my doctoral research in plasmonics and leave much to offer in motivation of continuing fundamental studies of these unique artificial photocatalytic platforms.

Appendix -
Supplementary Information

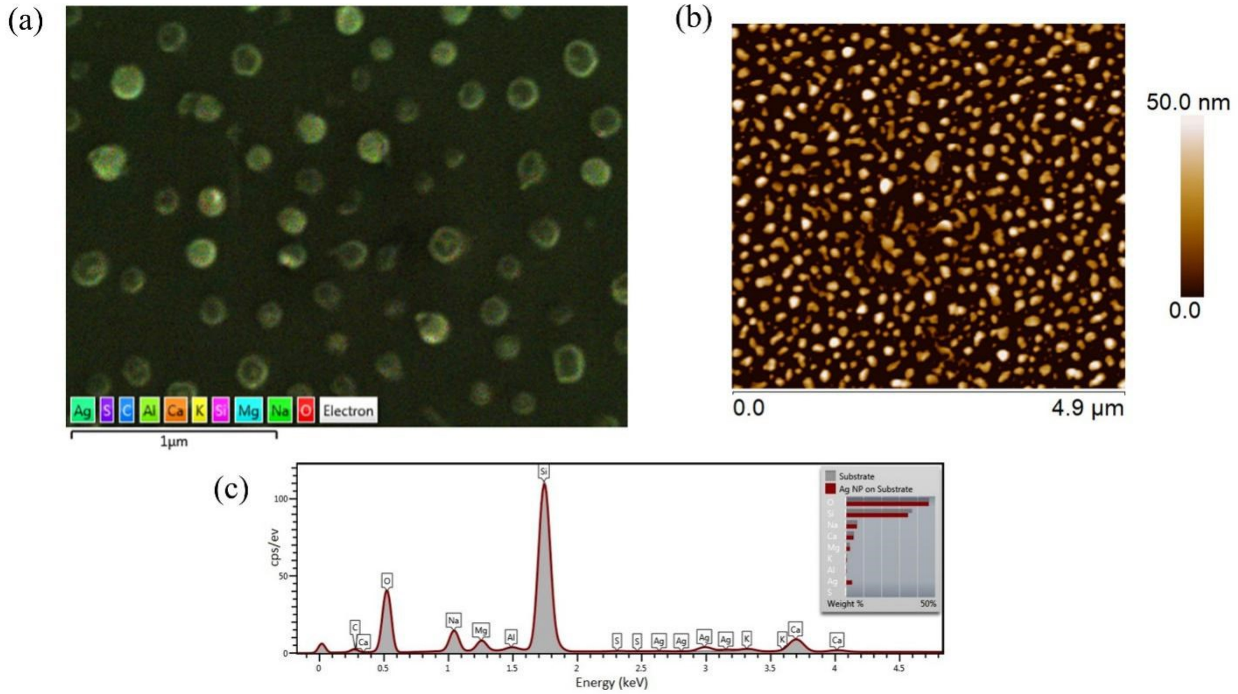

Figure S1. XRD image of Ag film annealed at 400⁰C; (b) AFM image of Ag film annealed at 150⁰C; (c) Elemental weight percentages of Ag film annealed at 400⁰C.

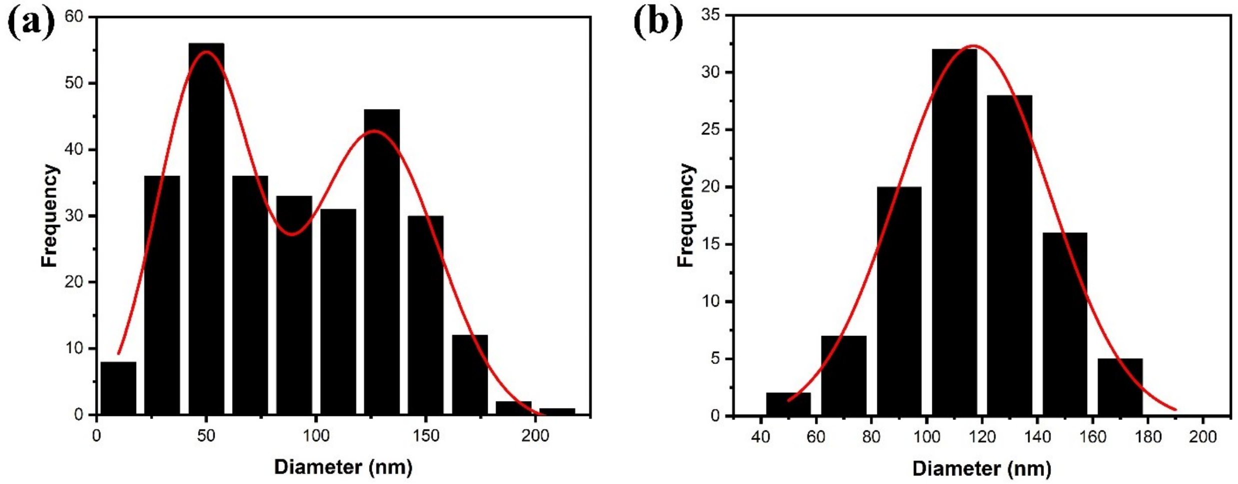

Figure S2. Ag nanoisland size distribution histograms fitted with a Gaussian for (a) Ag films annealed at 150⁰C and (b) Ag films annealed at 400⁰C.

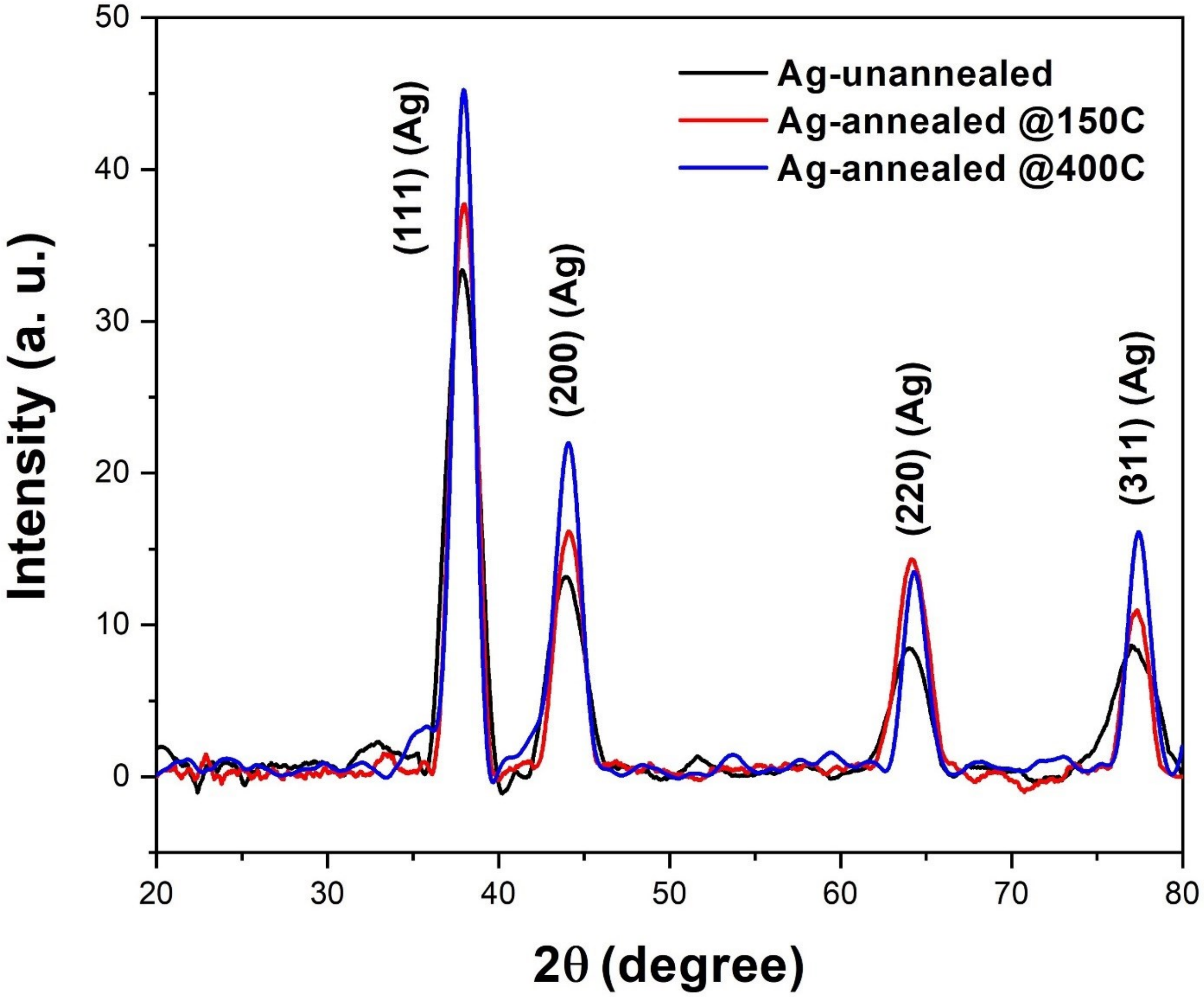

Figure S3. The effect of thermal annealing on the film's microstructure and optical properties have been investigated using XRD on Ag film samples prior to and post-annealing. The absence of the Ag_2O peaks prove minimal oxide has been generated via thermal annealing at 150^0C and 400^0C.

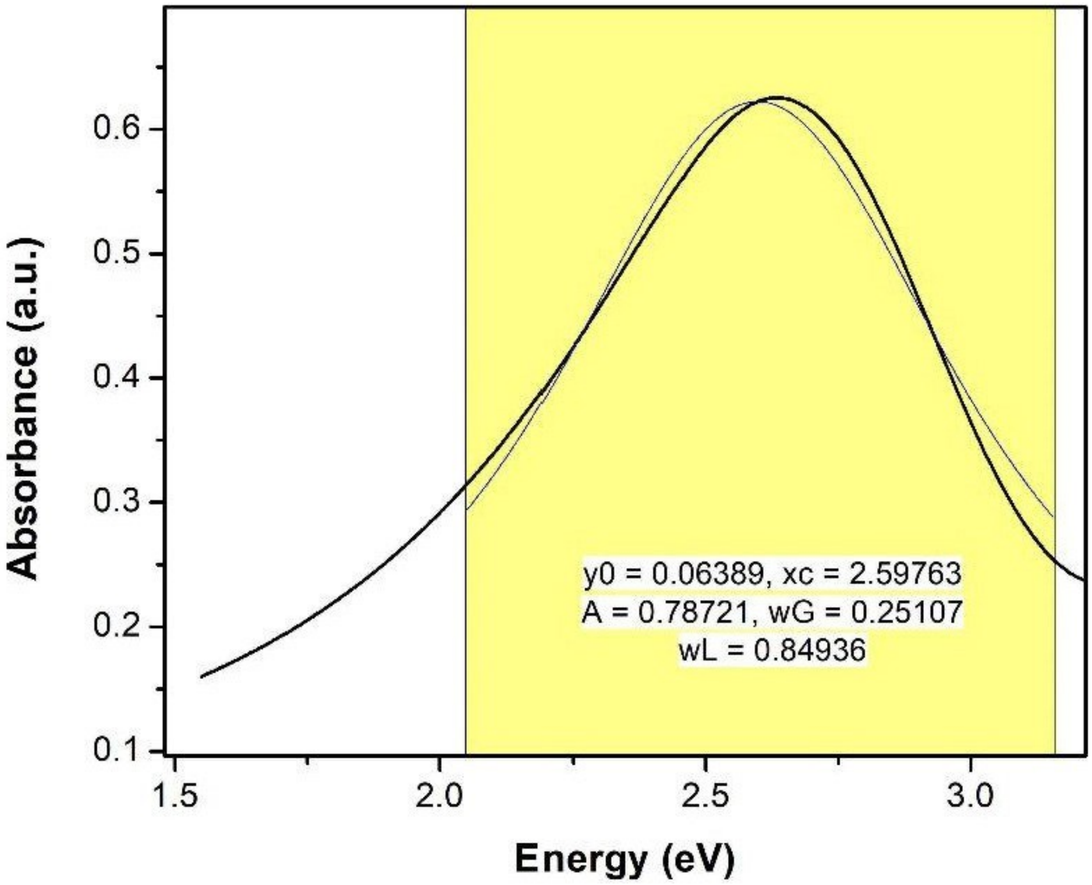

Figure S4. The dipole resonance of Ag nanoislands formed by 150^0C thermal annealing was fit to a Voigt profile to obtain the contributions of homogeneous (Lorentzian) and inhomogeneous (Gaussian) broadening to the overall linewidth.

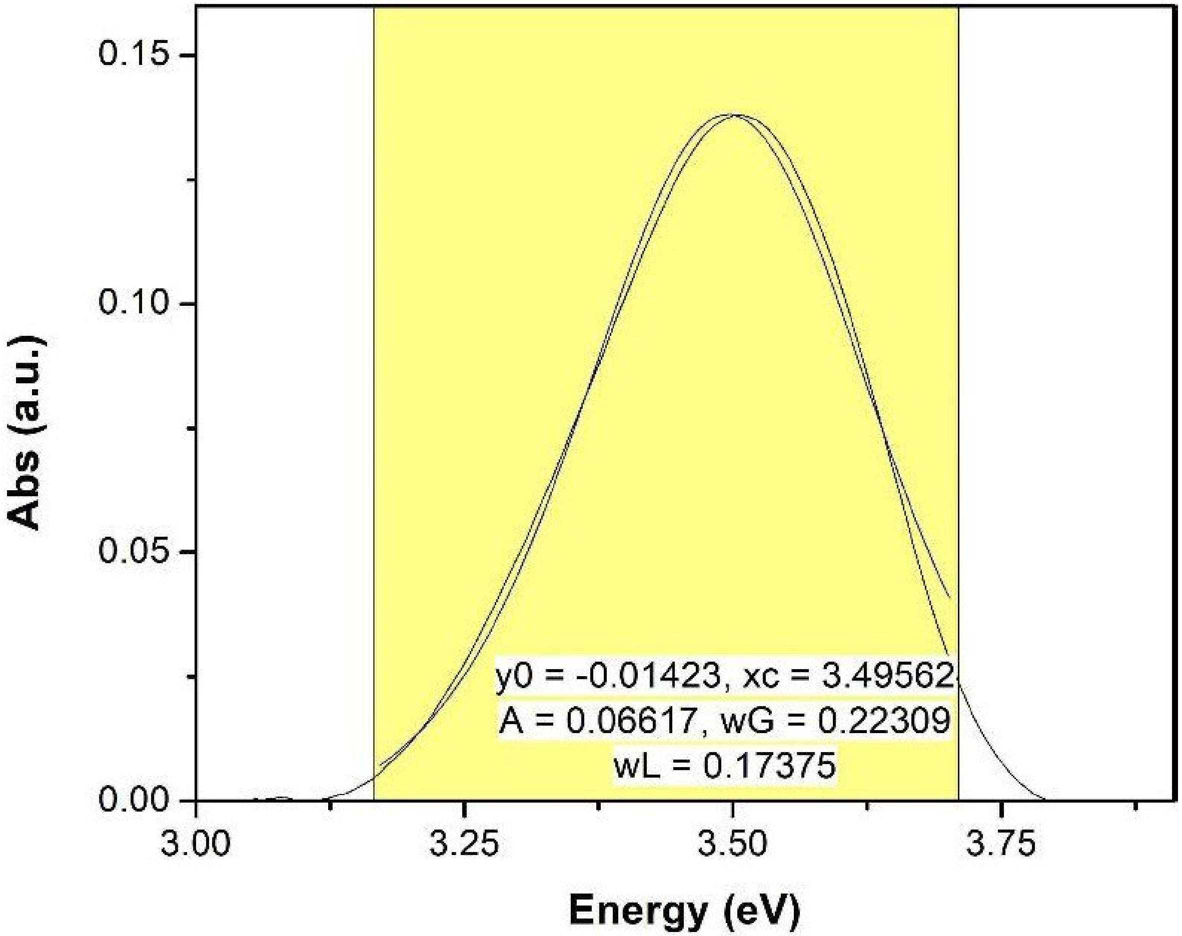

Figure S5. The quadrupole resonance of Ag nanoislands formed by 150^{0}C thermal annealing was fit to a Voigt profile to obtain the contributions of homogeneous (Lorentzian) and inhomogeneous (Gaussian) broadening to the overall linewidth.

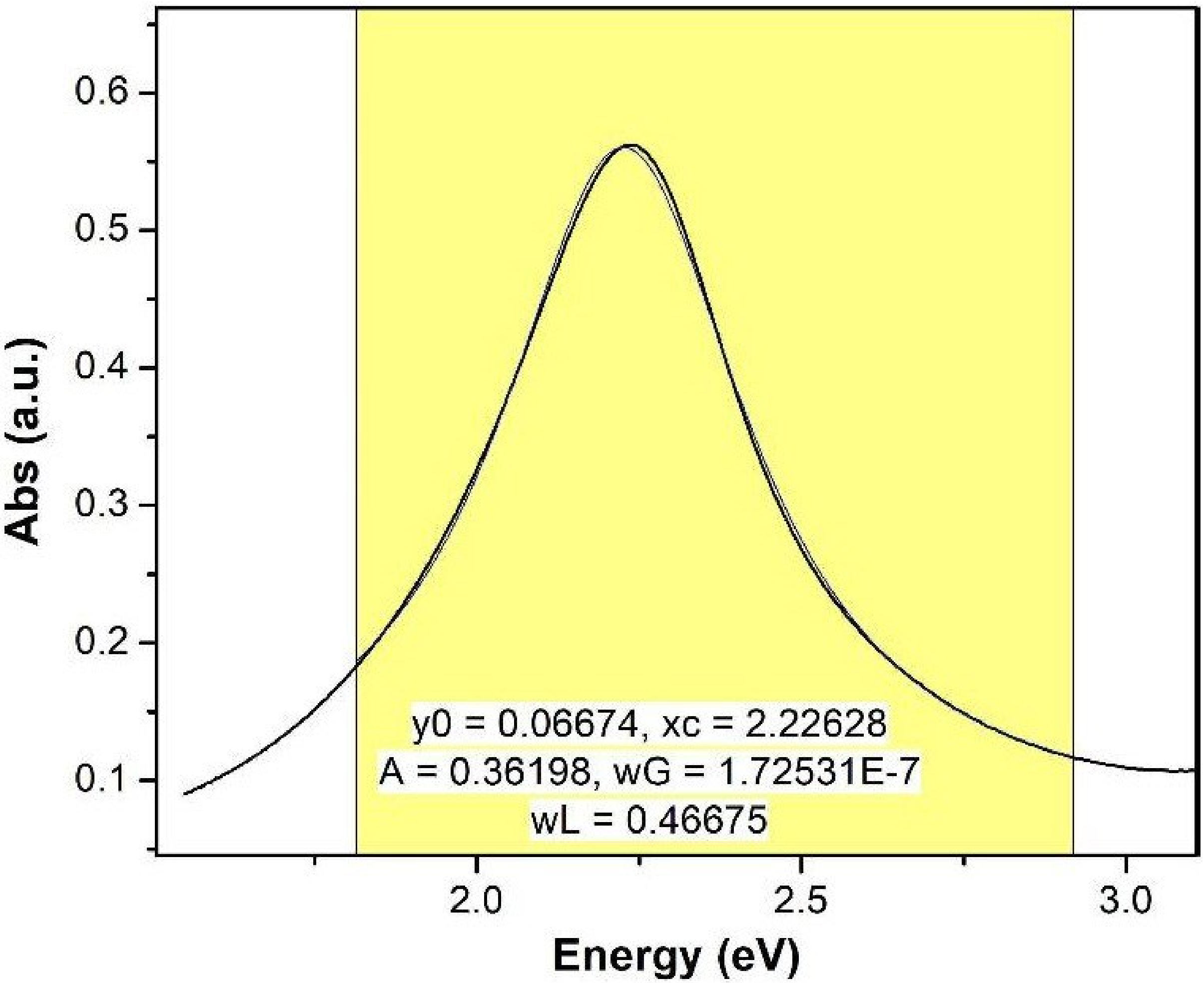

Figure S6. The dipole resonance of Ag nanoislands formed by 400^{0}C thermal annealing was fit to a Voigt profile to obtain the contributions of homogeneous (Lorentzian) and inhomogeneous (Gaussian) broadening to the overall linewidth.

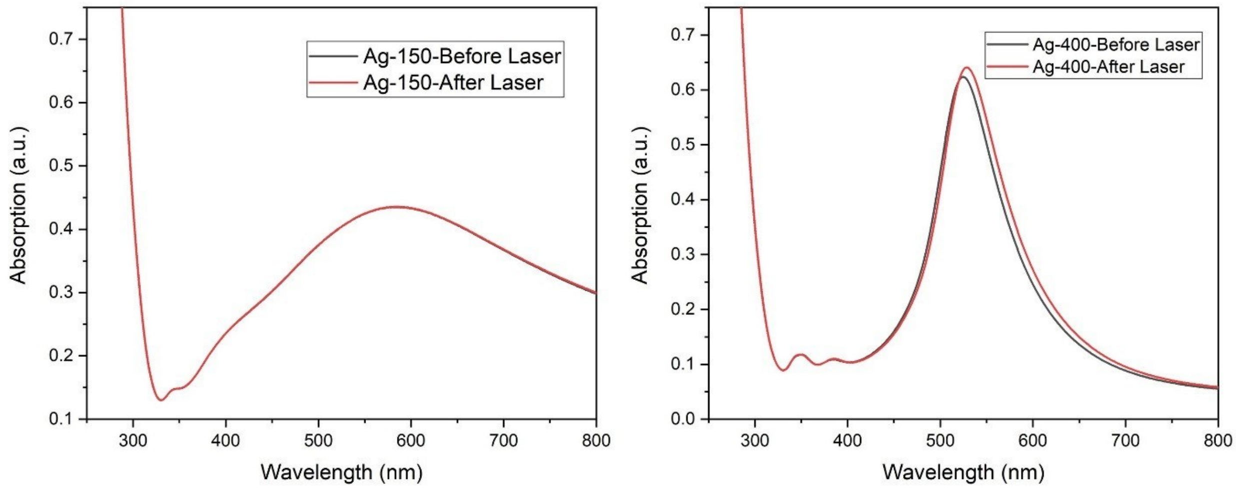

Figure S7. Extinction spectra of Ag nanoisland samples annealed at 150^{0}C (Left) and 400^{0}C (Right) before and after illumination with laser-light from the Raman spectrometer. The negligible change in the extinction spectra confirm minimal photothermal effect by the laser upon the morphology of the plasmonic substrates.

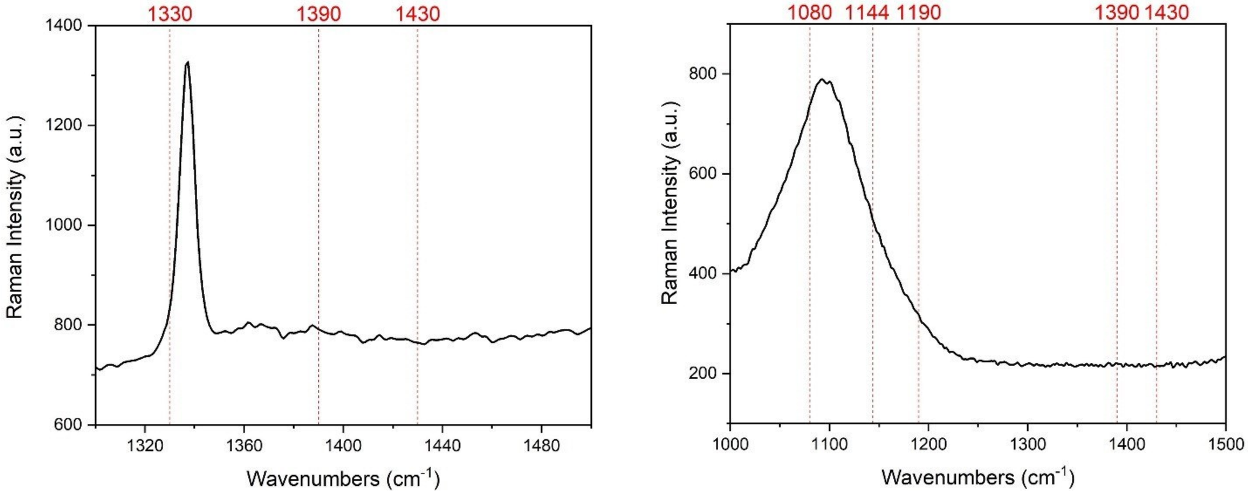

Figure S8. Raman spectra of bare 4NBT (Left) and PATP (Right) under maximum laser light illumination of 8 mW. The absence of peaks at wavenumbers 1390 cm^{-1} and 1430 cm^{-1} confirms zero production of DMAB.

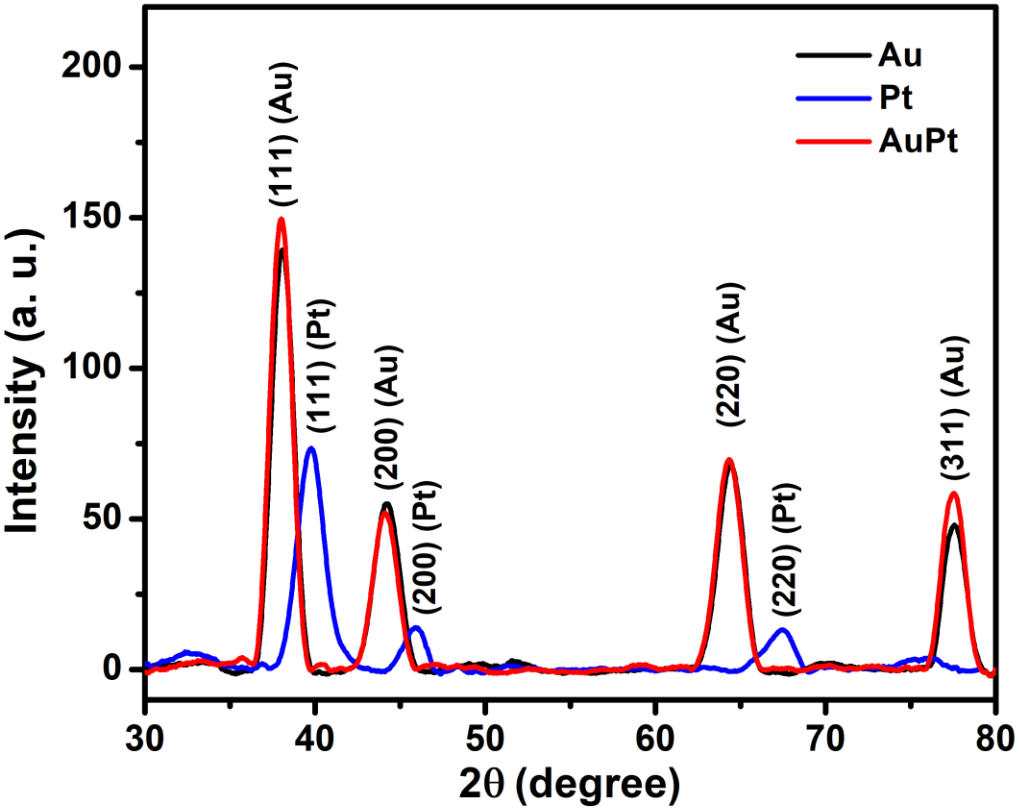

Figure S9. XRD plots of bare Au, bare Pt and Au@Pt hybrid showing the crystal planes of metallic face-centered cubic (fcc) phase.

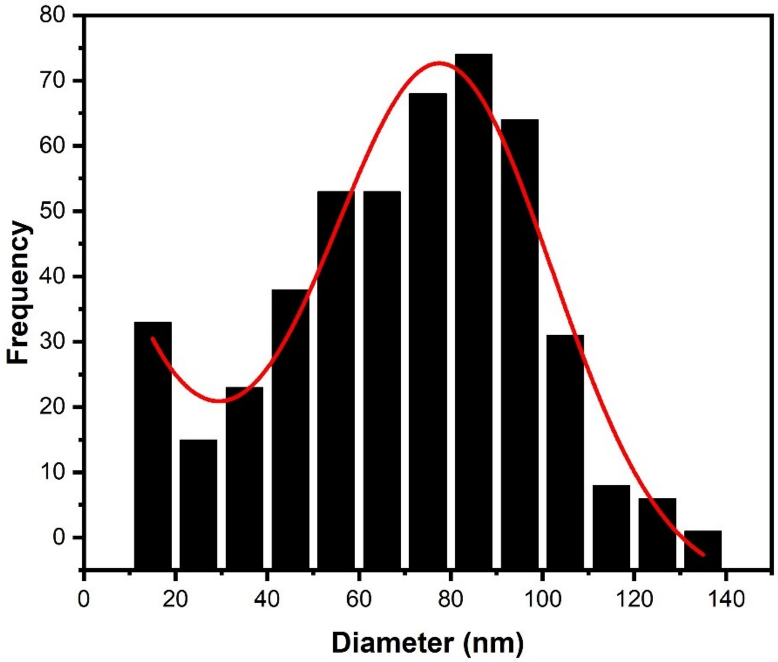

Figure S10. Au@Pt nanoisland size distribution histograms fitted with a Gaussian.

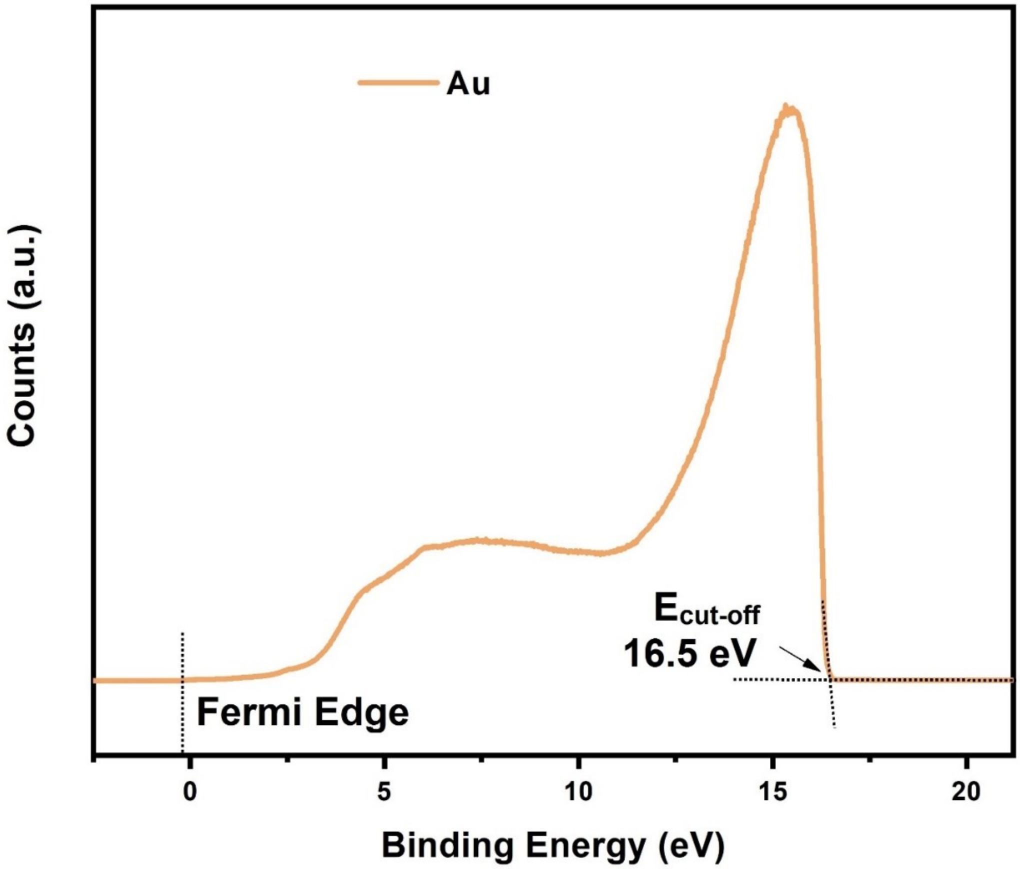

Figure S11. UPS spectra of monometallic Au film on glass substrate with its corresponding secondary electron energy cut-off value.

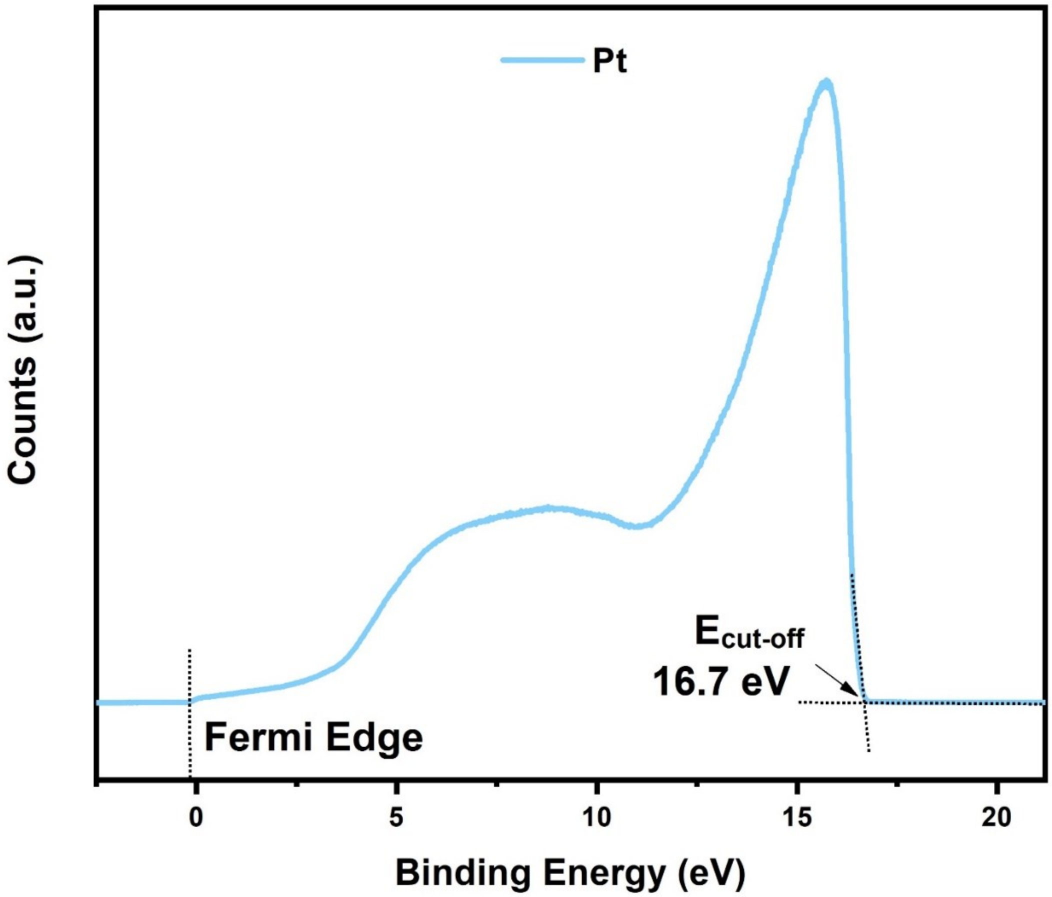

Figure S12. UPS spectra of monometallic Pt film on glass substrate with its corresponding secondary electron energy cut-off value.

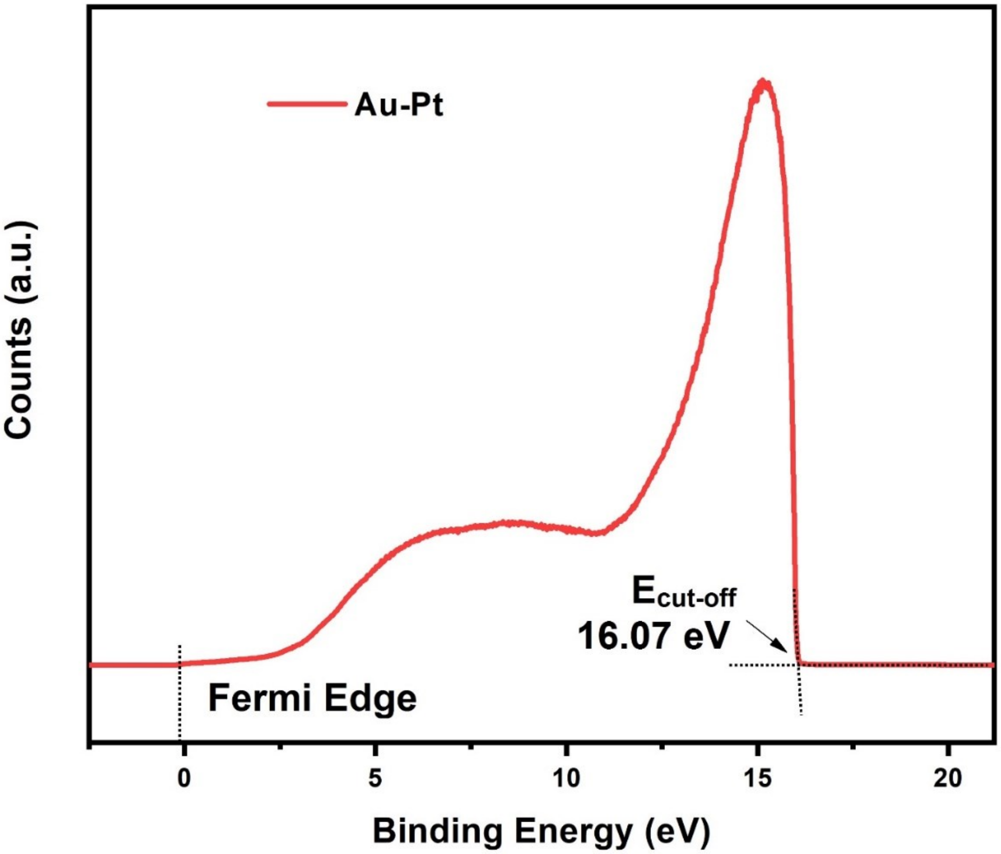

Figure S13.UPS spectra of Au@Pt core-shell nanoislands on glass with their corresponding secondary electron energy cut-off value.

References

1. Kalyanasundaram, K. & Graetzel, M. Artificial photosynthesis: biomimetic approaches to solar energy conversion and storage. *Curr. Opin. Biotechnol.* **21**, 298–310 (2010).
2. Dudley, B. *BP Statistical Review of World Energy*. https://www.bp.com/content/dam/bp/business-sites/en/global/corporate/pdfs/energy-economics/statistical-review/bp-stats-review-2018-full-report.pdf (2018).
3. I.E. Agency. Key World Energy Statistics. http://www.iea.org/weo/.
4. U.E.I. Administration. International Energy Outlook. http://www.eia.gov/forecasts/ieo/.
5. Roy, S. C., Varghese, O. K., Paulose, M. & Grimes, C. A. Toward Solar Fuels: Photocatalytic Conversion of Carbon Dioxide to Hydrocarbons. *ACS Nano* **4**, 1259–1278 (2010).
6. Wang, W.-N., Soulis, J., Yang, Y. J. & Biswas, P. Comparison of CO2 Photoreduction Systems: A Review. *Aerosol Air Qual. Res.* **14**, 533–549 (2014).
7. Cook, T. R. *et al.* Solar Energy Supply and Storage for the Legacy and Nonlegacy Worlds. *Chem. Rev.* **110**, 6474–6502 (2010).
8. Hammarström, L. Overview: capturing the sun for energy production. *Ambio* **41 Suppl 2**, 103–107 (2012).
9. Kudo, A. & Miseki, Y. Heterogeneous photocatalyst materials for water splitting. *Chem. Soc. Rev.* **38**, 253–278 (2009).
10. Fujishima, K. H. and H. I. and A. TiO 2 Photocatalysis: A Historical Overview and Future Prospects. *Jpn. J. Appl. Phys.* **44**, 8269 (2005).
11. Ollis, D. F. Photocatalytic purification and remediation of contaminated air and water. *Comptes Rendus l'Académie des Sci. - Ser. IIC - Chem.* **3**, 405–411 (2000).
12. Herrmann, J.-M. Heterogeneous photocatalysis: fundamentals and applications to the removal of various types of aqueous pollutants. *Catal. Today* **53**, 115–129 (1999).
13. Li, J. & Wu, N. Semiconductor-based photocatalysts and photoelectrochemical cells for solar fuel generation: a review. *Catal. Sci. Technol.* **5**, 1360–1384 (2015).
14. Indrakanti, V. P., Kubicki, J. D. & Schobert, H. H. Photoinduced activation of CO2 on Ti-based heterogeneous catalysts: Current state, chemical physics-based insights and outlook. *Energy Environ. Sci.* **2**, 745–758 (2009).
15. INOUE, T., FUJISHIMA, A., KONISHI, S. & HONDA, K. Photoelectrocatalytic reduction of carbon dioxide in aqueous suspensions of semiconductor powders. *Nature* **277**, 637 (1979).
16. Chatterjee, D. & Dasgupta, S. Visible light induced photocatalytic degradation of organic pollutants. *J. Photochem. Photobiol. C Photochem. Rev.* **6**, 186–205 (2005).
17. Wang, H. *et al.* Semiconductor heterojunction photocatalysts: Design, construction, and photocatalytic performances. *Chemical Society Reviews* (2014) doi:10.1039/c4cs00126e.

18. Wang, P., Huang, B., Dai, Y. & Whangbo, M.-H. Plasmonic photocatalysts: harvesting visible light with noble metal nanoparticles. *Phys. Chem. Chem. Phys.* **14**, 9813–9825 (2012).

19. Zhang, X., Chen, Y. L., Liu, R.-S. & Tsai, D. P. Plasmonic photocatalysis. *Reports Prog. Phys.* **76**, 46401 (2013).

20. Zhang, Y. *et al.* Surface-Plasmon-Driven Hot Electron Photochemistry. *Chem. Rev.* **118**, 2927–2954 (2018).

21. Takahashi, M., Tsukigi, K., Uchino, T. & Yoko, T. Enhanced photocurrent in thin film TiO2 electrodes prepared by sol–gel method. *Thin Solid Films* **388**, 231–236 (2001).

22. Wang, M., Ye, M., Iocozzia, J., Lin, C. & Lin, Z. Plasmonic Photocatalysis: Plasmon-Mediated Solar Energy Conversion via Photocatalysis in Noble Metal/Semiconductor Composites (Adv. Sci. 6/2016). *Adv. Sci.* **3**, (2016).

23. Farsinezhad, S. *et al.* Reduced Ensemble Plasmon Line Widths and Enhanced Two-Photon Luminescence in Anodically Formed High Surface Area Au–TiO2 3D Nanocomposites. *ACS Appl. Mater. Interfaces* **9**, 740–749 (2017).

24. Schneider, J. *et al.* Understanding TiO2 Photocatalysis: Mechanisms and Materials. *Chem. Rev.* **114**, 9919–9986 (2014).

25. Liu, L., Zhao, H., Andino, J. M. & Li, Y. Photocatalytic CO2 Reduction with H2O on TiO2 Nanocrystals: Comparison of Anatase, Rutile, and Brookite Polymorphs and Exploration of Surface Chemistry. *ACS Catal.* **2**, 1817–1828 (2012).

26. Pan, J. *et al.* Synthesis of anatase TiO2 rods with dominant reactive {010} facets for the photoreduction of CO2 to CH4 and use in dye-sensitized solar cells. *Chem. Commun.* **47**, 8361–8363 (2011).

27. Zhao, H., Liu, L., Andino, J. M. & Li, Y. Bicrystalline TiO2 with controllable anatase–brookite phase content for enhanced CO2 photoreduction to fuels. *J. Mater. Chem. A* **1**, 8209–8216 (2013).

28. Anpo, M. *et al.* Photocatalysis over binary metal oxides. Enhancement of the photocatalytic activity of titanium dioxide in titanium-silicon oxides. *J. Phys. Chem.* **90**, 1633–1636 (1986).

29. Wang, W.-N., Park, J. & Biswas, P. Rapid synthesis of nanostructured Cu–TiO2–SiO2 composites for CO2 photoreduction by evaporation driven self-assembly. *Catal. Sci. Technol.* **1**, 593–600 (2011).

30. Zhou, M. *et al.* Ordered Macroporous BiVO4 Architectures with Controllable Dual Porosity for Efficient Solar Water Splitting. *Angew. Chemie Int. Ed.* **52**, 8579–8583 (2013).

31. Riedl, M. J. *Optical Design Fundamentals for Infrared Systems, Second Edition*. *Optical Design Fundamentals for Infrared Systems, Second Edition* (2009). doi:10.1117/3.412729.

32. Pelton, M. & Bryant, G. W. *Introduction to Metal-Nanoparticle Plasmonics*. (John Wiley & Sons, Incorporated, 2013).

33. Novotny, L. & Hecht, B. *Principles of nano-optics*. (Cambridge University Press, 2012).

34. Bittencourt, J. A. *Fundamentals of Plasma Physics*. *Fundamentals of Plasma Physics* (2004).

doi:10.1007/978-1-4757-4030-1.

35. Freestone, I., Meeks, N., Sax, M. & Higgitt, C. The Lycurgus Cup - A Roman nanotechnology. *Gold Bull.* (2008) doi:10.1007/BF03215599.

36. Loos, M. Chapter 1 - Nanoscience and Nanotechnology. in (ed. Loos, M. B. T.-C. N. R. C.) 1–36 (William Andrew Publishing, 2015). doi:https://doi.org/10.1016/B978-1-4557-3195-4.00001-1.

37. SMITH, H. M. JOHANN KUNCKEL: 1630–1703. in *Torchbearers of Chemistry* (1949). doi:10.1016/b978-1-4831-9805-7.50137-7.

38. SMITH, H. M. JEREMÍAS BENJAMIN RICHTER: 1762–1807. in (ed. SMITH, H. M. B. T.-T. of C.) 216 (Academic Press, 1949). doi:https://doi.org/10.1016/B978-1-4831-9805-7.50212-7.

39. Faraday, M. The Bakerian Lecture: Experimental Relations of Gold (and Other Metals) to Light. *Philos. Trans. R. Soc. London* **147**, 145–181 (1857).

40. Zsigmondy, R. Ueber wässrige Lösungen metallischen Goldes. *Justus Liebigs Ann. Chem.* **301**, 29–54 (1898).

41. Mie, G. Beiträge zur Optik trüber Medien, speziell kolloidaler Metallösungen. *Ann. Phys.* **330**, 377–445 (1908).

42. Pines, D. & Bohm, D. A Collective Description of Electron Interactions: II. Collective vs Individual Particle Aspects of the Interactions. *Phys. Rev.* **85**, 338–353 (1952).

43. Ritchie, R. H. Plasma Losses by Fast Electrons in Thin Films. *Phys. Rev.* **106**, 874–881 (1957).

44. Fleischmann, M., Hendra, P. J. & McQuillan, A. J. Raman spectra of pyridine adsorbed at a silver electrode. *Chem. Phys. Lett.* **26**, 163–166 (1974).

45. Jeanmaire, D. L. & Van Duyne, R. P. Surface raman spectroelectrochemistry: Part I. Heterocyclic, aromatic, and aliphatic amines adsorbed on the anodized silver electrode. *J. Electroanal. Chem. Interfacial Electrochem.* **84**, 1–20 (1977).

46. Maier, S. A. *Plasmonics: Fundamentals and Applications*. (Springer, 2007).

47. Fox, M. *Optical Properties of Solids*. (Oxford University Press, Incorporated, 2010).

48. Hanson, G. W. *Fundamentals of Nanoelectronics*. (Pearson/Prentice Hall, 2008).

49. Zemann, J. Crystal structures, 2 nd edition. Vol. 1 by R. W. G. Wyckoff . *Acta Crystallogr.* (1965) doi:10.1107/s0365110x65000361.

50. Panagopoulos, C. N., Markaki, A. & Hontzopoulos, E. Excimer laser treatment of copper-coated mild steel. *J. Mater. Sci.* (1997) doi:10.1023/A:1018589514262.

51. Albuquerque, E. L. & Cottam, M. G. *Polaritons in Periodic and Quasiperiodic Structures*. *Polaritons in Periodic and Quasiperiodic Structures* (2004). doi:10.1016/B978-0-444-51627-5.X5000-7.

52. Eustis, S. & El-Sayed, M. A. Why gold nanoparticles are more precious than pretty gold: Noble metal surface plasmon resonance and its enhancement of the radiative and nonradiative properties of nanocrystals of different shapes. *Chem. Soc. Rev.* **35**, 209–217 (2006).

53. Bohren, C. F. *Absorption and scattering of light by small particles*. *Absorption and scattering of light by small particles* (1983). doi:10.1088/0031-9112/35/3/025.

54. Kreibig, U. & Vollmer, M. *Optical properties of metal clusters.* (Springer, 1995).

55. Mock, J. J., Smith, D. R. & Schultz, S. Local Refractive Index Dependence of Plasmon Resonance Spectra from Individual Nanoparticles. *Nano Lett.* **3**, 485–491 (2003).

56. Link, S. & El-Sayed, M. A. Size and Temperature Dependence of the Plasmon Absorption of Colloidal Gold Nanoparticles. *J. Phys. Chem. B* **103**, 4212–4217 (1999).

57. Jain, P. K., Lee, K. S., El-Sayed, I. H. & El-Sayed, M. A. Calculated Absorption and Scattering Properties of Gold Nanoparticles of Different Size, Shape, and Composition: Applications in Biological Imaging and Biomedicine. *J. Phys. Chem. B* **110**, 7238–7248 (2006).

58. Nishijima, Y., Ueno, K., Yokota, Y., Murakoshi, K. & Misawa, H. Plasmon-Assisted Photocurrent Generation from Visible to Near-Infrared Wavelength Using a Au-Nanorods/TiO2 Electrode. *J. Phys. Chem. Lett.* **1**, 2031–2036 (2010).

59. Rycenga, M. *et al.* Controlling the Synthesis and Assembly of Silver Nanostructures for Plasmonic Applications. *Chem. Rev.* **111**, 3669–3712 (2011).

60. Mock, J. J., Barbic, M., Smith, D. R., Schultz, D. A. & Schultz, S. Shape effects in plasmon resonance of individual colloidal silver nanoparticles. *J. Chem. Phys.* **116**, 6755–6759 (2002).

61. Lou, Z., Fujitsuka, M. & Majima, T. Pt–Au Triangular Nanoprisms with Strong Dipole Plasmon Resonance for Hydrogen Generation Studied by Single-Particle Spectroscopy. *ACS Nano* **10**, 6299–6305 (2016).

62. Huang, X. & El-Sayed, M. A. Gold nanoparticles: Optical properties and implementations in cancer diagnosis and photothermal therapy. *J. Adv. Res.* **1**, 13–28 (2010).

63. Sosa, I. O., Noguez, C. & Barrera, R. G. Optical Properties of Metal Nanoparticles with Arbitrary Shapes. *J. Phys. Chem. B* **107**, 6269–6275 (2003).

64. Kelly, K. L., Coronado, E., Zhao, L. L. & Schatz, G. C. The Optical Properties of Metal Nanoparticles: The Influence of Size, Shape, and Dielectric Environment. *J. Phys. Chem. B* **107**, 668–677 (2003).

65. Seh, Z. W. *et al.* Janus Au-TiO2 Photocatalysts with Strong Localization of Plasmonic Near-Fields for Efficient Visible-Light Hydrogen Generation. *Adv. Mater.* **24**, 2310–2314 (2012).

66. Rivera, V. A. G. Localized Surface Plasmon Resonances: Noble Metal Nanoparticle Interaction with Rare-Earth Ions. in (ed. Ferri, F. A.) Ch. 11 (IntechOpen, 2012). doi:10.5772/50753.

67. Chung, T., Lee, S.-Y., Song, E. Y., Chun, H. & Lee, B. Plasmonic nanostructures for nano-scale bio-sensing. *Sensors (Basel).* **11**, 10907–10929 (2011).

68. Maier, S. A., Kik, P. G. & Atwater, H. A. Observation of coupled plasmon-polariton modes in Au nanoparticle chain waveguides of different lengths: Estimation of waveguide loss. *Appl. Phys. Lett.* **81**, 1714–1716 (2002).

69. Lamprecht, B. *et al.* Metal Nanoparticle Gratings: Influence of Dipolar Particle Interaction on the

Plasmon Resonance. *Phys. Rev. Lett.* **84**, 4721–4724 (2000).

70. Haynes, C. L. *et al.* Nanoparticle Optics: The Importance of Radiative Dipole Coupling in Two-Dimensional Nanoparticle Arrays. *J. Phys. Chem. B* **107**, 7337–7342 (2003).

71. Hicks, E. M. *et al.* Controlling Plasmon Line Shapes through Diffractive Coupling in Linear Arrays of Cylindrical Nanoparticles Fabricated by Electron Beam Lithography. *Nano Lett.* **5**, 1065–1070 (2005).

72. Chen, F. F. *Introduction to Plasma Physics and Controlled Fusion*. *Introduction to Plasma Physics and Controlled Fusion* (2016). doi:10.1007/978-3-319-22309-4.

73. Knight, M. W. *et al.* Aluminum for plasmonics. *ACS Nano* (2014) doi:10.1021/nn405495q.

74. Gutiérrez, Y. *et al.* Plasmonics in the ultraviolet with aluminum, gallium, magnesium and rhodium. *Appl. Sci.* (2018) doi:10.3390/app8010064.

75. Mubeen, S., Hernandez-Sosa, G., Moses, D., Lee, J. & Moskovits, M. Plasmonic Photosensitization of a Wide Band Gap Semiconductor: Converting Plasmons to Charge Carriers. *Nano Lett.* **11**, 5548–5552 (2011).

76. Zhdanov, V. P., Hägglund, C. & Kasemo, B. Relaxation of plasmons in nm-sized metal particles located on or embedded in an amorphous semiconductor. *Surf. Sci.* **599**, L372–L375 (2005).

77. Langhammer, C., Yuan, Z., Zorić, I. & Kasemo, B. Plasmonic Properties of Supported Pt and Pd Nanostructures. *Nano Lett.* **6**, 833–838 (2006).

78. Torimoto, T. *et al.* Plasmon-Enhanced Photocatalytic Activity of Cadmium Sulfide Nanoparticle Immobilized on Silica-Coated Gold Particles. *J. Phys. Chem. Lett.* **2**, 2057–2062 (2011).

79. Hagfeldt, A. & Graetzel, M. Light-Induced Redox Reactions in Nanocrystalline Systems. *Chem. Rev.* **95**, 49–68 (1995).

80. Ridley, B. K. Hot electrons in semiconductors. *Sci. Prog. (1933-)* **70**, 425–459 (1986).

81. Etchegoin, E. L. R. P. *Principles of Surface-Enhanced Raman Spectroscopy 1st Edition and Related Plasmonic Effects*. (Elsevier Science, 2009).

82. Wark, A. W., Lee, H. J. & Corn, R. M. Long-range surface plasmon resonance imaging for bioaffinity sensors. *Anal. Chem.* **77**, 3904–3907 (2005).

83. Kale, M. J., Avanesian, T. & Christopher, P. Direct photocatalysis by plasmonic nanostructures. *ACS Catalysis* vol. 4 116–128 (2014).

84. Stewart, M. E. *et al.* Nanostructured plasmonic sensors. *Chemical Reviews* vol. 108 494–521 (2008).

85. Hirsch, L. R. *et al.* Nanoshell-mediated near-infrared thermal therapy of tumors under magnetic resonance guidance. *Proc. Natl. Acad. Sci. U. S. A.* (2003) doi:10.1073/pnas.2232479100.

86. Carpin, L. B. *et al.* Immunoconjugated gold nanoshell-mediated photothermal ablation of trastuzumab-resistant breast cancer cells. *Breast Cancer Res. Treat.* (2011) doi:10.1007/s10549-010-0811-5.

87. Zhou, W. *et al.* Lasing action in strongly coupled plasmonic nanocavity arrays. *Nat. Nanotechnol.* (2013) doi:10.1038/nnano.2013.99.

88. Jain, P. K., Huang, X., El-Sayed, I. H. & El-Sayed, M. A. Noble metals on the nanoscale: Optical and photothermal properties and some applications in imaging, sensing, biology, and medicine. *Acc. Chem. Res.* (2008) doi:10.1021/ar7002804.

89. Moskovits, M. Surface-enhanced spectroscopy. *Rev. Mod. Phys.* **57**, 783–826 (1985).

90. Moskovits, M. Surface-enhanced Raman spectroscopy: A brief retrospective. *J. Raman Spectrosc.* (2005) doi:10.1002/jrs.1362.

91. Atwater, H. A. & Polman, A. Plasmonics for improved photovoltaic devices. *Nat. Mater.* **9**, 205–213 (2010).

92. Linic, S., Christopher, P. & Ingram, D. B. Plasmonic-metal nanostructures for efficient conversion of solar to chemical energy. *Nat. Mater.* **10**, 911–921 (2011).

93. Boerigter, C., Aslam, U. & Linic, S. Mechanism of Charge Transfer from Plasmonic Nanostructures to Chemically Attached Materials. *ACS Nano* **10**, 6108–6115 (2016).

94. Keyling, R., Schöne, W.-D. & Ekardt, W. Comparison of the lifetime of excited electrons in noble metals. *Phys. Rev. B* **61**, 1670–1673 (2000).

95. Mukherjee, S. *et al.* Hot Electrons Do the Impossible: Plasmon-Induced Dissociation of H2 on Au. *Nano Lett.* **13**, 240–247 (2013).

96. Semenov, A. D., Gol'tsman, G. N. & Sobolewski, R. Hot-electron effect in superconductors and its applications for radiation sensors. *Superconductor Science and Technology* (2002) doi:10.1088/0953-2048/15/4/201.

97. Furube, A., Du, L., Hara, K., Katoh, R. & Tachiya, M. Ultrafast plasmon-induced electron transfer from gold nanodots into TiO2 nanoparticles. *J. Am. Chem. Soc.* (2007) doi:10.1021/ja076134v.

98. Zaleska, A. Doped-TiO2: A Review. *Recent Patents on Engineering* vol. 2 157–164 (2008).

99. Burda, C. *et al.* Enhanced Nitrogen Doping in TiO2 Nanoparticles. *Nano Lett.* **3**, 1049–1051 (2003).

100. Linic, S., Aslam, U., Boerigter, C. & Morabito, M. Photochemical transformations on plasmonic metal nanoparticles. *Nat. Mater.* **14**, 567–576 (2015).

101. Brongersma, M. L., Halas, N. J. & Nordlander, P. Plasmon-induced hot carrier science and technology. *Nature Nanotechnology* (2015) doi:10.1038/nnano.2014.311.

102. Christopher, P., Xin, H. & Linic, S. Visible-light-enhanced catalytic oxidation reactions on plasmonic silver nanostructures. *Nat. Chem.* **3**, 467 (2011).

103. Christopher, P., Xin, H., Marimuthu, A. & Linic, S. Singular characteristics and unique chemical bond activation mechanisms of photocatalytic reactions on plasmonic nanostructures. *Nat. Mater.* **11**, 1044 (2012).

104. Naldoni, A., Shalaev, V. M. & Brongersma, M. L. Applying plasmonics to a sustainable future. *Science (80-.).* **356**, 908 LP – 909 (2017).

105. Christopher, P. & Moskovits, M. Hot Charge Carrier Transmission from Plasmonic Nanostructures. *Annu. Rev. Phys. Chem.* **68**, 379–398 (2017).

106. Li, H. *et al.* Mesoporous Au/TiO2 nanocomposites with enhanced photocatalytic activity. *J. Am. Chem. Soc.* (2007) doi:10.1021/ja069113u.

107. Tsukamoto, D. *et al.* Gold nanoparticles located at the interface of anatase/rutile TiO 2 particles as active plasmonic photocatalysts for aerobic oxidation. *J. Am. Chem. Soc.* (2012) doi:10.1021/ja2120647.

108. Hou, W. *et al.* Photocatalytic conversion of CO2 to hydrocarbon fuels via plasmon-enhanced absorption and metallic interband transitions. *ACS Catal.* (2011) doi:10.1021/cs2001434.

109. Tsu, R. Landau Damping and Dispersion of Phonon, Plasmon, and Photon Waves in Polar Semiconductors. *Phys. Rev.* **164**, 380–383 (1967).

110. Sönnichsen, C., Franzl, T., Wilk, T., Von Plessen, G. & Feldmann, J. Plasmon resonances in large noble-metal clusters. *New J. Phys.* (2002) doi:10.1088/1367-2630/4/1/393.

111. Gieseking, R. L., Ratner, M. A. & Schatz, G. C. Review of Plasmon-Induced Hot-Electron Dynamics and Related SERS Chemical Effects. in *Frontiers of Plasmon Enhanced Spectroscopy Volume 1* vol. 1245 1 (American Chemical Society, 2016).

112. Perner, M. *et al.* Homogeneous line widths of surface plasmons in gold nanoparticles measured by femtosecond pump- and -probe and near-field optical spectroscopy. *J. Lumin.* (1998) doi:10.1016/S0022-2313(97)00145-2.

113. Hartland, G. V., Besteiro, L. V., Johns, P. & Govorov, A. O. What's so Hot about Electrons in Metal Nanoparticles? *ACS Energy Letters* (2017) doi:10.1021/acsenergylett.7b00333.

114. Govorov, A. O., Lee, J. & Kotov, N. A. Theory of plasmon-enhanced Förster energy transfer in optically excited semiconductor and metal nanoparticles. *Phys. Rev. B - Condens. Matter Mater. Phys.* (2007) doi:10.1103/PhysRevB.76.125308.

115. Voisin, C., Fatti, N. Del, Christofilos, D. & Vallee, F. Ultrafast electron dynamics and optical nonlinearities in metal nanoparticles. *J. Phys. Chem. B* (2001) doi:10.1021/jp0038153.

116. Voisin, C. *et al.* Size-dependent electron-electron interactions in metal nanoparticles. *Phys. Rev. Lett.* (2000) doi:10.1103/PhysRevLett.85.2200.

117. Shiraishi, Y. *et al.* Quantum tunneling injection of hot electrons in Au/TiO2 plasmonic photocatalysts. *Nanoscale* (2017) doi:10.1039/c7nr02310c.

118. Ratchford, D. C., Dunkelberger, A. D., Vurgaftman, I., Owrutsky, J. C. & Pehrsson, P. E. Quantification of Efficient Plasmonic Hot-Electron Injection in Gold Nanoparticle-TiO2 Films. *Nano Lett.* (2017) doi:10.1021/acs.nanolett.7b02366.

119. Du, L., Furube, A., Hara, K., Katoh, R. & Tachiya, M. Ultrafast plasmon induced electron injection mechanism in gold-TiO2 nanoparticle system. *Journal of Photochemistry and Photobiology C: Photochemistry Reviews* (2013) doi:10.1016/j.jphotochemrev.2012.11.001.

120. Du, L. *et al.* Plasmon-induced charge separation and recombination dynamics in gold-TiO2 nanoparticle systems: Dependence on TiO2 particle size. *J. Phys. Chem. C* (2009)

doi:10.1021/jp810576s.

121. Wu, K., Chen, J., McBride, J. R. & Lian, T. Efficient hot-electron transfer by a plasmon-induced interfacial charge-transfer transition. *Science (80-.).* **349**, 632 LP – 635 (2015).

122. Nosaka, Y., Takahashi, S., Sakamoto, H. & Nosaka, A. Y. Reaction Mechanism of Cu(II)-Grafted Visible-Light Responsive TiO2 and WO3 Photocatalysts Studied by Means of ESR Spectroscopy and Chemiluminescence Photometry. *J. Phys. Chem. C* **115**, 21283–21290 (2011).

123. Nogawa, T., Isobe, T., Matsushita, S. & Nakajima, A. Preparation and visible-light photocatalytic activity of Au- and Cu-modified TiO 2 powders. *Mater. Lett.* (2012) doi:10.1016/j.matlet.2012.05.031.

124. Zhang, X. *et al.* Photocatalytic conversion of diluted CO2 into light hydrocarbons using periodically modulated multiwalled nanotube arrays. *Angew. Chemie - Int. Ed.* (2012) doi:10.1002/anie.201205619.

125. Rtimi, S., Pulgarin, C., Sanjines, R. & Kiwi, J. Accelerated self-cleaning by Cu promoted semiconductor binary-oxides under low intensity sunlight irradiation. *Appl. Catal. B Environ.* (2016) doi:10.1016/j.apcatb.2015.06.047.

126. Bernareggi, M. *et al.* Flame-made Cu/TiO2 and Cu-Pt/TiO2 photocatalysts for hydrogen production. *Catalysts* (2017) doi:10.3390/catal7100301.

127. Asbury, J. B., Hao, E., Wang, Y., Ghosh, H. N. & Lian, T. Ultrafast electron transfer dynamics from molecular adsorbates to semiconductor nanocrystalline thin films. *J. Phys. Chem. B* (2001) doi:10.1021/jp003485m.

128. Andersen, N. A. & Lian, T. Ultrafast electron transfer at the molecule-semiconductor nanoparticle interface. *Annual Review of Physical Chemistry* (2005) doi:10.1146/annurev.physchem.55.091602.094347.

129. Boerigter, C., Campana, R., Morabito, M. & Linic, S. Evidence and implications of direct charge excitation as the dominant mechanism in plasmon-mediated photocatalysis. *Nat. Commun.* **7**, 10545 (2016).

130. Deng, X. Q. *et al.* Visible-light photocatalytic oxidation of CO over plasmonic Au/TiO2: Unusual features of oxygen plasma activation. *Appl. Catal. B Environ.* (2016) doi:10.1016/j.apcatb.2016.01.055.

131. Karbalaei Akbari, M., Hai, Z., Wei, Z., Hu, J. & Zhuiykov, S. Wafer-scale two-dimensional Au-TiO2 bilayer films for photocatalytic degradation of Palmitic acid under UV and visible light illumination. *Mater. Res. Bull.* (2017) doi:10.1016/j.materresbull.2017.08.001.

132. Lang, Q. *et al.* Graphene “bridge” in transferring hot electrons from plasmonic Ag nanocubes to TiO2 nanosheets for enhanced visible light photocatalytic hydrogen evolution. *Appl. Catal. B Environ.* (2018) doi:10.1016/j.apcatb.2017.08.045.

133. Foerster, B. *et al.* Chemical Interface Damping Depends on Electrons Reaching the Surface. *ACS Nano* (2017) doi:10.1021/acsnano.6b08010.

134. Xiao, Q. *et al.* Alloying Gold with Copper Makes for a Highly Selective Visible-Light Photocatalyst

for the Reduction of Nitroaromatics to Anilines. *ACS Catal.* **6**, 1744–1753 (2016).

135. Valenti, M. *et al.* Hot Carrier Generation and Extraction of Plasmonic Alloy Nanoparticles. *ACS Photonics* (2017) doi:10.1021/acsphotonics.6b01048.

136. Christopher, P., Ingram, D. B. & Linic, S. Enhancing Photochemical Activity of Semiconductor Nanoparticles with Optically Active Ag Nanostructures: Photochemistry Mediated by Ag Surface Plasmons. *J. Phys. Chem. C* **114**, 9173–9177 (2010).

137. Ingram, D. B. & Linic, S. Water Splitting on Composite Plasmonic-Metal/Semiconductor Photoelectrodes: Evidence for Selective Plasmon-Induced Formation of Charge Carriers near the Semiconductor Surface. *J. Am. Chem. Soc.* **133**, 5202–5205 (2011).

138. Hu, C., Lan, Y., Qu, J., Hu, X. & Wang, A. Ag/AgBr/TiO2 Visible Light Photocatalyst for Destruction of Azodyes and Bacteria. *J. Phys. Chem. B* **110**, 4066–4072 (2006).

139. Sun, Y. W. and L. K. and J. K. and H. L. and Z. J. and X. L. and H. D. and X. W. Enhanced photoelectrochemical water-splitting effect with a bent ZnO nanorod photoanode decorated with Ag nanoparticles. *Nanotechnology* **23**, 235401 (2012).

140. Lin, W.-C. *et al.* Controlling SERS intensity by tuning the size and height of a silver nanoparticle array. *Appl. Phys. A* **101**, 185–189 (2010).

141. Lin, W.-C. *et al.* Size Dependence of Nanoparticle-SERS Enhancement from Silver Film over Nanosphere (AgFON) Substrate. *Plasmonics* **6**, 201–206 (2011).

142. Parab, H. J. *et al.* Biosensing, Cytotoxicity, and Cellular Uptake Studies of Surface-Modified Gold Nanorods. *J. Phys. Chem. C* **113**, 7574–7578 (2009).

143. Hutter, E. & Fendler, J. H. Exploitation of Localized Surface Plasmon Resonance. *Adv. Mater.* **16**, 1685–1706 (2004).

144. Zheludev, N. I. The Road Ahead for Metamaterials. *Science (80-.).* **328**, 582 LP – 583 (2010).

145. Plum, E. *et al.* Metamaterials: Optical Activity without Chirality. *Phys. Rev. Lett.* **102**, 113902 (2009).

146. Chen, W. T. *et al.* Manipulation of multidimensional plasmonic spectra for information storage. *Appl. Phys. Lett.* **98**, 171106 (2011).

147. Schuller, J. A. *et al.* Plasmonics for extreme light concentration and manipulation. *Nat. Mater.* **9**, 193 (2010).

148. Smolyaninov, A. V. Z. and I. I. Near-field photonics: surface plasmon polaritons and localized surface plasmons. *J. Opt. A Pure Appl. Opt.* **5**, S16 (2003).

149. Liu, Z., Hou, W., Pavaskar, P., Aykol, M. & Cronin, S. B. Plasmon Resonant Enhancement of Photocatalytic Water Splitting Under Visible Illumination. *Nano Lett.* **11**, 1111–1116 (2011).

150. Tsai, D. P. & Lin, W. C. Probing the near fields of the super-resolution near-field optical structure. *Appl. Phys. Lett.* **77**, 1413–1415 (2000).

151. Ji Huang, H. *et al.* Plasmonic optical properties of a single gold nano-rod. *Opt. Express* **15**, 7132–7139 (2007).

152. Chen, M. W., Chau, Y.-F. & Tsai, D. P. Three-Dimensional Analysis of Scattering Field Interactions and Surface Plasmon Resonance in Coupled Silver Nanospheres. *Plasmonics* **3**, 157 (2008).

153. Lee, J. *et al.* Bioconjugated Ag Nanoparticles and CdTe Nanowires: Metamaterials with Field-Enhanced Light Absorption. *Angew. Chemie Int. Ed.* **45**, 4819–4823 (2006).

154. Lee, S. J., Morrill, A. R. & Moskovits, M. Hot Spots in Silver Nanowire Bundles for Surface-Enhanced Raman Spectroscopy. *J. Am. Chem. Soc.* **128**, 2200–2201 (2006).

155. Taguchi, M. *et al.* HITTM cells—high-efficiency crystalline Si cells with novel structure. *Prog. Photovoltaics Res. Appl.* **8**, 503–513 (2000).

156. Ding, Q. *et al.* Ultrafast Dynamics of Plasmon-Exciton Interaction of Ag Nanowire- Graphene Hybrids for Surface Catalytic Reactions. *Sci. Rep.* (2016) doi:10.1038/srep32724.

157. Aslam, U., Chavez, S. & Linic, S. Controlling energy flow in multimetallic nanostructures for plasmonic catalysis. *Nat. Nanotechnol.* **12**, 1000–1005 (2017).

158. Kühn, S., Håkanson, U., Rogobete, L. & Sandoghdar, V. Enhancement of single-molecule fluorescence using a gold nanoparticle as an optical nanoantenna. *Phys. Rev. Lett.* (2006) doi:10.1103/PhysRevLett.97.017402.

159. Anger, P., Bharadwaj, P. & Novotny, L. Enhancement and quenching of single-molecule fluorescence. *Phys. Rev. Lett.* (2006) doi:10.1103/PhysRevLett.96.113002.

160. Dulkeith, E. *et al.* Fluorescence Quenching of Dye Molecules near Gold Nanoparticles: Radiative and Nonradiative Effects. *Phys. Rev. Lett.* **89**, 203002 (2002).

161. Awazu, K. *et al.* A Plasmonic Photocatalyst Consisting of Silver Nanoparticles Embedded in Titanium Dioxide. *J. Am. Chem. Soc.* **130**, 1676–1680 (2008).

162. Wu, D. & Long, M. Visible light assisted photocatalytic degradation of methyl orange using Ag/N–TiO2 photocatalysts. *Water Sci. Technol.* **65**, 1027–1032 (2012).

163. Yu, J., Dai, G. & Huang, B. Fabrication and characterization of visible-light-driven plasmonic photocatalyst Ag/AgCl/TiO2 nanotube arrays. *J. Phys. Chem. C* (2009) doi:10.1021/jp905247j.

164. Valeur, B. & Berberan-Santos, M. N. *Molecular Fluorescence: Principles and Applications, Second Edition*. *Molecular Fluorescence: Principles and Applications, Second Edition* (2012). doi:10.1002/9783527650002.

165. Paul, K. K. & Giri, P. K. Role of Surface Plasmons and Hot Electrons on the Multi-Step Photocatalytic Decay by Defect Enriched Ag@TiO2 Nanorods under Visible Light. *J. Phys. Chem. C* (2017) doi:10.1021/acs.jpcc.7b05328.

166. Wu, X. *et al.* High-photoluminescence-yield gold nanocubes: For cell imaging and photothermal therapy. *ACS Nano* (2010) doi:10.1021/nn901064m.

167. Zhu, Y. *et al.* Ultrathin nanosheets of palladium in boosting its cocatalyst role and plasmonic effect towards enhanced photocatalytic hydrogen evolution. *RSC Adv.* (2016) doi:10.1039/c6ra09647f.

168. Wang, X. *et al.* Enhanced full-spectrum water splitting by confining plasmonic Au nanoparticles in

N-doped TiO2 bowl nanoarrays. *Nano Energy* (2016) doi:10.1016/j.nanoen.2016.04.013.

169. Zhang, Z., Zhang, L., Hedhili, M. N., Zhang, H. & Wang, P. Plasmonic gold nanocrystals coupled with photonic crystal seamlessly on TiO2 nanotube photoelectrodes for efficient visible light photoelectrochemical water splitting. *Nano Lett.* (2013) doi:10.1021/nl3029202.

170. Kar, P. *et al.* Enhanced CH4 yield by photocatalytic CO2 reduction using TiO2 nanotube arrays grafted with Au, Ru, and ZnPd nanoparticles. *Nano Res.* (2016) doi:10.1007/s12274-016-1225-4.

171. Wang, S., Hou, Y. & Wang, X. Development of a stable MnCo2O4 cocatalyst for photocatalytic CO2 reduction with visible light. *ACS Appl. Mater. Interfaces* (2015) doi:10.1021/am508766s.

172. Zhai, Q. *et al.* Photocatalytic conversion of carbon dioxide with water into methane: Platinum and Copper(I) oxide co-catalysts with a core-shell structure. *Angew. Chemie - Int. Ed.* (2013) doi:10.1002/anie.201301473.

173. Tu, W., Zhou, Y. & Zou, Z. Photocatalytic conversion of CO2 into renewable hydrocarbon fuels: State-of-the-art accomplishment, challenges, and prospects. *Advanced Materials* (2014) doi:10.1002/adma.201400087.

174. Marszewski, M., Cao, S., Yu, J. & Jaroniec, M. Semiconductor-based photocatalytic CO2 conversion. *Materials Horizons* (2015) doi:10.1039/c4mh00176a.

175. Habisreutinger, S. N., Schmidt-Mende, L. & Stolarczyk, J. K. Photocatalytic reduction of CO2 on TiO2 and other semiconductors. *Angewandte Chemie - International Edition* (2013) doi:10.1002/anie.201207199.

176. Wu, B.-H. *et al.* Plasmon-enhanced photocatalytic hydrogen production on Au/TiO2 hybrid nanocrystal arrays. *Nano Energy* **27**, 412–419 (2016).

177. Oubre, C. & Nordlander, P. Finite-difference time-domain studies of the optical properties of nanoshell dimers. *J. Phys. Chem. B* (2005) doi:10.1021/jp044382x.

178. Fuchs, R. Theory of the optical properties of ionic crystal cubes. *Phys. Rev. B* (1975) doi:10.1103/PhysRevB.11.1732.

179. Davis, L. C. Electostatic edge modes of a dielectric wedge. *Phys. Rev. B* **14**, 5523–5525 (1976).

180. Aizpurua, J., Rivacoba, A. & Apell, S. Electron-energy losses in hemispherical targets. *Phys. Rev. B - Condens. Matter Mater. Phys.* (1996) doi:10.1103/PhysRevB.54.2901.

181. Messinger, B. J., Von Raben, K. U., Chang, R. K. & Barber, P. W. Local fields at the surface of noble-metal microspheres. *Phys. Rev. B* (1981) doi:10.1103/PhysRevB.24.649.

182. Waterman, P. C. Symmetry, unitarity, and geometry in electromagnetic scattering. *Phys. Rev. D* (1971) doi:10.1103/PhysRevD.3.825.

183. Prodan, E. & Nordlander, P. Structural tunability of the plasmon resonances in metallic nanoshells. *Nano Lett.* (2003) doi:10.1021/nl034030m.

184. Miller, E. K. Time-domain modeling in electromagnetics. *J. Electromagn. Waves Appl.* (1994) doi:10.1163/156939394X00984.

185. Draine, B. T. & Flatau, P. J. Discrete-Dipole Approximation For Scattering Calculations. *J. Opt. Soc.*

Am. A (1994) doi:10.1364/josaa.11.001491.

186. Hafner, C. & Ballisti, R. COMPEL -The international journal for computation and mathematics in electrical and electronic engineering THE MULTIPLE MULTIPOLE METHOD (MMP) THE MULTIPLE MULTIPOLE METHOD (MMP). *PT) COMPEL—The Int. J. Comput. Math. Electr. Electron. Eng.* (1983).

187. Leung, K. M. & Liu, Y. F. Photon band structures: The plane-wave method. *Phys. Rev. B* (1990) doi:10.1103/PhysRevB.41.10188.

188. Markel, V., Shalaev, V. M. & Stechel, E. Small-particle composites. I. Linear optical properties. *Phys. Rev. B - Condens. Matter Mater. Phys.* (1996) doi:10.1103/PhysRevB.53.2425.

189. Novotny, L., Bian, R. X. & Xie, X. S. Theory of nanometric optical tweezers. *Phys. Rev. Lett.* (1997) doi:10.1103/PhysRevLett.79.645.

190. Xu, H., Aizpurua, J., Käll, M. & Apell, P. Electromagnetic contributions to single-molecule sensitivity in surface-enhanced Raman scattering. *Phys. Rev. E - Stat. Physics, Plasmas, Fluids, Relat. Interdiscip. Top.* (2000) doi:10.1103/PhysRevE.62.4318.

191. Kurz, S., Becker, U. & Maisch, H. Dynamic simulation of electromechanical systems: From maxwell's theory to common-rail diesel injection. *Naturwissenschaften* (2001) doi:10.1007/s001140100215.

192. Scherer, A., Painter, O., Vuckovic, J., Loncar, M. & Yoshie, T. Photonic crystals for confining, guiding, and emitting light. *IEEE Trans. Nanotechnol.* (2002) doi:10.1109/TNANO.2002.1005421.

193. Bian, R. X., Dunn, R. C., Xie, X. S. & Leung, P. T. Single molecule emission characteristics in near-field microscopy. *Phys. Rev. Lett.* (1995) doi:10.1103/PhysRevLett.75.4772.

194. Mitsugi, S., Kim, Y.-J. & Goto, K. Finite-Difference-Time-Domain Analysis for Electro-Magnetic Field Distribution on Near-Field Optical Recording Probe Head. *Opt. Rev.* **8**, 120–125 (2001).

195. Taflove, A. & Hagness, S. C. *Computational Electrodynamics: The Finite-Difference Time-Domain Method, Third Edition*. *Artech House* (2005).

196. Yu, W. & Mittra, R. A conformal finite difference time domain technique for modeling curved dielectric surfaces. *IEEE Microw. Wirel. Components Lett.* (2001) doi:10.1109/7260.905957.

197. Lavrinenko, A. V., Schmidt, F., Gregersen, N., Lægsgaard, J. & Sødergaard, T. *Numerical methods in photonics*. *Numerical Methods in Photonics* (2014). doi:10.1201/b17408.

198. Kisslinger, R. *et al.* Nonlithographic Formation of Ta2O5Nanodimple Arrays Using Electrochemical Anodization and Their Use in Plasmonic Photocatalysis for Enhancement of Local Field and Catalytic Activity. *ACS Appl. Mater. Interfaces* (2021) doi:10.1021/acsami.0c18580.

199. Kar, P. *et al.* High rate CO2 photoreduction using flame annealed TiO2 nanotubes. *Appl. Catal. B Environ.* (2019) doi:10.1016/j.apcatb.2018.08.002.

200. Vahidzadeh, E. *et al.* Asymmetric Multipole Plasmon-Mediated Catalysis Shifts the Product Selectivity of CO 2 Photoreduction toward C 2+ Products . *ACS Appl. Mater. Interfaces* (2021) doi:10.1021/acsami.0c21067.

201. Manuel, A. P., Kirkey, A., Mahdi, N. & Shankar, K. Plexcitonics – fundamental principles and optoelectronic applications. *J. Mater. Chem. C* **7**, 1821–1853 (2019).

202. Ford, G. W. & Weber, W. H. Electromagnetic interactions of molecules with metal surfaces. *Physics Reports* (1984) doi:10.1016/0370-1573(84)90098-X.

203. Yuen-Zhou, J. *et al.* Plexciton Dirac points and topological modes. *Nat. Commun.* (2016) doi:10.1038/ncomms11783.

204. Schlather, A. E., Large, N., Urban, A. S., Nordlander, P. & Halas, N. J. Near-field mediated plexcitonic coupling and giant Rabi splitting in individual metallic dimers. *Nano Lett.* (2013) doi:10.1021/nl4014887.

205. Karademir, E., Balci, S., Kocabas, C. & Aydinli, A. Plexcitonic crystals: a tunable platform for light-matter interactions. *Opt. Express* **22**, 21912–21920 (2014).

206. Kumar, P. *et al.* Noble Metal Free, Visible Light Driven Photocatalysis Using TiO2 Nanotube Arrays Sensitized by P-Doped C3N4 Quantum Dots. *Adv. Opt. Mater.* (2020) doi:10.1002/adom.201901275.

207. Alam, K. M. *et al.* CVD grown nitrogen doped graphene is an exceptional visible-light driven photocatalyst for surface catalytic reactions. *2D Mater.* **7**, 15002 (2019).

208. Mohammadpour, A. & Shankar, K. Anodic TiO2 nanotube arrays with optical wavelength-sized apertures. *J. Mater. Chem.* (2010) doi:10.1039/c0jm02198a.

209. Goswami, A., Aravindan, S. & Rao, P. V. Fabrication of substrate supported bimetallic nanoparticles and their optical characterization through reflection spectra. *Superlattices Microstruct.* **91**, 252–258 (2016).

210. Barman, B. *et al.* Fabrication of silver nanoparticles on glass substrate using low-temperature rapid thermal annealing. *Energy Environ.* **29**, 358–371 (2018).

211. Catchpole, K. R. & Polman, A. Plasmonic solar cells. *Opt. Express* **16**, 21793–21800 (2008).

212. Barman, B. *et al.* Formation of plasmonic silver nanoparticles using rapid thermal annealing at low temperature and study in reflectance reduction of Si surface. *Adv. Nat. Sci. Nanosci. Nanotechnol.* **8**, 35010 (2017).

213. Cheah, A. J. *et al.* Facile synthesis of a Ag/MoS2 nanocomposite photocatalyst for enhanced visible-light driven hydrogen gas evolution. *Catal. Sci. Technol.* **5**, 4133–4143 (2015).

214. Kumar, P. *et al.* C3N5: A Low Bandgap Semiconductor Containing an Azo-Linked Carbon Nitride Framework for Photocatalytic, Photovoltaic and Adsorbent Applications. *J. Am. Chem. Soc.* **141**, 5415–5436 (2019).

215. Lindquist, N. C., Nagpal, P., McPeak, K. M., Norris, D. J. & Oh, S.-H. Engineering metallic nanostructures for plasmonics and nanophotonics. *Reports Prog. Phys.* **75**, 36501 (2012).

216. Schmid, G. & Chi, L. F. Metal Clusters and Colloids. *Adv. Mater.* **10**, 515–526 (1998).

217. Kim, H.-J. & Kim, D.-E. Frictional behavior of Ag nanodot-pattern fabricated by thermal dewetting. *Surf. Coatings Technol.* **215**, 234–240 (2013).

218. Singh, R., Fakhruddin, M. & Poole, K. F. Rapid photothermal processing as a semiconductor manufacturing technology for the 21st century. *Appl. Surf. Sci.* **168**, 198–203 (2000).

219. Thompson, C. V. Solid-State Dewetting of Thin Films. *Annu. Rev. Mater. Res.* **42**, 399–434 (2012).

220. Farzinpour, P. *et al.* Altering the dewetting characteristics of ultrathin gold and silver films using a sacrificial antimony layer. *Nanotechnology* **23**, 495604 (2012).

221. Meškinis, Š. *et al.* Annealing Effects on Structure and Optical Properties of Diamond-Like Carbon Films Containing Silver. *Nanoscale Res. Lett.* **11**, 146 (2016).

222. Klar, T. *et al.* Surface-Plasmon Resonances in Single Metallic Nanoparticles. *Phys. Rev. Lett.* **80**, 4249–4252 (1998).

223. Jiang, M.-M. *et al.* Hybrid quadrupolar resonances stimulated at short wavelengths using coupled plasmonic silver nanoparticle aggregation. *J. Mater. Chem. C* **2**, 56–63 (2014).

224. Madou, M. J. *Manufacturing Techniques for Microfabrication and Nanotechnology*. *Manufacturing Techniques for Microfabrication and Nanotechnology* (2011). doi:10.1201/9781439895306.

225. P.J. Kelly, R. D. A. & Centre. Magnetron sputtering: a review of recent developments and applications. *Vacuum* (2000).

226. Tiwari, A. *Handbook of antimicrobial coatings*. *Handbook of Antimicrobial Coatings* (Elseiver, 2017). doi:10.1016/C2016-0-01441-9.

227. Senturia, S. D. *Microsystem Design*. *Microsystem Design* (Kluwer Academic Publishers, 2002). doi:10.1007/b117574.

228. Altomare, M., Nguyen, N. T. & Schmuki, P. Templated dewetting: designing entirely self-organized platforms for photocatalysis. *Chem. Sci.* (2016) doi:10.1039/C6SC02555B.

229. Jiran, E. & Thompson, C. V. Capillary instabilities in thin films. *J. Electron. Mater.* (1990) doi:10.1007/BF02673327.

230. Brandon, R. & Bradshaw, F. J. The mobility of the surface atoms of copper and silver evaporated deposits. *Tech. Rep.* (1966).

231. Hazle, M. A., Mehicic, M., Gardiner, D. J. & Graves, P. R. Practical Raman Spectroscopy. *Vib. Spectrosc.* (1990) doi:10.1016/0924-2031(90)80015-v.

232. Prezgot, D. & Ianoul, A. Probing the anisotropy of SERS enhancement with spatially separated plasmonic modes in strongly coupled silver nanocubes on a dielectric substrate. *J. Phys. Chem. C* (2015) doi:10.1021/jp512142a.

233. Princeton Instruments. Raman Spectroscopy Basics - Application Note. *Internet: http://content. piacton. com/Uploads/Princeton/* (2012).

234. Thermoscientific. DXR Raman Microscope. http://www.revbase.com/tt/sl.ashx?z=73090c66&dataid=256059&ft=1.

235. Palik, E. D. & Ghosh, G. *Handbook of optical constants of solids*. (Academic Press, 1998).

236. Yang, S. *et al.* Template-confined dewetting process to surface nanopatterns: Fabrication, structural tunability, and structure-related properties. *Adv. Funct. Mater.* (2011) doi:10.1002/adfm.201002387.

237. Quan, J. *et al.* A study on the correlation between the dewetting temperature of Ag film and SERS intensity. *Sci. Rep.* (2017) doi:10.1038/s41598-017-15372-y.

238. Smith, D. L. *Thin-film deposition : principles and practice*. (McGraw-Hill, 1995).

239. Chiyah, B. & Kayed, K. Effect of Annealing Temperature on the Structural and Optical Properties of Silver Oxide Thin Films Prepared by Thermal Evaporation with Subsequent Annealing. *J. Nanoelectron. Optoelectron.* **11**, (2018).

240. Wang, X., Li, S., Yu, H., Yu, J. & Liu, S. Ag2O as a new visible-light photocatalyst: Self-stability and high photocatalytic activity. *Chem. - A Eur. J.* (2011) doi:10.1002/chem.201101032.

241. Thouti, E., Chander, N., Dutta, V. & Komarala, V. Optical properties of Ag nanoparticle layers deposited on silicon substrates. *J. Opt.* **15**, 5005 (2013).

242. Paramelle, D. *et al.* A rapid method to estimate the concentration of citrate capped silver nanoparticles from UV-visible light spectra. *Analyst* **139**, 4855–4861 (2014).

243. Sundquist, B. E. A direct determination of the anisotropy of the surface free energy of solid gold, silver, copper, nickel, and alpha and gamma iron. *Acta Metall.* **12**, 67–86 (1964).

244. J. P. Clarkson, J. Winans, and P. M. F. On the scaling behavior of dipole and quadrupole modes in coupled plasmonic nanoparticle pairs. *Opt. Mater. Express* **1**, 970–979 (2011).

245. Haiss, W., Thanh, N. T. K., Aveyard, J. & Fernig, D. G. Determination of Size and Concentration of Gold Nanoparticles from UV−Vis Spectra. *Anal. Chem.* **79**, 4215–4221 (2007).

246. Karthikeyan, B. Optical studies on thermally surface plasmon tuned Au, Ag and Au:Ag nanocomposite polymer films. *Spectrochim. Acta Part A Mol. Biomol. Spectrosc.* **96**, 456–460 (2012).

247. Luk'yanchuk, B. *et al.* The Fano resonance in plasmonic nanostructures and metamaterials. *Nat. Mater.* **9**, 707–715 (2010).

248. Otieno, F., Airo, M., Ranganathan, K. & Wamwangi, D. Annealed silver-islands for enhanced optical absorption in organic solar cell. *Thin Solid Films* **598**, 177–183 (2016).

249. Ozel, T. *et al.* Surface-state emission enhancement in white-luminophor CdS nanocrystals using localized plasmon coupling. in *Conference Proceedings - Lasers and Electro-Optics Society Annual Meeting-LEOS* (2008). doi:10.1109/LEOS.2008.4688597.

250. Tompkins, H. G. & Hilfiker, J. N. *Spectroscopic ellipsometry : practical application to thin film characterization*. *Materials characterization and analysis collection* (Momentum Press, 2016).

251. Perera, M. N. M. N., Schmidt, D., Gibbs, W. E. K., Juodkazis, S. & Stoddart, P. R. Effective optical constants of anisotropic silver nanoparticle films with plasmonic properties. *Opt. Lett.* **41**, 5495–5498 (2016).

252. Oates, T. W. H., Wormeester, H. & Arwin, H. Characterization of plasmonic effects in thin films

and metamaterials using spectroscopic ellipsometry. *Prog. Surf. Sci.* **86**, 328–376 (2011).

253. Perera, M. N. M. N., Gibbs, W. E. K., Juodkazis, S. & Stoddart, P. R. Wavelength and refractive index dependence of the geometrical enhancement in surface-enhanced Raman scattering. *J. Raman Spectrosc.* **48**, 1182–1189 (2017).

254. Magnozzi, M., Bisio, F. & Canepa, M. Solid-state dewetting of thin Au films studied with real-time, in situ spectroscopic ellipsometry. *Appl. Surf. Sci.* **421**, 651–655 (2017).

255. Alford, R. *et al.* Toxicity of organic fluorophores used in molecular imaging: literature review. *Mol. Imaging* (2009).

256. Thaler, S. *et al.* In vivo toxicity study of rhodamine 6G in the rat retina. *Investig. Ophthalmol. Vis. Sci.* (2008) doi:10.1167/iovs.07-1476.

257. Smith, W. E. & Rodger, C. Surface-Enhanced Raman Scattering (SERS), Applications*. in *Encyclopedia of Spectroscopy and Spectrometry (Second Edition)* (ed. Lindon, J. C.) 2822–2827 (Academic Press, 1999). doi:https://doi.org/10.1016/B978-0-12-374413-5.00304-3.

258. Michaels, A. M., Nirmal, M. & Brus, L. E. Surface Enhanced Raman Spectroscopy of Individual Rhodamine 6G Molecules on Large Ag Nanocrystals. *J. Am. Chem. Soc.* **121**, 9932–9939 (1999).

259. Nie, S. & Emory, S. R. Probing Single Molecules and Single Nanoparticles by Surface-Enhanced Raman Scattering. *Science (80-.).* **275**, 1102 (1997).

260. Dieringer, J. A. *et al.* Surface-enhanced Raman excitation spectroscopy of a single rhodamine 6G molecule. *J. Am. Chem. Soc.* (2009) doi:10.1021/ja8080154.

261. Wahadoszamen, M. *et al.* Laser Raman spectroscopy with different excitation sources and extension to surface enhanced raman spectroscopy. *J. Spectrosc.* (2015) doi:10.1155/2015/895317.

262. Sivapalan, S. T. *et al.* Off-Resonance Surface-Enhanced Raman Spectroscopy from Gold Nanorod Suspensions as a Function of Aspect Ratio: Not What We Thought. *ACS Nano* **7**, 2099–2105 (2013).

263. Zhu, J., Gao, J., Li, J. J. & Zhao, J. W. Improve the surface-enhanced Raman scattering from rhodamine 6G adsorbed gold nanostars with vimineous branches. *Appl. Surf. Sci.* (2014) doi:10.1016/j.apsusc.2014.10.095.

264. Li, R. *et al.* Surface-enhanced Raman scattering from rhodamine 6G on gold-coated self-organized silicon nanopyramidal array. *J. Mater. Res.* (2013) doi:10.1557/jmr.2013.352.

265. Kha, N. M., Chen, C. H., Su, W. N., Rick, J. & Hwang, B. J. Improved Raman and photoluminescence sensitivity achieved using bifunctional Ag@SiO2 nanocubes. *Phys. Chem. Chem. Phys.* (2015) doi:10.1039/c4cp05217j.

266. Geitner, N. K. *et al.* The morphology and evolution of bipyramidal gold nanoparticles. *Nanotechnology* (2011) doi:10.1088/0957-4484/22/27/275607.

267. Zhang, L. *et al.* Gold nanoshurikens with uniform sharp tips for chemical sensing by the localized surface plasmon resonance. *Nanoscale* (2017) doi:10.1039/c7nr05585d.

268. Sun, M., Zhang, Z., Zheng, H. & Xu, H. In-situ plasmon-driven chemical reactions revealed by high vacuum tip-enhanced Raman spectroscopy. *Sci. Rep.* **2**, 647 (2012).

269. You, T. *et al.* Direct observation of p,p'-dimercaptoazobenzene produced from p-aminothiophenol and p-nitrothiophenol on Cu2O nanoparticles by surface-enhanced Raman spectroscopy. *J. Raman Spectrosc.* **45**, (2014).

270. Lin, W. *et al.* Electrically enhanced hot hole driven oxidation catalysis at the interface of a plasmon-exciton hybrid. *Nanoscale* (2018) doi:10.1039/c7nr08878g.

271. Gong, Z., Ji, J. & Wang, J. Photocatalytic reversible reactions driven by localized surface plasmon resonance. *Catalysts* (2019) doi:10.3390/catal9020193.

272. Devasenathipathy, R. Surface Plasmon Enhanced Chemical Reactions on Metal Nanostructures. in (ed. Wu, D.-Y.) Ch. 9 (IntechOpen, 2020). doi:10.5772/intechopen.89606.

273. Dong, B., Fang, Y., Chen, X., Xu, H. & Sun, M. Substrate-, wavelength-, and time-dependent plasmon-assisted surface catalysis reaction of 4-nitrobenzenethiol dimerizing to p,p'-dimercaptoazobenzene on Au, Ag, and Cu films. *Langmuir* (2011) doi:10.1021/la2018538.

274. Zhang, Q. & Wang, H. Mechanistic Insights on Plasmon-Driven Photocatalytic Oxidative Coupling of Thiophenol Derivatives: Evidence for Steady-State Photoactivated Oxygen. *J. Phys. Chem. C* (2018) doi:10.1021/acs.jpcc.8b00660.

275. Yang, X. *et al.* Plasmon-exciton coupling of monolayer MoS2-Ag nanoparticles hybrids for surface catalytic reaction. *Mater. Today Energy* (2017) doi:10.1016/j.mtener.2017.05.005.

276. Ren, X. *et al.* Recent advances in surface plasmon-driven catalytic reactions. *RSC Advances* (2017) doi:10.1039/c7ra05346k.

277. Engelbrekt, C., Crampton, K. T., Fishman, D. A., Law, M. & Apkarian, V. A. Efficient Plasmon-Mediated Energy Funneling to the Surface of Au@Pt Core–Shell Nanocrystals. *ACS Nano* **14**, 5061–5074 (2020).

278. Zeman, E. J. & Schatz, G. C. An accurate electromagnetic theory study of surface enhancement factors for silver, gold, copper, lithium, sodium, aluminum, gallium, indium, zinc, and cadmium. *J. Phys. Chem.* **91**, 634–643 (1987).

279. Hartland, G. Designing plasmon resonances. *Journal of Physical Chemistry Letters* (2014) doi:10.1021/jz500703x.

280. Hartland, G. V. Optical Studies of Dynamics in Noble Metal Nanostructures. *Chem. Rev.* **111**, 3858–3887 (2011).

281. Sytwu, K., Vadai, M. & Dionne, J. A. Bimetallic nanostructures: combining plasmonic and catalytic metals for photocatalysis. *Adv. Phys. X* **4**, 1619480 (2019).

282. Aslam, U., Rao, V. G., Chavez, S. & Linic, S. Catalytic conversion of solar to chemical energy on plasmonic metal nanostructures. *Nat. Catal.* **1**, 656–665 (2018).

283. Zhan, C. *et al.* From plasmon-enhanced molecular spectroscopy to plasmon-mediated chemical reactions. *Nat. Rev. Chem.* **2**, 216–230 (2018).

284. Sim, S. *et al.* Ultrafast relaxation dynamics in bimetallic plasmonic catalysts. *Nanoscale* **12**, 10284–10291 (2020).

285. Linic, S., Christopher, P. & Ingram, D. B. Plasmonic-metal nanostructures for efficient conversion of solar to chemical energy. *Nature Materials* (2011) doi:10.1038/nmat3151.

286. Huang, H. *et al.* Unraveling Surface Plasmon Decay in Core–Shell Nanostructures toward Broadband Light-Driven Catalytic Organic Synthesis. *J. Am. Chem. Soc.* **138**, 6822–6828 (2016).

287. Long, R. *et al.* Efficient Coupling of Solar Energy to Catalytic Hydrogenation by Using Well-Designed Palladium Nanostructures. *Angew. Chemie Int. Ed.* **54**, 2425–2430 (2015).

288. Wang, F. *et al.* Plasmonic Harvesting of Light Energy for Suzuki Coupling Reactions. *J. Am. Chem. Soc.* **135**, 5588–5601 (2013).

289. Adleman, J. R., Boyd, D. A., Goodwin, D. G. & Psaltis, D. Heterogenous Catalysis Mediated by Plasmon Heating. *Nano Lett.* **9**, 4417–4423 (2009).

290. Guo, L. *et al.* Photocatalytic glycerol oxidation on AuxCu–CuS@TiO2 plasmonic heterostructures. *J. Mater. Chem. A* **6**, 22005–22012 (2018).

291. Walker, J. M., Gou, L., Bhattacharyya, S., Lindahl, S. E. & Zaleski, J. M. Photothermal Plasmonic Triggering of Au Nanoparticle Surface Radical Polymerization. *Chem. Mater.* **23**, 5275–5281 (2011).

292. Haas, K. M. & Lear, B. J. Billion-fold rate enhancement of urethane polymerization via the photothermal effect of plasmonic gold nanoparticles. *Chem. Sci.* **6**, 6462–6467 (2015).

293. Araujo, T. P., Quiroz, J., Barbosa, E. C. M. & Camargo, P. H. C. Understanding plasmonic catalysis with controlled nanomaterials based on catalytic and plasmonic metals. *Curr. Opin. Colloid Interface Sci.* **39**, 110–122 (2019).

294. Amendola, V., Pilot, R., Frasconi, M., Maragò, O. M. & Iatì, M. A. Surface plasmon resonance in gold nanoparticles: a review. *J. Phys. Condens. Matter* **29**, 203002 (2017).

295. Lin, S.-C., Hsu, C.-S., Chiu, S.-Y., Liao, T.-Y. & Chen, H. M. Edgeless Ag–Pt Bimetallic Nanocages: In Situ Monitor Plasmon-Induced Suppression of Hydrogen Peroxide Formation. *J. Am. Chem. Soc.* **139**, 2224–2233 (2017).

296. Sarina, S. *et al.* Enhancing Catalytic Performance of Palladium in Gold and Palladium Alloy Nanoparticles for Organic Synthesis Reactions through Visible Light Irradiation at Ambient Temperatures. *J. Am. Chem. Soc.* **135**, 5793–5801 (2013).

297. Baida, F. I., Belkhir, A., Van Labeke, D. & Lamrous, O. Subwavelength metallic coaxial waveguides in the optical range: Role of the plasmonic modes. *Phys. Rev. B* **74**, 205419 (2006).

298. Leosson, K., Nikolajsen, T., Boltasseva, A. & Bozhevolnyi, S. I. Long-range surface plasmon polariton nanowire waveguides for device applications. *Opt. Express* **14**, 314–319 (2006).

299. Major, K. J., De, C. & Obare, S. O. Recent Advances in the Synthesis of Plasmonic Bimetallic Nanoparticles. *Plasmonics* **4**, 61–78 (2009).

300. Lang, H., Maldonado, S., Stevenson, K. J. & Chandler, B. D. Synthesis and Characterization of

Dendrimer Templated Supported Bimetallic Pt−Au Nanoparticles. *J. Am. Chem. Soc.* **126**, 12949–12956 (2004).

301. Lu, P., Teranishi, T., Asakura, K., Miyake, M. & Toshima, N. Polymer-Protected Ni/Pd Bimetallic Nano-Clusters: Preparation, Characterization and Catalysis for Hydrogenation of Nitrobenzene. *J. Phys. Chem. B* **103**, 9673–9682 (1999).

302. Mulvaney, P. Surface Plasmon Spectroscopy of Nanosized Metal Particles. *Langmuir* **12**, 788–800 (1996).

303. Sun, S., Murray, C. B., Weller, D., Folks, L. & Moser, A. Monodisperse FePt Nanoparticles and Ferromagnetic FePt Nanocrystal Superlattices. *Science (80-.).* **287**, 1989 LP – 1992 (2000).

304. Salem, A. K., Searson, P. C. & Leong, K. W. Multifunctional nanorods for gene delivery. *Nat. Mater.* **2**, 668 (2003).

305. Pullen, A. E. *et al.* Electrically Conducting Materials Based On μ-Tetrathiooxalato-Bridged Bimetallic Ni(II) Anionic Complexes. *Inorg. Chem.* **36**, 4163–4171 (1997).

306. Toshima, N. & Yonezawa, T. Bimetallic nanoparticles—novel materials for chemical and physical applications. *New J. Chem.* **22**, 1179–1201 (1998).

307. Duan, S. & Wang, R. Bimetallic nanostructures with magnetic and noble metals and their physicochemical applications. *Progress in Natural Science: Materials International* (2013) doi:10.1016/j.pnsc.2013.02.001.

308. Stern, E. A. & Ferrell, R. A. Surface Plasma Oscillations of a Degenerate Electron Gas. *Phys. Rev.* **120**, 130–136 (1960).

309. Lundqvist, P. A. and S. Surface Electromagnetic Waves and Surface Plasmons at a Bimetallic Interface. *Phys. Scr.* **30**, 360 (1984).

310. Belotelov, V. I. *et al.* Online monitoring of alloyed bimetallic nanoparticle formation by optical spectroscopy. *J. Appl. Phys.* **99**, 44304 (2006).

311. Zhang, C., Chen, B.-Q., Li, Z.-Y., Xia, Y. & Chen, Y.-G. Surface Plasmon Resonance in Bimetallic Core–Shell Nanoparticles. *J. Phys. Chem. C* **119**, 16836–16845 (2015).

312. Gao, J., Ren, X., Chen, D., Tang, F. & Ren, J. Bimetallic Ag–Pt hollow nanoparticles: Synthesis and tunable surface plasmon resonance. *Scr. Mater.* **57**, 687–690 (2007).

313. Patra, K. K. & Gopinath, C. S. Bimetallic and Plasmonic Ag–Au on TiO2 for Solar Water Splitting: An Active Nanocomposite for Entire Visible-Light-Region Absorption. *ChemCatChem* (2016) doi:10.1002/cctc.201600937.

314. Swearer, D. F. *et al.* Heterometallic antenna−reactor complexes for photocatalysis. *Proc. Natl. Acad. Sci.* **113**, 8916 LP – 8920 (2016).

315. Zhang, C. *et al.* Al–Pd Nanodisk Heterodimers as Antenna–Reactor Photocatalysts. *Nano Lett.* **16**, 6677–6682 (2016).

316. Blaber, M. G., Arnold, M. D. & Ford, M. J. A review of the optical properties of alloys and intermetallics for plasmonics. *J. Phys. Condens. Matter* **22**, 143201 (2010).

317. Ye, W. *et al.* Electrochemical deposition of Au–Pt alloy particles with cauliflower-like microstructures for electrocatalytic methanol oxidation. *Int. J. Hydrogen Energy* **37**, 4088–4097 (2012).

318. Zheng, Z., Tachikawa, T. & Majima, T. Single-Particle Study of Pt-Modified Au Nanorods for Plasmon-Enhanced Hydrogen Generation in Visible to Near-Infrared Region. *J. Am. Chem. Soc.* **136**, 6870–6873 (2014).

319. Guo, J. *et al.* Boosting Hot Electrons in Hetero-superstructures for Plasmon-Enhanced Catalysis. *J. Am. Chem. Soc.* **139**, 17964–17972 (2017).

320. Zhou, L. *et al.* Quantifying hot carrier and thermal contributions in plasmonic photocatalysis. *Science (80-.).* **362**, 69 LP – 72 (2018).

321. Weber, M. J., Mackus, A. J. M., Verheijen, M. A., van der Marel, C. & Kessels, W. M. M. Supported Core/Shell Bimetallic Nanoparticles Synthesis by Atomic Layer Deposition. *Chem. Mater.* **24**, 2973–2977 (2012).

322. Manuel, A. P. *et al.* Plasmonic photocatalysis and SAB - Silver nanoislands are key platforms for plasmonic photocatalysis, SERS sensing and optical metamaterials due to their localized surface plasmon resonances. The low intrinsic loss in Ag enables high local electromagneti. *Nanotechnology* **31**, 365301 (2020).

323. Ganbold, E. O., Park, J. H., Dembereldorj, U., Ock, K. S. & Joo, S. W. Charge-dependent adsorption of rhodamine 6G on gold nanoparticle surfaces: Fluorescence and Raman study. *J. Raman Spectrosc.* (2011) doi:10.1002/jrs.2907.

324. Ma, M. *et al.* Electrochemical reduction of CO2 on compositionally variant Au-Pt bimetallic thin films. *Nano Energy* **42**, 51–57 (2017).

325. Agarwal, N. R., Ossi, P. M. & Trusso, S. Driving electromagnetic field enhancements in tailored gold surface nanostructures: Optical properties and macroscale simulations. *Appl. Surf. Sci.* **466**, 19–27 (2019).

326. Ben Wannes, H. *et al.* Study of the stabilizer influence on the structural and optical properties of sol-gel spin coated zinc oxide films. *Materials Science in Semiconductor Processing* (2018) doi:10.1016/j.mssp.2017.10.017.

327. Qazi, S. J. S., Rennie, A. R., Cockcroft, J. K. & Vickers, M. Use of wide-angle X-ray diffraction to measure shape and size of dispersed colloidal particles. *J. Colloid Interface Sci.* (2009) doi:10.1016/j.jcis.2009.06.006.

328. Sahay, P. P. & Nath, R. K. Al-doped ZnO thin films as methanol sensors. *Sensors Actuators, B Chem.* (2008) doi:10.1016/j.snb.2008.06.006.

329. Geng, G. *et al.* Sheetlike gold nanostructures/graphene oxide composites: Via a one-pot green fabrication protocol and their interesting two-stage catalytic behaviors. *RSC Adv.* (2017) doi:10.1039/c7ra11188f.

330. Ozaki, T. Variationally optimized atomic orbitals for large-scale electronic structures. *Phys. Rev. B - Condens. Matter Mater. Phys.* (2003) doi:10.1103/PhysRevB.67.155108.

331. Bachelet, G. B., Hamann, D. R. & SchÏter, M. Pseudopotentials that work: From H to Pu. *Phys. Rev. B* (1982) doi:10.1103/PhysRevB.26.4199.

332. Perdew, J. P., Burke, K. & Ernzerhof, M. Generalized gradient approximation made simple. *Phys. Rev. Lett.* (1996) doi:10.1103/PhysRevLett.77.3865.

333. Niemantsverdriet, J. W. *Spectroscopy in Catalysis: An Introduction: Third Edition*. *Spectroscopy in Catalysis: An Introduction: Third Edition* (2007). doi:10.1002/9783527611348.

334. Boerigter, C., Aslam, U. & Linic, S. Mechanism of Charge Transfer from Plasmonic Nanostructures to Chemically Attached Materials. *ACS Nano* (2016) doi:10.1021/acsnano.6b01846.

335. Supur, M., Smith, S. R. & McCreery, R. L. Characterization of Growth Patterns of Nanoscale Organic Films on Carbon Electrodes by Surface Enhanced Raman Spectroscopy. *Anal. Chem.* **89**, 6463–6471 (2017).

336. McGrane, S. D., Moore, D. S., Goodwin, P. M. & Dattelbaum, D. M. Quantitative Tradeoffs between Spatial, Temporal, and Thermometric Resolution of Nonresonant Raman Thermometry for Dynamic Experiments. *Appl. Spectrosc.* **68**, 1279–1288 (2014).

337. Kracker, M., Wisniewski, W. & Rüssel, C. Textures of Au, Pt and Pd/PdO nanoparticles thermally dewetted from thin metal layers on fused silica. *RSC Adv.* (2014) doi:10.1039/c4ra07296k.

338. Müller, C. M., Mornaghini, F. C. F. & Spolenak, R. Ordered arrays of faceted gold nanoparticles obtained by dewetting and nanosphere lithography. *Nanotechnology* (2008) doi:10.1088/0957-4484/19/48/485306.

339. Wang, D. *et al.* Electronic behaviour of Au-Pt alloys and the 4f binding energy shift anomaly in Au bimetallics- X-ray spectroscopy studies. *AIP Adv.* **8**, 65210 (2018).

340. Tan, C. *et al.* A self-supporting bimetallic Au@Pt core-shell nanoparticle electrocatalyst for the synergistic enhancement of methanol oxidation. *Sci. Rep.* (2017) doi:10.1038/s41598-017-06639-5.

341. Wang, D. *et al.* Electronic behaviour of Au-Pt alloys and the 4f binding energy shift anomaly in Au bimetallics- X-ray spectroscopy studies. *AIP Adv.* (2018) doi:10.1063/1.5027251.

342. Bond, G. C. The electronic structure of platinum-gold alloy particles: Better catalysts for selective oxidations. *Platin. Met. Rev.* (2007) doi:10.1595/147106707X187353.

343. Wang, Y. & Hou, M. Ordering of bimetallic nanoalloys predicted from bulk alloy phase diagrams. *J. Phys. Chem. C* (2012) doi:10.1021/jp302260b.

344. Calvo, F. Thermodynamics of nanoalloys. *Physical Chemistry Chemical Physics* (2015) doi:10.1039/c5cp00274e.

345. Goubet, N. *et al.* Size and nanocrystallinity controlled gold nanocrystals: Synthesis, electronic and mechanical properties. *Nanoscale* (2015) doi:10.1039/c4nr06513a.

346. Staechelin, Y. U., Hoeing, D., Schulz, F. & Lange, H. Size-Dependent Electron-Phonon Coupling in Monocrystalline Gold Nanoparticles. *ACS Photonics* (2021) doi:10.1021/acsphotonics.1c00078.

347. García-Negrete, C. A. *et al.* Island-type growth of Au-Pt heterodimers: direct visualization of misfit

dislocations and strain-relief mechanisms. *RSC Adv.* (2015) doi:10.1039/c5ra09808d.

348. Bazán-Díaz, L., Mendoza-Cruz, R., Liao, C.-K. & Mahmoud, M. A. Asymmetric Deposition of Platinum Atoms on Gold Nanorods Reduced the Plasmon Field Distortion Induced by the Substrate. *J. Phys. Chem. C* **123**, 30509–30518 (2019).

349. Marinica, D.-C., Aizpurua, J. & Borisov, A. G. Quantum effects in the plasmon response of bimetallic core-shell nanostructures. *Opt. Express* (2016) doi:10.1364/oe.24.023941.

350. Griffin, S. *et al.* Imaging Energy Transfer in Pt-Decorated Au Nanoprisms via Electron Energy-Loss Spectroscopy. *J. Phys. Chem. Lett.* (2016) doi:10.1021/acs.jpclett.6b01878.

351. Li, J. F. *et al.* Surface-Enhanced raman spectroscopy using gold-core platinum-shell nanoparticle film electrodes: Toward a versatile vibrational strategy for electrochemical interfaces. *Langmuir* (2006) doi:10.1021/la061366d.

352. Murray, C. A. Using surface enhanced Raman scattering to study vibrations of adsorbates on thin metallic overlayers on silver. *J. Electron Spectros. Relat. Phenomena* (1983) doi:10.1016/0368-2048(83)80090-5.

353. Zou, S. & Weaver, M. J. Surface-Enhanced Raman Scattering on Uniform Transition-Metal Films: Toward a Versatile Adsorbate Vibrational Strategy for Solid-Nonvacuum Interfaces? *Anal. Chem.* (1998) doi:10.1021/ac9800154.

354. Zhang, K. *et al.* Enhanced optical responses of Au@Pd core/shell nanobars. *Langmuir* (2009) doi:10.1021/la803060p.

355. Nordlander, P., Oubre, C., Prodan, E., Li, K. & Stockman, M. I. Plasmon Hybridization in Nanoparticle Dimers. *Nano Lett.* **4**, 899–903 (2004).

356. Long, R., Li, Y., Song, L. & Xiong, Y. Coupling Solar Energy into Reactions: Materials Design for Surface Plasmon-Mediated Catalysis. *Small* **11**, 3873–3889 (2015).

357. Zhang, Z. *et al.* Catalysis by Metal Nanoparticles in a Plug-In Optofluidic Platform: Redox Reactions of p-Nitrobenzenethiol and p-Aminothiophenol. *ACS Catal.* **8**, 2443–2449 (2018).

358. Lin, L. *et al.* Nanooptics of Plasmonic Nanomatryoshkas: Shrinking the Size of a Core-Shell Junction to Subnanometer. *Nano Lett.* (2015) doi:10.1021/acs.nanolett.5b02931.

359. Liu, J. B. *et al.* Optical properties of Au-core Pt-shell nanorods studied using FDTD simulations. *Front. Phys.* (2016) doi:10.1007/s11467-015-0528-3.

360. Sundararaman, R., Narang, P., Jermyn, A. S., Goddard III, W. A. & Atwater, H. A. Theoretical predictions for hot-carrier generation from surface plasmon decay. *Nat. Commun.* **5**, 5788 (2014).

361. Douglas-Gallardo, O. A., Berdakin, M., Frauenheim, T. & Sánchez, C. G. Plasmon-induced hot-carrier generation differences in gold and silver nanoclusters. *Nanoscale* (2019) doi:10.1039/c9nr01352k.

362. Hou, C., Hu, B. & Zhu, J. Photocatalytic degradation of methylene blue over TiO2 pretreated with varying concentrations of NaOH. *Catalysts* (2018) doi:10.3390/catal8120575.

363. Zielińska-Jurek, A. Progress, Challenge, and Perspective of Bimetallic TiO_2-Based Photocatalysts. *J.*

Nanomater. **2014**, 208920 (2014).

364. Doremus, R. H. Optical properties of small gold particles. *J. Chem. Phys.* (1964) doi:10.1063/1.1725519.

365. Besteiro, L. V. & Govorov, A. O. Amplified Generation of Hot Electrons and Quantum Surface Effects in Nanoparticle Dimers with Plasmonic Hot Spots. *J. Phys. Chem. C* (2016) doi:10.1021/acs.jpcc.6b05968.

366. Brown, A. M. *et al.* Experimental and Ab Initio Ultrafast Carrier Dynamics in Plasmonic Nanoparticles. *Phys. Rev. Lett.* (2017) doi:10.1103/PhysRevLett.118.087401.

367. Chavez, S., Aslam, U. & Linic, S. Design Principles for Directing Energy and Energetic Charge Flow in Multicomponent Plasmonic Nanostructures. *ACS Energy Lett.* **3**, 1590–1596 (2018).

368. Patterson, J. LXXII. On the electrical properties of thin metal films. *London, Edinburgh, Dublin Philos. Mag. J. Sci.* **4**, 652–678 (1902).

369. Fischer, G., Hoffmann, H. & Vancea, J. Mean free path and density of conductance electrons in platinum determined by the size effect in extremely thin films. *Phys. Rev. B* (1980) doi:10.1103/PhysRevB.22.6065.

370. Dutta, S. *et al.* Thickness dependence of the resistivity of platinum-group metal thin films. *J. Appl. Phys.* (2017) doi:10.1063/1.4992089.

371. Gall, D. The search for the most conductive metal for narrow interconnect lines. *Journal of Applied Physics* (2020) doi:10.1063/1.5133671.

372. Hodak, J. H., Henglein, A. & Hartland, G. V. Tuning the spectral and temporal response in PtAu core-shell nanoparticles. *J. Chem. Phys.* (2001) doi:10.1063/1.1339266.

373. Maher, R. C., Galloway, C. M., Le Ru, E. C., Cohen, L. F. & Etchegoin, P. G. Vibrational pumping in surface enhanced Raman scattering (SERS). *Chem. Soc. Rev.* (2008) doi:10.1039/b707870f.

374. Manjavacas, A., Liu, J. G., Kulkarni, V. & Nordlander, P. Plasmon-induced hot carriers in metallic nanoparticles. *ACS Nano* (2014) doi:10.1021/nn502445f.

375. Huang, Y.-F. *et al.* Activation of Oxygen on Gold and Silver Nanoparticles Assisted by Surface Plasmon Resonances. *Angew. Chemie Int. Ed.* **53**, 2353–2357 (2014).

376. Marimuthu, A., Zhang, J. & Linic, S. Tuning Selectivity in Propylene Epoxidation by Plasmon Mediated Photo-Switching of Cu Oxidation State. *Science (80-.).* **339**, 1590 LP – 1593 (2013).

377. Chen, X., Zhu, H., Zhao, J.-C., Zheng, Z.-F. & Gao, X.-P. *Visible-Light-Driven Oxidation of Organic Contaminants in Air with Gold Nanoparticle Catalysts on Oxide Supports*. *Angewandte Chemie (International ed. in English)* vol. 47 (2008).

378. Ohtani, B., Iwai, K., Nishimoto, S. & Sato, S. Role of Platinum Deposits on Titanium(IV) Oxide Particles: Structural and Kinetic Analyses of Photocatalytic Reaction in Aqueous Alcohol and Amino Acid Solutions. *J. Phys. Chem. B* **101**, 3349–3359 (1997).

379. Zhang, D. *Visible light-induced photocatalysis through surface plasmon excitation of platinum-metallized titania for photocatalytic bleaching of rhodamine B*. *Monatshefte für Chemie -*

Chemical Monthly vol. 143 (2011).

380. Westcott, S. L., Jackson, J. B., Radloff, C. & Halas, N. J. Relative contributions to the plasmon line shape of metal nanoshells. *Phys. Rev. B* **66**, 155431 (2002).

381. Chung, T. *et al.* Nanoislands as plasmonic materials. *Nanoscale* (2019) doi:10.1039/c8nr10539a.

382. Kang, M., Park, S. G. & Jeong, K. H. Repeated Solid-state Dewetting of Thin Gold Films for Nanogap-rich Plasmonic Nanoislands. *Sci. Rep.* (2015) doi:10.1038/srep14790.